PREPARATION AND CHARACTERIZATION OF TITANIA BASED POWDERS AND SUSPENSIONS FOR PHOTOCATALYTIC APPLICATIONS

A Thesis Submitted to
the Graduate School of Engineering and Sciences of
İzmir Institute of Technology
in Partial Fulfillment of the Requirements for the Degree of

DOCTOR OF PHILOSOPHY

in Chemical Engineering

by
Hüsnü Arda YURTSEVER

June 2015
İZMİR

We approve the thesis of **Hüsnü Arda YURTSEVER**

Examining Committee Members:

Prof. Dr. Muhsin ÇİFTÇİOĞLU
Department of Chemical Engineering, İzmir Institute of Technology

Prof. Dr. Serdar ÖZÇELİK
Department of Chemistry, İzmir Institute of Technology

Prof. Dr. Oğuz BAYRAKTAR
Department of Chemical Engineering, Ege University

Prof. Dr. Mustafa DEMİRCİOĞLU
Department of Chemical Engineering, Ege University

Assist. Prof. Dr. Berna TOPUZ
Department of Chemical Engineering, Ankara University

19 June 2015

Prof. Dr. Muhsin ÇİFTÇİOĞLU
Supervisor, Department of Chemical
Engineering, İzmir Institute of
Technology

Prof. Dr. Fehime ÇAKICIOĞLU ÖZKAN
Head of the Department of Chemical
Engineering

Prof. Dr. Bilge KARAÇALI
Dean of the Graduate School of
Engineering and Sciences

ACKNOWLEDGEMENTS

I would like to express my deepest gratitude to my advisor, Prof. Dr. Muhsin ÇİFTÇİOĞLU for his guidance, support, motivation and encouragement during my thesis.

I would like to express my gratitude to Prof. Dr. Serdar ÖZÇELİK and Prof. Dr. Oğuz BAYRAKTAR for their precious contributions.

I am especially grateful to my laboratory colleagues for their support and assistance to my work.

I would also like to thank Metin UZ, Mert TUNÇER, Emre KILIÇ, Özgün DELİİSMAİL, Ali Emrah ÇETİN, Rukiye ÇİFTÇİOĞLU and Burcu ALP for their assistance during this study.

I would like to thank İzmir Institute of Technology Environmental Development Application and Research Center for providing technical support and help.

I would also thank to my wife Merve ÇAPKIN YURTSEVER for her technical, spiritual support during my PhD study and in our shared life. Her presence and love gave me the determination to work through out this study.

Lastly, I offer sincere thanks to my family; Bilgi YURTSEVER, Rasim YURTSEVER, Ayda MUTLU, Ayça TÜRKOĞLU and Mehmet ÇETİNKAYA for their love, continuous support and unlimited patience throughout my education.

This study was supported by The Scientific and Technological Research Council of Turkey (TUBITAK) within the context of MAG-ARDEB 110M739 project.

ABSTRACT

PREPARATION AND CHARACTERIZATION OF TITANIA BASED POWDERS AND SUSPENSIONS FOR PHOTOCATALYTIC APPLICATIONS

Growing environmental concerns related to the extensive use of nonsustainable fossil fuels and increasing energy demand will force mankind, sooner or later, to tap into clean and sustainable sources of energy and artificial photosynthesis is being considered as a promising prospect for this concern. Photocatalysis is expected to make a great contribution to solutions for environmental problems and renewable energy generation. Titania based photocatalytic materials are one of the widely used materials in artificial photosynthesis research due to their unique chemical and optical properties.

Recent research have shown that rare earth element (REE) doping improves the photocatalytic activity of TiO_2 phases in the visible region. The effects of REE doping level and heat treatment temperature on the microstructure evolution, optical properties and the photocatalytic water splitting/CO_2 photoreduction activities of mostly sol-gel derived titania powders were investigated in this thesis.

The results of this thesis indicated that REE ions may enter the interstitial voids of TiO_2 lattice or segregate on the grain boundaries of TiO_2 as a separate phase and $RE_2Ti_2O_7$ phases were formed for the REEs with relatively smaller ionic sizes. The experimental work conducted revealed the importance of surface area, crystallinity, light absorption, the presence of oxygen vacancies and structural defects in the efficiency of photocatalytic processes. Results have shown that REE doping improves the artificial photosynthesis activity of TiO_2 at relatively low doping levels and 700^{o}C heat treatment temperature as the production rate of H_2 and CO/CH_4 were significantly higher with REE doped TiO_2 compared to pure TiO_2.

ÖZET

TİTAN BAZLI TOZLAR VE ASILTILARIN FOTOKATALİTİK UYGULAMALARA YÖNELİK HAZIRLANMASI VE KARAKTERİZASYONU

Günümüzde ağırlıklı olarak sürdürülebilir olmayan fosil yakıtlara dayanan ve artan enerji ihtiyacının neden olduğu olumsuz etkiler ve bunların yarattığı kaygılar insanlığı er ya da geç sürdürülebilir temiz enerji kaynaklarına yöneltecektir. Hem küresel CO_2 miktarını azaltan ve hem de yenilenebilir yakıt üretimini sağlayan yapay fotosentez önemli bir seçenek oluşturmaktadır. Fotokatalitik süreçler çevresel sorunların çözümüne ve yenilenebilir enerji üretimine önemli katkılar yapacaktır. Titanya bazlı fotokatalitik malzemeler kimyasal ve optik özelliklerinden ötürü yapay fotosentez uygulamalarında en yaygın kullanılan malzemelerdendir.

Son yıllardaki araştırmalar nadir toprak elementi (NTE) katkılarının titanya fazlarını güneş ışınlarını görünür bölgede daha verimli kullanır hale getirebileceği yönünde önemli bulgular içermektedir. Bu tezde ağırlıklı olarak sol-jel temelli teknikler kullanılarak nadir toprak elementlerinin katkı düzeyleri ve ısıl işlem sıcaklığının titanya tozlarının mikroyapısal evrimine, optik özelliklerine ve fotokatalitik su parçalama/CO_2 indirgeme aktivitelerine etkisi araştırılmıştır.

Bu tezin sonuçları NTE iyonlarının ayrı bir oksit fazı olarak yapıda yer aldığını veya TiO_2 kafes boşluklarına yerleştiğine ve düşük iyonik çaplı NTE iyonlarının $NTE_2Ti_2O_7$ fazlarını oluşturabildiğine işaret etmektedir. Fotokatalitik süreçlerde yüzey alanı, kristalinite, ışık soğurma, oksijen boşlukları ve yapısal hataların aktivitede önemli rol oynadığı bu proje kapsamında yapılan deneylerle ortaya çıkmıştır. NTE katkısının TiO_2'in yapay fotosentez aktivitesini olumlu yönde etkilediği saptanmıştır. Bu tez çalışmasının sonuçları düşük katkı düzeyleri ve 700°C dolayında ısıl işleme tabi tutulan tozların H_2 üretimini ve CO/CH_4 üretimini önemli ölçüde artırdığını göstermektedir.

TABLE OF CONTENTS

APPENDICES

LIST OF FIGURES

Figure **Page**

LIST OF TABLES

CHAPTER 1

GENERAL INTRODUCTION

1.1. Introduction

Light energy of the sun captured and utilized by the plants through photosynthesis processes by the utilization of inorganic substances like CO_2 and water for the synthesis of organic compounds necessary for their survival started and sustains the life processes of animals (Collings and Critchley 2005). The balance in the plant-animal life processes was disturbed by human activities in the last two hundred years. Anthropogenic CO_2 emissions increased due to the increasing fossil fuel use since the beginning of industrial revolution and the excess CO_2 which cannot be consumed by the plants started to accumulate in the atmosphere. This accumulated CO_2 and other chlorofluorohydrocarbons in the atmosphere caused what is known as "Greenhouse Effect" phenomenon and global warming (Houghton 2004).

Growing environmental concerns related to the extensive use of nonsustainable fossil fuels (oil, natural gas and coal) and a constantly increasing energy demand will force mankind, sooner or later, to tap into clean and sustainable sources of energy. Photocatalysis is expected to make a great contribution to both environmental treatment (emission cleaning and water purification) and renewable energy generation (Zhu and Zach 2009).

Research on the utilization of solar energy in order to satisfy the increasing energy demand and to prevent "Global Warming" attracted significant interest in the last couple of decades. Artificial photosynthesis is being considered as a promising technique for the synthesis of renewable, sustainable fuels like methane, methanol and hydrogen in addition to the reduction of the global CO_2 content in the environment (Cogdell et al. 2010).

Photocatalyst materials play a central role in the success of the photocatalytic processes and artificial photosynthesis. These materials should be corrosion resistant (Zhu and Zach 2009), chemically stable and cheap with high and efficient visible light absorption (Silija et al. 2012). Nanoscience and nanotechnology are opening a new vista in the development of highly active, nanostructured photocatalysts with large surface areas for optimized light absorption, minimized distances (or times) for charge-carrier transport, and further favorable properties. The commonly known anatase and rutile phases of titania (TiO_2) are the most important and widely used materials in environmental related photocatalytic research and applications. The most important disadvantage of these titania phases is their relatively high bandgap energies commonly reported in the 3.0-3.2 eV range which results in the very limited absorption of sun light in the ultra-violet (UV) range which represents < 5% of solar radiation spectrum (Nassoko et al. 2012). The reduction and modification of the bandgap energies of the titania phases by doping with various elements for more efficient absorption in the visible range, the determination of the activities of these materials in the photocatalytic decomposition of organic structures and artificial photosynthesis are the main concern of intense research in the last 10-15 years. These dopants comprise heavily nonmetals like C, N, S etc. (Cong et al. 2007, Dong et al. 2011, Park et al. 2006, Rockafellow et al. 2009, Shen et al. 2007, Yang et al. 2010) and transition metals like Cu, Ag, Fe, Co etc. (Akpan and Hameed 2010, Silija et al. 2012, Baiju et al. 2007, Nie et al. 2009).

Research conducted in the last 5-10 years on the effects of titania phase stability and dye decomposition activities have shown that rare earth incorporation to the titania phases reduced the bandgap energy, widened the absorption of light in the visible region and increased the photocatalytic activity (Choudhury et al. 2013, Li et al. 2004, Obregon et al. 2013, Ranjit et al. 2001, Xiao et al. 2007). Despite all these desired observations, there is no consensus on whether the dopant ions are incorporated in the titania lattice structure (Li et al. 2005, Nassoko et al. 2012, Ningthoujam et al. 2009, Setiawati et al. 2008, Shah et al. 2002, Wang et al. 2010), the solubility limits of the metal ions in these phases, if the metal ions are not incorporated (Antić et al. 2012, Luo et al. 2008, Shahmoradi et al. 2010) in the lattice structure what mechanisms are responsible for the higher wavelength absorption in the resultant multi-phase nanostructure. One group of researchers claims that lattice incorporation of the dopant metal ions is not possible due to the significantly larger sizes of the lanthanide ions compared to Ti^{4+} whereas a second group believes that they can sit in the anion, cation or tetrahedral/octahedral interstitial sites. One common observation is that the lanthanide incorporation retards the anatase-to-rutile phase transformation and generates a high surface area material (Hishita et al. 1983, Nguyen-Phan et al. 2009, Zhang et al. 2004). Binary phase diagrams for a better understanding of these multiphase systems are present at high temperatures (Gong and Zhang 2013, Skapin et al. 2000) and the information about the presence or absence of some of the high temperature compounds is not available in the 400-800^{o}C temperature range. A better understanding of the effect of the nature and electronic structures of the phase interface on bandgap reduction, electron-hole recombination, increases in the dye decomposition activity is very important and is not clearly known yet. Lanthanide incorporated titania phases were used in a few studies towards hydrogen production by water splitting (Zalas and Laniecki 2005) and CO_2 photoreduction related artificial photosynthesis (Matejova et al. 2014, Ogura et al. 1992, Wang et al. 2013, Zhao et al. 2012).

Photocatalytic reduction of CO_2 will contribute to finding an effective solution to global warming if efficient photocatalytic materials are properly designed and fabricated in the near future. Reducing CO_2 level in the atmosphere along with producing alternatives to fossil fuels can be accomplished by using highly active photocatalytic materials in artificial photosynthesis.

The nanodesign of rare earth (lanthanides, Y, Zr, La, Ce, Nd etc.) and transition elements (Cu, Ag, Cr, Fe, Ni etc.) incorporated titania based nanostructured materials by using various sol-gel and chemical precipitation techniques was conducted in this PhD study in order to clarify the dopant sites in the structure and the effect of rare earth element/transition metal doping on the artificial photosynthesis activity of TiO_2 phases. Phase structures of these materials (the locations of the dopant metals and the resultant lattice structure changes, new phase formations), the effect of the dopants on the bandgap and absorption behavior, particle/pore size and surface area changes were investigated. Nanostructured materials were prepared by using precursors mixed at the atomic scale/level by using sol-gel and chemical precipitation techniques. The activities of the selected nanodesigned materials with high surface areas and micro-mesoporous pore structures in photocatalytic water splitting and CO_2 photoreduction were determined in the context of this PhD study.

1.2. Global Warming and Energy

A French mathematician, Jean Baptiste Fourier discovered in 1824 that earth's temperature was increasing gradually. This discovery which is about the reflection of sunlight scattered from the earth's surface by the atmosphere led the basic theory of

"Global Warming" arise. This theory was named as the "Greenhouse Effect" since 1990s. Scientific research showed that CO_2 emission originating from the fossil fuel consumption as the main energy source is the reason for global warming (Collings and Critchley 2005).

Scientists found that earth's global temperature and sea levels raised approximately 0.6°C and 20 cm, respectively, during 20th century. Figure 1.1A shows the deviation of earth's surface temperature for the last 140 years from the average value calculated for the time period from 1961 to 1990. The average temperature difference reaches to 0.6°C by 2000s. Temperature differences for a period of 160 000 years from present and the change of CO_2 concentration in the atmosphere are given in Figure 1.1B. In the year 2100, global CO_2 concentration will reach from the present value of 369 ppmv to 650 ppmv unless the excessive fossil fuel consumption is stopped (Houghton 2004).

Many governments are trying to take precautions by regulations since the discovery and acceptance of Global Warming. The most important international agreement to find a solution towards global warming is the "Kyoto Protocol" which was accepted in 1997. According to this protocol, greenhouse gases emissions would have been reduced beginning from 2005 by 125 countries which accepted this protocol (Collings and Critchley 2005).

In the U.S. Energy Information Administration 2014 Report a projection was made that energy related CO_2 emissions will decrease from 5999 million metric tons in 2005 to 5599 million metric tons in 2040 as shown in Figure 1.2. Energy related CO_2 emissions will decline by 0.2%/year on average from 2005 to 2040, as compared with an average increase of 0.9%/year from 1980 to 2005 (Conti 2014).

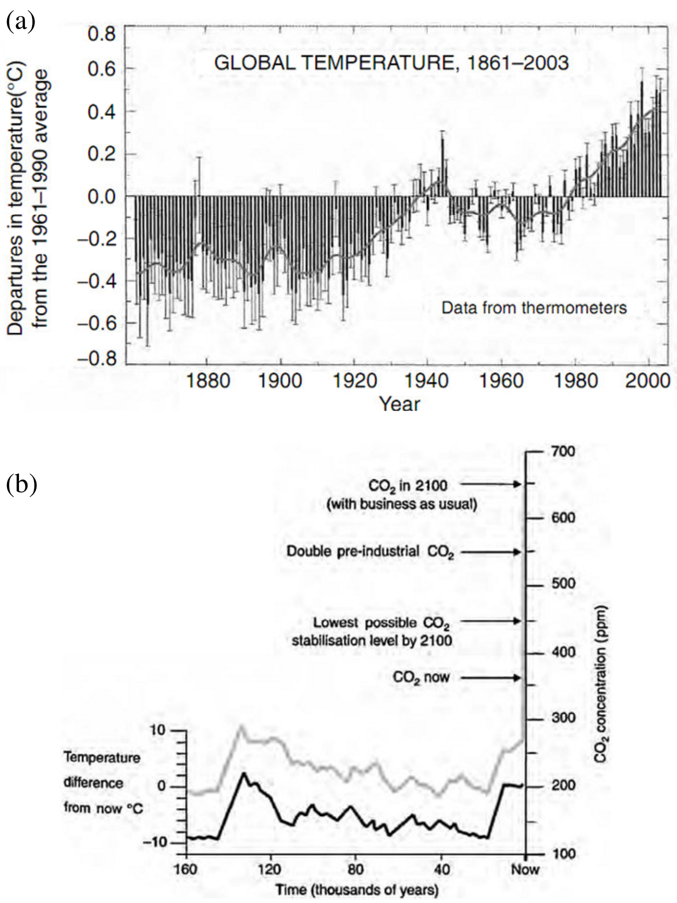

Figure 1.1. (a) The change of the deviation of temperature in 140 years from the average value calculated for the time period from 1961 to 1990. (b) The change of atmospheric CO$_2$ concentration and polar temperature which were derived from the Vostok ice core for the last 160 000 years. (Source: Houghton 2004)

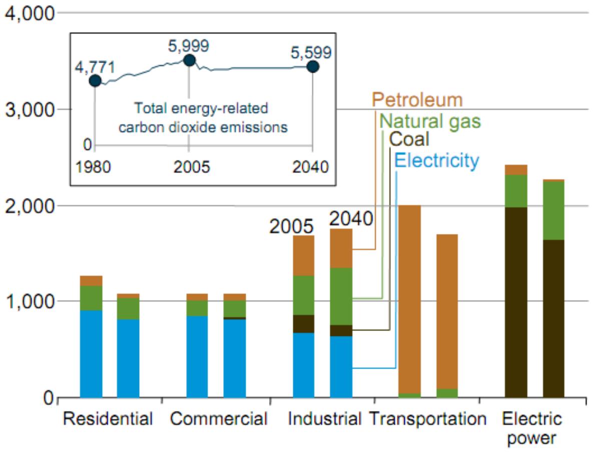

Figure 1.2. U.S. energy-related carbon dioxide emissions by sector and fuel in the Reference case, 2005 and 2040 (million metric tons). (Source: Conti 2014)

1.3. Energy from the Sun

Energy from fossil fuels (oil, natural gas and coal), nuclear energy and renewable energy (solar, wind, geothermal and biomass) are possible choices that can be used to satisfy the energy demand of humanity and sustain life on earth. Geopolitical issues about fossil fuels, capital costs of constructing renewable energy producing facilities force us to use non-sustainable fossil fuels. More than 80% of global energy need is provided by fossil fuels at present. The dependence on fossil fuels to create and sustain the well-being and development of society damages the nature irreversibly.

Use of fossil fuels to sustain the energy production until now caused the aforesaid global warming and pollution problem. Growing environmental concerns related to the extensive use of non-sustainable fossil fuels and a constantly increasing energy demand will force mankind, sooner or later, to tap into clean and sustainable sources of energy. Solar energy is one of these sustainable energy resources to meet our present and future energy demand. Being limitless and free makes it a promising choice among these renewable resources. The hourly solar energy flux to the earth is more than the energy that we consume in a year. Our energy need can be provided by harvesting 0.02% of the energy from the sun without using any other energy resources. Solar energy can be converted into electrical energy for the simultaneous production and use or can be converted into heat or chemical energy and stored for further use (Hammarstrom and Hammes-Schiffer 2009).

The earth is heated with an energy flux of 1369 W/m^2 after 30% of solar energy is absorbed and scattered in the atmosphere. The reason for the loss of energy is the absorption by gases such as water, ozone, CO_2 and the scattering by clouds and aerosols in the atmosphere. Light with wavelengths lower than 300 nm is absorbed by ozone, nitrogen and oxygen. Absorption in the infrared region is caused by water and CO_2. Solar radiation spectrum at the top of the atmosphere and at sea level is given in Figure 1.3. Solar light spectrum in the range of 300 to 2500 nm is present on the surface of the earth which is partially absorbed in the atmosphere. Solar radiation spectrum consists mainly of UV (300-400 nm), visible (400-800 nm) and infrared (800-2500 nm) regions representing 5%, 40% and 55% of the total solar energy flux, respectively.

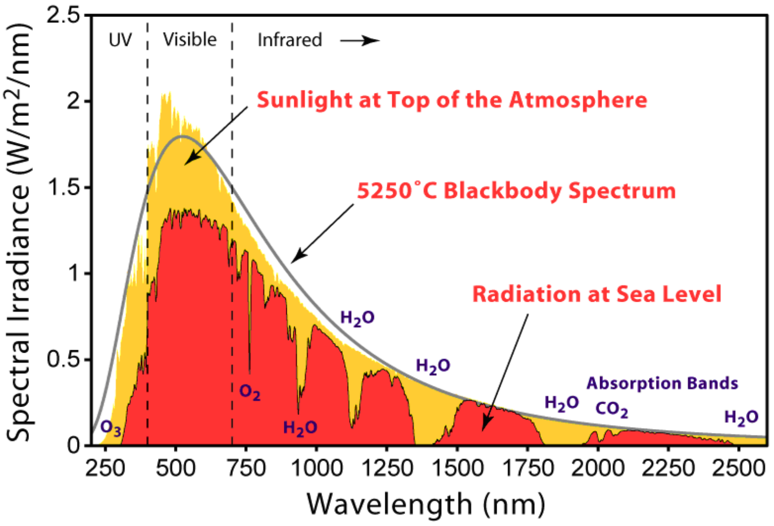

Figure 1.3. Solar radiation spectrum.
(Source: http://www.globalwarmingart.com)

Turkey has a very high potential for the production of renewable energy (hydro, solar, wind, biomass and geothermal energy), however this potential is not used properly in the energy production today. Energy need of Turkey is mostly supplied by burning of coal and imported oil/natural gas. Energy dependency of Turkey on imported sources may be significantly decreased by the proper use of high solar energy potential. The solar energy potential atlas of Turkey is given in Figure 1.4. Except Blacksea and Marmara Region the solar radiation is about 1500 kWh/m^2-year, which is higher than most countries.

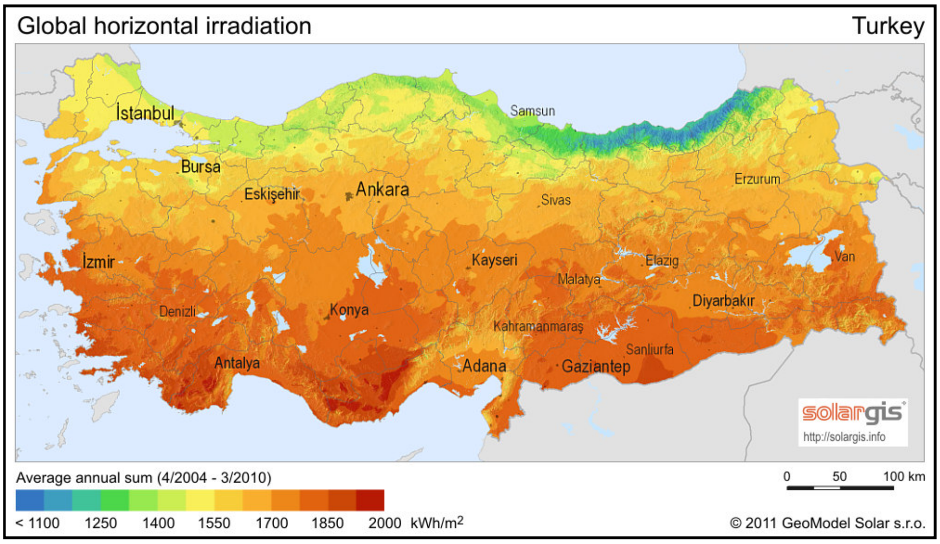

Figure 1.4. Solar energy potential atlas of Turkey.
(Source: http://solargis.info)

1.4. Natural and Artificial Photosynthesis

In natural photosynthesis plants and cyanobacteria (which are photoautotrophic) synthesize their own building block materials from inorganic compounds such as CO_2, nitrates, sulfates with the help of sunlight energy. Photon energy splits water into oxygen and hydrogen which is then bounded to NADPH (Nicotinamide adenine dinucleotide phosphate). This process, which is called as *Light Reactions*, is conducted at photosynthesis reaction centers embedded in cell wall and includes the electron transfer related to ATP (Adenozine triphosphate) synthesis. In *Dark Reactions,* NADPH, ATP and CO_2 is consumed in Calvin Cycle (Figure 1.5) to produce carbohydrates (Heldt 2005).

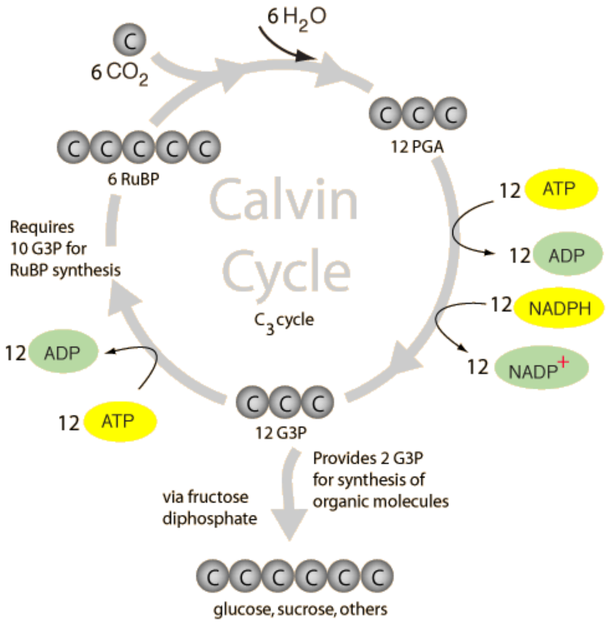

Figure 1.5. The Calvin cycle.
(Source: Moore et al. 1995)

Biomass, oxygen and also fossil fuels are the products of photosynthesis organized by plants and cyanobacteria. Life on earth is tied to photosynthesis and is a cycle of CO_2 (Figure 1.6). Animals are heterotrophic and need carbohydrates/other organics to survive. They provide the energy for their own life processes by oxidizing biomass which is produced by plants. Oxygen is consumed and CO_2 is thus produced during this process. In brief, sun light captured and utilized by plants is the source of life and related processes on earth (Heldt 2005).

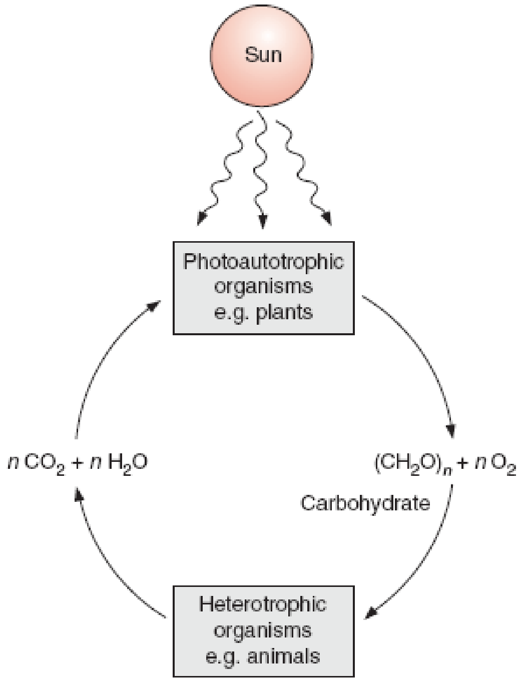

Figure 1.6. Life on earth with a CO_2 cycle.
(Source: Heldt 2005)

Photosynthesis by green plants basically starts with the capture and absorption of sunlight with wavelengths smaller than 480 nm and between 550-700 nm by pigments called chlorophyll. Plants are green because light in the 480-550 nm wavelength range cannot be absorbed. Chlorophyll has two main types which are chlorophyll-a and chlorophyll-b. Chlorophyll-a constitutes 80% of whole chlorophyll family. The absorption spectrum of light by the pigments in green plants is given in Figure 1.7A. Chlorophyll-b (in which a formyl group is present rather than a methyl group as in chlorophyll-a) is in charge of capturing and delivering the light to chlorophyll-a effectively. In this sense green plants have nanocomposite structures in molecular level to maximize capture of sun light. The absorption spectra given in Figure 1.7B belong to red algae and cyanobacteria which live in the deeper parts of the oceans and these spectra indicate that a nanocomposite structure in molecular level is present in these organisms similar to green plants. Pychobiliprotein (which is also called accessory pigment) content of cyanobacteria and red algea makes them absorb green light and survive in the deeper parts of the ocean. Structural difference of the light absorbing pigments is the main reason for different absorption spectra of organisms living in different environments.

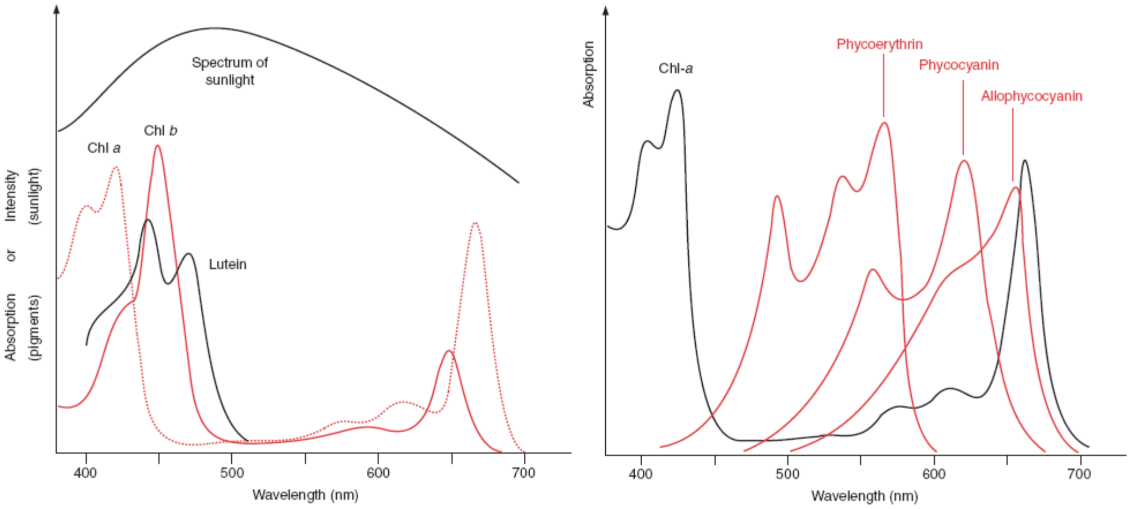

Figure 1.7. Absorption spectra of light capturing molecules in green plants (on the left), solar radiation spectrum (upper left part of the figure) and absorption spectra of light capturing molecules in red algae and cyanobacteria that live in deeper parts of the oceans (on the right). (Source: Heldt 2005)

Solar energy can be utilized by different ways. Solar cells can transform solar energy into electricity, solar ponds can store the energy from the sun as heat energy and solar energy can be used to generate steam for turbines or transformed into chemical energy via photocatalysis (Hammarstrom and Hammes-Schiffer 2009). Each method has both advantages and disadvantages. Photocatalysis is expected to make a great contribution to both environmental treatment (emission cleaning and water purification) and renewable energy generation (Fujishima et al. 2000). Photocatalysis may transform harmful industrial wastes into harmless disposable species. Special chemical reactions (e.g. CO_2 reduction) which may occur only in harsh conditions (high temperatures and high pressures) may also be conducted at room temperature and pressure via photocatalysis.

Artificial photosynthesis is the mimicking of natural photosynthesis and is one of the common photocatalytic processes which convert CO_2 and water into useful chemicals such as methanol, methane, carbon monoxide, other hydrocarbons and hydrogen which can be stored and used as energy source.

Intensive research on artificial photosynthesis (hydrogen production via water splitting and hydrocarbon production by the reduction of CO_2) which may become a key process in the future for sustainable energy needs of humanity and global pollution/warming prevention have been conducted in the last 10 years (Wu et al. 2005, Matejova et al. 2014, Raja et al. 2011, Tan et al. 2012, Uner et al. 2011, Zhang et al. 2009).

Protecting the environment and effective use of renewable energy sources are becoming globally concerned issues for the sustainability of human life. Photocatalysis is expected to be the solution to both problems. Photocatalysts are materials that can degrade organic pollutants in water, air and on some surfaces and are capable of triggering special chemical reactions. Photocatalysts used in artificial photosynthesis, will contribute to the generation of renewable energy resources by hydrogen production via water splitting and hydrocarbon production via CO_2 reduction. Research conducted on materials developed towards photocatalytic hydrogen splitting and artificial photosynthesis was reviewed in a number of articles published in the last decade (Dey 2007, Fan et al. 2009, Inoue 2009, Kalyanasundaram and Graetzel 2010, Neatu et al. 2014, de-Richter et al. 2013, Zhu and Zach 2009). “Artificial Photosynthesis Center” which was founded in California, U.S.A has a budget of 120 million $. In this center researchers from the universities and national laboratories of the country will work for realizing artificial photosynthesis which can be stated as a significant development indicating the global importance of artificial photosynthesis (Subbaraman 2010, web).

1.5. CO_2 Photoreduction Mechanism

The mechanism of photocatalytic reduction of CO_2 consists of water splitting and reduction of CO_2 with species formed in water splitting reactions. Mechanisms for photocatalytic water splitting and surface reactions in photocatalytic reduction of CO_2 are given schematically in Figure 1.8. Structural and electronic properties of semiconducting photocatalysts determine the important steps in photocatalysis such as the absorption of photons, charge separation/migration and surface adsorption/reactions. Captured holes react with water adsorbed on the surface of the semiconducting material to produce O_2 and H^+. H· radicals are formed by the interaction of H^+ ions with excited electrons. Union of two H· radicals forms one H_2 molecule. These two steps explain the photocatalytic water splitting mechanism. In the presence of CO_2, electrons interact with CO_2 molecules to form $\cdot CO_2^-$ radicals (Koci et al. 2009). Newly formed H· and $\cdot CO_2^-$ radicals react to form CO. Consecutive reactions transform CO to $\cdot CH_3$ radicals. Finally, CH_4 (methane) or CH_3OH (methanol) molecules are formed when $\cdot CH_3$ radicals react with H· or OH· radicals, respectively. These steps along with water splitting steps explain the photocatalytic reduction mechanism of CO_2 into hydrocarbons. The recombination of produced electron-hole pairs can cause releasing of heat without chemical work which is not desired in photocatalysis.

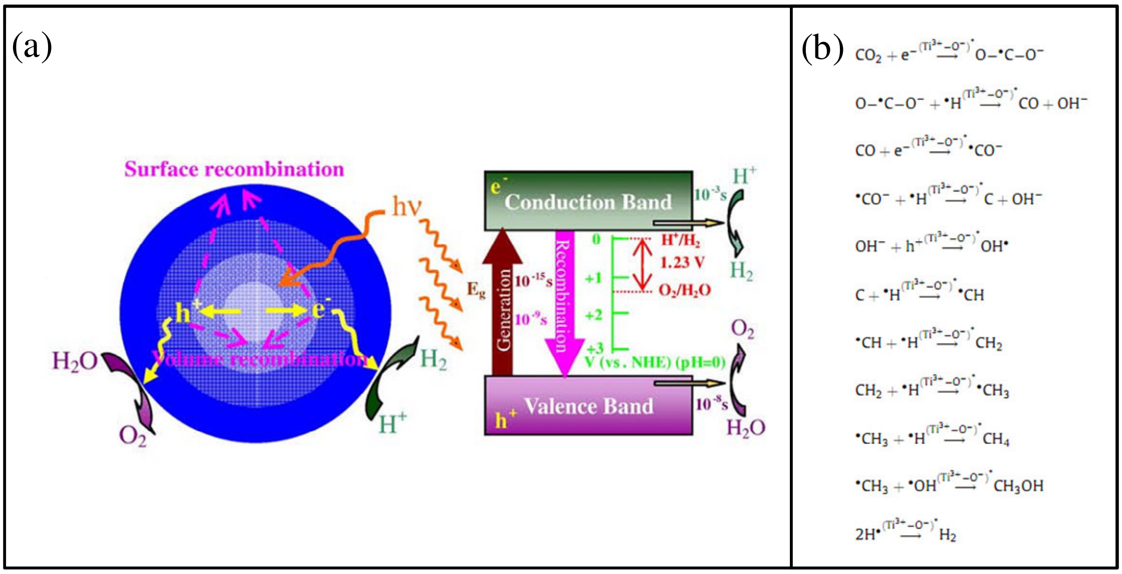

$$CO_2 + e^- \xrightarrow{(Ti^{3+}-O^-)^*} O-{}^\bullet C-O^-$$

$$O-{}^\bullet C-O^- + {}^\bullet H \xrightarrow{(Ti^{3+}-O^-)^*} CO + OH^-$$

$$CO + e^- \xrightarrow{(Ti^{3+}-O^-)^*} {}^\bullet CO^-$$

$${}^\bullet CO^- + {}^\bullet H \xrightarrow{(Ti^{3+}-O^-)^*} C + OH^-$$

$$OH^- + h^+ \xrightarrow{(Ti^{3+}-O^-)^*} OH^\bullet$$

$$C + {}^\bullet H \xrightarrow{(Ti^{3+}-O^-)^*} {}^\bullet CH$$

$${}^\bullet CH + {}^\bullet H \xrightarrow{(Ti^{3+}-O^-)^*} CH_2$$

$$CH_2 + {}^\bullet H \xrightarrow{(Ti^{3+}-O^-)^*} {}^\bullet CH_3$$

$${}^\bullet CH_3 + {}^\bullet H \xrightarrow{(Ti^{3+}-O^-)^*} CH_4$$

$${}^\bullet CH_3 + {}^\bullet OH \xrightarrow{(Ti^{3+}-O^-)^*} CH_3OH$$

$$2H^\bullet \xrightarrow{(Ti^{3+}-O^-)^*} H_2$$

Figure 1.8. (a) Photocatalytic water splitting (b) Surface reactions.
(Source: Koci et al. 2009, Zhu and Zach 2009)

1.6. Photocatalysts

Photocatalyst is a semiconductor which is mostly an oxide of a metal having a specific bandgap energy (E_g) between the conduction and valence band. Semiconductor becomes active when it is exposed to light having photons with energies equal to or higher than the bandgap energy of that material (Figure 1.9). An electron (e^-) hops to the conduction band of the semiconductor leaving a hole in the valence band which can act as a positively charged electron when the material is excited by photons (Linsebigler et al. 1995).

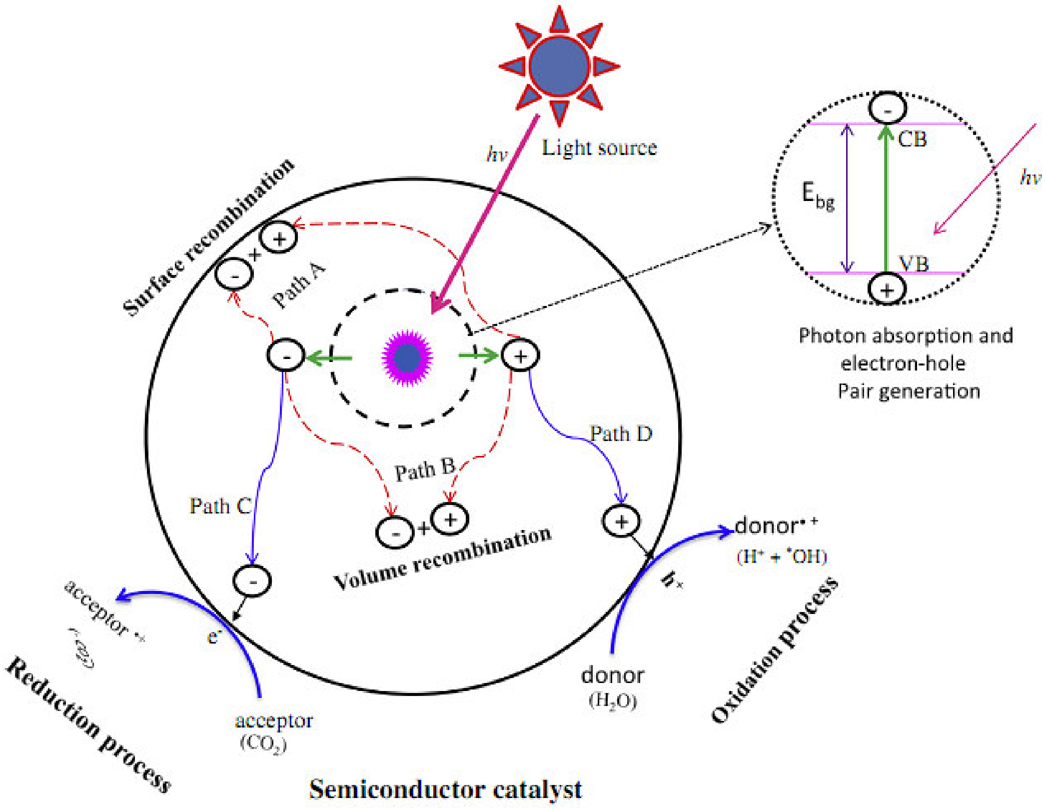

Figure 1.9. Schematic of photoexcitation of a semiconductor.
(Source: Tahir and Amin 2013)

An ideal photocatalyst should have the following characteristics:

i. photoactivity
ii. biologically and chemically inert
iii. photostable (i.e., not prone to photocorrosion)
iv. inexpensive
v. non-toxic

Photocatalytic processes are started and carried on by the electron-hole pairs which are formed by the absorption of light, energy transfer from the absorbed photons to the semiconductor and hopping of electrons from the valence band to the conduction band leaving holes acting as positively charged electrons. Electrons and holes are generated and separated on the surface of the semiconducting material when it is excited by an energy equal to or greater than the bandgap energy of this material. Excited electrons and holes can recombine dissipating the input energy as heat, get trapped in metastable surface states or react with electron donors/acceptors adsorbed on or near the semiconductor surface leading to oxidation-reduction reactions (Zaleska 2008).

Electron-hole pairs generated in the lattice are separated and captured in suitable parts of the nanostructure to avoid recombination on the surface or in the volume (path A or B). Holes conduct oxidation reactions (path D) and electrons conduct reduction reactions (path C) (Linsebigler et al. 1995). Electron transfer process is more efficient if the species are preadsorbed on the surface of the photocatalyst. The probability and the rate of charge transfer process depend strictly on the band edge position of the semiconducting material and the redox potential of the adsorbed species. The bottom of conduction band of the semiconductor must be at a more negative potential than H^+/H_2 (0 V vs. NHE at pH 0) and the top of the valence band must be at a more positive potential than H_2O/O_2 (1.23 V vs. NHE at pH 0) (Figure 1.10). The minimum electron energy should be 1.23 eV (corresponding wavelength c.a. 1000 nm) for water splitting reaction to be thermodynamically possible (Zang 2011). Some examples of photocatalysts and redox potentials of water splitting are also given in Figure 1.11.

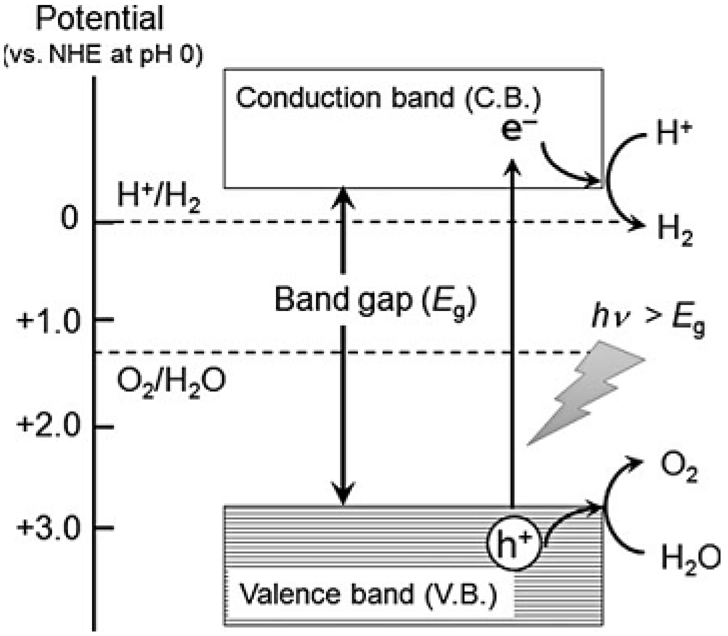

Figure 1.10. Mechanism of water splitting on a photo-activated semiconductor.
(Source: Zang 2011)

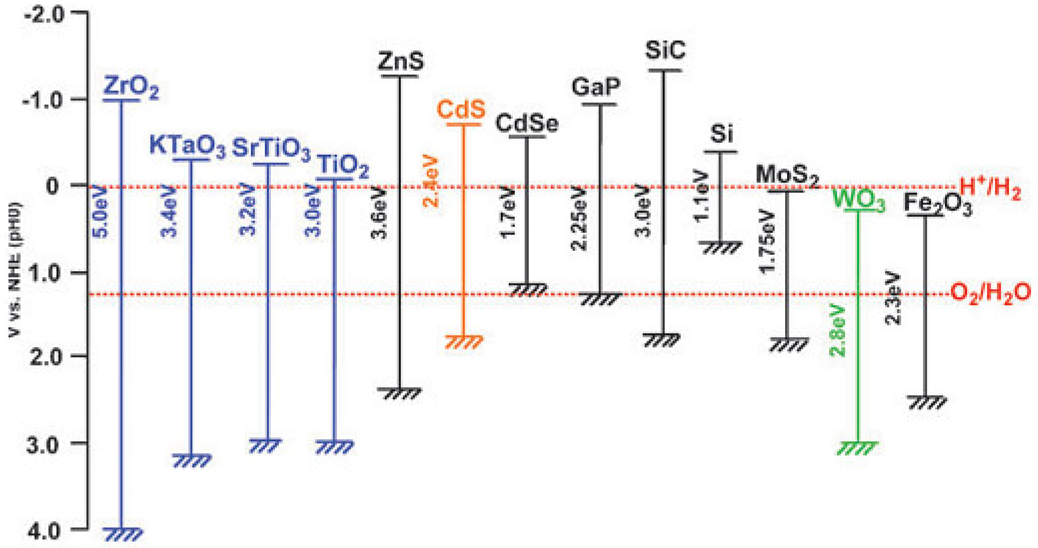

Figure 1.11. Relationship between band structure of semiconductor and redox potentials of water splitting. (Source: Kudo and Miseki 2008)

Intense research and advances in nanoscience and nanotechnology in the last 10 years improved the preparation techniques and expanded the application area of nanostructured photocatalytic materials. Fujishima and Honda conducted the pioneering studies in 1970s to produce renewable energy (artificial photosynthesis and water splitting to produce hydrocarbons and hydrogen) via photocatalytic processes by using solar energy (Fujishima and Honda 1972, Inoue et al. 1979). Since then many photocatalytic materials were prepared to be used in various photocatalytic processes. There are many examples in the literature and there is a huge variety of photocatalytic materials to be used in many different photocatalytic processes.

Many oxide, sulfide, nitride based semiconducting materials are used as photocatalysts since they have sufficient bandgap energies for photocatalysis. Some examples are TiO_2, WO_3, $SrTiO_3$ α-Fe_2O_3, ZnO, CuO, ZnS, CdS, CdSe, GaN. The bandgap energies of these materials are 3.2, 2.8, 3.2, 3.1, 3.2, 1.2, 3.6, 2.4, 1.7, 3.4 eV, respectively (Hoffman et al. 1995). These materials are used in many applications including photocatalysis (Figure 1.12). TiO_2 is the most extensively used photocatalyst since it is biologically and chemically inert, stable with respect to photocorrosion and chemical corrosion and inexpensive.

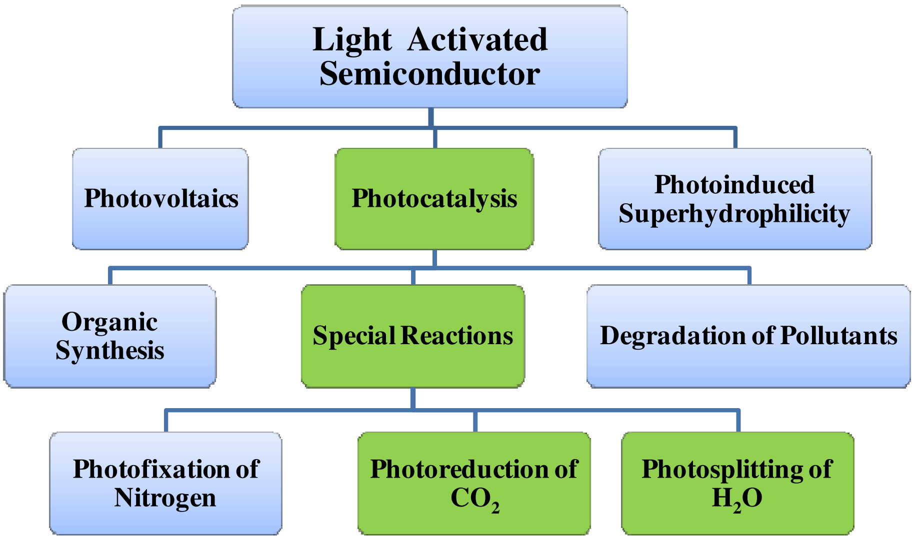

Figure 1.12. Applications of semiconducting materials.
(Source: Carp 2004)

Photoreduction of CO_2 and photosplitting of H_2O with semiconducting materials have great importance since both applications may be the solution to global warming and a convenient way to produce energy by utilizing renewable resources. A review paper published in 2009 shows the variety of nanomaterials prepared for photocatalytic hydrogen production investigated in research papers published during 10 years before the publication of the review paper in Figure 1.13 (Zhu and Zach 2009).

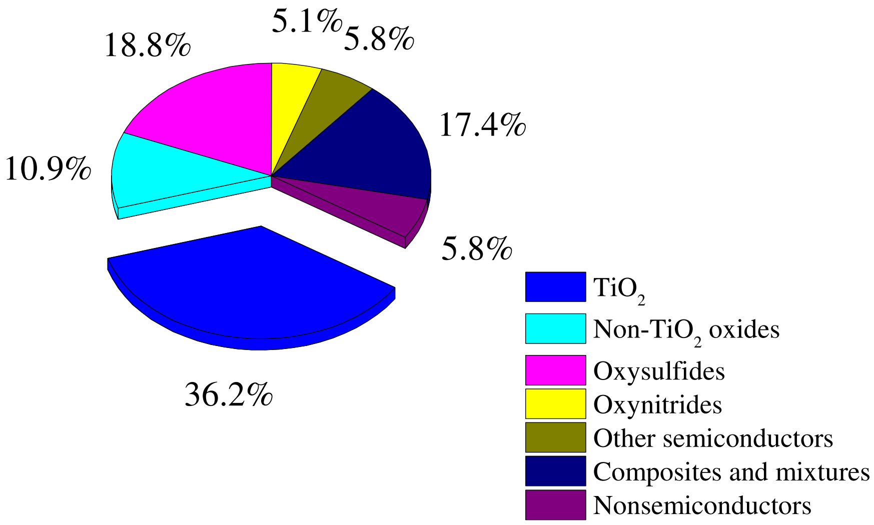

Figure 1.13. The variation of nanomaterials investigated for photocatalytic hydrogen production in literature. (Source: Zhu and Zach 2009)

1.7. Titanium Dioxide (Titania, TiO_2)

Extensive use of TiO_2 in the research and applications of photocatalytic processes is a consequence of its chemical stability/inertness, low cost and absorption capability of UV light. Hopping of one electron from the valence band to the conduction band of TiO_2 requires near UV or UV light to be absorbed since it has a bandgap of 3.0-3.2 eV. TiO_2 is active only under UV illumination which means less than 5% of solar radiation can be utilized by TiO_2 (Carp 2004). Photocatalysts which can absorb and utilize photons of solar radiation effectively are the products of well designed materials of nanoscience. Enhancement of the absorption of visible light photons by TiO_2 can be achieved by various methods which will be described in the following sections.

TiO_2 has three stable phases which are anatase, rutile, brookite along with three metastable and five high pressure phases. The lattice structures, lattice parameters and bond lengths/angles of anatase and rutile, most frequently used phases, are shown in Figure 1.14 and Table 1.1.

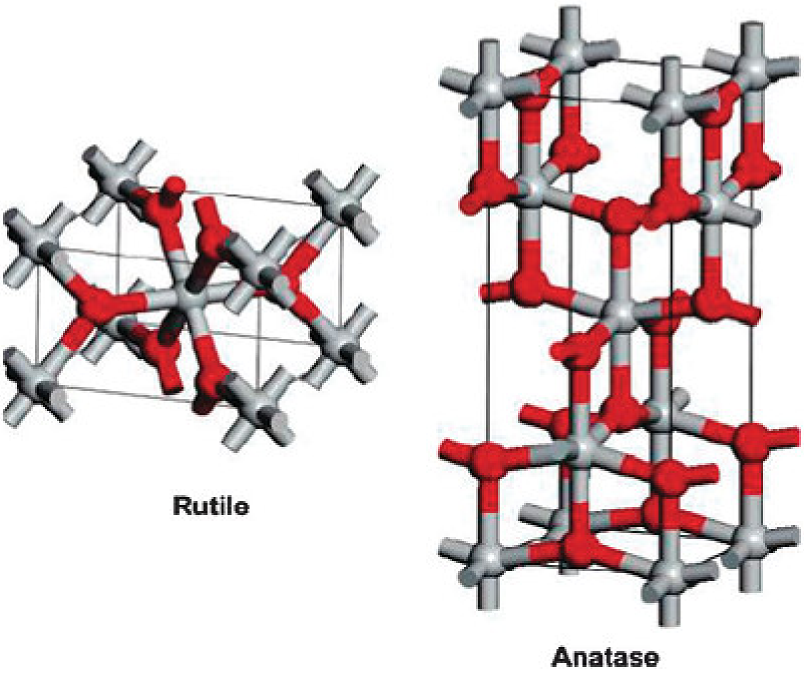

Figure 1.14. Tetragonal lattice structures of anatase and rutile (Ti atoms are gray).
(Source: Thompson and Yates 2006)

Table 1.1. Lattice parameters, bond lengths and angles of anatase and rutile. (Source: Labouriao and Earl 1997)

	Ti-O bond length (nm)	**O-Ti-O bond angle (°)**	**Lattice parameters (Å)**		
			a	b	c
Anatase	4-0.1934 2-0.1980	4-92.4 4-78.1 4-101.9	3.782	3.782	9.502
Rutile	4-0.1949 2-0.1980	2-98.8 2-81.2 8-90.0	4.594	4.594	2.958

TiO_2 can be synthesized by various methods for industrial or laboratory use. Sulfate and chloride methods are widely used for high production rates; however alkoxide method is widely used in research for lab-scale applications. These methods are based on the chemical source of the desired product, however chemical vapor deposition, precipitation, hydrothermal and solvo-thermal, sol-gel, emulsion and micro-emulsion, ultrasound and microwave irradiation, spray pyrolysis, electrochemical synthesis are common methods based on different apparatus used and different chemical and physical principles (Anpo and Kamat 2010). Based on the titanium precursor, *Sulfate, Chloride* and *Alkoxide* methods*,* based on the involved reactions and mechanisms *Sol-Gel* and *Chemical Precipitation* methods are described below.

Sulfate method:

In sulfate method, titanium oxysulphate ($TiOSO_4$) which is formed by dissolving titanium minerals in sulfuric acid is treated with a base to form hydrated TiO_2. After heat treatment (calcination) crystalline TiO_2 powders are obtained. Hydrated TiO_2 synthesized by sulfate method has low photocatalytic activity since it has crystal defects which act as centers for recombination of electron-hole pairs, despite the high surface area. The calcined hydrated TiO_2 has also low photocatalytic activity because of the contaminants (sulfate ion or ions from minerals) originating from the method (Gazquez et al. 2014).

Chloride method:

This method is also called as vapor method because titanium minerals are reacted with chlorine gas yielding titanium tetrachloride ($TiCl_4$) and oxidized to TiO_2 at 700-1000°C. Crystallization of TiO_2 into anatase or rutile also occurs because of the application of high temperatures. Commercially available Degussa P-25 which is commonly used by researchers is synthesized by using this method. Degussa P-25 has 80 wt.% anatase and 20 wt.% rutile phases and has a very high photocatalytic activity under UV illumination (Gazquez et al. 2014).

Alkoxide method (Sol-Gel):

Metal alkoxides are mostly used precursors for metal oxide synthesis in laboratory scale since the product of sulfate method has contaminations and chlorine method reaction conditions are hard to control. Also metal alkoxide can be produced in highly pure grade which leads to highly pure metal oxide. TiO_2 can be synthesized from various titanium alkoxides (e.g. titanium ethoxide, titanium propoxide, titanium butoxide). Titanium alkoxide is hydrolysed to form TiO_2 sol/precipitate. TiO_2 sol is then gelated to form polymeric TiO_2. Proper heat treatment of TiO_2 gels leads to highly active TiO_2 with high specific surface areas (Kaneko and Okura 2002). This method is known as the ***"Sol-gel"*** method in the literature. The main reactions in sol-gel processing of titanium alkoxides are given below:

Hydrolysis and esterification reactions;

$Ti(OR)_4 + H_2O \rightarrow HO\text{-}Ti\text{-}(OR)_3 + R\text{-}OH$ (partial hydrolysis)
$Ti(OR)_4 + 2H_2O \rightarrow (OR)_2\text{–}Ti\text{-}(OH)_2 + 2R\text{-}OH$ (partial hydrolysis)
$Ti(OR)_4 + 3H_2O \rightarrow (OR)\text{–}Ti\text{-}(OH)_3 + 3R\text{-}OH$ (partial hydrolysis)
$Ti(OR)_4 + 4H_2O \rightarrow Ti(OH)_4 + 4R\text{-}OH$ (total hydrolysis)

Alcohol condensation and alcoholysis reactions;

$(OR)_3\text{–}Ti\text{-}OR + HO\text{–}Ti\text{-}(OR)_3 \rightarrow [(OR)_3Ti\text{–}O\text{–}Ti(OR)_3] + R\text{-}OH$

Water condensation and hydrolysis reactions;

$$(OR)_3\text{–Ti-OH} + \text{HO–Ti-}(OR)_3 \rightarrow [(OR)_3\text{Ti–O–Ti}(OR)_3] + \text{H-O-H}$$

The hydrolysis and condensation reactions are catalyzed in acidic media. H^+ ion protonates an oxygen atom in the alkoxide ligand which leads to the formation of reactive cationic alkoxide species. This step is rate-determining resulting in an S_N1-type mechanism. Cationic alkoxide species is attacked by a water molecule, forming a Ti–OH bond, release of an alcohol molecule and regeneration of a proton catalyst (Topuz 2009).

Sol-gel method has several advantages such as high purity and homogenous product, low temperature synthesis, excellent atomic mixing, precise control of size and surface properties, wide variety of precursors or other chemicals, possibility of different form of products such as films or powders. High amount of solvent usage in this method makes it unfeasible for the high production rates of TiO_2 (Tseng et al. 2010).

Chemical precipitation:

Chemical precipitation is a liquid phase reaction which is used to synthesize insoluble solid particles. Solid particles obtained during precipitation, the precipitate, are formed in the solution due to a reaction or when the solution has been supersaturated by a compound. Titanium precipitates as titanium hydroxide ($Ti(OH)_4$), TiO_2 or titanium oxy hydroxide ($TiO(OH)_3$). Titanium precursor can be alkoxide based or inorganic (e.g. $TiCl_4$). The dissolved precursor solution is mostly precipitated by the use of an alkali solution since Ti^{4+} is soluble in acidic conditions. The precipitates can be crystalline or amorphous particles. Rare earths mostly precipitate as hydroxides in aqueaous media. Crystalline oxide/hydroxide nanoparticles are synthesized by the application of heat treatment to the as-precipitated hydroxide particles. Usually an aqueous or alcohol solution of inorganic salt (nitrate, chloride, sulfate) of the desired rare earth is reacted with an alkali solution (of NaOH, NH_4OH) in this method. However unwanted growth of particles is inevitable during calcination. Direct precipitation from a non-aqueous solution should be carried out in order to obtain ultrafine particles (2-5 nm) (Adachi et al. 2004).

1.8. Rare Earth Element Doped TiO_2

Bandgap engineering for improving the photocatalytic activity of TiO_2 can be accomplished by;

i. doping TiO_2 with various cations/anions (metal or nonmetal) to introduce sub energy levels between conduction and valence band (Figure 1.15) (Zaleska 2008).

ii. combining with low bandgap materials; a coupled semiconductor mechanism in which low bandgap semiconductor absorbs the photons of visible light and transfers them to the surface of TiO_2 (Magesh et al. 2009)

iii. surface modification (Dugandzic et al. 2012)

iv. using different synthesis routes to modify the crystallite sizes.

Doping TiO_2 with anions/cations is the most preferred one since it is easy to tune the absorption edge by the type or amount of doping ion which leads to the improvement of photocatalytic activity. Interpretations on the contribution of doped ions to the electronic structure of TiO_2 can be accomplished by considering the valence band of TiO_2 is at oxygen 2p state and conduction band is at titanium 3d&4s state.

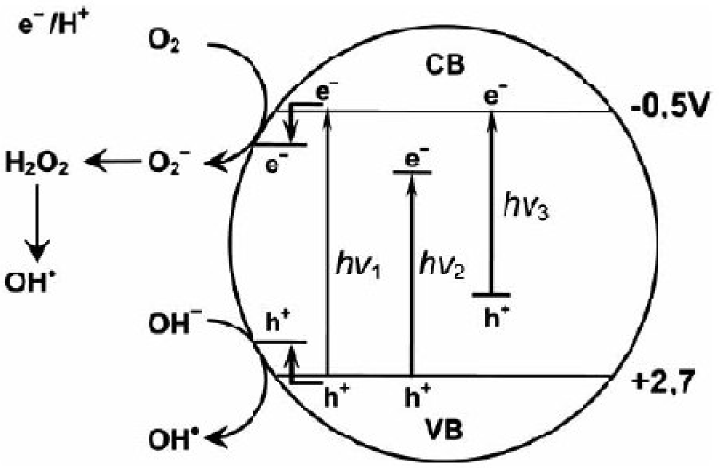

Figure 1.15. Mechanism of TiO_2 photocatalysis: $h\nu_1$: pure TiO_2; $h\nu_2$: metal-doped TiO_2 and $h\nu_3$: nonmetal-doped TiO_2. (Source: Zaleska 2008)

Metal doping introduces a new energy level in the bandgap of TiO_2 which narrows the bandgap and improves the light absorption characteristics of TiO_2. Transition metal doping also enables the trapping of electrons which inhibits the electron-hole recombination and improves oxidation-reduction activity of TiO_2.

Nonmetal doping improves the light absorption and photocatalytic activity of TiO_2 by three mechanisms. First one is the bandgap narrowing by hybridization of oxygen 2p with nonmetal 2p by introducing a new valence band closer to the conduction band. Second one is the introduction of isolated impurity levels in which electrons are excited only by visible light. Electrons in the valence band and impurity level are both excited with UV irradiation, however visible light only excites the electrons in the impurity level. Third one is the creation of holes localized in oxygen vacancies forming $O^{2-\cdot}$ and $OH^{-\cdot}$ radicals which trigger the oxidation reactions (Zaleska 2008).

Doping can be achieved by various methods e.g. ion-assisted sputtering, ion implantation, chemical vapor deposition and chemical synthesis methods such as sol-gel and chemical precipitation. Mostly used methods are chemical precipitation and sol-gel which were described previously.

Transition metals (such as V, Cr, Fe, Co, Ni, Cu) and nonmetals (N, S, C, B, P, I, F) doped TiO_2 photocatalysts were prepared in various research papers presenting the bandgap tuning, however there are contradicting results about the bandgap energy of TiO_2 (Anpo and Kamat 2010, Bellardita et al. 2011, Magesh et al. 2009, Zaleska 2008). Examples of UV-Vis DR spectra from different research papers presenting the bandgap tuning and red shift of the absorption edge of TiO_2 are given in Figure 1.16.

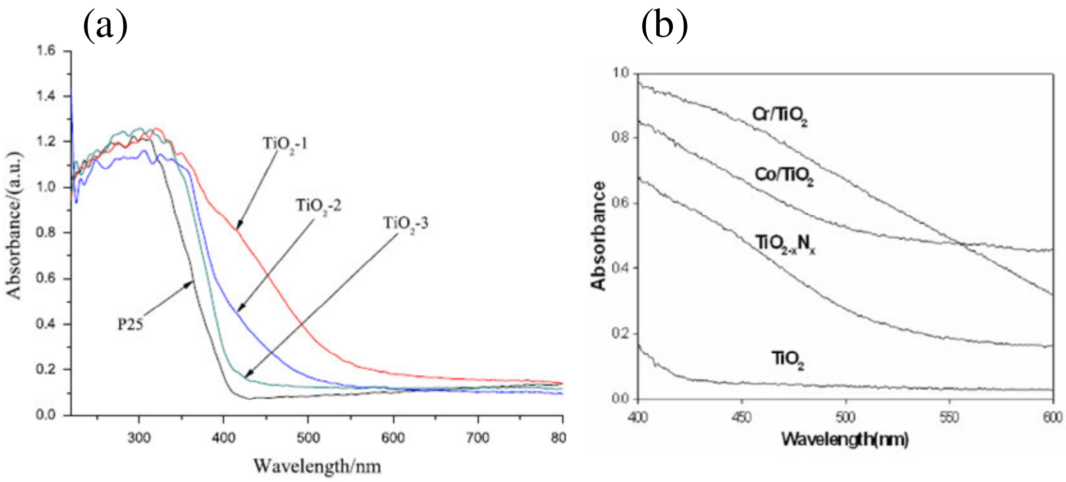

Figure 1.16. UV-Vis DR spectra of (a) S-N (nonmetal) co-doped (1, 2, 3 correspond to different calcination temperatures), (b) Co/Cr (transition metal) doped TiO_2. (Source: Bae et al. 2007, Li et al. 2008)

Rare earth elements, such as La, Nd, Eu, Sm, Yb, Pr and Ce doped TiO_2 showed photocatalytic activity in the visible region of solar radiation according to the research papers published in the last ten years (Bellardita et al. 2007 and 2011, Chiou and Juang 2007, Hassan et al. 2012, Jian et al. 2010, Reszczynska et al. 2014, de la Cruz Romero et al. 2010, Tong et al. 2007, Wang et al. 2010, Xie and Yuan 2004, Xie et al. 2005, Xu et al. 2009, Yan et al. 2005). These studies are mostly on the environmental applications such as photocatalytic degradation of dyes in wastewaters.

Valence band of a rare earth element is at 4f state. An electron hops from the valence band of TiO_2 to 4f level of rare earth ion instead of 3d level of TiO_2 which is at a higher energy level as schematically shown in Figure 1.17. This phenomenon introduces sub energy levels in the bandgap energy of TiO_2 which improves light absorption (Xie and Yuan 2004).

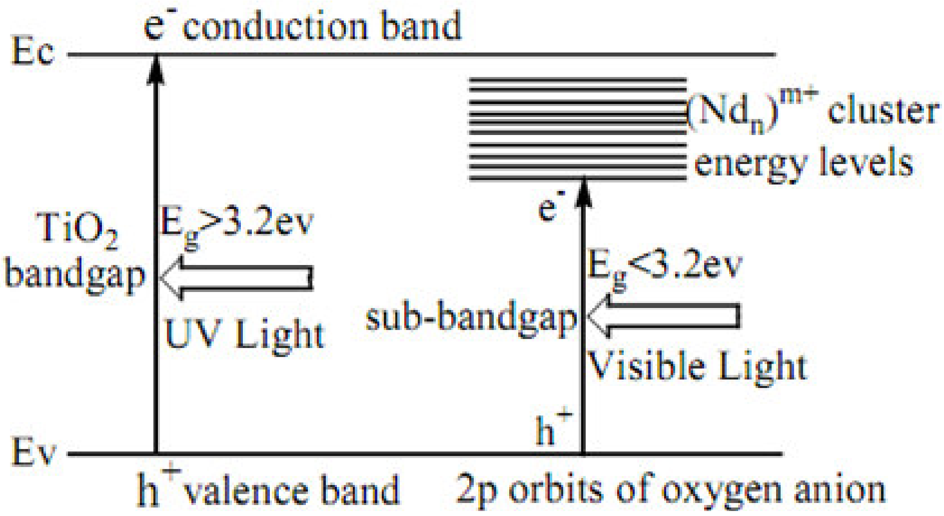

Figure 1.17. The bandgap structure of RE^{3+}-TiO_2 and the mechanism of photoresponse under visible light and photogenerated electron transfer. (Source: Xie and Yuan 2004)

Rare earth elements also hinder the recombination of electron-hole pairs, keeping them on the TiO_2 surface and resulting in higher photocatalytic activities (Xie and Yuan 2004, Xie et al. 2005). Artificial photosynthesis activities of rare earth doped TiO_2 have only been investigated by a few researchers (Matejova et al. 2014, Ogura et al. 1992, Wang et al. 2013, Zhao et al. 2012) and research on these materials have great importance to improve the current state of understanding. The ionic radius, bandgap energies of the oxide forms of rare earth elements along with some transition metals and precipitation pH values for the hydroxides of rare earths are given in Table 1.2.

Table 1.2. Ionic radii of metal ions, bandgap energy of oxides and precipitation pH of lanthanide hydroxides. (Source: Jia 1991, Moeller and Kremers 1944, Sato et al. 2007)

Rare earth / Transition metal	**Ion**	**Ionic radius (pm)**	**Oxide bandgap (eV)**	**Hydroxide precipitation pH**
Lanthanum	La^{3+}	117.2	4.3	7.82
Scandium	Sc^{3+}	87	5.7	
Cerium	$Ce^{3+/4+}$	101	2.7-3.4	7.6
Prasedimium	Pr^{3+}	113	3.4	7.35
Neodymium	Nd^{3+}	112.3	4.0	7.31
Samarium	Sm^{3+}	109.8	4.33	6.92
Europium	Eu^{3+}	108.7	1.5	6.82
Gadolinium	Gd^{3+}	107.8	5.8	6.83
Terbium	Tb^{3+}	106.3	5.3	-
Dysprosium	Dy^{3+}	105.2	-	-
Holmium	Ho^{3+}	104.1	5.3	-
Erbium	Er^{3+}	103	5.7	6.76
Tulium	Tm^{3+}	102	5.1	6.40
Ytterbium	Yb^{3+}	100.8	6.0	6.30
Lutetium	Lu^{3+}	100.1	-	6.30
Yttrium	Y^{3+}	90	5.5	6.95
Titanium	Ti^{4+}	68	3.0-3.2	-
Copper	Cu^{2+}	73	1.2	-
Silver	Ag^{1+}	115	-	-
Iron	Fe^{3+}	55	2.0-2.2	-
Cobalt	Co^{3+}	65	2.4	-
Zirconium	Zr^{4+}	86	5-7	-

Hewer et al. (2011) investigated the effect of Nd doping on the photocatalytic activity of TiO_2 prepared by sol-gel and precipitation. The photocatalytic activities of the prepared powders were evaluated in the degradation of Remazol Black B dye. The powders containing Nd had better photocatalytic activities compared to pure TiO_2. The bandgap of these doped/undoped TiO_2 was not reported in the article. Nassoko et al. (2012) prepared Nd doped TiO_2 by sol-gel. Bandgap of TiO_2 was narrowed from 3.11 eV to 2.33 eV by doping TiO_2 with a Ti:Nd elemental ratio of 11:1. UV-Vis DR Spectra of these powders are given in Figure 1.18. The photocatalytic activity of TiO_2 was found to be improved by the incorporation of Nd to the TiO_2 lattice. Complete incorporation of Nd to the TiO_2 lattice was supported by XPS analysis presenting the binding energies at 460.05, 458.86, and 458.27 eV which indicated the presence of Ti^{4+}, Nd-Ti, and Ti^{3+}, respectively.

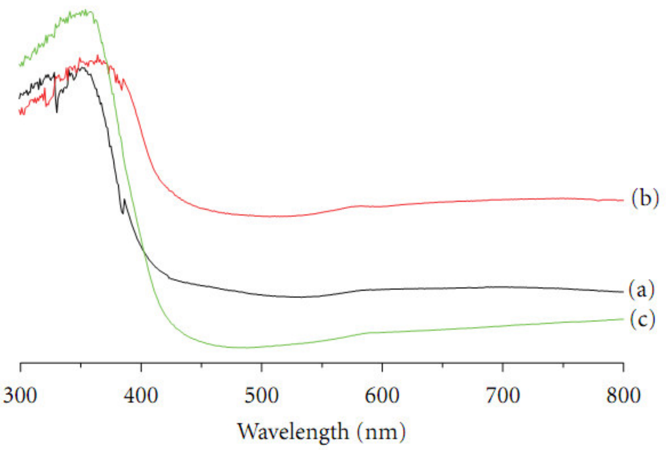

Figure 1.18. UV-Vis DR spectra of (a) pure TiO_2, (b) Nd-doped TiO_2 with Ti:Nd = 23:1, (c) Nd-doped TiO_2 with Ti:Nd = 11:1. (Source: Nassoko et al. 2012)

The photocatalytic activity of Ce doped TiO_2 in the visible region towards dye degradation and water splitting was reported in the studies published in the past 10 years (Charanpahari et al. 2013, Rapsomanikis et al. 2014, Tian et al. 2014, Tong et al. 2007). Ce is one of the most abundant rare earth elements with lanthanum, praseodymium and neodymium. Cerium oxide (CeO_2) is frequently used in fuel cell and pollution prevention applications since it has photocatalytic activity, oxygen vacancy and redox behavior. Catalytic activity of CeO_2 originates from the defect regions of Ce^{3+} and oxygen vacancies. CeO_2 has bandgap energies varying between 2.7 and 3.4 eV according to the preparation method employed. Although scientists have great interest on the visible light activity of Ce doped TiO_2, a comprehensive investigation of the mechanism was not conducted yet. Elucidating the mechanism of the visible light activity of Ce doped TiO_2 is important to prepare highly active phases in the visible light region of solar radiation. The incorporation of Ce ion to the lattice of TiO_2 phases creating sub-levels between the valence and conduction band shifting the bandgap energy to the visible region was proposed as a possible reason for this behavior (Magesh et al. 2009, Tong et al.2007). The difference in the size of Ti and Ce atoms (Ce^{4+}: 0.093 nm, Ce^{3+}: 0.103 nm, Ti^{4+}: 0.068 nm) makes it difficult for Ce atom to enter the TiO_2 lattice substitutionally. It was stated that redox behavior of Ce^{4+}/ Ce^{3+} couple hinders the recombination of charge carriers (electron-hole pairs) hence the photocatalytic activity of Ce doped TiO_2 becomes higher than undoped TiO_2 under UV illumination (Magesh et al. 2009). Magesh et al. evaluated the photocatalytic activities of the prepared powders in the degradation of methylene blue and a coupled semiconductor mechanism was suggested as shown in Figure 1.19. According to this coupled mechanism, CeO_2 on the surface of TiO_2 absorbs visible light photons and transfers electrons to the conduction band of TiO_2 and redox reactions start. Absorption edges of doped samples were found to be between pure TiO_2 and pure CeO_2 similar to the photocatalytic activities. They indicated that anatase phase became stable with increasing Ce concentration within the range of 0-9% and Ce^{4+} ion did not enter and accommodate (for any doping concentration) in TiO_2 lattice and formed CeO_2 phase on the surface of TiO_2 particles. This was supported by the XRD results. Mixture of CeO_2 (6 phases which are reported in Joint Committee on Powder Diffraction Standards - JCPDS database) and TiO_2 phases were detected by XRD, so a coupled semiconductor mechanism was suggested to be responsible for the visible light activity.

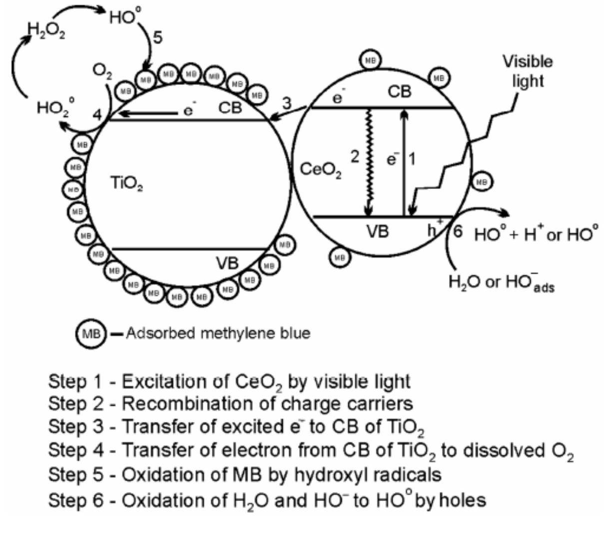

Figure 1.19. Mechanism of methylene blue degradation with visible light active CeO_2-TiO_2 composite photocatalyst. (Source: Magesh et al. 2009)

Pavasupree et al. (2005) prepared TiO_2 doped with Ce^{4+} ion between 0-100 mol% CeO_2. Cubic CeO_2 and anatase were detected at doping levels higher than 25 mol%, however only anatase phase was detected at 5 mol% CeO_2 and crystallinity decreased with increasing CeO_2 content. It was found that 50 mol% CeO_2 containing sample showed absorption at higher wavelengths which indicated a red shift in the bandgap energy compared to pure TiO_2 and pure CeO_2.

De la Cruz Romero et al. (2010) conducted a study with rare earth elements (Ce, Nd, La, Pr) doped sol-gel TiO_2 powders in which they tested the activities of these powders in photocatalytic phenol degradation. TiO_2 powders doped with 0.1-0.5% rare earth had higher bandgap energies compared to pure TiO_2. Only anatase and rutile were detected by XRD indicating no rare earth oxide phases were formed at 0.5 wt% doping level and at 800°C. Variable photocatalytic activities were observed for various rare earths such as Ce doped TiO_2 had higher activity than pure TiO_2, however Pr doped sample had lower activity.

Lanthanum doped TiO_2 photocatalysts were prepared by Kim et al. (2007). La doped TiO_2 photocatalysts were synthesized by sol-gel method. La^{3+} ion (whose radius is larger than the radius of Ce^{4+} ion) was stated to accommodate in TiO_2 lattice according to their XRD patterns, however Magesh et al. (2009) claims that Ce^{4+} cannot enter TiO_2 lattice with a smaller ionic radius then La as mentioned above. It was stated that La^{3+} ion in the lattice did not affect the light absorption of TiO_2. However a red shift was detected in the absorption spectra of the prepared powders which was attributed to the size effect. The increase in the particle size due to varying La content was claimed to be the main reason for the shift to the visible region.

Jin et al. (2008) stated that the phase structure of TiO_2 was hardly affected by lanthanum doping, in addition to this, the La phase was not detected in the XRD patterns indicating that La^{3+} did not substitute with Ti^{4+} in the TiO_2 crystal lattice. In this study lanthanum doped TiO_2 powders were prepared by sol-gel and tested in photocatalytic degradation of methylene blue and gaseous acetaldehyde. Adsorption of methylene blue molecule was enhanced by La doping whereas the rate constant of degradation of methylene blue decreased with La doping.

Research conducted on rare earth doped TiO_2 showed no consensus on the localization of the rare earth ion in the TiO_2 microstructure and the effect of rare earth doping on the light absorption characteristics. A major portion of the researchers in this field claim that rare earth ions cannot enter TiO_2 lattice substitutionally, can accommodate in the interstitial voids of TiO_2 lattice or segregate on the grain boundaries forming rare earth oxides since rare earth ionic radii are much larger than Ti^{4+}. There are also studies indicating the formation of a new phase containing both rare earth and titanium ions (Jin et al. 2008).

Phase diagrams of titania with rare earth oxides are present for the heat treatment temperatures above 1000°C and diagrams indicate that two phases are insoluble in each other. Figure 1.20 and similar phase diagrams indicate that there are oxide phases of RE_2Ti_2 (pyrochlore), RE_4Ti_9, and RE_2Ti_4. The structure of phase diagrams at low temperatures is very important since it is crucial to maintain high surface area and porous structure for achieving high photocatalytic activities in various applications. Low temperature binary phase diagrams of TiO_2 and rare earth oxides are not available yet. It would be useful to have information about the nature of the phases and solid state solubilities at low temperatures to see the effect of phase structure on the photocatalytic activity of rare earth doped TiO_2 or titanium-rare earth mixed oxides.

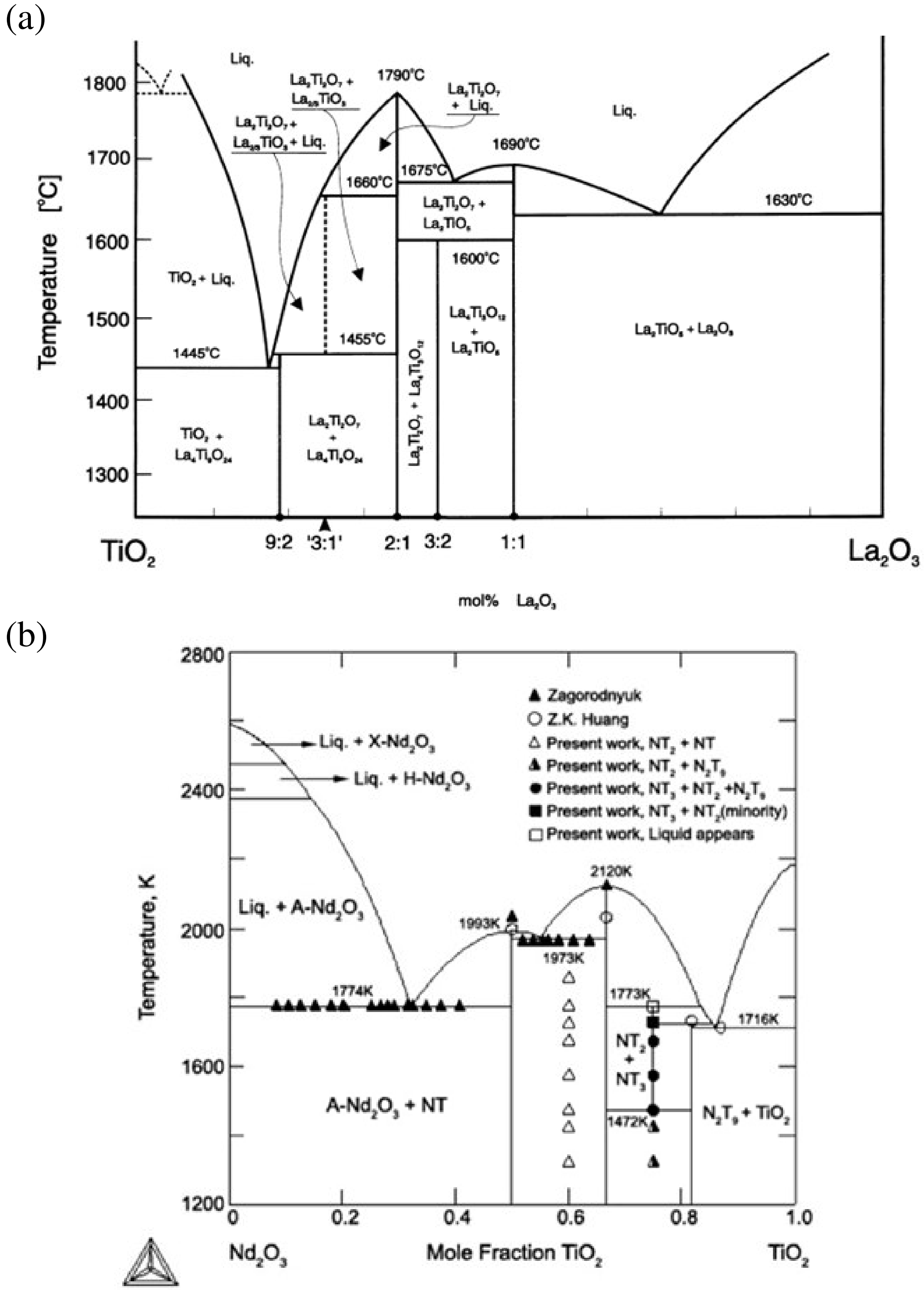

Figure 1.20. (a) TiO_2-La_2O_3, (b) TiO_2-Nd_2O_3 phase diagrams.
(Source: Gong and Zhang 2013, Skapin et al. 2000)

1.9. Artificial Photosynthesis on TiO_2 Based Photocatalysts

Artificial photosynthesis utilizes the energy from the sunlight to reduce CO_2 into CH_4, CO, CH_3OH or other hydrocarbons. CO_2 is a linear molecule (O=C=O) without a dipole moment and is one of the most stable compounds (but not inert) which is mostly produced by oxidation/combustion reactions. CO_2 needs high energy reducing molecules to be converted into hydrocarbons. The Gibbs free energy change of a reaction should be negative in order to be thermodynamically favorable. Most reactions given in Table 1.3 have positive Gibbs free energy changes and reaction of CO_2 with H_2O seems extremely thermodynamically unfavorable. High energy input is needed to convert CO_2 into hydrocarbons. Therefore, high temperatures and pressures are needed to activate CO_2. In photocatalysis, CO_2 can be activated by electrons and react with holes at room temperature and atmospheric pressure by the energy input from sun light. Reducing molecules such as H_2, H_2O or CH_4 are needed for this purpose among which H_2 seems to be more attractive since the Gibbs free energy changes of the reactions involving H_2 are low or negative. However it is meaningless to reduce CO_2 with H_2 which has more chemical potential and the system loses its chemical potential by consuming H_2. If H_2 is produced by water splitting without synthetic energy input e.g. solar energy, not the energy from burning fossil fuels, the process would be feasible.

Table 1.3. Change of Gibbs free energy at 298 K for various reactions related to the photocatalytic reduction of CO_2. (Source: Ling 2011)

Reductant	**Product**	**Chemical equation**	**ΔG^0 (kJ/mol)**
H_2	CO	$CO_2+H_2 \rightarrow CO+H_2O$	29
	HCOOH	$CO_2+H_2 \rightarrow HCOOH$	43
	HCHO	$CO_2+2H_2 \rightarrow HCHO+H_2O$	63
	CH_3OH	$CO_2+3H_2 \rightarrow CH_3OH+H_2O$	4
	CH_4	$CO_2+4H_2 \rightarrow CH_4+2H_2O$	-114
	C	$CO_2+2H_2 \rightarrow C+2H_2O$	-63
CH_4	CO	$CO_2+CH_4 \rightarrow 2CO+2H_2$	171
	CH_3COCH_3	$CO_2+2CH_4 \rightarrow CH_3COCH_3+H_2O$	115
	CH_3COOH	$CO_2+CH_4 \rightarrow CH_3COOH$	71
	HCHO	$CO_2+CH_4 \rightarrow 2HCHO$	240
	C	$CO_2+CH_4 \rightarrow 2C+2H_2O$	-12
H_2O	HCOOH	$CO_2+H_2O \rightarrow HCOOH+1/2O_2$	272
	CO	$CO_2+H_2O \rightarrow CO+H_2+O_2$	486
	HCHO	$CO_2+H_2O \rightarrow HCHO+O_2$	521
	CH_3OH	$CO_2+2H_2O \rightarrow CH_3OH+3/2O_2$	690
	CH_4	$CO_2+2H_2O \rightarrow CH_4+2O_2$	801
	CO	$CO_2 \rightarrow CO+1/2O_2$	257
		$H_2O(g) \rightarrow H_2+1/2O_2$	229
		$H_2O(l)\ ) \rightarrow H_2+1/2O_2$	237

The reaction of CO_2 with H_2 can be carried out either in gaseous or liquid phases. The form of CO_2 may vary depending on the phase (gas or a dissolved ion in water). Aqueous solutions of NaOH are used mostly in order to increase CO_2 solubility since it is soluble at high pH. CO_2 dissolves in water according to the following equilibrium reactions (Wojtowicz, 2001):

$CO_2\,(aq) + H_2O \leftrightarrow H_2CO_3$

$H_2CO_3 \leftrightarrow H^+ + HCO_3^-$

$HCO_3^- \leftrightarrow H^+ + CO_3^{2-}$

The form of ionic CO_2 also depends on the pH as shown in Figure 1.21 which represents the pH-CO_2 equilibrium.

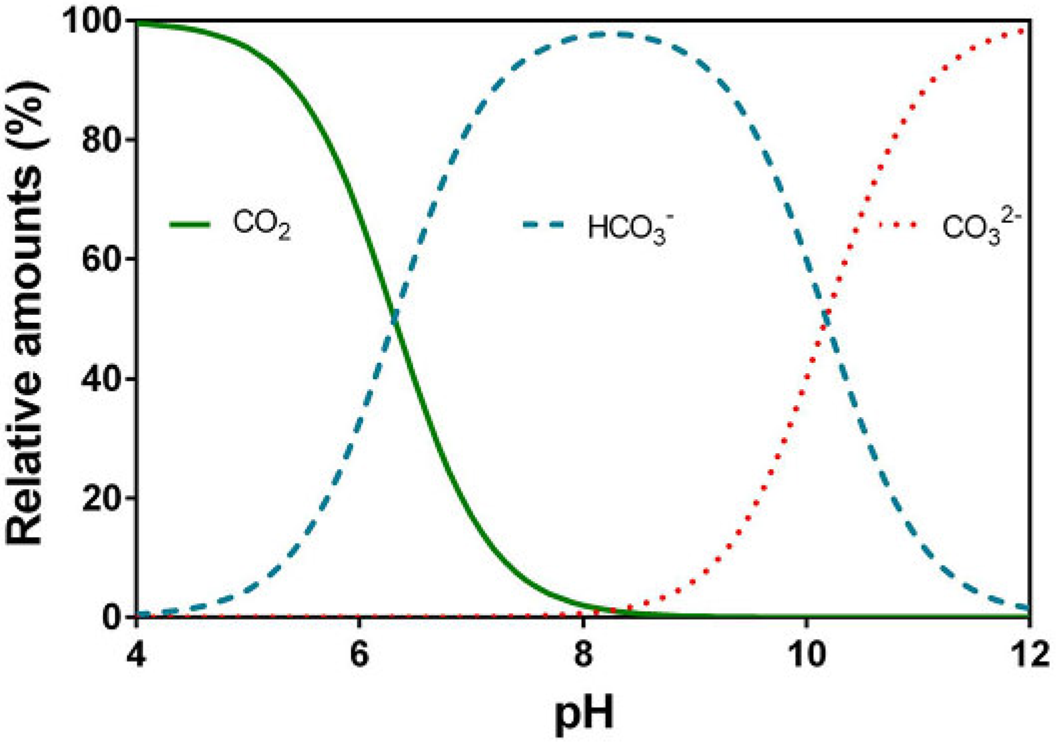

Figure 1.21. CO_2-pH equilibrium. (Source: Pedersen et al. 2013)

The band edge positions of some selected photocatalysts and redox potentials involving CO_2 species and hydrocarbons are given in Figure 1.22 and Table 1.4. Gaseous CO_2 can be reduced to CO, CH_3OH, CH_4, HCOOH or water dissolved CO_2 (H_2CO_3) can be reduced to HCOOH, HCHO or CH_3OH with anatase TiO_2 as can be seen from Figure 1.22. It is also seen that the reduction of gaseous CO_2 would be easier due to the closeness of the reduction potentials and conduction band potential of anatase TiO_2 (-0.5 eV), however the products of photocatalytic CO_2 reduction with TiO_2 are not restricted to the given ones in Table 1.4 since the photocatalytic properties of TiO_2 can easily be tuned by several modification methods which may shift the band edge positions or change the reaction mechanism. This figure and table is an illustration of the possible products that may be produced with TiO_2. There are reports of gaseous CO and CH_4 production when CO_2 reduction was carried out in aqueous conditions (Koci et al. 2009 and 2011, Rajalakshmi et al. 2012).

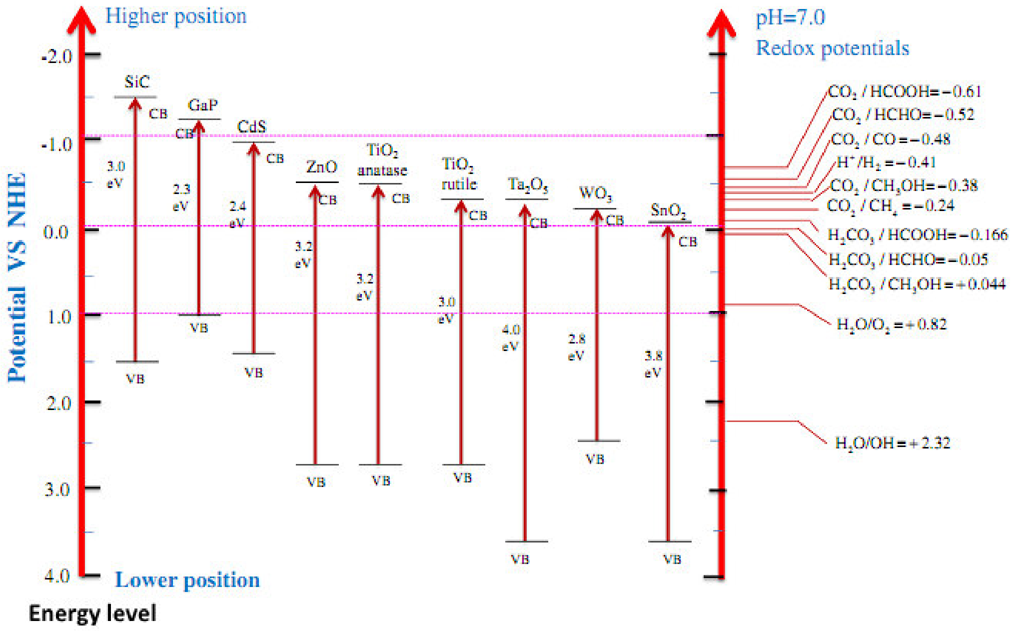

Figure 1.22. A schematic illustration of the band positions of semiconductors and redox couples in water. (Source: Tahir and Amin 2013)

Table 1.4. Summary of reduction potentials for half-cell reactions at pH 7 in aqueous solution vs. the normal hydrogen electrode. (Source: Tahir and Amin 2013)

Chemical equations	**Thermodynamic potential, V vs. NHE**
$CO_2 + e^- \rightarrow CO_2^-$	-2.0
$2H^+ + 2e^- \rightarrow H_2$	-0.41
$CO_2 + 2H^+ + 2e^- \rightarrow HCOOH$	-0.61
$CO_2 + 4H^+ + 4e^- \rightarrow HCHO + H_2O$	-0.52
$CO_2 + 2H^+ + 2e^- \rightarrow CO + H_2O$	-0.48
$CO_2 + 6H^+ + 6e^- \rightarrow CH_3OH + H_2O$	-0.38
$CO_2 + 8H^+ + 8e^- \rightarrow CH_4 + 2H_2O$	-0.24
$H_2CO_3 + 2H^+ + 2e^- \rightarrow HCOOH + H_2O$	-0.166
$H_2CO_3 + 4H^+ + 4e^- \rightarrow HCHO + 2H_2O$	-0.050
$H_2CO_3 + 6H^+ + 6e^- \rightarrow CH_3OH + 2H_2O$	+0.044
$2CO_3^{2-} + 4H^+ + 2e^- \rightarrow C_2O_4^{2-} + 2H_2O$	+0.478
$CO_3^{2-} + 3H^+ + 2e^- \rightarrow HCOO^- + H_2O$	+0.311
$CO_3^{2-} + 8H^+ + 6e^- \rightarrow CH_3OH + 2H_2O$	+0.209
$HCOO^- + 5H^+ + 4e^- \rightarrow CH_3OH + H_2O$	+0.157

Probable reaction mechanisms and pathways for CO_2 photoreduction in liquid or gas phase are schematically given in Figure 1.24. According to the proposed mechanism simultaneous multi-electronic processes occur during the photocatalytic reduction of CO_2. Electron-hole pairs are generated when TiO_2 excited with the wavelengths no less than its bandgap energy. Generated holes react with water adsorbed on the surface of TiO_2 to produce ·OH, H^+ and O_2. H· radicals are formed by the interaction of H^+ ions with excited electrons. Union of two H^+ ions forms one H_2 molecule. Electrons interact with CO_2 molecules and HCO_3^- ions to form $\cdot CO_2^-$ radicals (Hussain et al. 2015, Sreekanth and Phani 2014). H· and $\cdot CO_2^-$ radicals react to form CO. CO may be reduced by one electron to $\cdot CO^-$.

Reaction of H· radical with $\cdot CO^-$ yields ·C and OH^-. Consequtive addition of H· to ·C yields $\cdot CH_3$ radicals. Finally, CH_4 (methane) or CH_3OH (methanol) molecules are formed when $\cdot CH_3$ radicals react with H· or OH· radicals, respectively.

HCO_2^- (formate ion) may be formed when HCO_3^- is reduced by an electron to $\cdot HCO_3^{--}$ which then reacts with H· forming HCO_2^-. HCOOH (formic acid) is formed by the reaction of H· and $\cdot HCO_2^{--}$ which is formed by the reduction of HCO_2^-.

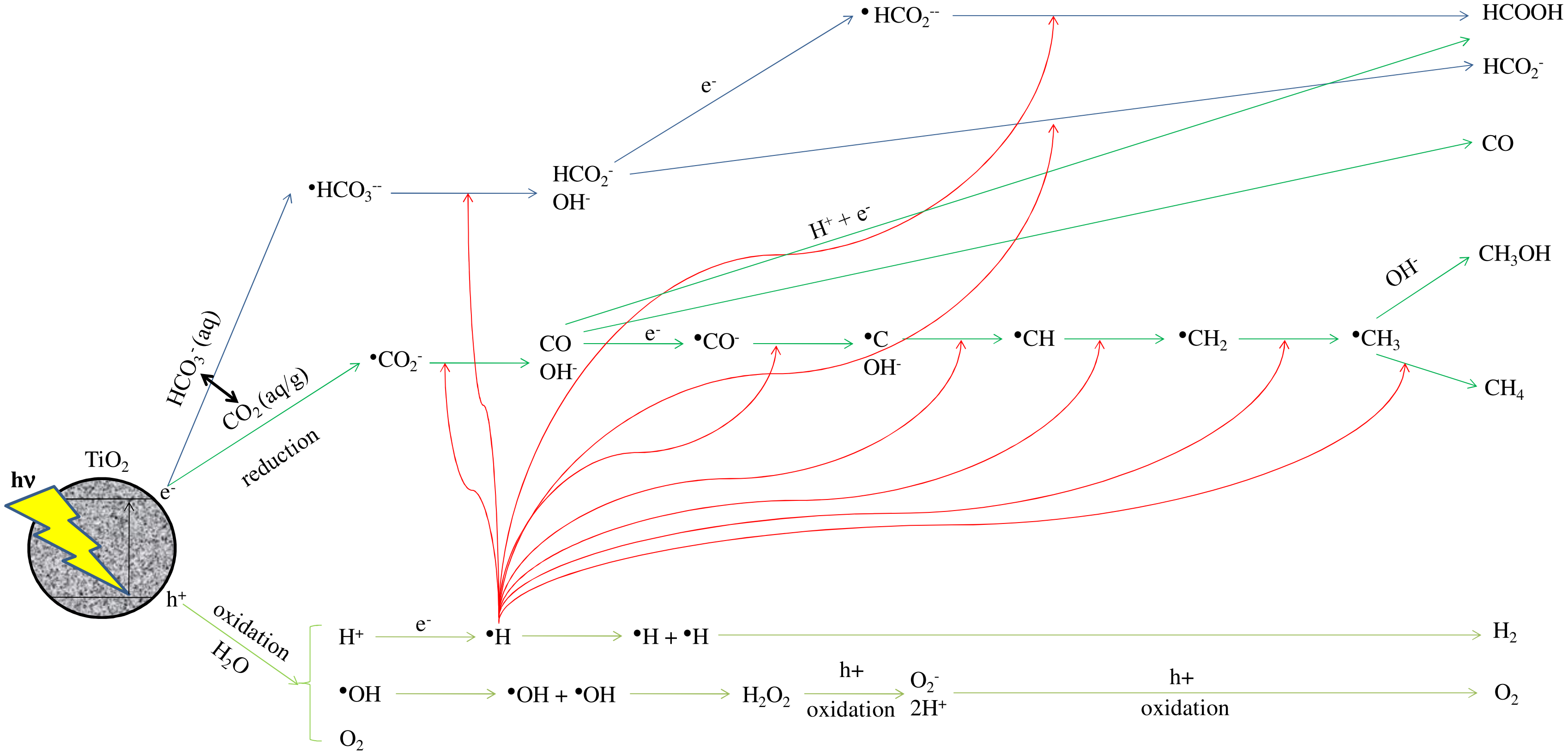

Figure 1.23. Photocatalytic CO_2 reduction pathways and reaction mechanisms.
(Source: Hussain et al. 2015, Sreekanth and Phani 2014, Zhang et al. 2015)

Fujishima and Honda conducted the pioneering study in 1972 to produce hydrogen on a TiO_2 electrode (Fujishima and Honda 1972) and Inoue et al. (Fujishima and Honda who are the leading researchers of photocatalysis of TiO_2 were the co-workers in this study) reported the first photocatalytic reduction of CO_2 in aqueous media via photocatalytic processes by using solar energy in 1979. They used different photocatalysts such as TiO_2, ZnO, CdS, GaP, WO_3 and SiC. The products of the reactions were formic acid, methanol, methane and formaldehyde (Inoue et al. 1979). Since then many studies on photoreduction of CO_2 were conducted.

Early studies of photocatalytic reduction of CO_2 involved the use of SiC, GaP, $SrTiO_3$, WO_3, $BaTiO_3$, $LiNbO_3$, $CaFe_2O_4$, Cu_2OxH_2O, ZnS, CdS photocatalysts by Inoue et al. (1979), Ogura et al. (1992) and Yoneyama (1997). Intensive research on the photoreduction of CO_2 by using TiO_2 was conducted after this period due to the recognition of its extraordinary properties.

Many review articles were published on the photocatalytic water splitting (Abe 2010, Chen et al. 2010, Maeda 2011, Ni et al. 2007) and reduction of CO_2 covering different photocatalysts (Anpo 2013, Das and Daud 2014, de-Richter et al. 2013, Izumi 2013, Liu et al. 2012, Molinari et al. 2014, Rani et al. 2014, Uner et al. 2011, Windle and Perutz 2012).

TiO_2 was doped with various transition metals and light absorbing dyes in the studies conducted in the last 20 years (Abou Asi et al. 2011, Koci et al. 2010 and 2009, Li et al. 2014, Li et al. 2010, Liu et al. 2007, Matejova et al. 2013, Nguyen and Wu 2008, Ozcan et al. 2007, Sasirekha et al. 2006, Tahir and Amin 2013, Tang et al. 2014, Truong et al. 2012, Tseng et al 2002, Wu et al. 2005, Zhang et al. 2009, Zhang et al 2011). Zinc phthalocyanin, ruthenium, palladium, platinum, gold and rhodium doped TiO_2 were also used in various studies (Zhao et al. 2007, Sasirekha et al. 2006, Dey 2007). Research on rare earth doped TiO_2 photocatalysts prepared for photocatalytic reduction of CO_2 is not common yet, besides there are few research papers on rare earth (only Ce) doped TiO_2 powders that were used in photocatalytic CO_2 reduction (Matejova et al. 2014, Ogura et al. 1992, Wang et al. 2013, Zhao et al. 2012).

Different forms of photocatalysts (film or powder) and reaction conditions (including illumination source, reducing agent etc.) were investigated since Inoue et al. (1979). A brief review of recent research on the topic including the synthesis method, products of CO_2 reduction and reaction conditions are given in the following paragraphs and the results of selected articles are briefly explained. Research on photocatalytic reduction of CO_2 with TiO_2 powders tested in batch slurry reactors (except Ozcan et al. 2007) were summarized here since this PhD work focuses on the photocatalytic CO_2 reduction and water splitting with rare earth doped TiO_2 tested in a slurry reactor. Examples of CO_2 (g) reduction with H_2O vapor were also given.

The commonly used photocatalytic water splitting and CO_2 reduction setup examples are presented in Figure 1.24. Photocatalyts are mostly powders which are dispersed in the reaction medium. TiO_2 powder photocatalysts were used in the setups given in Figure 1.24a, 1.24b, 1.24d and a TiO_2 film photocatalyst was used in the setup given in Figure 1.24c. Film photocatalyts are easy to handle, however larger surface areas can be achieved with powders. The most commonly used photoreaction setups are generally annulus, slurry reactors as seen in Figure 1.24a. A light source is positioned in the center of the reactor surrounded by reaction medium which allows homogeneous irradiation of the suspended photocatalyst particles. Photocatalyst particles are dispersed in CO_2 saturated 0.1 M NaOH solution generally at a pH of 12-13. The pH of the solution decreases to c.a. pH 7 after CO_2 saturation. The photocatalytic reaction setup constructed for this PhD study is similar to the one presented in Figure 1.24b in which the photocatalyst particles are suspended in 0.1 M aqueous NaOH solution purged with CO_2 (g) instead of liquid CO_2.

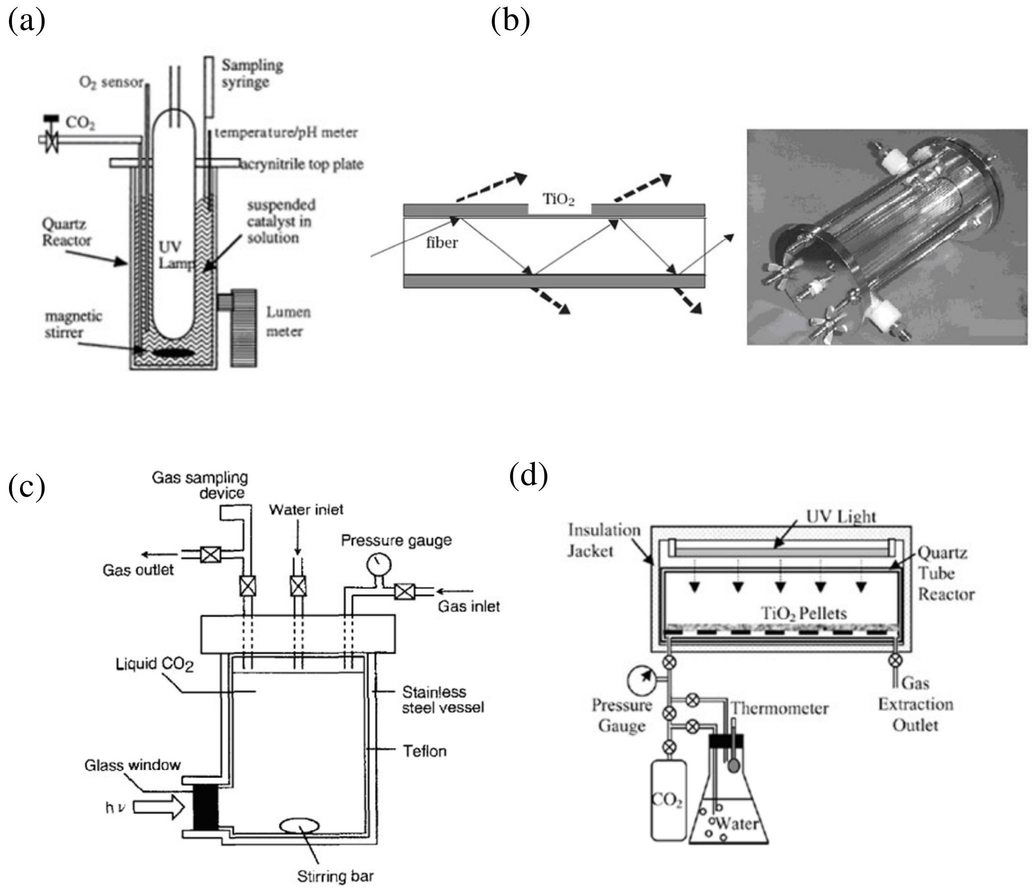

Figure 1.24. Photoreactor setups from literature.
(Source: Kaneco et al. 1997, Tan et al. 2006, Tseng et al. 2002, Wu et al. 2005)

The activity of various transition metals doped TiO_2 photocatalysts in CO_2 photoreduction was investigated in many research papers. Copper was commonly used as the dopant to increase the activity of TiO_2 (Slamet et al. 2005, Tseng et al. 2002, Wu et al. 2005). Sol-gel technique was used by Tseng et al. (2002) for the preparation of pure and Cu doped TiO_2 powders. The effect of Cu doping level was investigated throughout this study. Bandgap energy was determined to be 2.86 eV for wt 6% Cu doped TiO_2 which was 2.95 eV for pure TiO_2. The highest methanol yield of 118.5 μmol/g-cat in 6 hours was obtained with an optimum doping level of 2 wt%. Methanol yield with Degussa P25 was determined to be 38.2 μmol/g-cat in hours. Impregnation is also a popular method for loading TiO_2 with dopant ions. Slamet et al. (2005) impregnated Cu with different valency (Cu^0, Cu^{1+}, Cu^{2+}) on TiO_2 nanoparticles. Different preparation procedures were applied in order to vary the valency of Cu. Copper nitrate ($Cu(NO_3)_2$) containing Degussa P25 powder slurry was ultra-sonicated and stirred at 95°C followed by drying, calcination and reduction-oxidation treatment to form Cu^0 and Cu^I doped TiO_2. Atmospheric calcination was predicted to form Cu^{2+} doped TiO_2. Reduction at 300°C with H_2/He formed Cu^0 doped TiO_2 and with the final step oxidation with N_2O at 80°C Cu^{1+} doped TiO_2 was obtained. The lowest bandgap energy was determined to 2.73 eV for Cu^{1+} doped TiO_2 and the maximum methanol yield was determined to be 2655 μmol/g-cat in 6 hours for Cu^{2+} doped TiO_2. Cu doped TiO_2 film photocatalysts were also prepared (Wu et al. 2005). The films were prepared by dipping optical quartz fibers in Cu doped TiO_2 sols. The bandgap energies of the films were determined to be ~3.3 eV which were relatively higher compared to the values obtained with Cu doped TiO_2 in powder form (Slamet et al. 2005, Tseng et al. 2002), however a relatively high methanol production rate of 0.45 mmole/g-cat in 1 hour was obtained with 1.2 wt% Cu doped TiO_2 film photocatalyst.

There are also different dopants used to improve the photocatalytic CO_2 reduction activity of TiO_2. Gold (Au) (Matejova et al. 2013), silver (Ag) (Koci et al. 2010) or ruthenium (Ru) (Sasirekha et al. 2006) are some examples for the dopants other than Cu. Au enriched TiO_2-ZrO_2 nanocomposite photocatalysts were prepared by Matejova et al. (2013) via sol-gel technique. Au was deposited on the prepared powders by wet impregnation method. Bandgap energies of pure TiO_2, Au enriched TiO_2, TiO_2-ZrO_2 and Au enriched TiO_2-ZrO_2 were determined to be 3.15, 2.87, 3.44 and 3.29 eV, respectively. Methane, hydrogen and carbon monoxide were detected as photocatalytic CO_2 reduction products. Production rates of methane, hydrogen and carbon monoxide were 15.0, 170.0 and 1.1 μmol/g-cat in 24 hours, respectively. These production rates were obtained with TiO_2-ZrO_2 nanocomposite despite the higher bandgap energy. The specific surface area of TiO_2-ZrO_2 was slightly higher than 0.4 wt% Au enriched TiO_2-ZrO_2; however methane production rate was almost double without Au enrichment. This phenomenon was attributed to the presence of large Au crystallites which masked the TiO_2-ZrO_2 particle surface leading to a decrease in the light absorption capability or increase in the number recombination centers. The role of absorption edge and the intersection between the absorption spectrum of the material and UV-Vis spectrum of the lamp was investigated by using two UV lamps with maximum intensities at 254 nm and 365 nm. The activity of TiO_2-ZrO_2 was higher at 254 nm compared to TiO_2, but TiO_2 had higher activity than TiO_2-ZrO_2 at 365 nm. These results supported their observations on the importance of the similarity between the irradiation source spectrum and the bandgap energy of the prepared photocatalyst in photocatalytic applications. Ag was used as the dopant to increase the photocatalytic CO_2 reduction activity of TiO_2.

Sol-gel technique was used to prepare Ag doped TiO_2 powders. Bandgap energies of pure and 7 wt% Ag doped TiO_2 powders were determined as 2.98 and 2.74 eV, respectively. The products were hydrogen, carbon monoxide, methane and methanol. The highest product yield was obtained with 7 wt% Ag doped TiO_2 which was attributed to the possible formation of metallic Ag clusters. It was concluded that these metallic clusters formed in the microstructure above 5 wt% doping level decreased the recombination rate of photo-generated electron-hole pairs and improved the photocatalytic activity. Methanol and methane yields were 1.8 and 9 µmol/g-cat in 24 hours, respectively. (Ru) doped TiO_2 powders were also prepared (Sasirekha et al. 2006) for the use in photocatalytic CO2 reduction. Bandgap energy of Ru doped anatase mounted silica was determined as 3.04 eV at 0.5 wt% doping level. The main products in the photocatalytic CO_2 reduction tests were hydrogen, formic acid, methane, formaldehyde along with trace amounts of methanol. Variable formation rates were obtained depending on Ru loading or hole scavenger (2-propanol) concentration. A production rate of ~200-250 µmol/g-cat in 6 hours were obtained for formic acid, formaldehyde, methane or methanol at different reaction conditions.

Dye sensitization is also used to improve the light absorption and the photocatalytic activity of TiO_2 (Ozcan et al. 2007, Zhao et al. 2007). Phthalocynaine (ZnPc) loaded TiO_2 photocatalysts were prepared by Zhao et al. (2007). It was found that ZnPc improved the light absorption of TiO_2. Formic acid was determined to be the main product and higher yield was obtained with in-situ ZnPc doped TiO_2 compared to the ZnPc doped TiO_2 photocatalyst prepared by impregnation method. Perylene diimide based dyes were used for the sensitization of Pt-TiO_2 films coated on borosilicate glass beads by Ozcan et al. (2007). The photocatalytic activities of Pt-TiO_2 films sensitized by BrGly and BrAsp and RuBpy dyes were compared. Methane was detected as the main product of gas phase CO_2 photoreduction. It was found that methane yield was 2 times higher with thick TiO_2 film compared to the thin TiO_2 film.

The effect of non-metal doping on the photocatalytic CO_2 reduction activity of TiO_2 was also investigated (Zhao et al. 2012). Nitrogen doped TiO_2 powders and nanotubes were prepared with different heat treatment temperatures. Formic acid with a production rate of 12435 µmol/g-cat in 12 hours was obtained with the nanotubes heat treated at 500^{o}C. Activities of the nanotubes heat treated at 300^{o}C and 400^{o}C were lower. High activity at high heat treatment temperature was attributed to stable combination of Ti and N atoms forming Ti-N bond and higher crystallinity at this temperature which decreased the recombination rate of electron-hole pairs.

The effect of REE doping on the photocatalytic CO_2 reduction activity of TiO_2 was investigated in a few research papers. Wang et al. (2013) prepared CeO_2-TiO_2 nanocomposites by hard template method. Ordered mesoporous silica SBA-15 was used as the template material. The effect of Ce:Ti molar ratio on the photocatalytic reduction of CO_2 in gas phase was investigated. Bandgap energies of pure TiO_2 and CeO_2 were estimated as 2.81 and 2.64 eV, respectively. Nanacomposites with different Ce:Ti molar ratios had lower bandgap energies compatred to pure TiO_2 and pure CeO_2 and the values were ~2.2 eV. The surface area of the pure TiO_2 decreased from 250 m^2/g to 130 m^2/g with increasing Ce content in the structure. Methane and carbon monoxide were the main products and produced at a rate of 11 mmol/g-cat and 70 mmol/g-cat in 6 hours, respectively. XPS analysis confirmed the increase of the surface chemisorbed oxygen species by CeO_2 addition. These oxygen species can capture electrons and form oxygen radicals which can reduce CO_2. The existence of mixture of Ce^{3+}/Ce^{4+} oxidation states were also shown by XPS. According to Wang et al. Ce^{3+} species on the surface of CeO_2-TiO_2 composites interacted with holes preventing the recombination of photogenerated electrons and holes, resulting in a higher photocatalytic activity. The same group investigated the effect of cerium (Ce) doping on the activity of sol-gel TiO_2 powders (Matejova et al. 2014). Pure and doped TiO_2 powders containing 0.28 to 10 mol% Ce were prepared and tested in the photocatalytic reduction of CO_2 under UV irradiation. Absorption edge of TiO_2 was reduced from 3.19 eV to 2.64 eV by 10 mol% Ce doping. Crystallographic characterization of the prepared powders by XRD was conducted and phases of Ce or Ti-Ce oxide were not detected in the patterns, except TiO_2 anatase phase. Crytallite size decreased with increasing Ce level which was attributed to the phase transformation inhibition by Ce. It was stated thet CeO_2 clusters preferentially nucleate on the oxygen vacancies in TiO_2 lattice. An interface is formed between CeO_2 and TiO_2 bridged with oxygen (Ce-O-Ti) and this occurs in the bulk of TiO_2 since the surface oxygen vacancies are hydroxylated at low Ce doping levels. CeO_2 clusters begin to grow with increasing Ce level and Ce-O-Ti bridge and the decrease in oxygen vacancy sites inhibit the anatase crystallite formation. The products of CO_2 photoreduction experiments were detected as methane and hydrogen. The highest yield of methane (16.0 μmol/g-cat) was obtained with 0.28 mol% Ce doped TiO_2 in 18 hours. Hydrogen yields were similar (~750 μmol/g-cat), except 10 mol% Ce doped TiO_2 (~300 μmol/g-cat). Low activities at high doping levels were attributed to the result of the decrease in the energy of electrons in the conduction band which decreased below the required H^+ reduction potential. Thus photocatalytic reduction of CO_2 efficiency decreased since reduction reaction occurs on the conduction band.

Gas phase photocatalytic reduction of CO_2 with TiO_2 based photocatalysts was also studied by many researchers. CO_2 is dissolved as CO_2 (g), HCO_3^- or H_2CO_3 in aqueous solutions of NaOH (which is the most used hole scavenger and increases the CO_2 solubility in water). These carbon containing molecules react with H_2O in aqueous systems. In the gas phase the only carbon containing molecule is CO_2 (g) and this molecule reacts with H_2O (v). Thus photocatalytic reduction of CO_2 products show variance according to the reactant molecules. In aqueous systems, formic acid, methanol and formaldehyde (Baeissa 2014, Lee et al. 2014, Li et al. 2012, Ohno et al. 2014, Qian et al. 2012, Qin et al. 2013, Tang et al. 2014, Wang et al. 2014, Zhao et al. 2012) or in some cases gaseous products such as methane and carbon monoxide (Koci et al. 2014, Ola et. al. 2012, Matejova et al. 2013, Matejova et al. 2014, Tan et al. 2012) are the main products; however in gaseous systems the main products are mostly methane and carbon monoxide (Ahmad Beigi et al. 2014, Gui et al. 2014, Hussain et al. 2013, Kong et al. 2013, Li et al. 2012, Li et al. 2014, Mahmodi et al. 2013, Mao et al. 2014, Marci et al. 2014, Merajin et al. 2013, Rani et al. 2014, Tahir and Amin 2013 and 2015, Wang et al. 2012, Wang et al. 2013, Yazdanpour and Sharifnia 2013, Zhao et al. 2012, Zhou et al. 2014)

The photocatalyst, estimated bandgap energies, main products, yield of main products, reaction conditions and irradiation source type from the selected and summarized research papers focused on the photocatalytic reduction of CO_2 with TiO_2 based materials in batch slurry systems are tabulated in Table 1.5.

Hydrocarbon production rate of 160 μL/gh with N doped TiO_2 nanotube arrays under 100 mW/cm^2 (natural sunlight) was reported as the highest rate until 2009 (Vargehese et al. 2009). Formic acid production rate of 439 μL/gh was achieved by Xue et al.(2011). Formic acid production rate of 12435 μmol/g-cat in 12 hours under visible light irradiation with N doped TiO_2 nanotubes prepared by Zhao et al. (2012) can be considered as the highest hydrocarbon production rate via CO_2 photoreduction until now.

Table 1.5. Important parameters in the selected research papers on CO_2 photoreduction.

Photocatalyst	**Estimated bandgap energy (eV)**	**Products**	**PY**	**Reaction temperature (^{o}C)**	**Irradiation type**	**Reference**
2.0 wt. % Cu/TiO_2	3.0	MOH	118.5	50	UV	Tseng et. al (2002)
3.0 wt. % Cu/TiO_2	2.88	MOH	2655	60	UV	Slamet et. al. (2005)
1.2 wt. % Cu/TiO_2	3.3	MOH	0.4	75	UV	Wu et. al. (2005)
$Ru/TiO_2/SiO_2$	3.04	H, FA, FAL	200.0	RT	UV	Sasirekha et.al. (2006)
$ZnPc/TiO_2$	-	FA	978.6	N/A	Vis	Zhao et. al. (2007)
$RuBpy/TiO_2$	-	MN	1.2	N/A	UV	Ozcan et. al. (2007)
Ag/TiO_2	2.74	MN, MOH	9.0, 1.8	N/A	UV	Koci et al. (2010)
TiO_2 nanotube	3.1	FA	12435	N/A	Vis	Zhao et al. (2012)
TiO_2-ZrO_2	3.44	MN, H	15.0, 170.0	N/A	UV	Matejova et al. (2013)
Ce/TiO_2	2.65	MN, H	16.0, 750.0	N/A	UV	Matejova et al. (2014)
TiO_2-CeO_2	2.2	MN, CO	11.0, 70.0	30^{o}C	UV	Wang et al. (2013)

PY: Product Yield (μmole/g-catalyst) at the end of the total irradiation time according to the referenced studies.
MOH: Methanol, FA: Formic acid, FAL: Formaldehyde, H: Hydrogen, CO: Carbon monoxide, MN: Methane.
RT: Room temperature.
N/A: Reaction temperature was not mentioned in the text and is supposed to be room temperature.

1.10. Explanation of Dissertation Format

The dissertation includes seven chapters. The first chapter is a review of the research on artificial photosynthesis processes conducted mostly with TiO_2 based photocatalysts. A brief introduction was given at the beginning of this chapter. The following five chapters were written in a form suitable for publication in a scientific journal. The techniques utilized and the results obtained on the detailed investigation of the phase evolution of rare earth element doped nanocrystalline titania powders are summarized in the second chapter. The results of the effect of REE doping and powder preparation methods on the artificial photosynthesis activity of titania powders are discussed in chapters 3 & 4 respectively. The following two chapters (5th and 6th) are on preliminary characterization results of lanthanum-titanium pyrochlore powders and neodymium-cerium co-doped sol-gel titania powders which may be further tested in artificial photosynthesis. A summary of the dissertation and recommendations are given in the final (7th) chapter. The references cited in each section are given at the end of the dissertation.

CHAPTER 2

THE EFFECT OF RARE EARTH ELEMENT DOPING ON THE MICROSTRUCTURAL EVOLUTION OF SOL-GEL TITANIA POWDERS

2.1. Introduction

Photocatalysis is expected to make a great contribution to both environmental treatment (emission cleaning and water purification) and renewable energy generation. Photocatalysts play a central role in the success of the photocatalytic processes. Intense research and advances in nanoscience and nanotechnology in the last 20 years improved the preparation techniques and expanded the application area of nanostructured photocatalytic materials. Fujishima and Honda conducted the pioneering studies in 1970s to produce renewable energy via photocatalytic processes by using solar energy (Fujishima et al. 1972, Inoue et al. 1979). Since then many photocatalytic materials were prepared to be used in various photocatalytic processes. There are many examples in the literature and there is a huge variety of photocatalytic materials to be used in many different photocatalytic processes. Titania (TiO_2) is the most extensively used photocatalyst since it is biologically and chemically inert, stable with respect to photocorrosion and chemical corrosion and inexpensive.

The major disadvantage of these titania phases is their relatively high bandgap energies commonly reported in the 3.0-3.2 eV range which results in the very limited absorption of sun light (Nassoko et al. 2012). The reduction and modification of the bandgap energies of the titania phases by doping with various elements for more efficient absorption in the visible range and the determination of the activities of these materials in the photocatalytic decomposition of organic structures is the main concern of intense research in the last 10-15 years (Bokare et al. 2013, Chiou and Juang 2007, Castañeda-Contreras et al. 2012, Gao et al. 2012, Liang et al. 2006, Romero et al. 2010, Silva et al. 2009, Wang et al. 2010, Xiao et al. 2008, Xie et al. 2010, Xu et al. 2009, Xu et al. 2009). Doping TiO_2 with various rare earth ions can increase the photocatalytic activity by enhancing the light absorption along with tuning the phase structure (anatase-rutile) and surface morphology. It is well known that doped rare earth (RE) ions can inhibit the anatase to rutile phase transformation and increase the surface area of TiO_2. Research conducted in the last 10 years indicated that La, Nd, Eu, Sm, Yb, Pr and Ce doped TiO_2 showed higher activities than pure TiO_2 due to their enhanced light absorption, higher surface areas and altered phase structure (Bellardita et al. 2007 and 2011, Chiou and Juang 2007, Hassan et al. 2012, Jian et al. 2010, Reszczynska et al. 2014, Romero et al. 2010, Tong et al. 2007, Wang et al. 2010, Xie and Yuan 2004, Xie et al. 2005, Xu et al. 2009, Yan et al. 2005). These studies are mostly on the environmental applications like photocatalytic degradation of dyes in wastewaters.

Research conducted on REE doped TiO_2 showed no consensus on whether the dopant ions are incorporated in the titania lattice structure (Li et al. 2005, Nassoko et al. 2012, Ningthoujam et al. 2009, Setiawati et al. 2008, Shah et al. 2002, Wang et al. 2010), the solubility limits of the metal ions in these phases, if the metal ions are not incorporated (Luo et al. 2008, Shahmoradi et al. 2010, Antić et al. 2012) in the lattice structure what mechanisms are responsible for the higher wavelength absorption in the resultant multi-phase nanostructure. A small group of researchers claimed that RE ions can occupy the substitutional sites based on their XRD results (Burns et al. 2004, Devi and Kumar 2012, Ghigna et al. 2007, Li et al. 2005, Obregon et al. 2013, Xin and Liu 2011). A major portion of the researchers in this field claimed that substitutional incorporation of RE ions is not possible due to the significantly larger ionic radii compared to Ti^{+4} ion. According to their results, RE ions can accommodate on the interstitials or segregate as oxide/hydroxide phases on the grain boundaries of TiO_2. There are also studies indicating the formation of a new phase containing both RE and titanium ions (Jin et al. 2008). Zhang et al. (2004) conducted a systematic study on the formation of RETiO phases in TiO_2 matrix doped with RE elements. They discovered that anatase to rutile phase transformation was significantly inhibited by RE ions and inhibitory effect increased with dopant ionic radius. They have also found that different RETiO phases are formed depending on the RE ionic radius.

Research on the effect of REE doping on sol particle size, phase structure properties such as new phase formation, crystallite size, lattice constants, lattice strain, anatase-rutile weight fraction or Ti-O chemical bonding energy is limited for now.

In addition phase diagrams of TiO_2 with RE oxides are present for the heat treatment temperatures above 1000°C and these diagrams indicated that two phases are insoluble in each other (Gong and Zhang 2013, Skapin et al. 2000). Present phase diagrams show that there are oxide phases of RE_2Ti_2 (pyrochlore), RE_4Ti_9, RE_2Ti_4 which may be formed at high REE levels and heat treatment temperatures. The structure of phase diagrams at low temperatures is very important since it is crucial to maintain high surface area and porous structure for photocatalytic applications. Low temperature phase diagrams of TiO_2 and RE oxides are not available yet. It would be useful to have information about the nature of the phases and solid state solubilities at low RE levels and low temperatures to see the effect of phase structure on the photocatalytic activity of RE doped TiO_2 or Ti-RE mixed oxides.

The nanodesign of REE incorporated TiO_2 based nanostructured materials by using sol-gel technique was conducted in this study in order to clarify the effect of REE doping on the phase structure of TiO_2 phases. Phase structure of these materials (the location of the dopant ions and the resultant lattice structure changes, new phase formation), the effect of the dopant ions on sol particle size, particle/pore size and surface area were investigated. Nanocomposites were prepared by using precursors mixed at the atomic level.

2.2. Materials and Methods

2.2.1. Preparation of the Powders

REE doped TiO_2 powders were prepared by sol-gel using titanium tetraisopropoxide (TTIP, Aldrich 97%) as titanium precursor. Cerium(III) nitrate hexahydrate ($Ce(NO_3)_3.6H_2O$, Aldrich 99.99% trace metal basis), neodymium nitrate hexahdrate ($Nd(NO_3)_3.6H_2O$, Aldrich 99.99% trace metal basis), lanthanum nitrate hexahydrate ($La(NO_3)_3.6H_2O$, Aldrich 99.99% trace metal basis), praseodmium(III) nitrate hexahydrate ($Pr(NO_3)_3.6H_2O$, Aldrich 99.9% trace metal basis), erbium(III) nitrate pentahydrate ($Er(NO_3)_3.5H_2O$, Aldrich 99.9% trace metal basis), dysporsium(III) nitrate pentahydrate ($Dy(NO_3)_3.5H_2O$, Alfa aesar 99.9% trace metal basis), samarium(III) nitrate hexahydrate ($Sm(NO_3)_3.6H_2O$, Alfa aesar 99.9% trace metal basis), gadolinium(III) nitrate hexahydrate ($Gd(NO_3)_3.6H_2O$, Aldrich 99.9% trace metal basis), terbium(III) nitrate pentahydrate ($Tb(NO_3)_3.5H_2O$, Aldrich 99.9% trace metal basis), ytterbium (III) nitrate pentahydrate ($Yb(NO_3)_3.5H_2O$, Aldrich 99.9% trace metal basis), europium(III) nitrate pentahydrate ($Eu(NO_3)_3.5H_2O$ Aldrich 99.9% trace metal basis), yttrium(III) nitrate hexahydrate ($Y(NO_3)_3.6H_2O$ Alfa aesar 99.9% trace metal basis) or zirconium(IV) propoxide (Aldrich 70%) were used as dopant precursors.

Pure TiO_2 powders were prepared by the dropwise addition of a solution (nitric acid (HNO_3, Merck 65%) and water in ethanol (Merck absolute)) to a titanium tetraisopropoxide/ethanol solution under vigorous stirring at room temperature. The resulting transparent sol with the molar ratios of TTIP:H_2O:HNO_3:EtOH as 1:2:0.06:5.9 was stirred until complete gelation was observed. RE doped TiO_2 powders were prepared by following the same route with the addition of predetermined amounts of RE nitrates to nitric acid/water/ethanol solution. The obtained gels were dried at 50°C overnight prior to heat treatment at 400-1000°C for 3 hours. TiO_2 powders doped with 0-10% RE_2O_3 (on molar basis) were prepared in the context of this study.

Gelation time for pure TiO_2 was 3 minutes and the time necessary for the complete gelation of the doped TiO_2 sols increased up to 4 days with the increasing doping level. The increase in the gelation time with doping level may be due to the increase of nitrate ion concentration originating from the use of nitrate salts of rare earths as dopant precursors. A schematic representation for the preparation of REE doped sol-gel TiO_2 powders is given in Figure 2.1.

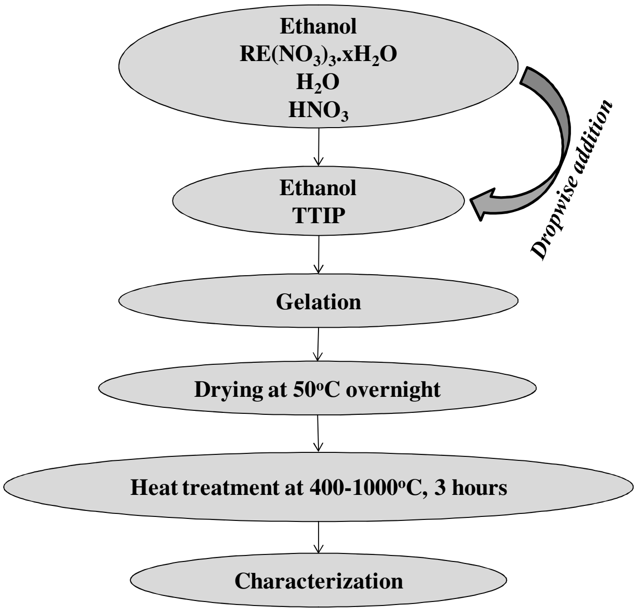

Figure 2.1. A schematic representation of RE_2O_3 doped sol-gel TiO_2 powder preparation process.

2.2.2. Characterization of the Powders

Phase characterization of the prepared powders was performed by Philips X'pert Pro XRD equipment with monochromated high-intensity (λ=1.54Å) CuKα radiation. The scanning rate was set as 2.5 2Θ/min between 5° and 80° with 0.033° step size. Characterization was conducted with 1-2 g powder pressed in an aluminum cassette which was also used as reference material to calculate the accurate peak positions.

The crystallite sizes were calculated from the broadening of the (101) reflection for anatase and (110) reflection for rutile using Scherrer's equation:

$$d = \frac{k.\lambda}{\beta.\cos\theta} \tag{2.1}$$

where d is the crystallite size (nm), k is the shape constant (0.9 for spherical particles), λ is the X-ray wavelength (nm), β is the full width at half maximum of the selected peak and θ is the Bragg's angle of diffraction (Sun et al. 2014).

The rutile and anatase weight fractions were determined by using the following relation:

$$x_A = \left(1 + 1.26\frac{I_R}{I_A}\right)^{-1} \tag{2.2}$$

where x_A is the anatase weight fraction, I_R and I_A are the intensities of the rutile (110) and anatase (101) peaks, respectively (Spurr and Mayers 1957).

The determination of the crystal lattice constants for tetragonal geometry (a and c) was conducted using the following expression:

$$\frac{1}{d_{hkl}^2} = \frac{h^2+k^2}{a^2} + \frac{l^2}{c^2} \tag{2.3}$$

where d_{hkl} is the interplane distance and hkl are the Miller (plane) indices. The lattice constants were determined by selecting two peaks ((101) and (200) peaks for anatase) (Tripathi et al. 2013).

Lattice strain in the TiO_2 crystal lattice was calculated by using Williamson-Hall (W-H) plot with at least 4 diffraction peaks to be used in the following relation:

$$\frac{\beta\cos\theta}{\lambda} = \frac{1}{\sigma} + \frac{\eta.\sin\theta}{\lambda} \tag{2.4}$$

where σ is the effective particle size and η is the effective strain (Tripathi et al. 2013).

Dynamic light scattering (DLS) analyses were conducted with Malvern NanoZS90 in order to determine doped/undoped TiO_2 sol average particle sizes. Nd_2O_3 doped or pure TiO_2 sols were prepared with ¼ of Ti^{4+} concentration of the original recipes to prevent rapid gelation for proper DLS analyses, whereas H_2O/Ti^{4+} and H_3O^+/Ti^{4+} ratios were kept constant.

X-ray photoelectron spectroscopy (XPSSPECS EA 300) was used to identify the existence and bonding states of the elements in the prepared powders. Carbon C1s line at 284.8 eV was taken as a reference for the correction of the peak shifts (Kruse and Chenakin 2011). The fitting of C1s spectrum was performed by Gaussian line shape with constant background (Cappelletti et al. 2008) and fitting of O1s and Ti2p spectra were performed by pseudo-Voigt line shape with Shirley background. Peak fitting examples are given in Appendices and in the figures.

Nitrogen adsorption and desorption isotherms and surface areas were obtained with Micromeritics Gemini V surface area analyzer.

Transmission electron microscopy (Jem Jeol 2100F 200kV HRTEM) was used to investigate the surface morphology and determine neodymium doping level of the prepared powders.

2.3. Results and Discussion

2.3.1. Phase Structure of Pure TiO_2 Powders

XRD patterns, lattice strain/crystallite sizes and anatase-rutile weight fractions of pure TiO_2 powders heat treated in the 400-1000°C temperature range are given in Figures 2.2, 2.3 and 2.4, respectively. The characteristic diffraction peaks of anatase (JCPDS card is given in APPENDICES) were identified in the XRD patterns of the prepared powders at relatively low heat treatment temperatures (400-600^{o}C). The anatase phase was found to be the only phase for the powders heat treated up to 600^{o}C. It was found that anatase coexists with the rutile phase (JCPDS card is given in APPENDICES) at 700^{o}C with a contribution of 31 wt%, while XRD patterns showed only reflections of rutile phase at 800^{o}C and above. The crystallite size increased from 15 nm to 115 nm while lattice strain decreased with increasing heat treatment temperature. A negative slope in the W-H plot indicates the presence of compressive strain, while a positive slope indicates the presence of tensile strain (Maurya et al. 2011). Slopes of the W-H plots of pure TiO_2 were positive up to 700^{o}C and were negative for the temperature interval of 700-1000^{o}C. Pure TiO_2 powders composed of anatase crystallites showed tensile strain, while powders containing rutile phase showed compressive strain which may be due to the densification during phase change and larger crystallite sizes.

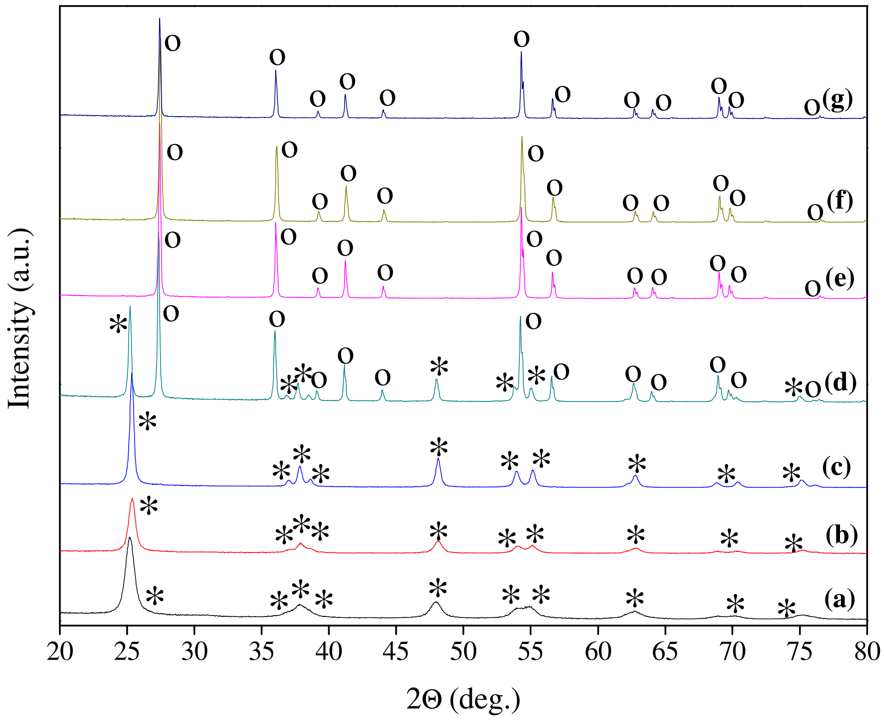

Figure 2.2. XRD patterns of pure TiO_2 powders heat treated at (a) 400^{o}C, (b) 500^{o}C, (c) 600^{o}C, (d) 700^{o}C, (e) 800^{o}C, (f) 900^{o}C, (g) 1000^{o}C (*: anatase, o: rutile).

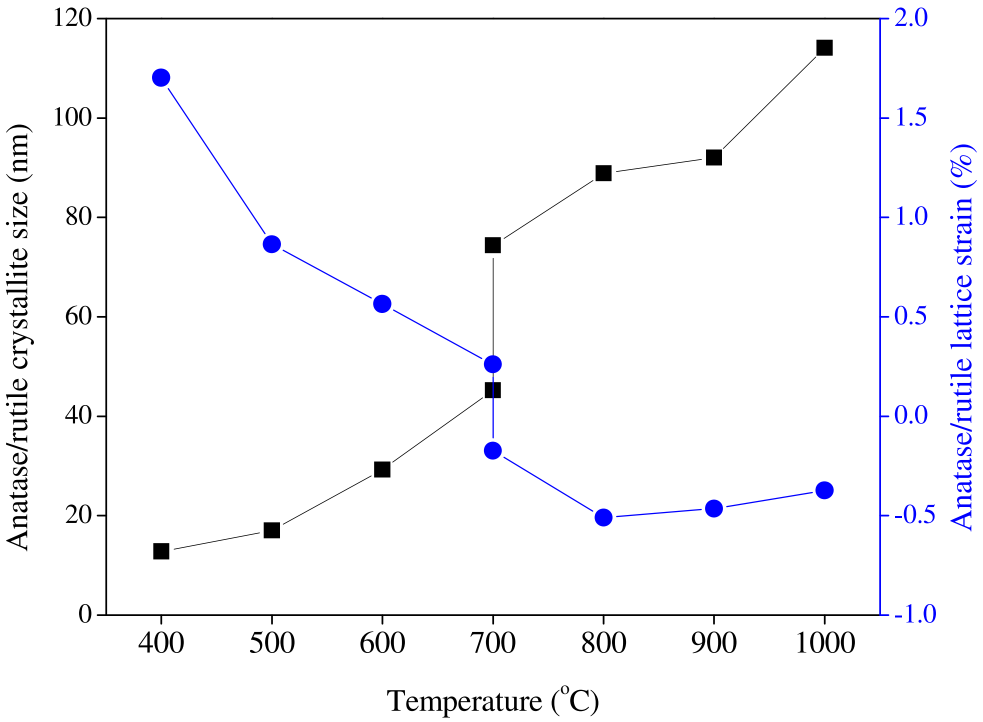

Figure 2.3. Anatase/rutile crystallite size (■) and anatase/rutile lattice strain (●) of pure TiO_2 powders heat treated in the 400-1000°C temperature range.

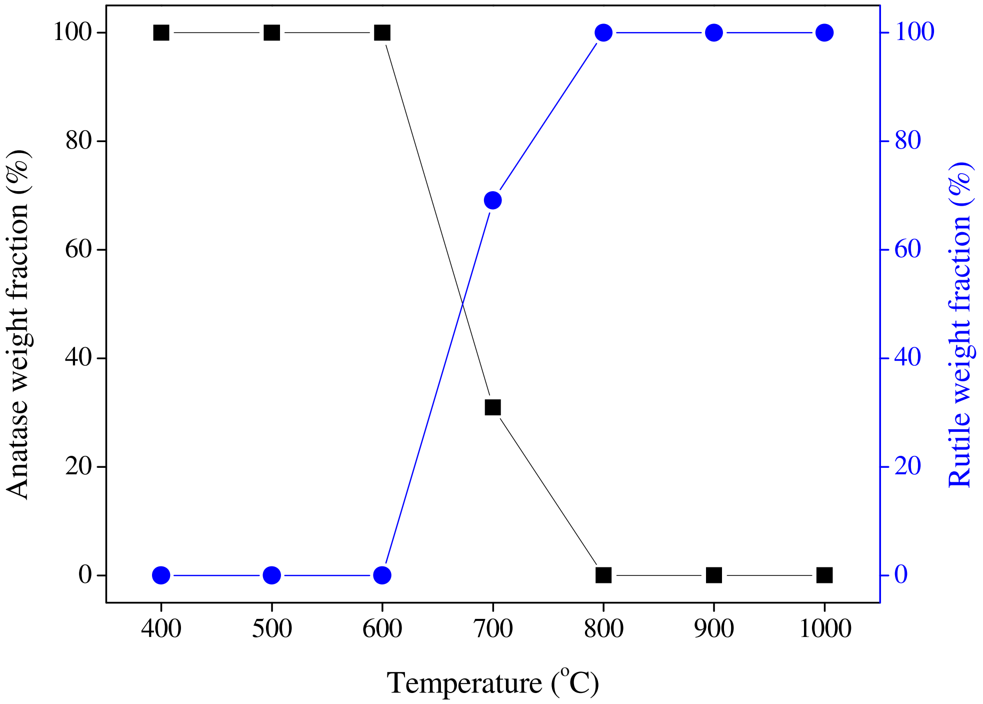

Figure 2.4. Anatase (■) and rutile (●) weight fractions of pure TiO_2 powders heat treated in the 400-1000°C temperature range.

The change in volume average particle size with aging time/Nd_2O_3 doping level and size distribution curves on the 8th day of Nd_2O_3 doped TiO_2 sols are given in Figures 2.5 and 2.6, respectively. Particle sizes of freshly prepared sols are given as 0th day. The activation energy and the onset temperature for the phase transformation decreases with decreasing initial particle size leading to decreased thermal stability according to Li et al. 2004, Gribb and Banfield (1997), Zhang and Banfield (2000) and Ranade et al. (2002). Particle size of TiO_2 can either be reduced or increased by doping (Borlaf et al. 2013, 2014, Ruzmanova et al. 2013). The initial particle sizes show variation depending on the doping level according to these references which is in agreement with our results. A slight increase in the volume average particle size was observed with increasing Nd_2O_3 doping level which became significant when the aging time was increased to 8 days. TiO_2 sol particle size slightly decreased at low doping levels (at 0.1 and 0.25 %) and increased at higher doping levels in general. The average particle size range of freshly prepared TiO_2 sols were detected to increase from ~2 nm to ~2.5 nm at the end of 8 days aging.

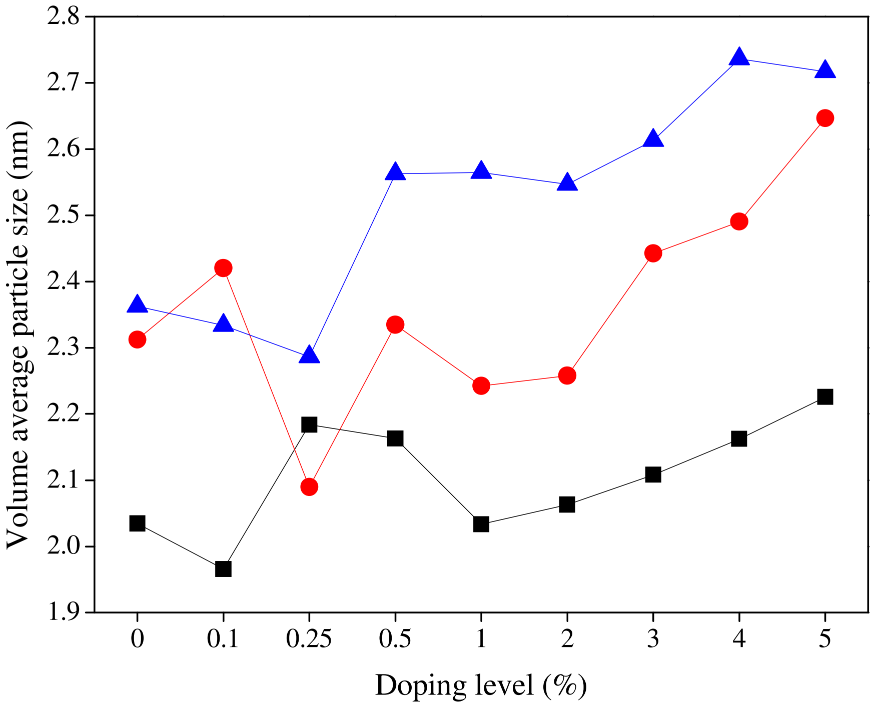

Figure 2.5. Volume average particle sizes of Nd_2O_3 doped TiO_2 sols (■: 0th day, ●: 1st day, ▲: 8th day).

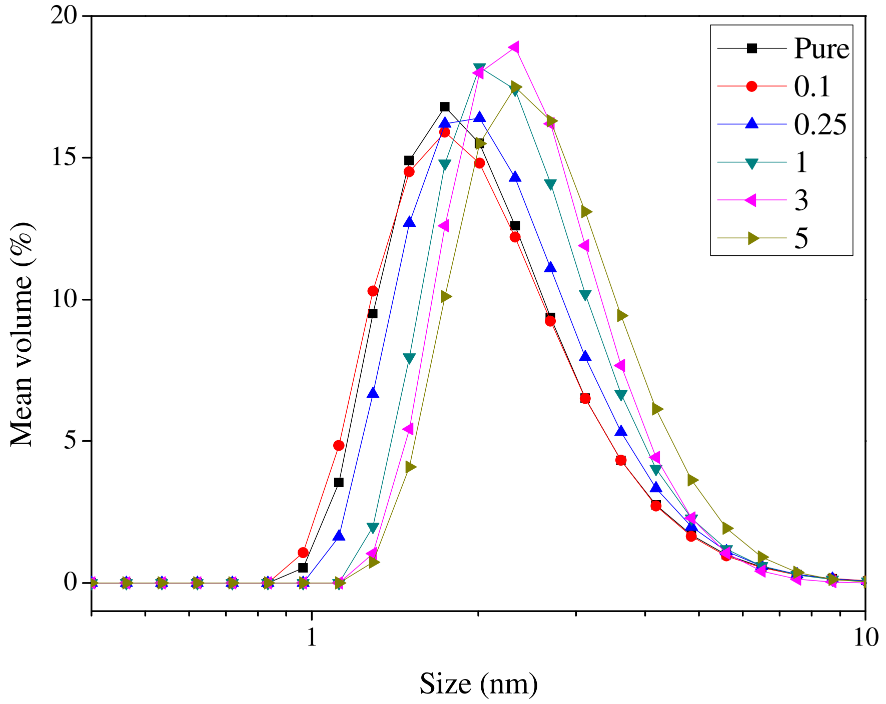

Figure 2.6. Volume average particle size distribution of Nd_2O_3 doped TiO_2 sols on the 8th day.

2.3.2. Phase Structure of Nd_2O_3 and Er_2O_3 Doped TiO_2 Powders

XRD patterns of Nd_2O_3 doped TiO_2 powders heat treated in the 400-1000°C temperature range are shown in Figures 2.7-2.13. Anatase was found to be the main phase in all Nd_2O_3 doped TiO_2 powders at 400-800°C heat treatment temperature interval. The powders heat treated at 400-600°C consist of only anatase crystals. Rutile phase began to show up at 700°C and was detected for doping levels up to 0.25% at 700°C and 0.5% at 800°C; reflections of rutile phase were not detected for Nd_2O_3 doped TiO_2 powders above 0.5% doping level at these temperatures. $Nd_4Ti_9O_{24}$ phase was detected in 10% Nd_2O_3 doped TiO_2 powder at 800°C. The relative intensity of (101) reflection peak significantly decreased and FWHM of this peak increased with increasing doping level which indicated that anatase to rutile phase transformation was significantly inhibited by Nd doping level.

The ionic radius of RE^{3+} (>100 pm) is between that of Ti^{4+} (68 pm) and O^{2-} (132 pm). Therefore, it is difficult for RE^{3+} ions to replace with Ti^{4+} ions in the lattice (Sibu et al. 2002). It is likely for RE^{3+} ions to accommodate on the interstitials or segregate in the grain boundaries in the form of oxide/hydroxide phases depending on the concentration of RE ions (Antic et al. 2012). There are 3 possible reasons for the inhibition of anatase to rutile phase transformation. First one is the possible presence of interstitial Nd^{3+} ions which may create localized positive charge around Ti^{4+} ions and form oxygen vacancies due to being more electropositive than Ti^{4+} (Li et al. 2005, Shah et al. 2002). Second one is a possible increase in the diffusion barrier at the TiO_2-TiO_2 grain contact needed for the grain growth process by the segregated Nd-oxide/hydroxide phases in the grain boundaries (Asal et al. 2011, Bokare et al. 2013, Kibombo et al. 2013, Xiao et al. 2008). The last one is the possible substitution of Ti^{4+} ions for Nd^{3+} ions in Nd-oxide/hydroxide lattice on the interface of Nd^{3+}-TiO_2 and the formation of Nd-O-Ti bonds which stabilize the Ti-O bonds and inhibit Ti-O bond breakage needed for anatase crystal nucleation/growth (Saif and Abdel-Mottaleb 2007). Stabilization of Ti-O bond by Nd doping may lead to a decrease in the atomic mobility which may also lead to the inhibition of anatase to rutile phase transformation.

Formation of $Nd_4Ti_9O_{24}$ phase at 10% doping level and 800°C may be attributed to the presence of Nd^{3+} ions in the interstitials or segregation of Nd-oxide/hydroxide on the surface of TiO_2. Enhanced atomic/ionic diffusion with increasing heat treatment temperature and increased dopant concentration may increase the probability of RE^{3+} ions to make contact to form Nd-oxide phases or Nd-Ti-oxide phases.

$Nd_4Ti_9O_{24}$ phase was formed beginning from 0.5% doping level at 900°C with small contribution of $Nd_2Ti_4O_{11}$ phase (beginning from 1%). Anatase peak intensity increased up to 1% doping level and gradually decreased beyond this doping level. The detection of a mixed oxide phase ($Nd_4Ti_9O_{24}$ or $Nd_2Ti_4O_{11}$) rather than a single phase of Nd (Nd_2O_3) at 10% doping level at 800°C and beginning from 0.5% doping level at 900°C and 1000°C and the decrease in the anatase peak intensity beyond 1% a t 900°C indicated that interstitial accommodation of Nd^{3+} ions in the TiO_2 lattice structure up to a possible limit of ~0.5-1% and formation of Nd-Ti-O phases by the consumption of anatase crystals may be possible.

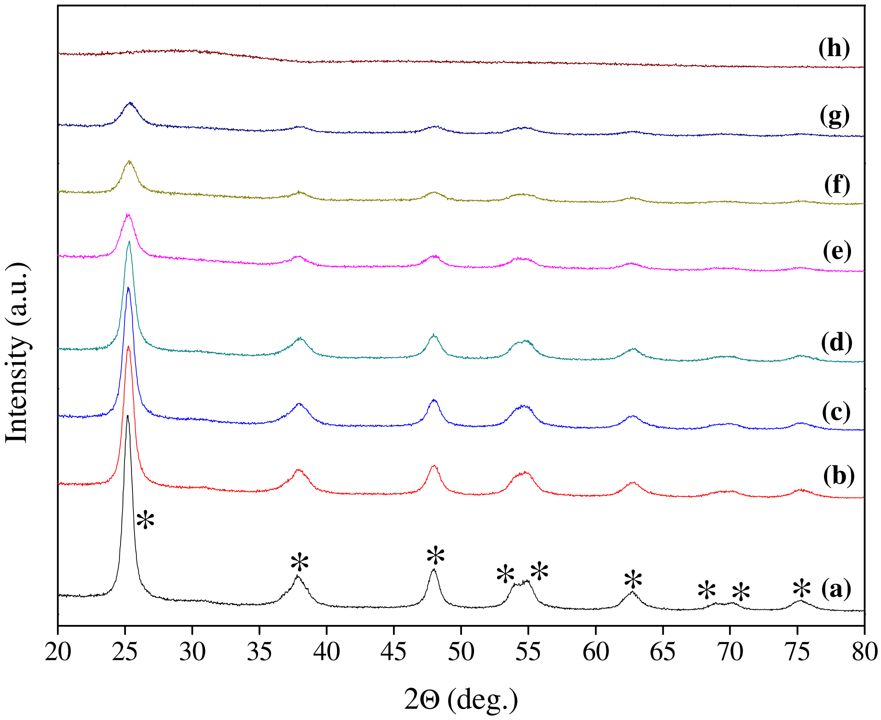

Figure 2.7. XRD patterns of Nd doped TiO_2 powders heat treated at 400°C: (a) pure, (b) 0.25%, (c) 0.5%, (d) 1%, (e) 2%, (f) 3%, (g) 4%, (h) 5% doped TiO_2 powder (*: anatase).

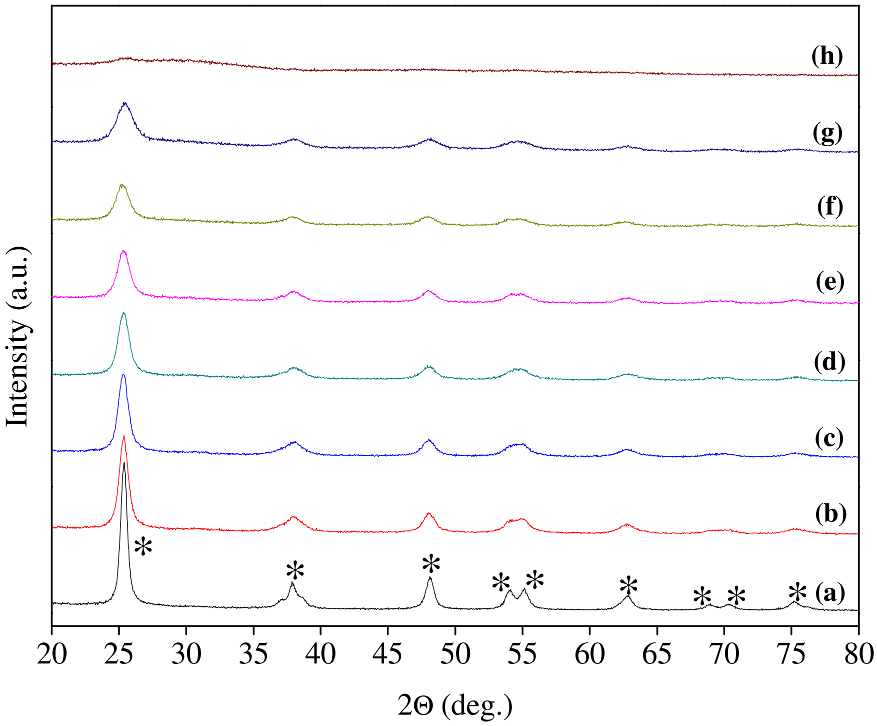

Figure 2.8. XRD patterns of Nd_2O_3 doped TiO_2 powders heat treated at 500°C: (a) pure, (b) 0.25%, (c) 0.5%, (f) 1%, (e) 2%, (f) 3%, g) 4%, (h) 5% doped TiO_2 powder (*: anatase).

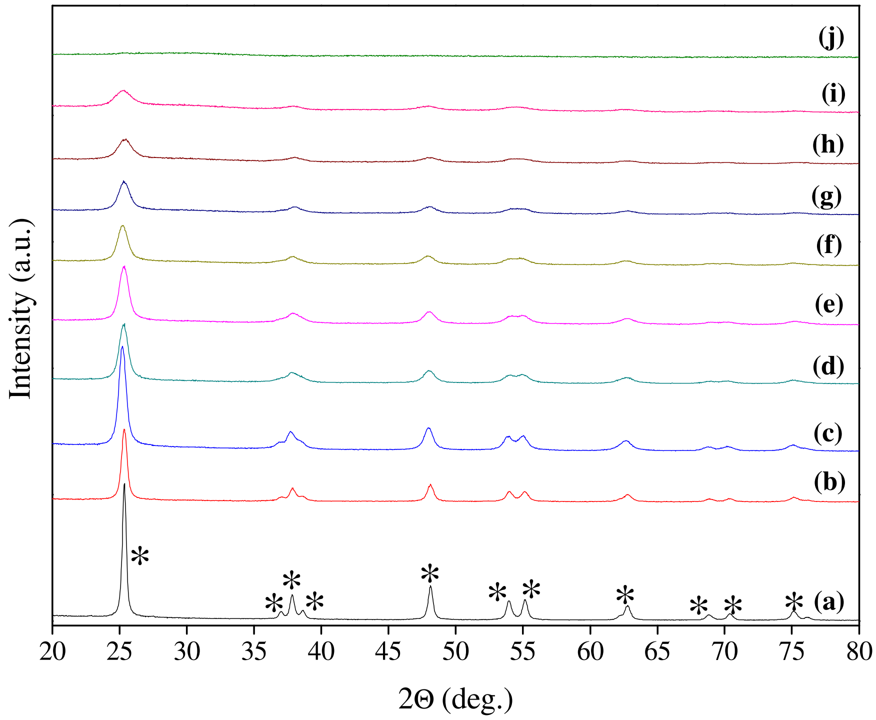

Figure 2.9. XRD patterns of Nd_2O_3 doped TiO_2 powders heat treated at 600°C: (a) pure, (b) 0.1%, (c) 0.25%, (d) 0.5%, (e) 1%, (f) 2%, (g) 3%, (h) 4%, (i) 5%, (j) 10% doped TiO_2 powder (*: anatase).

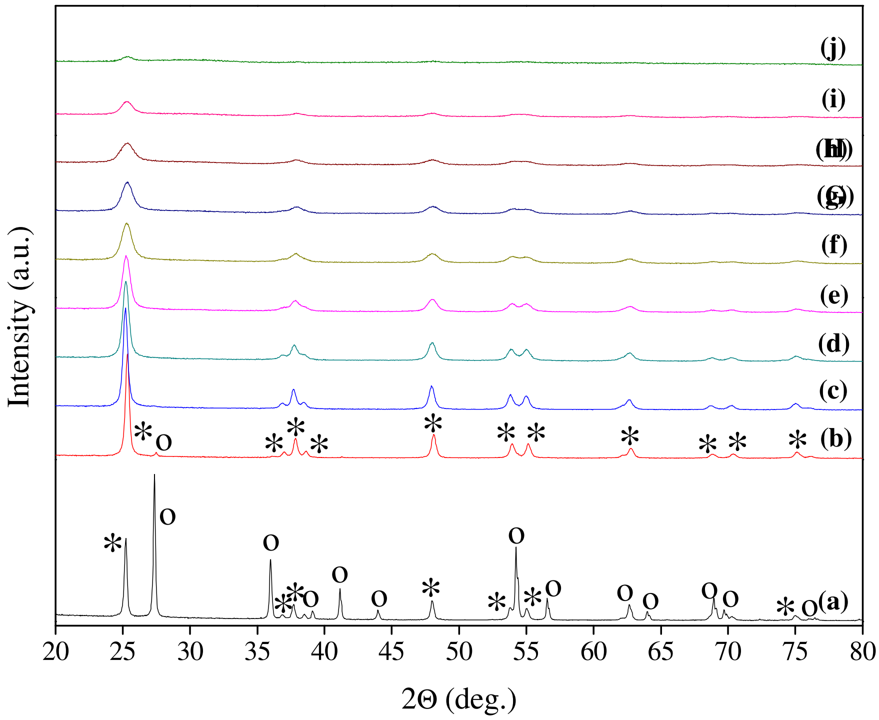

Figure 2.10. XRD patterns of Nd_2O_3 doped TiO_2 powders heat treated at 700°C: (a) pure, (b) 0.1%, (c) 0.25%, (d) 0.5%, (e) 1%, (f) 2%, (g) 3%, (h) 4%, (i) 5%, (j) 10% doped TiO_2 powder (*: anatase, o: rutile).

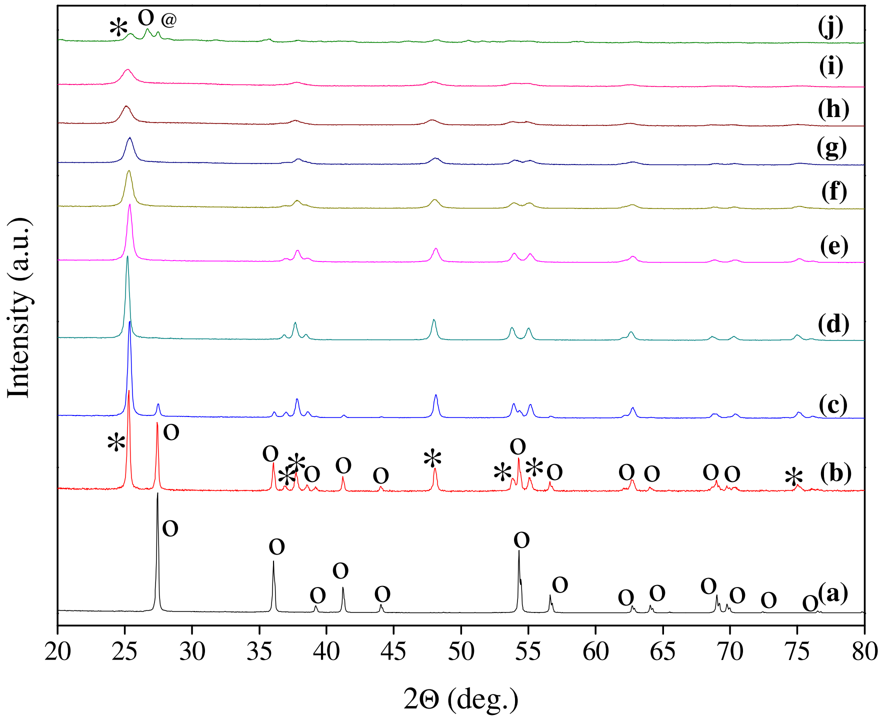

Figure 2.11. XRD patterns of Nd_2O_3 doped TiO_2 powders heat treated at 800°C: (a) pure, (b) 0.1%, (c) 0.25%, (d) 0.5%, (e) 1%, (f) 2%, (g) 3%, (h) 4%, (i) 5%, (j) 10% doped TiO_2 powder (*: anatase, o: rutile, @: $Nd_4Ti_9O_{24}$).

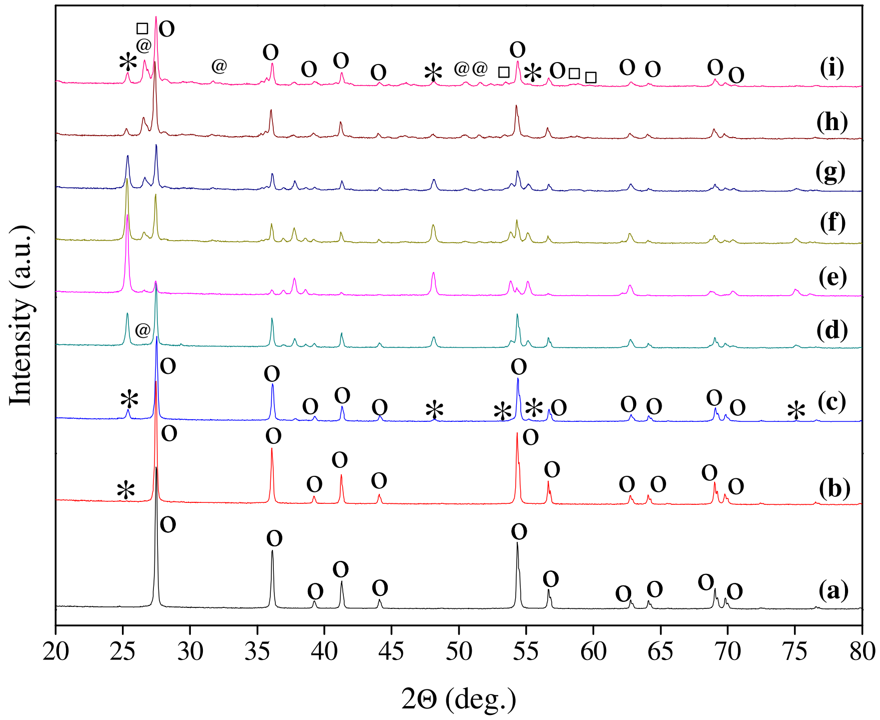

Figure 2.12. XRD patterns of Nd_2O_3 doped TiO_2 powders heat treated at 900°C: (a) pure, (b) 0.1%, (c) 0.25%, (d) 0.5%, (e) 1%, (f) 2%, (g) 3%, (h) 4%, (i) 5% doped TiO_2 powder (*: anatase, o: rutile, @: $Nd_4Ti_9O_{24}$, □: $Nd_2Ti_4O_{11}$).

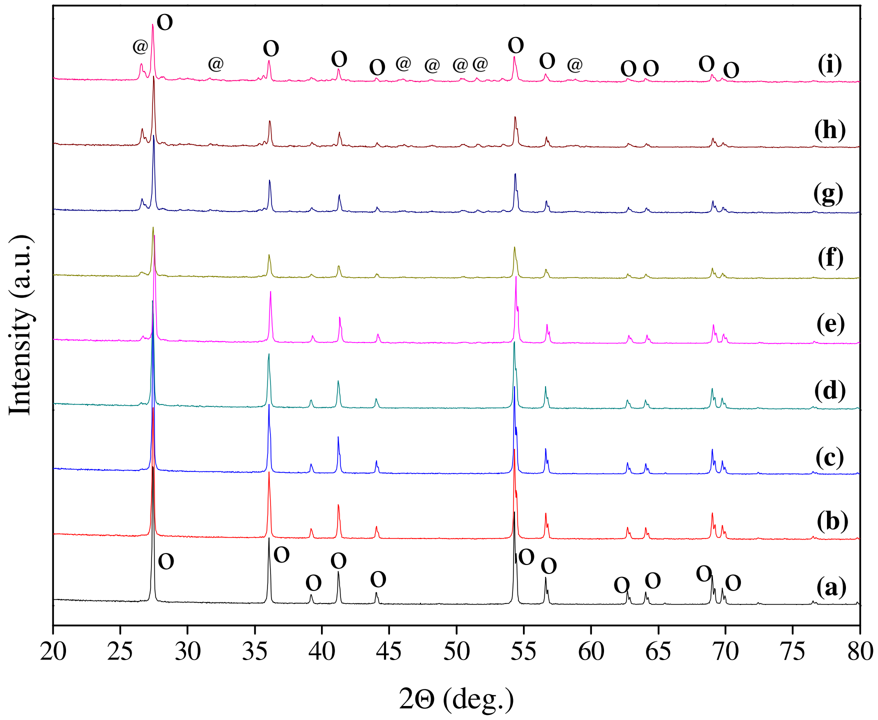

Figure 2.13. XRD patterns of Nd_2O_3 doped TiO_2 powders heat treated at 1000°C: (a) pure, (b) 0.1%, (c) 0.25%, (d) 0.5%, (e) 1%, (f) 2%, (g) 3%, (h) 4%, (i) 5% doped TiO_2 powder (o: rutile, @: $Nd_4Ti_9O_{24}$).

XRD patterns of Er_2O_3 doped TiO_2 powders heat treated in the 800-1000°C temperature range are given in Figures 2.14- 2.16, respectively. XRD patterns of the powders heat treated at 600 and 700°C were given in Appendix A since the patterns were similar to the patterns of Nd_2O_3 doped TiO_2 powders heat treated at the same temperatures. The differences are stated in the text below. Anatase was found to be the main phase in all Er_2O_3 doped TiO_2 powders between 600-800°C similar to Nd_2O_3 doped TiO_2 powders. Rutile was detected at low doping levels at 700°C and 800°C. Erbium titanate ($Er_2Ti_2O_7$) phase was detected at doping levels beginning from 2% at 800°C; however Nd_2O_3 doped TiO_2 powders were composed of only anatase crystals at these doping levels and temperature. Anatase to rutile phase transformation kinetics was also affected by Er_2O_3 doping level. Higher heat treatment temperatures were also applied in order to investigate the formation of $Er_2Ti_2O_7$ phase in TiO_2 matrix. Anatase phase was observed even at 900°C at 3-5 % doping levels; however rutile and $Er_2Ti_2O_7$ phases detected to be significantly the dominant phases at 900 and 1000°C. A mixture of anatase-rutile-$Er_2Ti_2O_7$ phases at almost even compositions was detected at 5% doping level at 900°C. Rutile and $Er_2Ti_2O_7$ phases dominate the microstructure for the heat treatment temperature of 1000°C and no reflections belonging anatase phase were detected in the XRD patterns of the powders heat treated at this temperature. $RE_2Ti_2O_7$ phase was formed by Er_2O_3 doping unlike the formation $Nd_4Ti_9O_{24}$ phase. Restricted atomic mobility of RE ions in TiO_2 matrix due to relatively large ionic radii causes RE_2O_3 or RETiO phases to form at elevated temperatures where the atomic mobility increases or at high doping levels for REEs with large ionic radii. $Er_2Ti_2O_7$ phase was detected beginning from 2% doping level at 800^{o}C for Er_2O_3 doping, the doping level for the formation of $Nd_4Ti_9O_{24}$ phase was 10% for Nd_2O_3. The ionic size of Er^{3+} (103 pm) is smaller than that of Nd^{3+} (112 pm), hence it is more possible for Er to make contact with neighboring Ti or Er atoms to form RETiO phases. The ionic radius decreases with increasing atomic number, hence decreasing the coordination number. This phenomenon leads to the formation of lower coordination number compounds of RETiO phases (Zhang et al. 2004). There is another possible reason for the formation of $Nd_4Ti_9O_{24}$ instead of $Nd_2Ti_2O_7$ may be the increasing electropositivity with decreasing atomic number for rare earths which may increase the oxygen coordination number.

According to Borlaf et al. (2013) $Er_2Ti_2O_7$ pyrochlore forms from rutile. Reflections of anatase phase began to appear with 3% Er_2O_3 doping level at 900^{o}C. Anatase to rutile phase transformation is known to be reconstructive involving the breaking and reforming of bonds (Hanaor and Sorrel 201) and can be inhibited by the surrounding RE ions in TiO_2 grain boundaries or intersititial Er ions in TiO_2 lattice. Therefore interstitial or segregated Er ions may form $Er_2Ti_2O_7$ with rutile TiO_2. The XRD patterns and the figure obtained from XRD patterns (Figure 2.18) indicated that rutile phase disappeared while $Er_2Ti_2O_7$ phase continued to grow.

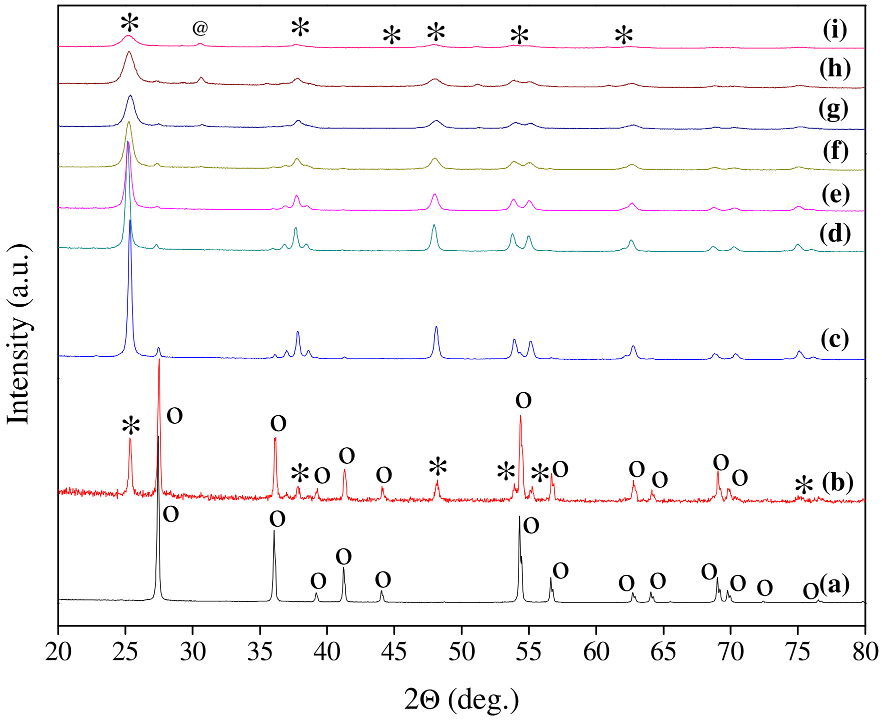

Figure 2.14. XRD patterns of Er_2O_3 doped TiO_2 powders heat treated at 800°C: (a) pure, (b) 0.1%, (c) 0.25%, (d) 0.5%, (e) 1%, (f) 2%, (g) 3%, (h) 4%, (i) 5% doped TiO_2 powder (*: anatase, o: rutile).

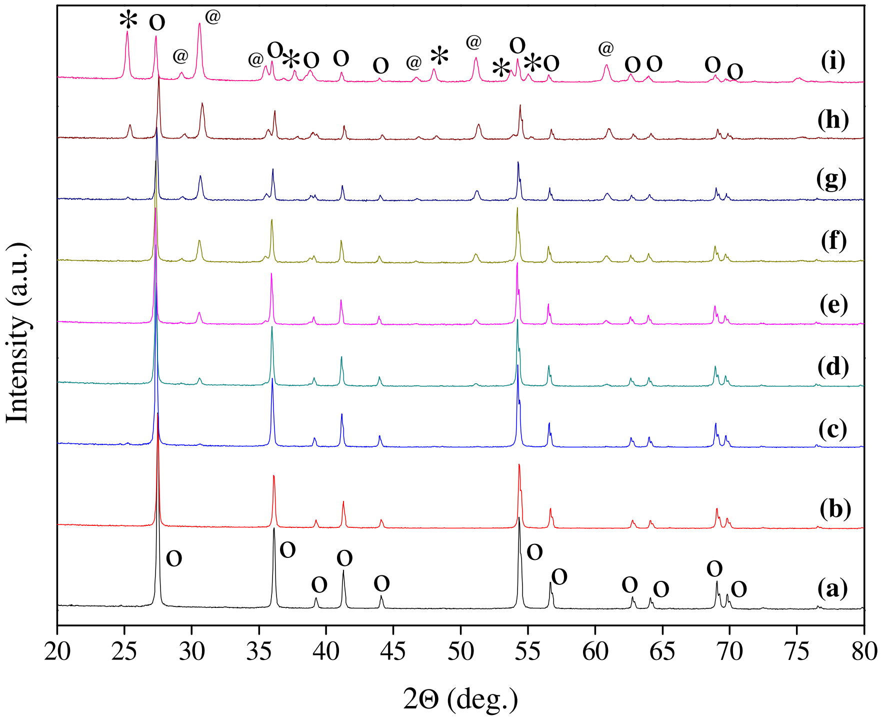

Figure 2.15. XRD patterns of Er_2O_3 doped TiO_2 powders heat treated at 900°C: (a) pure, (b) 0.1%, (c) 0.25%, (d) 0.5%, (e) 1%, (f) 2%, (g) 3%, (h) 4%, (i) 5% doped TiO_2 powder (*: anatase, o: rutile, @: $Er_2Ti_2O_7$).

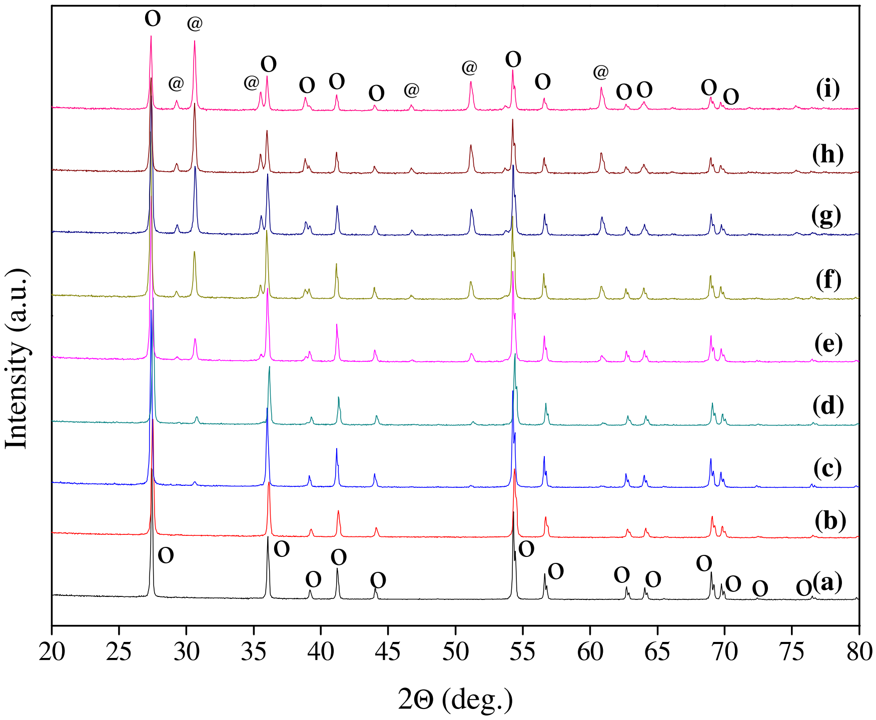

Figure 2.16. XRD patterns of Er_2O_3 doped TiO_2 powders heat treated at 1000°C: (a) pure, (b) 0.1%, (c) 0.25%, (d) 0.5%, (e) 1%, (f) 2%, (g) 3%, (h) 4%, (i) 5% doped TiO_2 powder (o: rutile, @: $Er_2Ti_2O_7$).

The effects of heat treatment temperature, RE ion and doping level on anatase weight fraction and anatase:rutile weight ratio are given in Figures 2.17 and 2.18, respectively. Anatase weight fraction vs. heat treatment temperature curve shifted significantly to higher temperatures with increasing Nd_2O_3 doping level. This curve indicates that the evolution of anatase to rutile may be retarded and sensitive design of nanophase structure may be achieved by adjusting Nd_2O_3 doping level and heat treatment temperature. The effect of REE type is also seen in the figure. The curve shifts to lower temperatures when Er was used instead of Nd as the dopant ion. This shift indicates that Nd has more inhibitory effect on anatase to rutile phase transformation compared to Er. Figure 2.18 indicates that the inhibition of anatase to rutile phase transformation becomes significant at higher Er_2O_3 doping levels compared to Nd_2O_3. The results indicated that the formation of $Nd_4Ti_9O_{24}$ phase may be reconstructive involving the breaking of Ti-O and reforming of Nd-Ti-O bonds as the formation of rutile from anatase, however $Er_2Ti_2O_7$ pyrochlore forms from rutile according to Borlaf et al. (2013) and the XRD patterns of Er doped TiO_2 powders heat treated at 900-1000°C.

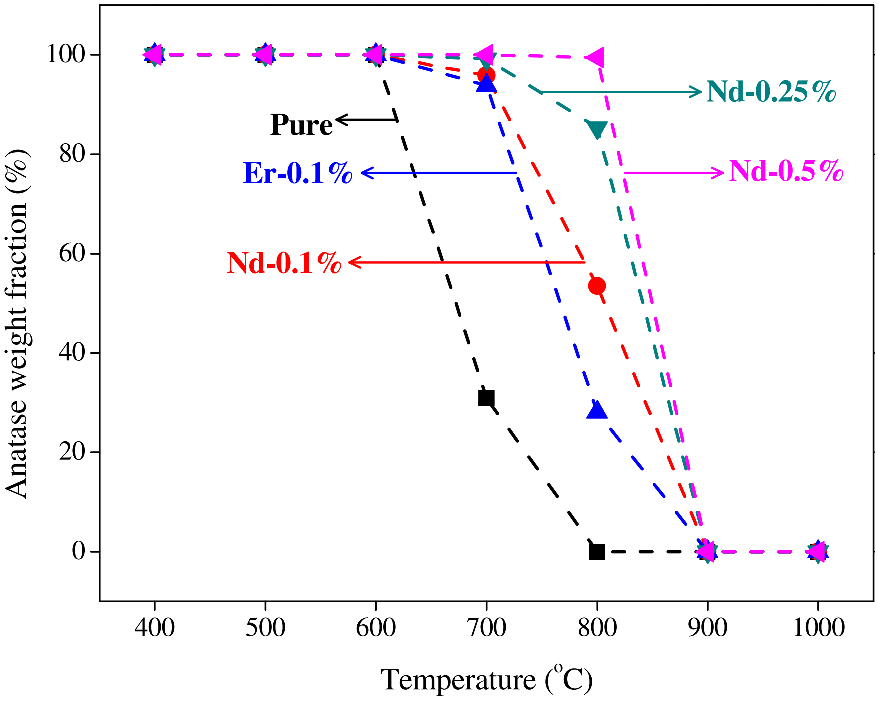

Figure 2.17. Anatase weight fraction vs. temperature curves of Nd_2O_3 and Er_2O_3 doped TiO_2 powders.

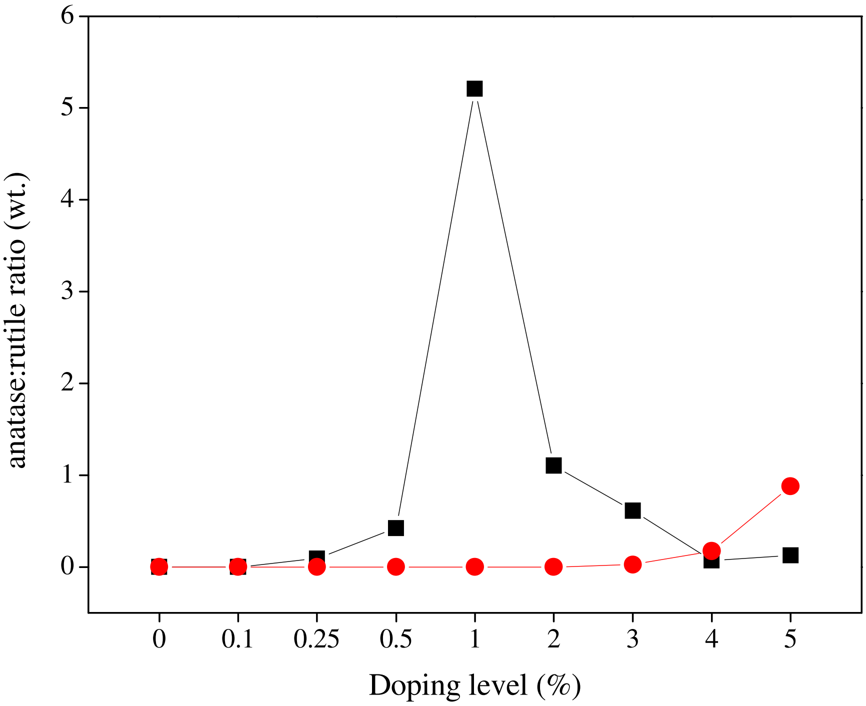

Figure 2.18. Anatase:rutile weight ratio vs. doping level of Nd_2O_3 (■) and Er_2O_3 (●) doped TiO_2 powders heat treated at 900°C.

Anatase crystallite sizes calculated from XRD patterns of Nd_2O_3 or Er_2O_3 doped TiO_2 powders are given in Figure 2.19. The crystallite sizes increase with increasing heat treatment temperature and decrease with increasing doping level. The variation of crystallite size is more significant at low doping levels (up to 1%). The crystallite sizes are similar (c.a. 10-12 nm) above 1% doping level for all heat treatment temperatures. The crystallite sizes of Nd_2O_3 doped TiO_2 powders are generally lower than that of Er_2O_3 doped TiO_2 powders (e.g. anatase crystallite sizes of 0.1% Nd_2O_3 and Er_2O_3 doped TiO_2 powders heat treated at 800°C are 45 nm and 50 nm, respectively) which may indicate that larger RE atom (Nd^{3+}) has higher inhibitory effect on the anatase to rutile phase transformation.

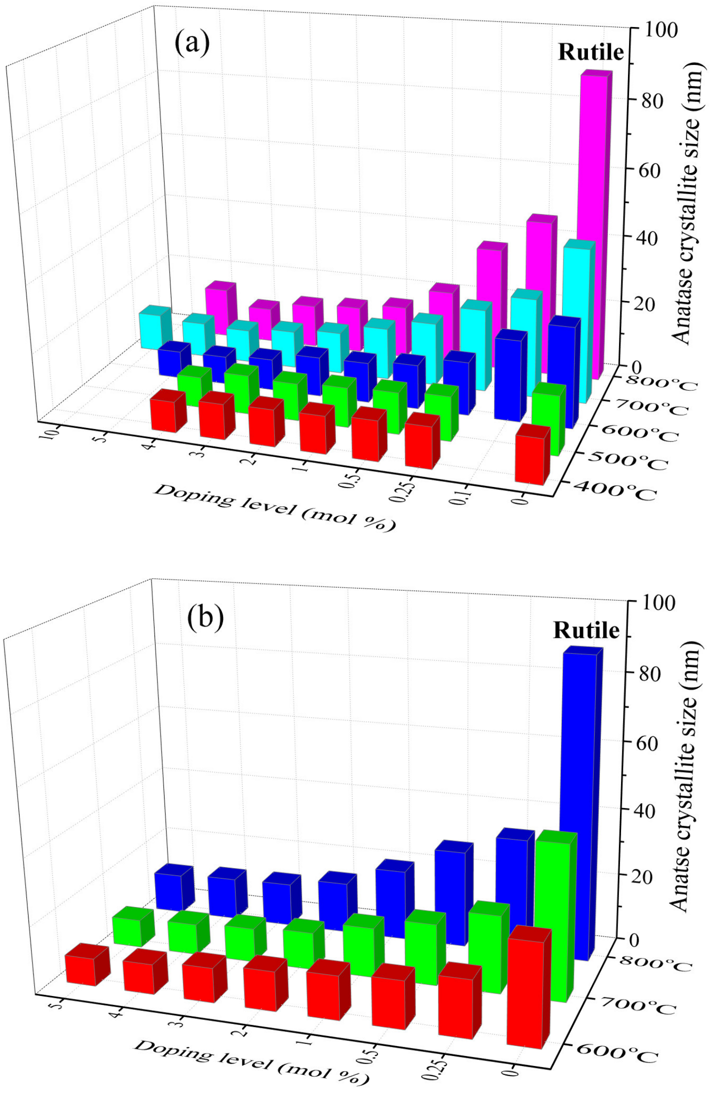

Figure 2.19. Anatase crystallite sizes of (a) Nd_2O_3 and (b) Er_2O_3 doped TiO_2 powders heat treated in the 600-800°C temperature range.

Anatase lattice constants a and c of Nd_2O_3 or Er_2O_3 doped TiO_2 powders heat treated at 700^{o}C and anatase lattice constant c of Nd_2O_3 doped TiO_2 powders heat treated in the 400-700^{o}C temperature range are given in Figures 2.20 and 2.21, respectively. Anatase lattice constant a slightly decreased where as c significantly decresead with increasing doping level. Lattice could shrink due to surface tension in the powders with nanosized particles (Swamy et al. 2006) or due to oxygen vacancies. The decrease in the lattice constants may be due to the decrease in the crystallite size or the presence of oxygen vacancies in the nanostructure. These findings indicated a possible seggregation of Nd/Er oxides/hydroxides in the grain boundaries or intersititial accomadation of Nd/Er^{3+} ions in the TiO_2 lattice. As discussed in the phase analysis of Nd_2O_3 or Er_2O_3 doped TiO_2 powders, the more electropositivity of seggregated RE ions in the grain boundaries and the attraction of O^{2-} ions to form oxygen defficiencies in the TiO_2 lattice may cause contraction. According to Wang et al. (2010) Nd^{3+} ions can form bond with non-bridging oxygen ion in the surroundings of –Ti–O–Ti–O– network structure. O^{2-} ions would be expelled from the lattice when a RE ion accomodates in the grain boundaries and attract oxygen. Lattice shrinks along c axis due to leaving of O^{2-} ion with a larger ionic radius (126 pm) than RE ion or Ti^{4+}. Another important reason may be the significant decrease of the crystallite size of TiO_2 nanoparticles with increasing REE doping level due to notable sinsitivity of lattice constants a and c to crystallite size change similar to lattice strain.

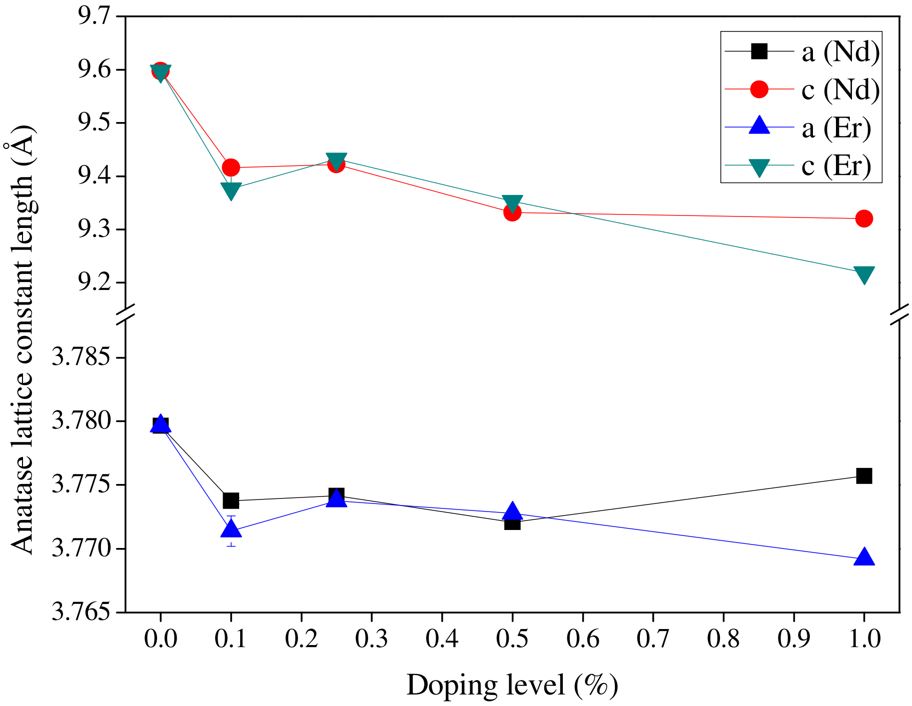

Figure 2.20. Anatase lattice constants a and c of Nd_2O_3 or Er_2O_3 doped TiO_2 powders heat treated at 700°C.

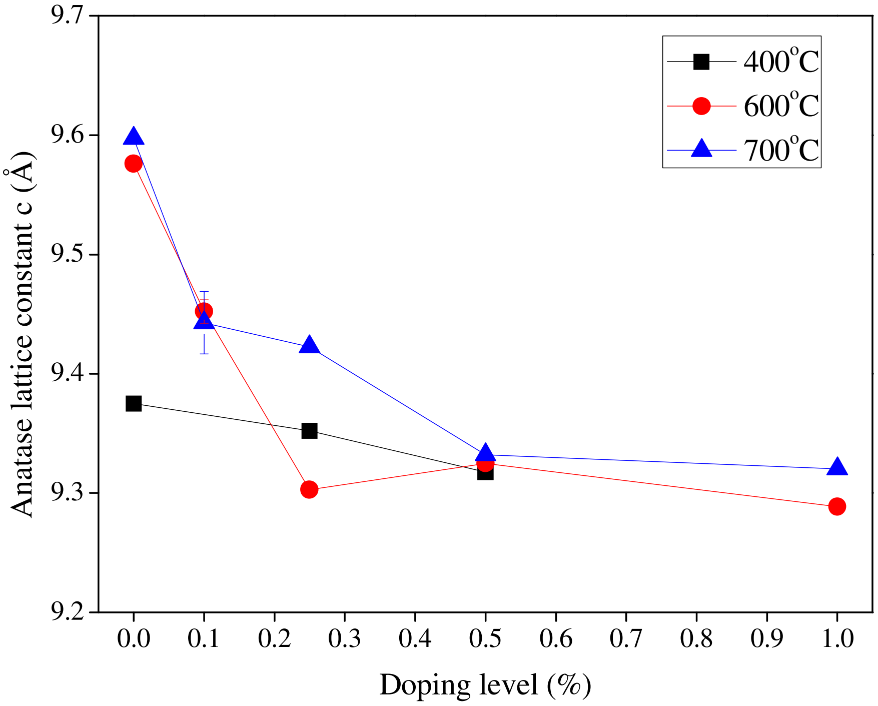

Figure 2.21. Anatase lattice constant c of Nd_2O_3 doped TiO_2 powders heat treated in the 400-700°C temperature range.

Anatase lattice strain of Nd_2O_3 or Er_2O_3 doped TiO_2 powders are given in Figure 2.22. Lattice strain increases continuosly with doping level at 500°C and 600°C, however the presence of rutile phase (even trace amounts at 1% Er_2O_3 doping level) at 700°C signicantly affected the strain in the microstructure. Lattice strain in rutile particles are be less compared to anatase particles since rutile is more stable and has a more ordered structure. Presence of both rutile and anatase phase with Er oxide phases, the c values are flactuating at 700°C (not shown in the figure). Powders heat treated at 500°C exhibit higher lattice strain and strain decreases with heat treatment temperature. The high lattice strain at 500°C is due to excess number of disordered atoms and defects in the grain boundaries. These atoms and defects cause a stress field (surface strain). Lattice strain of all the powders are positive indicating a tensile strain. Tensile strain can be induced by a decrease in crystallite size. Crystallite size decreases with increasing doping level and lattice strain increases unlike lattice parameter c. The effect of crystallite size difference in Nd_2O_3 and Er_2O_3 doped TiO_2 powders on the lattice strain is obvious as can be seen from Figure 2.22. The strain in Nd_2O_3 doped powders increase more significantly than Er_2O_3 doped powders since the cristallite sizes of Nd_2O_3 doped powders are smaller and particles are subjected to more surface strain. According to Choudhury and Choudhury (2013) oxygen defficiencies can induce lattice strain in the structure. The increase in the lattice strain is the result of both crystal size decrease and introduced oxygen defficiencies formed due to the attraction of oxygen by Nd or Er in the interstitials and grain boundaries of TiO_2 phases. Defects in the grain boundaries can be partially and gradually reduced by increasing the heat treatment temperature causing a decrease in the lattice strain. The strain decreases with increasing heat treatment temperature for both undoped and Nd_2O_3 doped TiO_2 powders as shown in Figure 2.22.

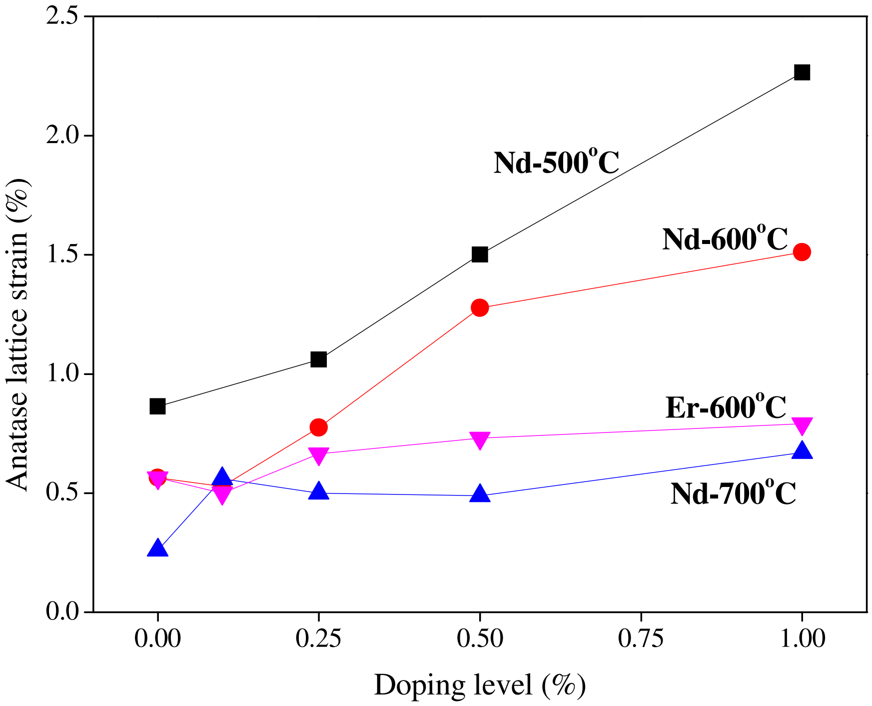

Figure 2.22. Anatase lattice strain of Nd_2O_3 and Er_2O_3 doped TiO_2 powders heat treated in the 500-700°C temperature range.

2.3.3. Nitrogen Adsorption-Desorption Characteristics of Nd_2O_3 and Er_2O_3 Doped TiO_2 Powders

Selected nitrogen adsorption-desorption isotherms and specific surface areas of Nd_2O_3 and Er_2O_3 doped TiO_2 powders are given in Figures 2.23 and 2.24, respectively. The isotherms are of Type IV (BDDT classification) with a hysteresis loop (H3), which is typical for mesoporous materials. This type of isotherm is an indication of mesoporous structure with high adsorption energies and formation of narrow slit-like pores by the segregation of particles. This structure was observed in all doped TiO_2 powders on the contrary of pure TiO_2. Pure TiO_2 is considered to be composed of large pores (average pore diameters: 12.9 nm, pore volume: 0.00804 cm^3/g) formed by sintered grains (supported by TEM) which also leads to a decrease in the surface area. Increased surface areas indicated that Nd_2O_3 and Er_2O_3 doping significantly affect the surface area of TiO_2. Surface area of pure TiO_2 was increased by 5 to 35 folds depending on the doping level. Doping TiO_2 with rare earth elements decreases the average particle size and increases thermal stability which lead to an increase in the surface area; however higher doping level than 2% leads to a decrease in the surface area which may be attributed to agglomeration of RE oxides in the grain boundaries of TiO_2.

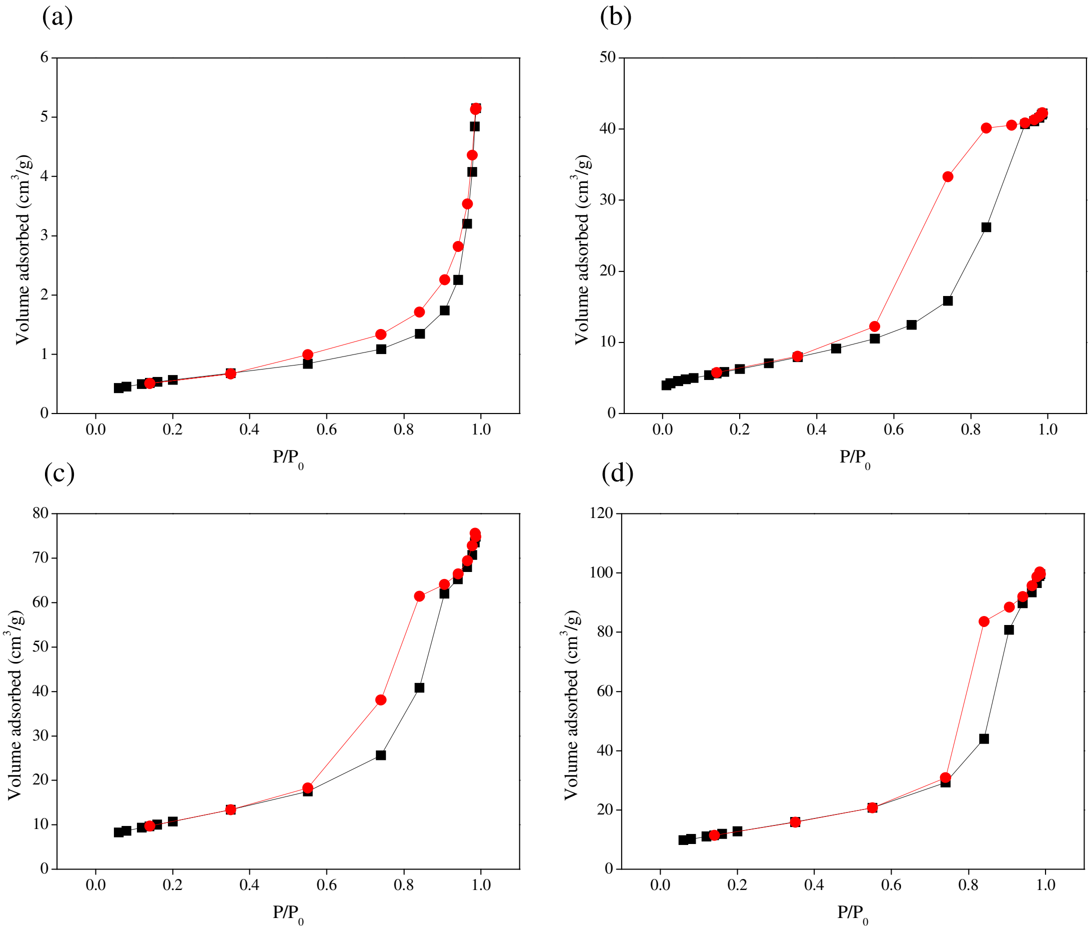

Figure 2.23. Nitrogen adsorption (■) desorption (●) isotherms of (a) pure, (b) 0.25%, Nd_2O_3, (c) 0.5% Nd_2O_3, and (d) 0.25% Er_2O_3 doped TiO_2 powders heat treated at 700°C.

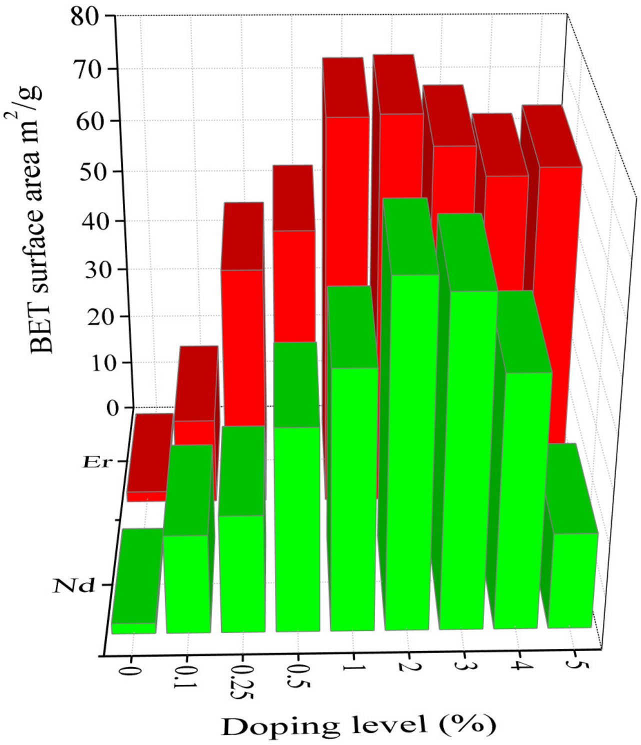

Figure 2.24. Surface areas of Nd_2O_3 and Er_2O_3 doped TiO_2 powders heat treated at 700°C.

2.3.4. Phase Structure of Various RE_2O_3 Doped TiO_2 Powders

Various REEs (La, Pr, Nd, Sm, Eu, Gd, Tb, Dy, Er Ce, Yb) doped TiO_2 powders were also prepared in order to investigate the effect of RE ionic radius on the nanostructure of TiO_2. Figure 2.25 shows the XRD patterns of 5% RE_2O_3 doped TiO_2 powders heat treated at 800°C, the XRD patterns of 0-5% various REEs doped TiO_2 powders heat treated at 600-700°C are given in Appendix A. Formation of $RE_2Ti_2O_7$ phases were detected which have similar reflections at 2Θ values of ~30.6, ~29.3 (deg.) and 28.5 (deg.) for CeO_2 according to the corresponding JCPDS cards (given in Appendices) of each $RE_2Ti_2O_7$ phases and CeO_2 phase. The formation of these phases were detected for the RE elements between/including Eu and Yb with moderate and the smallest ionic radius, respectively. At this temperature and doping level $RE_4Ti_9O_{24}$ phases were not detected which may support that an adequate atomic mobility is needed to increase the probability for the formation of this phase. The ionic radii of REs vary between 117.2 and 100.8 pm in the following order: $La^{3+} > Pr^{3+} > Nd^{3+} > Sm^{3+} > Eu^{3+} > Gd^{3+} > Tb^{3+} > Dy^{3+} > Er^{3+} > Yb^{3+}$ (Ce is excluded since it has both 3+ and 4+ oxidation states). The magnitude of the anatase to rutile phase transformation inhibitory effect of REs decreases with decreasing RE ionic radius. This was also supported by the decrease of anatase weight fraction and crystallite size with increasing RE ionic radius as shown in Figures 2.26 and 2.27, respectively. Anatase weight fraction slightly increased and anatase crystallite size decreased (significantly at higher temperature) with increasing RE ionic radius since larger RE ions have more inhibitory effect as discussed above.

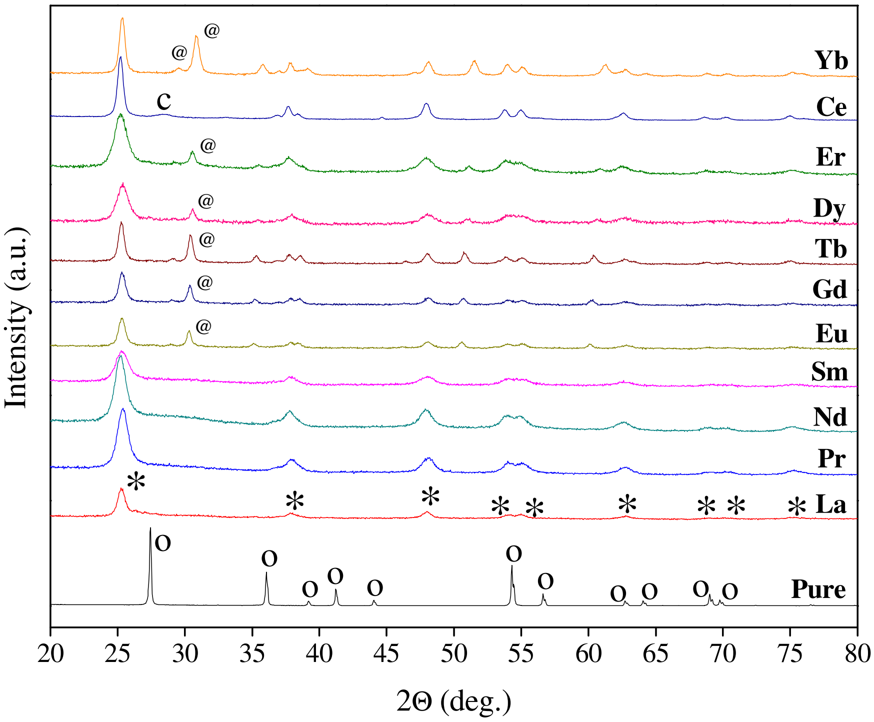

Figure 2.25. XRD patterns of 5% RE_2O_3 doped TiO_2 powders heat treated at 800°C (*: anatase, o: rutile, @: $RE_2Ti_2O_7$, c: CeO_2).

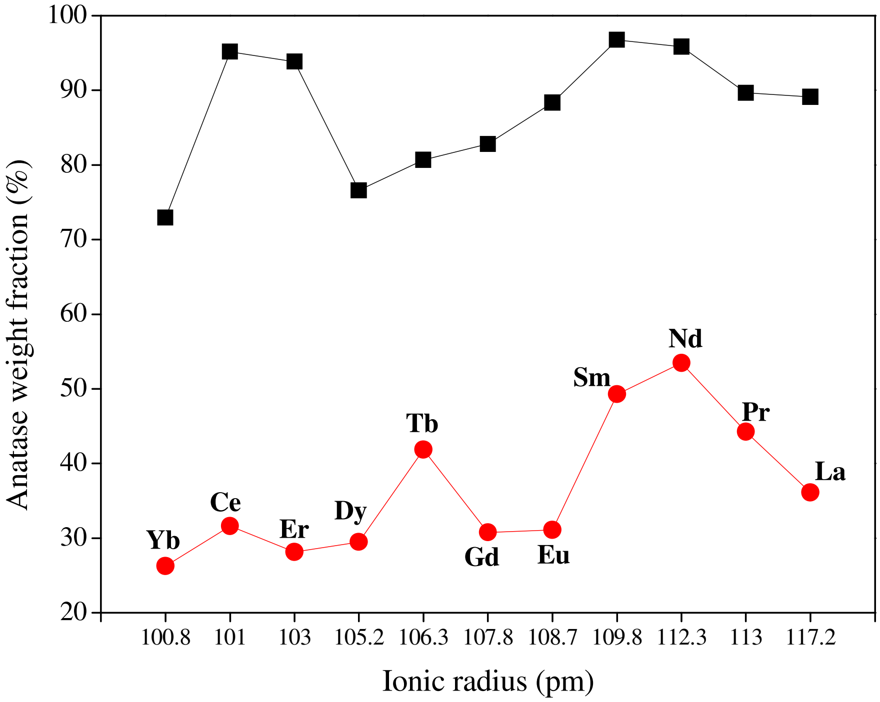

Figure 2.26. Anatase weight fractions of 0.1% RE_2O_3 doped TiO_2 powders heat treated at (■) 700°C and (●) 800°C.

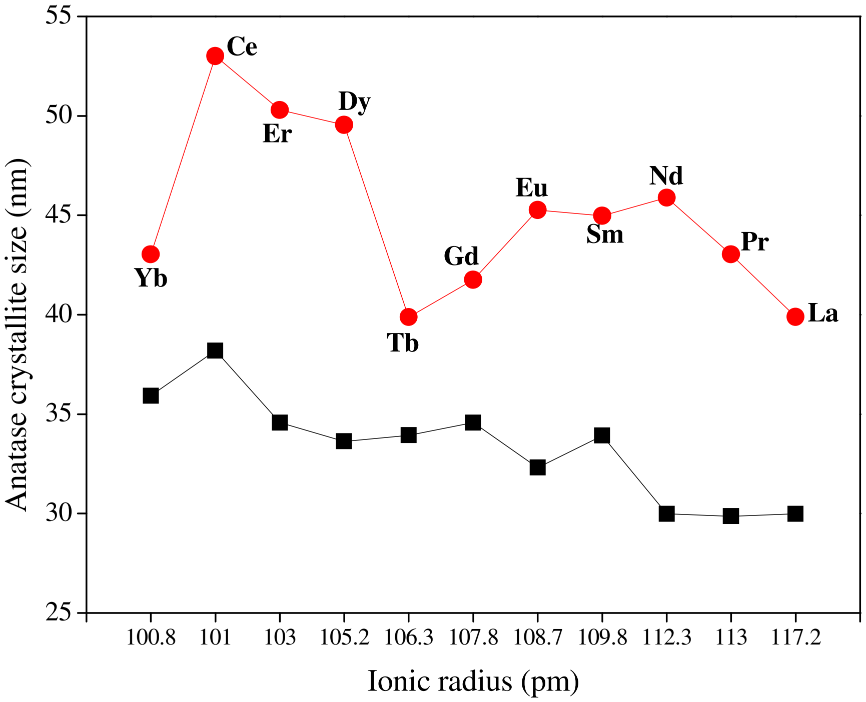

Figure 2.27. Anatase crystallite sizes of 0.1% RE_2O_3 doped TiO_2 powders heat treated at (■) 700°C and (●) 800°C.

The crystallite sizes of $RE_2Ti_2O_7$ phases in 5% RE_2O_3 doped TiO_2 powders heat treated at 800°C are given in Figure 2.28. The crystallite size increases with RE ionic radius which indicates that nucleation of this phase is more favorable for REEs with relatively lower ionic radius. The number of nucleation points for low ionic radius REs is more than large ionic radius REs which may be due to higher atomic mobility which increases the possibility of the formation of $RE_2Ti_2O_7$ phase.

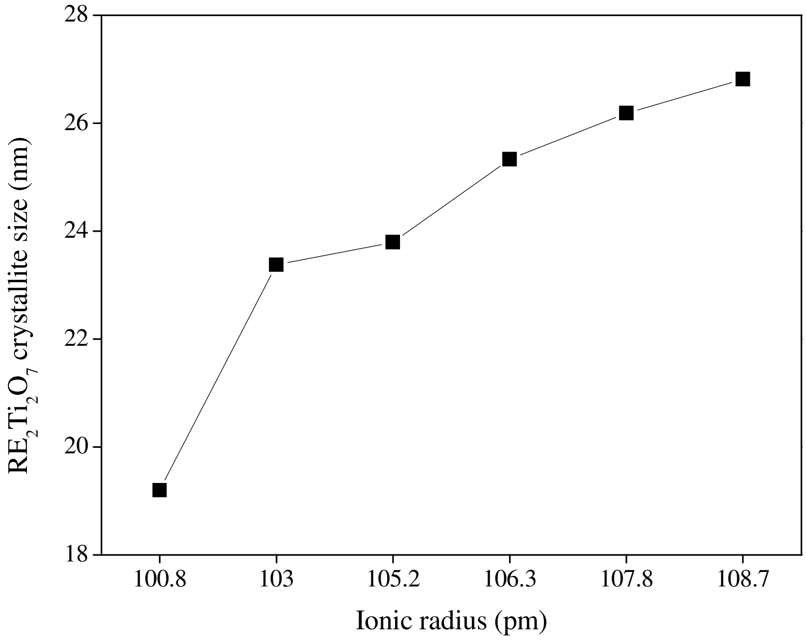

Figure 2.28. Crystallite sizes of $RE_2Ti_2O_7$ phases in 5% RE_2O_3 doped TiO_2 powders heat treated at 800°C.

Tentative phase diagrams of RE_2O_3-TiO_2 systems in the temperature-composition plane are shown in Figures 2.29-2.34. Data points are represented by stars (☆). All the powders have anatase as the main phase at low heat treatment temperatures. Rutile was detected in the powders at 700°C at doping levels up to 0.1% for large ionic radius (Nd, Pr, Sm) and up to 0.25% for relatively smaller ionic radius (Er, Dy); at 800°C these values became 0.25% and 2%, respectively. $RE_2Ti_2O_7$ phases were detected at 800°C from 2% in general. High heat treatment temperatures were applied to Nd_2O_3 and Er_2O_3 doped TiO_2 powders since Nd was chosen as a representative for RE elements with large ionic radius (112 pm) and Er for small ionic radius (103 pm). $Er_2Ti_2O_7$ was detected at doping levels higher than 0.1% at 900°C and at all doping levels at 1000°C. $Nd_4Ti_9O_{24}$ was detected beginning from 0.5% doping level at 900°C and at all doping levels at 1000°C.

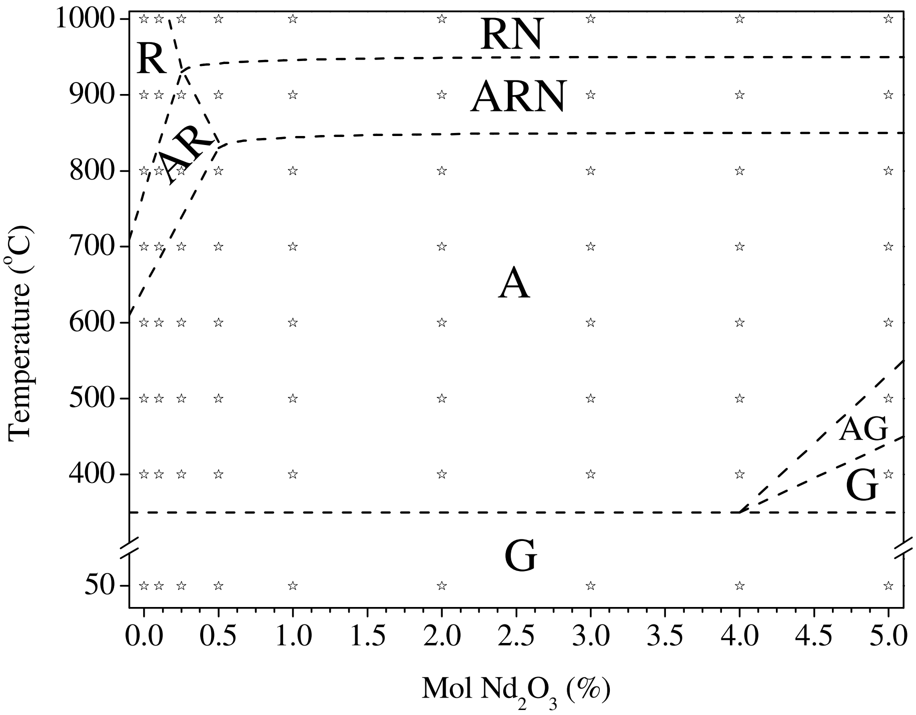

Figure 2.29. The low temperature tentative Nd_2O_3-TiO_2 phase diagram (0-5 mol % Nd_2O_3, A: anatase, R: rutile, G: glassy, N: $Nd_4Ti_9O_{24}$).

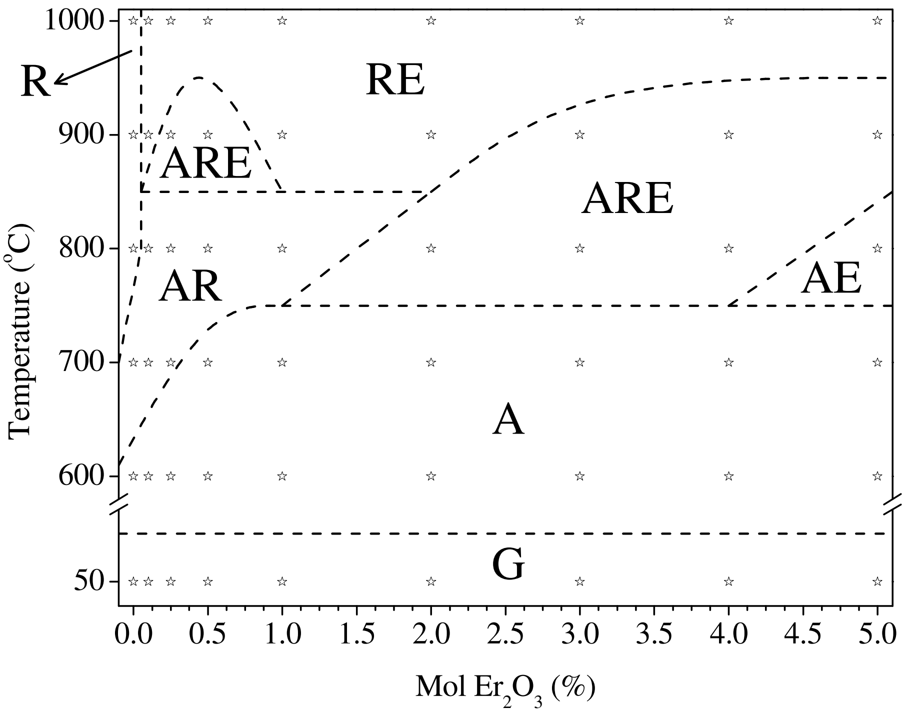

Figure 2.30. The low temperature tentative Er_2O_3-TiO_2 phase diagram (0-5 mol % Er_2O_3, A: anatase, R: rutile, G: glassy, E: $Er_2Ti_2O_7$).

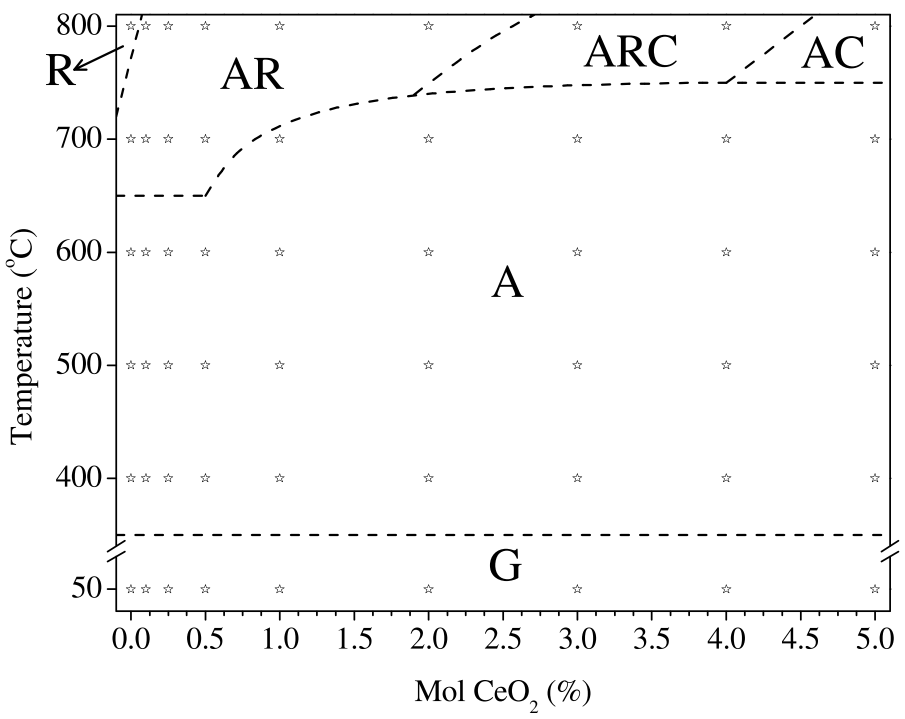

Figure 2.31. The low temperature tentative CeO_2-TiO_2 phase diagram (0-5 mol % CeO_2, A: anatase, R: rutile, G: glassy, C: CeO_2).

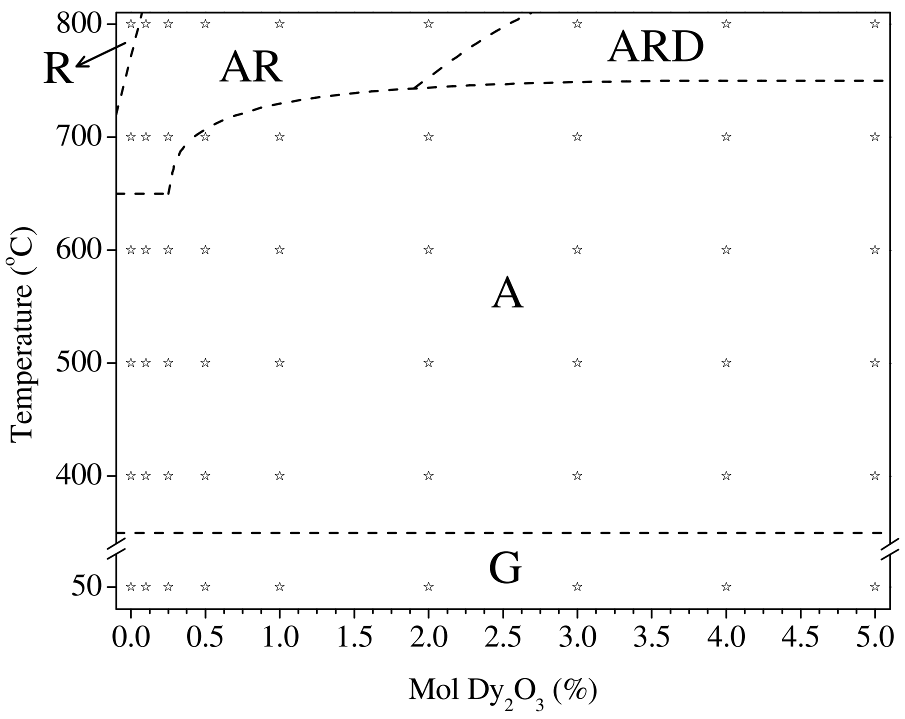

Figure 2.32. The low temperature tentative Dy_2O_3-TiO_2 phase diagram (0-5 mol % Dy_2O_3, A: anatase, R: rutile, G: glassy, D: $Dy_2Ti_2O_7$).

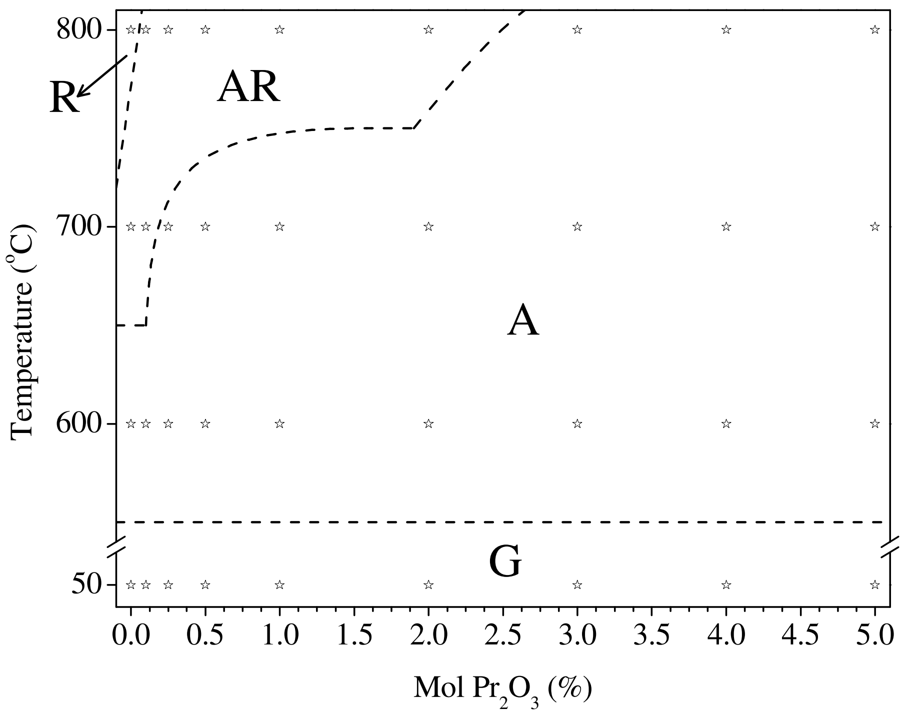

Figure 2.33. The low temperature tentative Pr_2O_3-TiO_2 phase diagram (0-5 mol % Pr_2O_3, A: anatase, R: rutile, G: glassy).

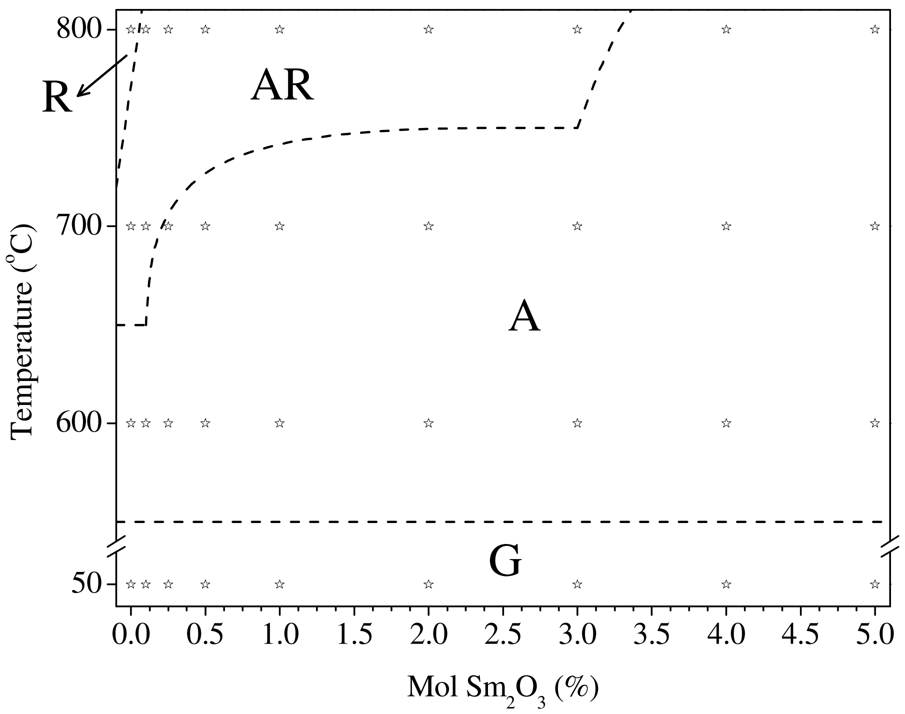

Figure 2.34. The low temperature tentative Sm_2O_3-TiO_2 phase diagram (0-5 mol % Sm_2O_3, A: anatase, R: rutile, G: glassy).

2.3.5. TEM and XPS Analysis of Nd_2O_3 and Er_2O_3 Doped TiO_2 Powders

TEM images of pure, 0.1, 1, 3 and 5% Nd_2O_3 doped TiO_2 powders heat treated at 700°C are given in Figure 2.35. Crystallite sizes calculated from Scherrer equation by using XRD patterns are almost identical with the sizes measured from TEM images. Pure TiO_2 at 700°C was interpreted to be consisting of sintered grains considering very low surface area (2 m^2/g) and large pore sizes. TEM images supported this interpretation.

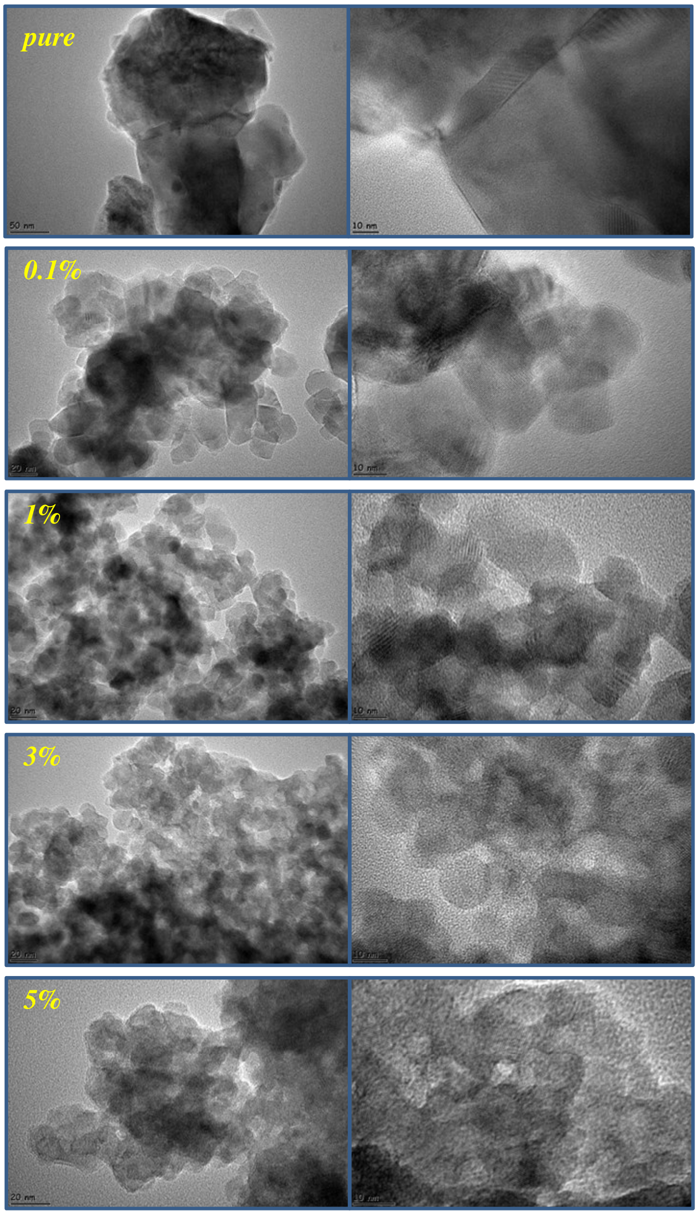

Figure 2.35. TEM images of Nd_2O_3 doped TiO_2 powders heat treated at 700°C.

TEM-EDX images of 0.5 and 5 % Nd_2O_3 doped TiO_2 powders heat treated at 700°C are given in Figures 2.36 and 2.37, respectively. Nd peaks were detected beginning with 0.5 % doping level. The predetermined value for the synthesis of 5% Nd_2O_3 doped TiO_2 powder was calculated from TEM-EDX as 5.67% Nd_2O_3.

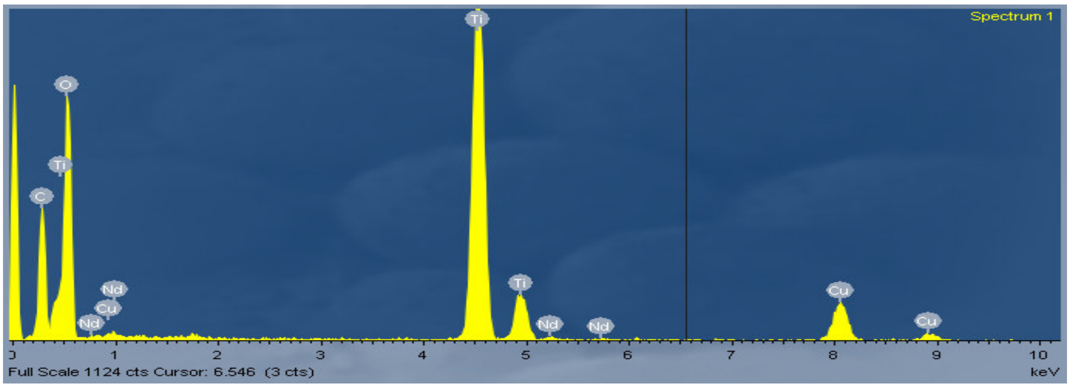

Figure 2.36. TEM-EDX image of 0.5% Nd_2O_3 doped TiO_2 powder heat treated at 700°C.

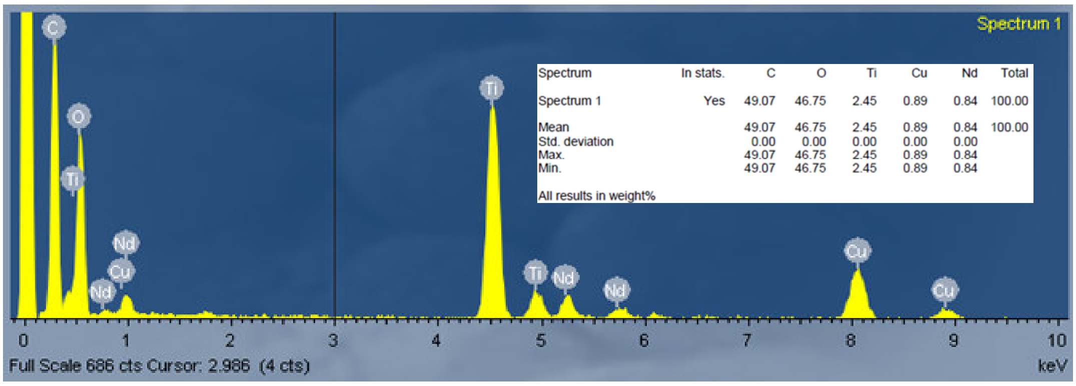

Spectrum	In stats.	C	O	Ti	Cu	Nd	Total
Spectrum 1	Yes	49.07	46.75	2.45	0.89	0.84	100.00
Mean		49.07	46.75	2.45	0.89	0.84	100.00
Std. deviation		0.00	0.00	0.00	0.00	0.00	
Max.		49.07	46.75	2.45	0.89	0.84	
Min.		49.07	46.75	2.45	0.89	0.84	

All results in weight%

Figure 2.37. TEM-EDX image of 5% Nd_2O_3 doped TiO_2 powder heat treated at 700°C.

Ti2p, O1s, Nd3d XPS spectra of Nd_2O_3 doped and Er3d XPS spectra of Er_2O_3 doped TiO_2 powders heat treated at 700°C are given in Figures 2.38-41 and 2.33, respectively. Ti2p and O1s XPS spectra of Er_2O_3 doped TiO_2 powders were not given in the text due to the close similarity with the spectra of Nd_2O_3 doped TiO_2 powders. Ti2p core level spectrum contains two main peaks of $Ti2p_{1/2}$ and $Ti2p_{3/2}$. The $Ti2p_{1/2}$ and $Ti2p_{3/2}$ spin-orbital splitting photoelectrons for all powders are located at binding energies of c.a. 465.2 and 459.3 eV, respectively (with the correction by using C1s line). The difference between these two lines is about 5.9 eV which showed that prepared TiO_2 powders mostly consist of Ti^{4+} oxidation state with small contribution of

Ti^{3+} which is formed due to oxygen deficiencies in TiO_2 lattice. O1s peak appearing at 529 eV is attributed to the signal of oxygen in TiO_2 lattice. Shoulder appearing at 531.5 eV is the signal of Ti-OH or C-OH. The intensity of this peak decreases with Nd_2O_3 doping level, preserving its existence. Carbon residuals may exist in pure TiO_2 since it consists of sintered grains resulting a closed pore structure which does not allow carbon burn out as CO_2 during calcination. This may be the result of an intense C-OH peak.

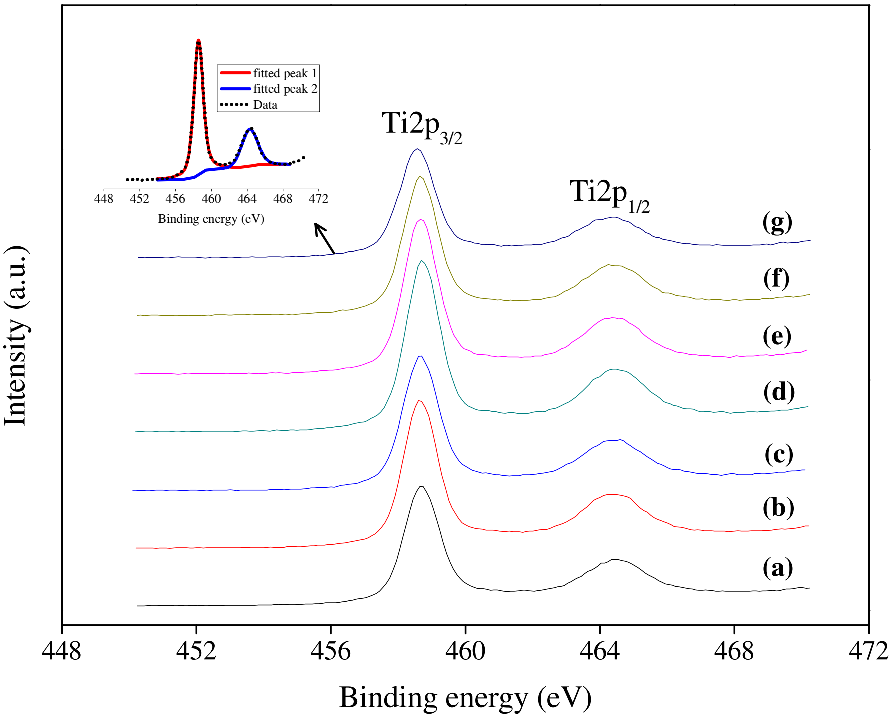

Figure 2.38. Ti2p XPS spectra of Nd_2O_3 doped TiO_2 powders heat treated at 700°C: (a) pure, (b) 0.1%, (c) 0.25%, (d) 0.5%, (e) 1%, (f) 3%, (g) 5%.

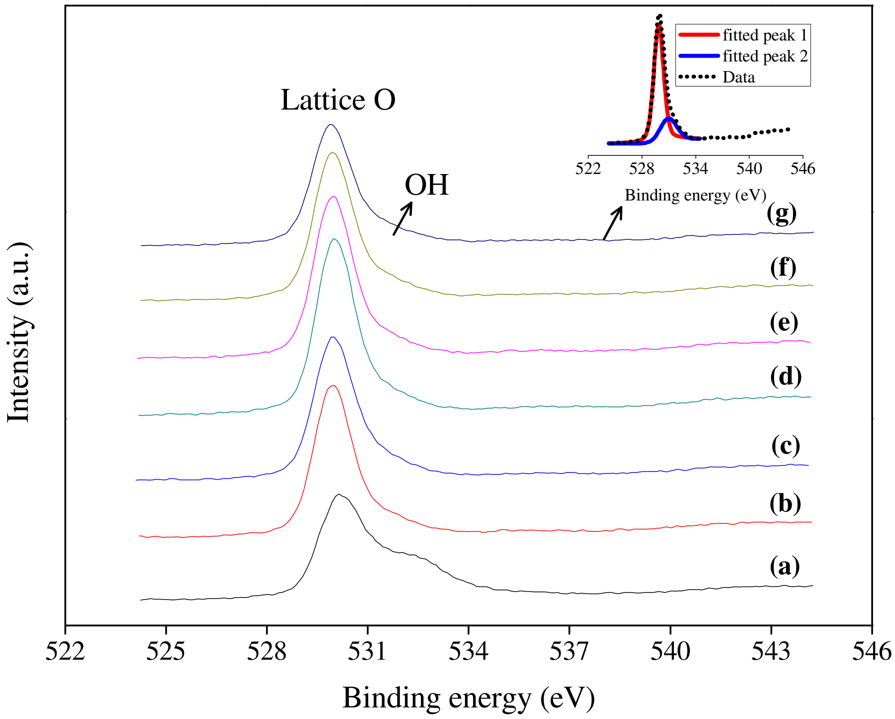

Figure 2.39. O1s XPS spectra of Nd_2O_3 doped TiO_2 powders heat treated at 700°C: (a) pure, (b) 0.1%, (c) 0.25%, (d) 0.5%, (e) 1%, (f) 3%, (g) 5%.

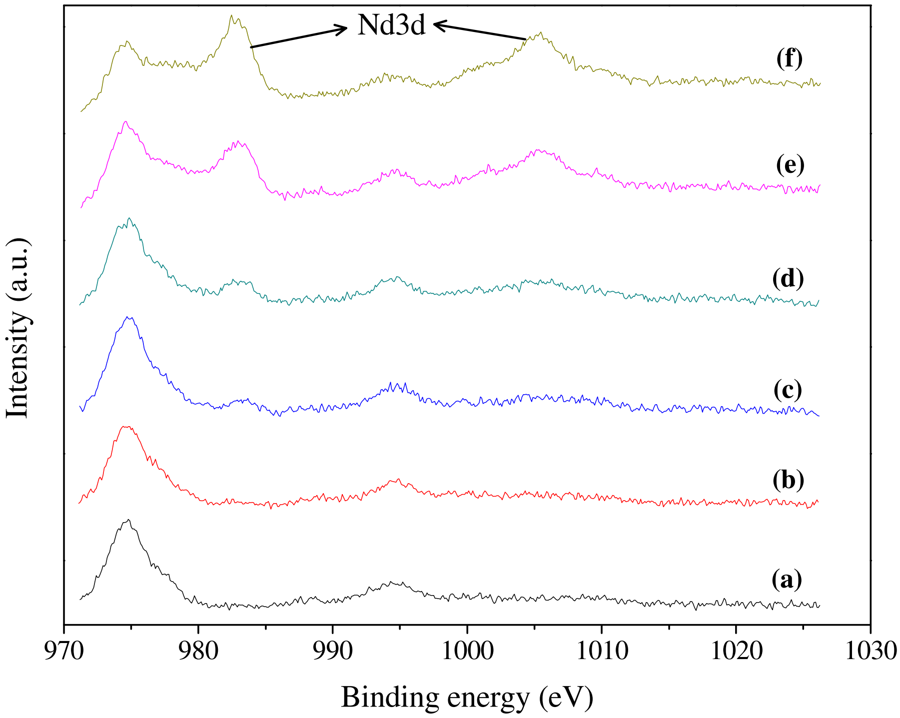

Figure 2.40. Nd3d XPS spectra of Nd_2O_3 doped TiO_2 powders heat treated at 700°C: (a) 0.1%, (b) 0.25%, (c) 0.5%, (d) 1%, (e) 3%, (f) 5%.

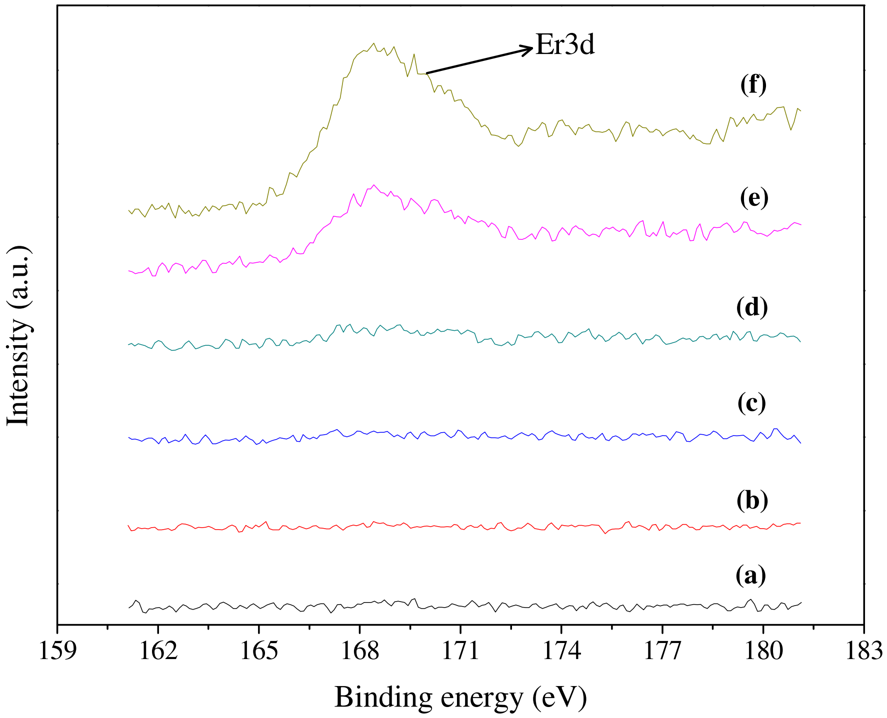

Figure 2.41. Er3d XPS spectra of Er_2O_3 doped TiO_2 powders heat treated at 700°C: (a) 0.1%, (b) 0.25%, (c) 0.5%, (d) 1%, (e) 3%, (f) 5%.

Binding energies of $Ti2p_{3/2}$ and O1s lines with the correction by using C1s line of Nd_2O_3 and Er_2O_3 doped TiO_2 powders are given in Figure 2.42. $Ti2p_{3/2}$ and O1s binding energies of doped TiO_2 powders shifted towards lower energy levels at low doping levels for both Nd_2O_3 and Er_2O_3 doping. For all doping levels binding energies are lower than pure TiO_2, and the binding energies in Er_2O_3 doped TiO_2 powders are also lower than Nd_2O_3 doped TiO_2 powders. Decrease in both $Ti2p_{3/2}$ and O1s binding energies could be attributed to Ti^{4+} and O^{2-} local environment change by the introduction of Nd or Er atoms. Reduction of Ti^{4+} atoms are partially reduced to a lower oxidation state (Ti^{3+}) due to bonding with Nd or Er species in the grain boundaries or to the possible higher amount of oxygen vacancies (Beranek and Kisch 2008, Zhao et al. 2008).

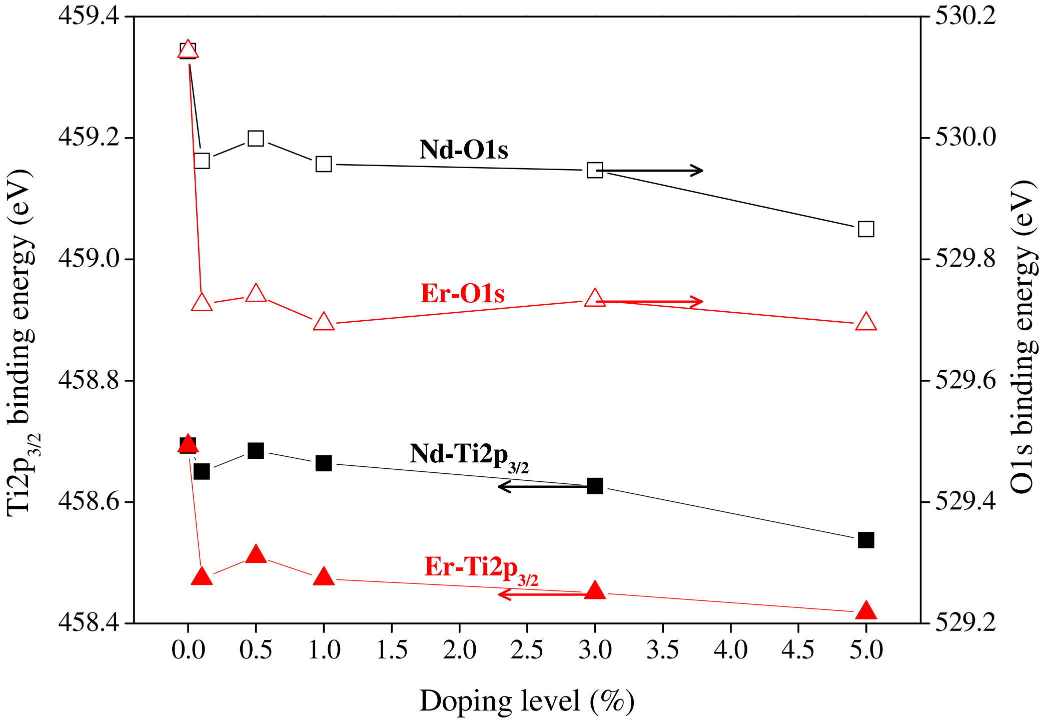

Figure 2.42. Binding energies of Ti2p$_{3/2}$ and O1s corrected by using C1s peak of Nd_2O_3 and Er_2O_3 doped TiO_2 powders heat treated at 700°C.

2.4. Conclusions

The location of the dopant ion and the effect of REE doping on the nanophase structure, physical and electronic properties of TiO_2 were investigated by using XRD, XPS, TEM, DLS and N_2 adsorption-desorption.

Volume average particle size and gelation time of RE_2O_3 doped TiO_2 sols increased with doping level. The gelation of pure TiO_2 sol completed in 3 minutes; whereas gelation time of 5% Nd_2O_3 doped TiO_2 sol completed in a week.

Anatase was determined to be the main phase in all doped TiO_2 powders up to 900°C. Rutile formation was observed beginning with 700°C and rutile was the dominant phase with $RE_2Ti_2O_7$ phases at 1000°C. $RE_2Ti_2O_7$ phases first appeared at 2% doping levels at 800°C for RE ions with small ionic radii (between Eu and Yb). $Nd_4Ti_9O_{24}$ phase was formed at 10% doping level at 800°C and even at low doping levels at 900 and 1000°C. It was found that the phase evolution from anatase to rutile was significantly inhibited by REE doping. The results indicated that RE ions can accommodate in the TiO_2 lattice interstitial voids or segregate on the grain boundaries of TiO_2 crystallites rather than a substitutional accommodation. Resulting lattice oxygen and structural defects developed due to the presence of RE ions in the microstructure can significantly affect the nanophase, physical and electronic properties of TiO_2.

Nitrogen adsorption-desorption analyses of the prepared powders showed that RE doping increased the surface area of TiO_2. Er_2O_3 doped TiO_2 powders possessed higher surface areas than Nd_2O_3 doped TiO_2 powder, loss of surface area at 5% doping level was determined to be at a lower level for Er compared to Nd.

Crystallite sizes of Nd_2O_3 doped TiO_2 powders calculated by using Scherrer Equation from XRD patterns were determined to be similar with the results of TEM analyses. Nd_2O_3 amount was calculated as 5.4% (molar basis) for 5Nd700 which showed that intended composition of 5% Nd_2O_3 was achieved.

CHAPTER 3

ARTIFICIAL PHOTOSYNTHESIS ACTIVITIES OF RARE EARTH ELEMENT DOPED TITANIA POWDERS PREPARED BY SOL-GEL TECHNIQUES

3.1. Introduction

Growing environmental concerns related to the extensive use of non-sustainable fossil fuels and a constantly increasing energy demand will force mankind, sooner or later, to tap in to clean and sustainable sources of energy. Scientific research showed that CO_2 emission originating from the fossil fuel usage as the main reason for global warming (Collings and Critchley 2005). Many governments are trying to take precautions by regulations since the discovery and acceptance of Global Warming; however CO_2 emission reduction doesn't seem to be a long-term solution due to extensive use of non-sustainable carbonaceous fossil fuels and a constantly increasing energy demand. Transforming CO_2 into reusable fuels may be a solution to global warming which will create a recycling system for CO_2 (de-Richter et al. 2013, Tahir and Amin 2013). Solar energy can be converted into chemical energy and stored for the further use (Hammarstrom and Hammes-Schiffer 2009). Production of hydrocarbons from CO_2 and hydrogen from water via photocatalytic processes appears to be a promising alternative to fossil fuel usage.

Artificial photosynthesis is the mimicking of natural photosynthesis and is one of the common photocatalytic processes which convert CO_2 and water into useful chemicals such as carbon monoxide, methane, methanol, other hydrocarbons and hydrogen which further can be stored and used as energy source. Intensive research on artificial photosynthesis (hydrogen production via water splitting and hydrocarbon production by the reduction of CO_2) which may become a key process in the future for sustainable energy needs of humanity and global pollution/warming prevention have been conducted in the last 10 years (Wu et al. 2005, Matejova et al. 2014, Raja et al. 2011, Tan et al. 2012, Uner et al. 2011, Zhang et al. 2009). Research conducted on materials developed towards photocatalytic hydrogen splitting and artificial photosynthesis was reviewed in a number of articles published in the last decade (Dey 2007, Fan et al. 2009, Inoue 2009, Kalyanasundaram and Graetzel 2010, Neatu et al. 2014, de-Richter et al. 2013, Zhu and Zach 2009).

Research and advances in nanoscience and nanotechnology in the last 10 years improved the preparation techniques and expanded the application area of nanostructured photocatalytic materials. Fujishima and Honda conducted the pioneering studies in 1970s to produce renewable energy (artificial photosynthesis and water splitting to produce hydrocarbons and hydrogen) via photocatalytic processes by using solar energy (Fujishima et al. 1972, Inoue et al. 1979). Since then many photocatalytic materials were prepared to be used in various photocatalytic processes. TiO_2 is the most extensively used photocatalyst since it is biologically and chemically inert, stable with respect to photocorrosion and chemical corrosion, however many researchers are still trying to improve the photocatalytic activity of TiO_2. Physicochemical, phase structure and optical properties (light absorption) of TiO_2 can be altered by; doping with various cations/anions (Zaleska 2008), combining with low bandgap materials (Magesh et al. 2009), surface modification (Dugandzic et al. 2012) or using different synthesis routes to modify the crystalline structure. Doping TiO_2 with anions/cations is the most preferred one since it is easy to tune the phase structure, electronic structure and light absorption properties by the type or amount of doping ion which leads to the improvement of photocatalytic activity.

Transition metals (such as V, Cr, Fe, Co, Ni, Cu) and nonmetals (N, S, C, B, P, I, F) doped TiO_2 photocatalysts showed increased photocatalytic activities in recent research (Anpo and Kamat 2010, Bellardita et al. 2011, Magesh et al. 2009, Zaleska 2008). Alternative to transition metals, rare earth element (REE) doping may increase the photocatalytic activity by increasing the light absorption, altering the phase structure (anatase-rutile), physical and electronic properties (surface area, pore size, light absoprtion). Research conducted in the last 10 years showed that REEs, such as La, Nd, Eu, Sm, Yb, Pr and Ce doped TiO_2 showed higher activities than pure TiO_2 (Bellardita et al. 2007 and 2011, Chiou and Juang 2007, Hassan et al. 2012, Jian et al. 2010, Reszczynska et al. 2014, Romero et al. 2010, Tong et al. 2007, Wang et al. 2010, Xie and Yuan 2004, Xie et al. 2005, Xu et al. 2009, Yan et al. 2005). These research are mostly on the environmental related applications such as photocatalytic degradation of dyes in wastewater. REEs hinder the recombination of electron-hole pairs, keeping them on the TiO_2 surface and resulting in higher photocatalytic activities (Xie and Yuan 2004, Xie et al. 2005, Li et al. 2005). REE incorporated titania phases were used in a few studies towards hydrogen production by water splitting (Asal et al. 2011, Puskelova 2014, Zalas and Laniecki 2005, Zhang et al. 2013) and CO_2 photoreduction related artificial photosynthesis (Liu et al. 2015, Matejova et al. 2014, Ogura et al. 1992, Wang et al. 2013, Zhao et al. 2012). Research on these materials has great importance to improve the current state of understanding.

Asal et al. (2011) prepared Sm and Eu doped TiO_2 powders by using sol-gel techniques and tested them in the photocatalytic water splitting in the presence of acetic acid. The main gaseous products were detected as CO_2 and CH_4 with H_2. The main purpose of this study is the generation of useful hydrocarbons from acetic acid which is a by-product of degradation of organic compounds. Their results revealed that REE incorporation increased the photocatalytic activity of TiO_2 in acetic acid degradation by increasing the surface area, altering phase composition, crystallite size of anatase and improving the separation of the photogenerated electrons and holes. Zalas and Laniecki (2005) investigated the effect of REE doping on the photocatalytic water splitting activity of TiO_2. They prepared TiO_2 powders doped with many of the REEs. The highest activities were obtained with photocatalysts containing 0.5% of Gd, Eu, Yb, or Ho oxides and this was related to their high potential of tetravalent dopant ions. La doped TiO_2 powders were prepared by Zhang et al. (2013). The photocatalytic water splitting of water Pt-loaded La doped TiO_2 in the presence of methanol. They observed that the surface phase junctions of anatase and rutile contribute activity. Matejova et al. (2014) investigated the effect of cerium (Ce) doping on the photocatalytic CO_2 reduction activity of sol-gel TiO_2 powders. Pure and doped TiO_2 powders were prepared and tested in the photocatalytic reduction of CO_2 under UV irradiation. The products of CO_2 photoreduction experiments were detected as methane and hydrogen. Wang et al. (2013) prepared CeO_2-TiO_2 nanocomposites by hard template method. The effect of Ce:Ti molar ratio on the photocatalytic reduction of CO_2 in gas phase was investigated. Methane and carbon monoxide were main products.

REE incorporated TiO_2 photocatalytst powders were prepared by using sol-gel technique in this study. The effects of REE doping level and RE ionic size on the nanophase structure, physical and electronic properties were investigated and a correlation between nanophase structure and artificial photosynthesis activity of the powders was developed.

3.2. Materials and Methods

3.2.1. Preparation of the Powders

REE doped TiO_2 powders were prepared by sol-gel using titanium tetraisopropoxide (TTIP, Aldrich 97%) as titanium precursor. Cerium(III) nitrate hexahydrate ($Ce(NO_3)_3.6H_2O$, Aldrich 99.99% trace metal basis), neodymium nitrate hexahdrate ($Nd(NO_3)_3.6H_2O$, Aldrich 99.99% trace metal basis), lanthanum nitrate hexahydrate ($La(NO_3)_3.6H_2O$, Aldrich 99.99% trace metal basis), praseodmium(III) nitrate hexahydrate ($Pr(NO_3)_3.6H_2O$, Aldrich 99.9% trace metal basis), erbium(III) nitrate pentahydrate ($Er(NO_3)_3.5H_2O$, Aldrich 99.9% trace metal basis), dysporsium(III) nitrate pentahydrate ($Dy(NO_3)_3.5H_2O$, Alfa aesar 99.9% trace metal basis), samarium(III) nitrate hexahydrate ($Sm(NO_3)_3.6H_2O$, Alfa aesar 99.9% trace metal basis), gadolinium(III) nitrate hexahydrate ($Gd(NO_3)_3.6H_2O$, Aldrich 99.9% trace metal basis), terbium(III) nitrate pentahydrate ($Tb(NO_3)_3.5H_2O$, Aldrich 99.9% trace metal basis), ytterbium (III) nitrate pentahydrate ($Yb(NO_3)_3.5H_2O$, Aldrich 99.9% trace metal basis), europium(III) nitrate pentahydrate ($Eu(NO_3)_3.5H_2O$ Aldrich 99.9% trace metal basis), yttrium(III) nitrate hexahydrate ($Y(NO_3)_3.6H_2O$ Alfa aesar 99.9% trace metal basis) or zirconium(IV) propoxide (Aldrich 70%) were used as dopant precursors.

Pure TiO_2 powders were prepared by the dropwise addition of a solution (nitric acid (HNO_3, Merck 65%) and water in ethanol (Merck absolute)) to a titanium tetraisopropoxide/ethanol solution under vigorous stirring at room temperature. The resulting transparent sol with the molar ratios of TTIP:H_2O:HNO_3:EtOH as 1:2:0.06:5.9 was stirred until complete gelation was observed. REE doped TiO_2 powders were prepared by following the same route with the addition of predetermined amounts of RE nitrates to nitric acid/water/ethanol solution. The obtained gels were dried at 50^oC overnight prior to heat treatment at 700^oC for 3 hours. TiO_2 powders doped with 0-5% RE_2O_3 (on molar basis) were prepared in the context of this study.

Nd and Er was selected to investigate the effect of doping level on the artificial photosynthesis activity and 0-5% doping was conducted. The effect of REE type was investigated by setting the doping level as 0.1%. Powder preparation process is schematically shown in Figure 3.1.

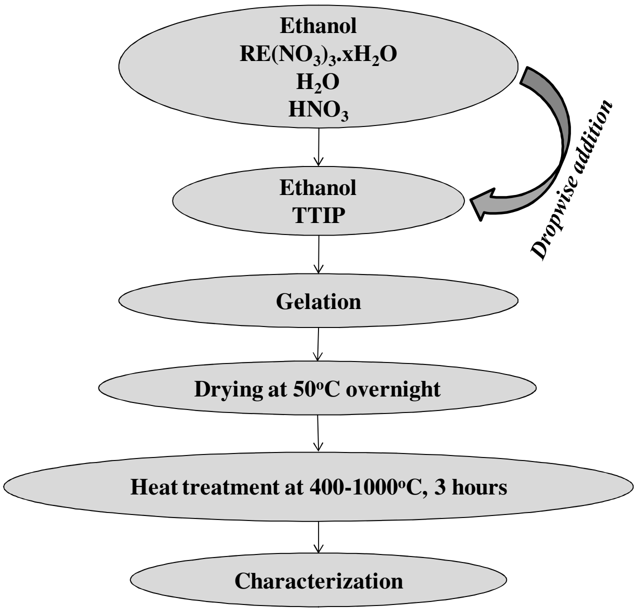

Figure 3.1. A schematic representation of RE_2O_3 doped sol-gel TiO_2 powder preparation process.

Deposition of copper on the prepared TiO_2 powders was performed by in-situ photodeposition. Copper stock solution was first prepared by dissolving copper (II) nitrate ($Cu(NO_3)_2.2.5H_2O$ Aldrich 99.9% trace metal basis) in deionized water at room temperature with a concentration of $1.5x10^{-4}$ g Cu/mL (2.4 mM Cu^{2+} ions). TiO_2 powders (0.15 g) were dispersed in water and the suspension was sonicated to break up loosely attached aggregates. Required amounts of Cu stock solution and methanol (Merck, absolute) were then added and made up to the final volume (100 mL, 25 % v/v methanol-water) and the irradiation was started. A schematic illustration of copper photodeposition process is given in Figure 3.2.

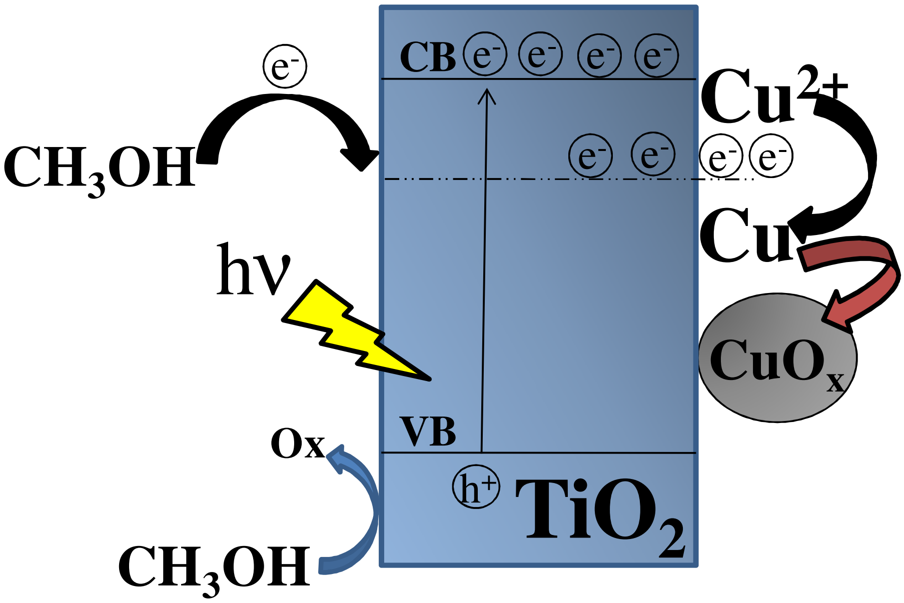

Figure 3.2. Schematic illustration of copper photodeposition on TiO_2.

3.2.2. Characterization of the Powders

Phase characterization of the prepared powders was performed on Philips X'pert Pro XRD equipment with monochromated high-intensity (λ=1.54Å) CuKα radiation. The scanning rate was set as 2.5 2Θ/min between 5^o and 80^o with 0.033^o step size. Characterization was conducted with 1-2 g powder pressed in an aluminum cassette which was also used as reference material to calculate the accurate peak positions.

The crystallite sizes were calculated from the broadening of the (101) reflection for anatase and (110) reflection for rutile using Scherrer's equation:

$$d = \frac{k.\lambda}{\beta.\cos\theta} \tag{3.1}$$

where d is the crystallite size (nm), k is the shape constant (0.9 for spherical particles), λ is the X-ray wavelength (nm), β is the full width at half maximum of the selected peak and θ is the Bragg's angle of diffraction (Sun et al. 2014).

The rutile and anatase weight fractions were determined by using the following relation:

$$x_A = \left(1 + 1.26\frac{I_R}{I_A}\right)^{-1} \quad (3.2)$$

where x_A is the anatase weight fraction, I_R and I_A are the intensities of the rutile (110) and anatase (101) peaks, respectively (Spurr and Mayers 1957).

The determination of the crystal lattice constants for tetragonal geometry (a and c) was conducted using the following expression:

$$\frac{1}{d_{hkl}^2} = \frac{h^2+k^2}{a^2} + \frac{l^2}{c^2} \quad (3.3)$$

where d_{hkl} is the interplane distance and hkl are the Miller (plane) indices. The lattice constants were determined by selecting two peaks ((101) and (200) peaks for anatase) (Tripathi et al. 2013).

Lattice strain in the TiO_2 crystal lattice was calculated by using Williamson-Hall (W-H) plot with at least 4 diffraction peaks to be used in the following relation:

$$\frac{\beta\cos\theta}{\lambda} = \frac{1}{\sigma} + \frac{\eta.\sin\theta}{\lambda} \quad (3.4)$$

where σ is the effective particle size and η is the effective strain (Tripathi et al. 2013).

X-ray photoelectron spectroscopy (XPSSPECS EA 300) was used to identify the existence and bonding states of the elements (electronic structure of the surface) in the prepared powders. Carbon C1s line at 284.8 eV was taken as a reference for the correction of the peak shifts (Kruse and Chenakin 2011). The fitting of C1s spectrum was performed by Gaussian line shape with constant background (Cappelletti et al. 2008) and fitting of O1s and Ti2p spectra were performed by pseudo-Voigt line shape with Shirley background. Peak fitting examples are given in Appendices and in the figures. Quantitative analyses for the calculation of O:Ti atomic ratios were performed by using the corresponding peak areas and the atomic sensitivity factors of O and Ti as 0.66 and 1.8, respectively (Wagner et al. 1981).

Optical absorption characteristics of the prepared powders were investigated by using UV-Vis Spectrophotometer (Perkin Elmer Lamda25) equipped with DRS (Diffuse Reflectance Spectrometer) accessory. Pellets with 15mm diameter and 2-3mm thickness were prepared with uniaxial press for the optical characterization. Bandgaps of the prepared powders were determined by using Kubelka-Munk transformation for indirect band gap (n=0.5):

$$F(R) = \frac{(1-R)^n}{2R} \quad (3.5)$$

where R is the reflectance and F(R) is Kubelka-Munk function (Lopez et al. 2012).

Nitrogen adsorption and desorption isotherms and surface areas were obtained with a Micromeritics Gemini V.

Artificial photosynthesis products (H_2, CO, CH_4) were identified and quantified by Agilent 7820A (Gas Chromatograph-GC) equipped with a Molecular Sieve 5A column and thermal conductivity detector (TCD). He (High purity, 99.99%) carrier gas volumetric flow rate was 20 mL/min. Inlet, oven and detector temperature was 200^{o}C, 105^{o}C and 250^{o}C, respectively.

3.2.3. Artificial Photosynthesis Experimental Setup

Photocatalytic water splitting and CO_2 reduction setup was constructed as shown in Figure 3.3. The setup consists of mainly 3 parts:

- High purity (99.99%) CO_2 and N_2 source.
- Pyrex glass photoreactor with N_2/CO_2 inlet and product gas outlet connecting to online GC in water splitting experiments or sealed with a rubber septum for the sampling of gaseous products evolved in CO_2 reduction experiments. Total volume of the reactor was 133 mL, liquid and gas volumes were 100 mL and 33 mL, respectively. Continuous agitation was supported by a magnetic bar and a stirrer during the photocataytic activity tests to avoid mass transfer limitations and to hold the photocatalyst particles suspended.
- GC system for tracing artificial photosynthesis products.

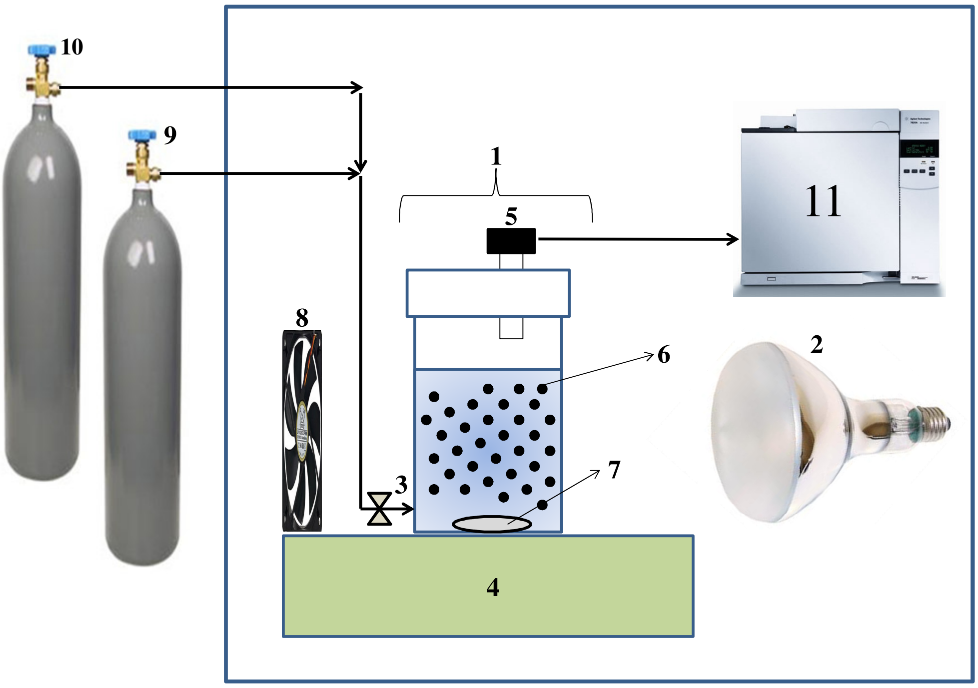

Figure 3.3. Photocatalytic water splitting/CO_2 reduction setup. 1: Photoreactor, 2: UV-Vis lamp, 3: N_2/CO_2 inlet, 4: Magnetic stirrer, 5: Gas outlet, 6: Photocatalyst particles, 7: Magnetic bar, 8: Cooling fan, 9: N_2 tube, 10: CO_2 tube, 11: Gas Chromatograph.

Photocatalytic water splitting experiments were performed in continuous (by online GC quantification) operating mode. Photocatalytic water splitting experiments were performed with in situ Cu photodeposited powders. Photocatalyst powders were dispersed in the reaction mixture which contaings 25 v.% methanol and predetermined amount of Cu^{2+} aqueous solution. N_2 was purged for 15 minutes prior to illumination in order to maintain anaerobe conditions in the reactor. Samples were taken by GC sampling valve (0.5 mL loop) every 10 minutes. Online calibration was conducted by a gaseous mixture containing H_2, CO and CH_4 (Refinery Gas Test Sample Agilent P/N 5080-8755). Online injections (four times) were performed by a sampling valve of the GC system. A sample chromatogram of the refinery gas test sample is given in Figure 3.4.

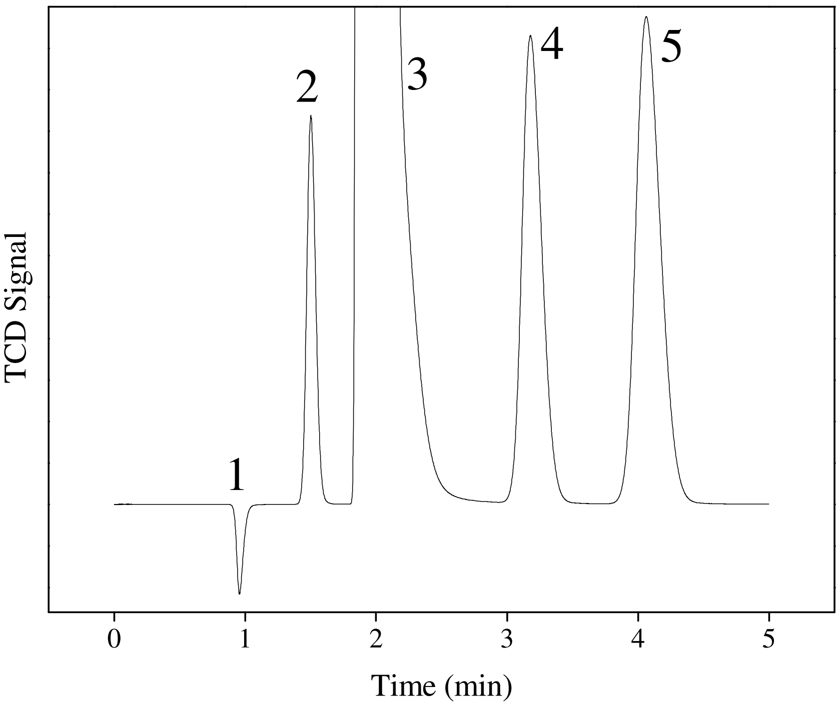

Figure 3.4. Sample chromatogram of the refinery gas test sample. Elution order: 1: H_2, 2: O_2, 3: N_2, 4: CH_4, 5: CO.

Photocatalytic CO_2 reduction experiments were performed in batch mode. Photocatalyst powders were dispersed in 0.1M NaOH to enhance CO_2 solubility in water and act as hole scavenger. CO_2 was purged for 30 minutes prior to illumination to saturate the 0.1M NaOH solution. The solution pH decreased from 12.6 to 6.9 at the end of CO_2 purge. Gas samples (Volume: 1 mL) were taken with predetermined time intervals and injected to GC system manually with a gas-tight syringe (Agilent, PN 5190-1535, 2.5 mL). The temperature inside the photoreactor was kept at ~45°C by using a cooling fan and the pressure in the headspace was 1-1.1 bar during the experiments.

Calibration curves as shown in Figures 3.5, 3.6 and 3.7 were constructed by using the refinery gas test sample to quantify the products evolved during photocatalytic CO_2 reduction. Samples with varying volumes were taken from H_2 tube, diluted with N_2 in the photoreactor (133 mL) and injected to GC for manual calibration of H_2. CO and CH_4 were calibrated by using the refinery gas test sample. CO was calibrated with two points (four repeats) and CH_4 was calibrated with one point (four repeats).

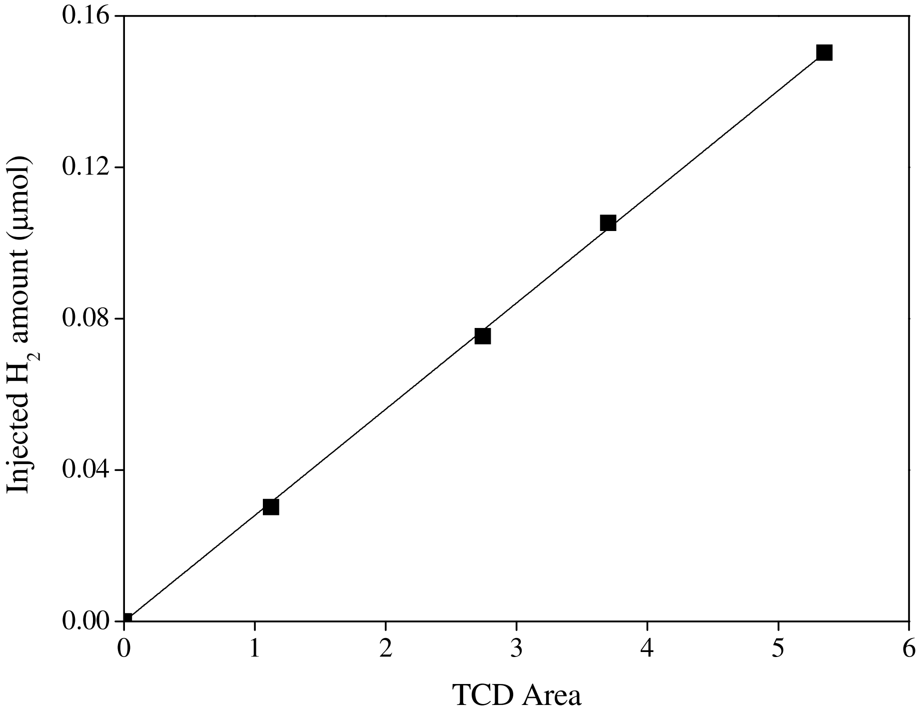

Figure 3.5. Calibration line for H_2 quantification.

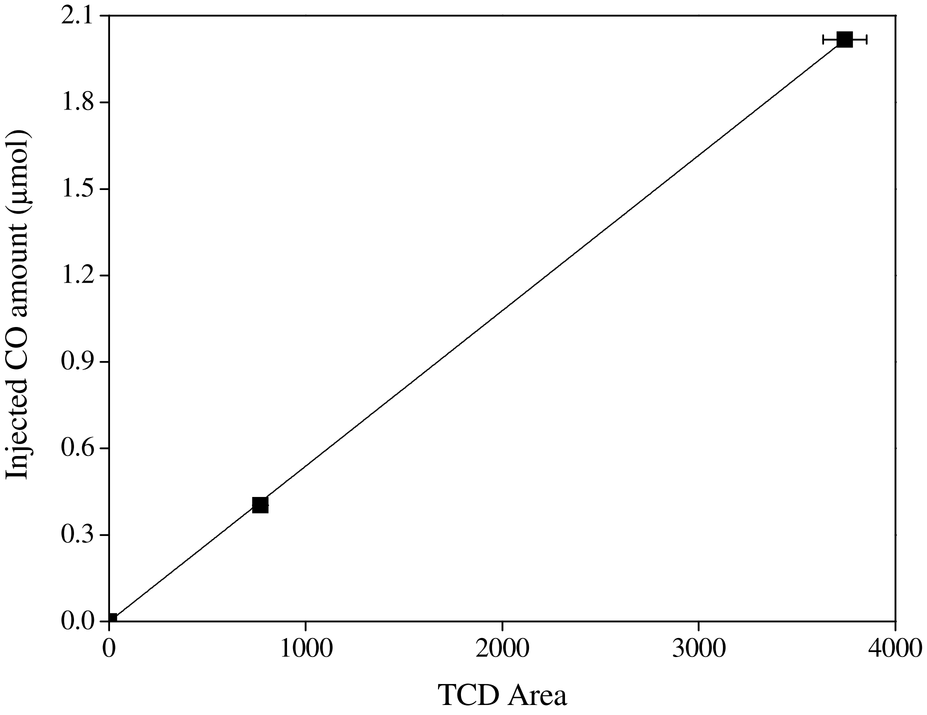

Figure 3.6. Calibration line for CO quantification.

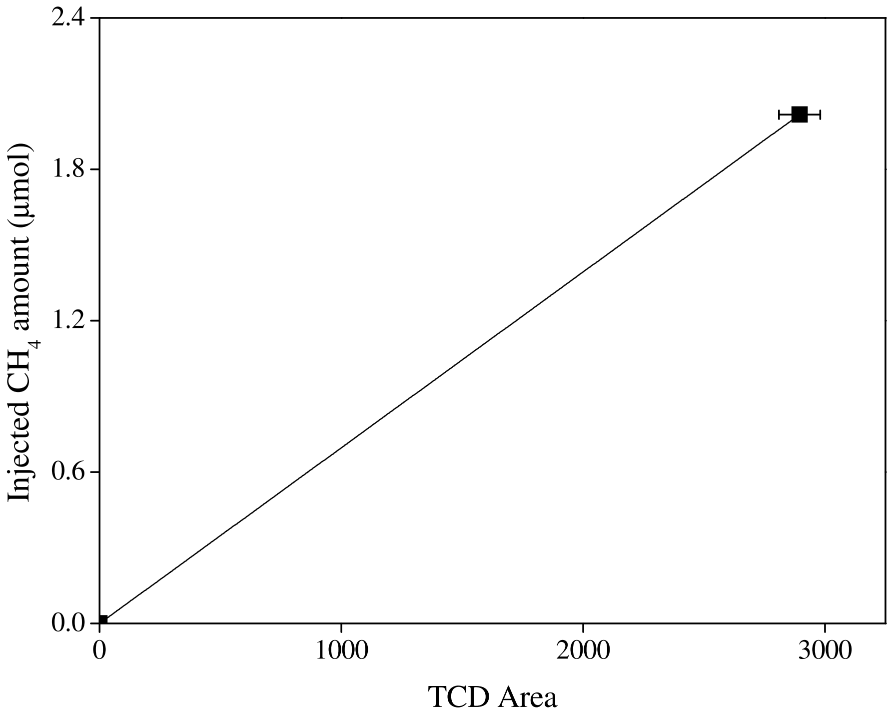

Figure 3.7. Calibration line for CH_4 quantification.

3.3. Results and Discussion

3.3.1. Characterization of the Powders

XRD patterns of Nd_2O_3, Er_2O_3 doped and 0.1% RE_2O_3 doped TiO_2 powders are given in Figures 3.8, 3.9 and 3.10, respectively. Anatase was found to be the main phase in all doped TiO_2 powders. Rutile phase was detected up to 0.25% and 0.5% doping level for Nd_2O_3 and Er_2O_3, respectively. Nd or Er oxide phases were not detected in the XRD patterns. The relative intensity of anatase (101) reflection peak significantly decreased, FWHM of this peak increased and rutile phase formation was hindered by increasing Nd_2O_3 and Er_2O_3 doping level. Anatase to rutile phase transformation kinetics was significantly affected by the doping level and dopant ion size. The structural properties such as crystallite size, rutile weight fraction, lattice constants and surface area of the prepared powders are given in Tables 3.1 and 3.2. Anatase crystallite size decreased with increasing doping level for both Nd_2O_3 and Er_2O_3 doping level. Crystallite size difference is significant at 0.1% doping level; Nd_2O_3 doped TiO_2 powder has lower average crystallite size and rutile weight fraction compared to Er_2O_3 doped TiO_2 powder. According to Zhang et al. (2004) rare earth doping inhibits the A-R phase transformation, retards the diminishing of surface area at high heat treatment temperatures and rare earth ions with larger ionic radius have stronger inhibitory effect on the A-R phase transformation kinetics. Our results are in accordance with Zhang et al. (2004) which indicated that Nd (ionic radius: 112 pm) has more inhibitory effect than Er (ionic radius: 103 pm) on the A-R phase transformation kinetics.

Zr doping was also performed in order to see the effect of doping TiO_2 with the same valence of Ti^{4+}. Rutile phase was not observed in Zr doped TiO_2 powder. Zr was found to be more inhibitory effect on the A-R phase transformation kinetics compared to REs even at a lower doping level. It was found that Nd, La, Pr and Sm is more active in the phase evolution retardation compared to other REEs according to their lower crystallite sizes and rutile weight fractions (except Er and Ce).

Anatase lattice constants a and c slightly decreased with increasing doping level. The decrease in the lattice constants may support that Nd^{3+} or Er^{3+} ions were located in the interstitials of TiO_2 or seggregated in the grain boundaries and substitution of these ions with Ti^{4+} is not possible. The contraction in c direction may be due to the more electropositivity of RE ions and attracting more O^{2-} than Ti^{4+} ions and forming oxygen deficiencies in the TiO_2 lattice. The lattice constant c is also sensitive to crystallite size. The decrease in the crystallite size may be another reason for the decrease in the lattice constant c. The effect of doping level on the lattice constants is more significant in Nd_2O_3 doped TiO_2 powders compared to Er_2O_3 doped TiO_2 powders which may be due to the higher electropositvity of Nd than Er or the larger crystallite sizes of Er_2O_3 doped TiO_2 powders. Lattice constants slightly changed with RE ionic radius for low doping levels (0.1%), however it was found that rutile weight fraction significantly depends on the RE ionic size which significantly affects the inhibitory property.

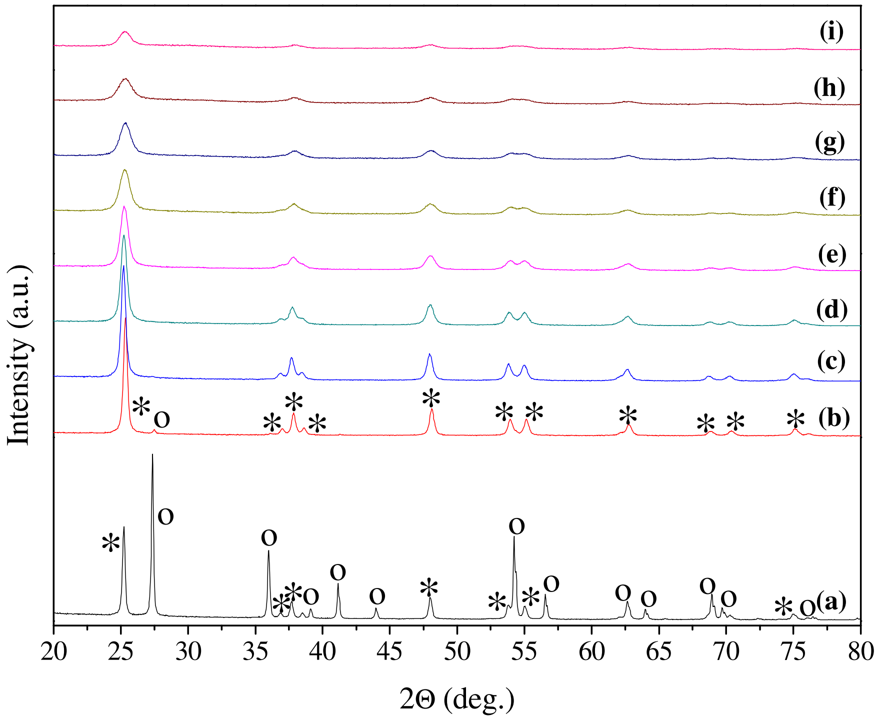

Figure 3.8. XRD patterns of Nd_2O_3 doped TiO_2 powders: (a) pure, (b) 0.1%, (c) 0.25%, (d) 0.5%, (e) 1%, (f) 2%, (g) 3%, (h) 4%, (i) 5% (*: anatase, o: rutile).

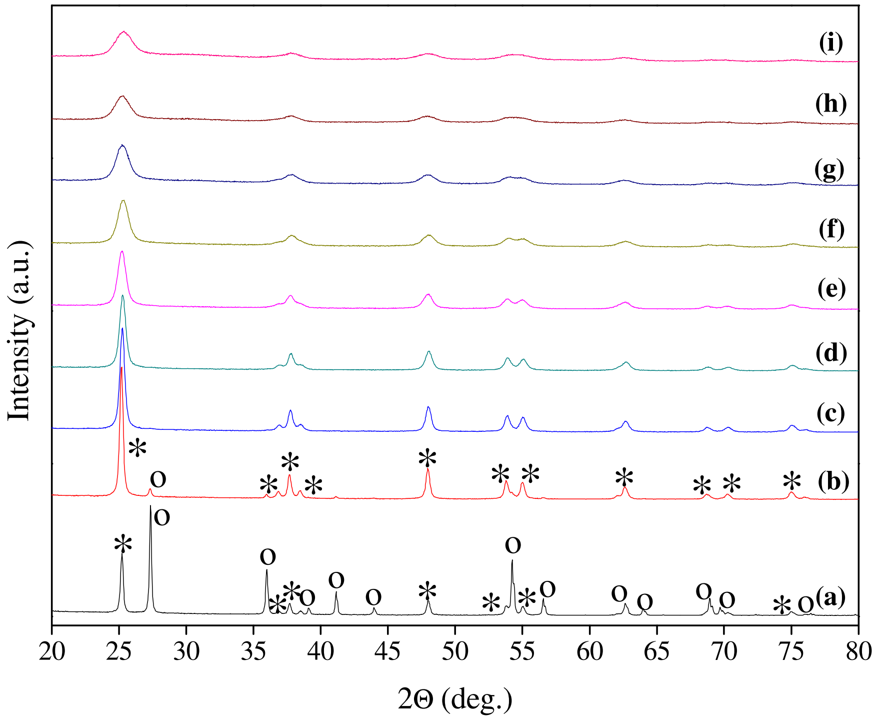

Figure 3.9. XRD patterns of Er_2O_3 doped TiO_2 powders: (a) pure, (b) 0.1%, (c) 0.25%, (d) 0.5%, (e) 1%, (f) 2%, (g) 3%, (h) 4%, (i) 5% (*: anatase, o: rutile).

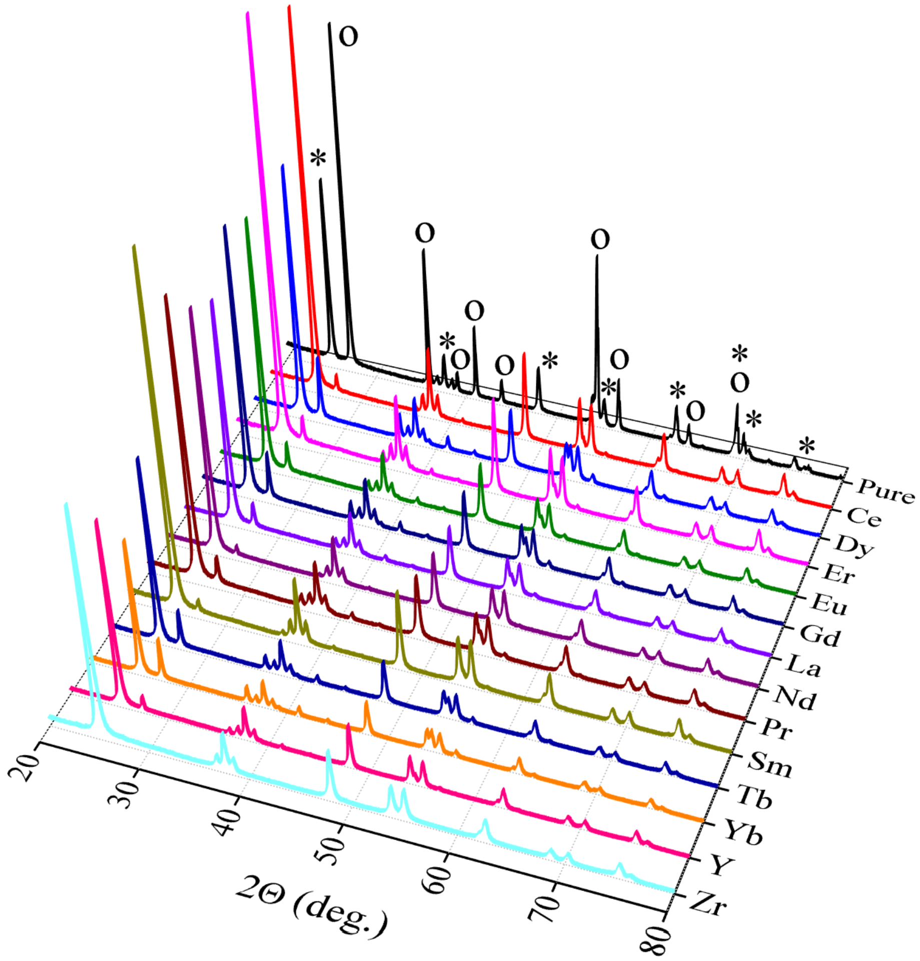

Figure 3.10. XRD patterns of 0.1% RE_2O_3 doped TiO_2 powders (*: anatase, o: rutile).

Table 3.1. Properties of Nd_2O_3/Er_2O_3 doped TiO_2 powders.

Photocatalyst	**Anatase crystallite size (nm)**	**Rutile wt. frac. (%)**	**Anatase lattice parameters**		**Lattice volume (Å^3)**	**BET surface area (m^2/g)**	**Direct / Indirect bandgap energy (eV)**	**Zeta potential (mV)**
			a (Å)	**c (Å)**				
pure	45.2	69.1	3.78	9.59	137.1	2.1	3.08 / 2.90	-33.7 (±3.6)
0.1Nd	29.2	4.2	3.77	9.42	134.2	18.9	3.13 / 2.81	-29.7 (±3.1)
0.25Nd	24.3	0.6	3.77	9.42	134.2	22.6	3.18 / 2.89	-30.9 (±3.6)
0.5Nd	18.6	0	3.77	9.33	132.8	38.7	3.17 / 2.95	-33.1 (±8.9)
1Nd	15.4	0	3.78	9.32	132.9	49.2	3.19 / 3.03	-34.2(±0.7)
2Nd	12.4	0	3.77	9.23	131.2	64.9	3.20 / 2.99	-30.1 (±3.9)
3Nd	11.1	0	3.78	9.24	131.6	62.1	3.22 / 3.03	-33.3 (±0.9)
4Nd	9.8	0	N/A	N/A	N/A	48.0	3.24 / 2.99	-29.3 (±2.5)
5Nd	N/A	0	N/A	N/A	N/A	18.4	3.22 / 3.03	-33.7 (±3.8)
0.1Er	34.6	6.2	3.77	9.47	134.9	16.7	3.08 / 2.90	-31.5 (±2.9)
0.25Er	22.8	0.6	3.77	9.45	134.6	46.3	3.18 / 2.91	-32.4 (±3.3)

(cont. on next page)

Table 3.1. (cont.).

Photocatalyst	Anatase crystallite size (nm)	Rutile wt. frac. (%)	Anatase lattice parameters		Lattice volume (Å^3)	BET surface area (m^2/g)	Direct / Indirect bandgap energy (eV)	Zeta potential (mV)
			a (Å)	c (Å)				
0.5Er	18.1	Trace	3.78	9.47	134.9	53.6	3.17 / 2.90	-32 (±4.0)
1Er	14.7	0	3.77	9.41	134.1	74.2	3.27 / 3.01	-30.3 (±2.3)
2Er	11.1	0	3.78	9.55	136.7	74.7	3.28 / 3.03	-35.1 (±8.6)
3Er	10.1	0	N/A	N/A	N/A	68.9	3.28 / 3.03	-35.7 (±3.7)
4Er	9.2	0	N/A	N/A	N/A	63.4	3.26 / 3.00	-33.4 (±1.7)
5Er	N/A	0	N/A	N/A	N/A	65.0	3.28 / 3.07	-35.2 (±6.1)

Table 3.2. Properties of 0.1% RE_2O_3 doped TiO_2 powders.

Rare earth	**Ionic radius (pm) / oxidation state (Jia et al. 1991)**	**Anatase crystallite size (nm)**	**Rutile wt. frac. (%)**	**Anatase lattice parameters**		**Lattice volume (Å^3)**	**BET surface area (m^2/g)**	**Direct / Indirect bandgap energy (eV)**	**Zeta potential (mV)**
				a (Å)	**c (Å)**				
La	117 / +3	29.9	10.88	3.78	9.47	134.9	14.8	3.23 / 2.81	-34.8 (±4.2)
Pr	113 / +3	29.9	10.34	3.77	9.45	134.7	15.0	3.23 / 2.81	-34.3 (±2.8)
Nd	112 / +3	29.2	4.16	3.77	9.42	134.2	18.9	3.13 / 2.81	-29.7 (±3.1)
Sm	110 / +3	33.9	3.24	3.78	9.45	134.7	8.6	3.10 / 2.84	-32.4 (±3.3)
Eu	109 / +3	32.3	11.67	3.77	9.45	134.4	13.5	3.22 / 2.80	-37.4 (±1.2)
Gd	108 / +3	34.6	17.21	3.78	9.47	135.1	10.0	3.13 / 2.81	-33.7 (±3.2)
Tb	106 / +3	33.9	19.33	3.77	9.43	134.2	11.5	3.22 / 2.80	-34.6 (±1.2)
Dy	105 / +3	33.6	23.41	3.77	9.44	134.5	12.4	3.17 / 2.80	-36.5 (±1.5)
Er	103 / +3	34.6	6.16	3.77	9.47	134.9	16.7	3.20 / 2.87	-31.5 (±2.9)
Yb	101 / +3	35.9	27.06	3.78	9.48	135.1	6.9	3.21 / 2.82	-32.6 (±2.3)
Zr	86 / +4	27.7	Trace	3.77	9.45	134.6	17.8	3.28 / 2.93	-32.6 (±2.5)
Y	90 / +3	34.3	8.08	3.77	9.45	134.6	6.8	3.22 / 2.83	-34.1 (±2.6)
Ce	101 / +4	38.2	4.84	3.78	9.49	135.4	13.2	3.27 / 2.79	-34.0 (±1.0)

Anatase lattice strain in 0-5% Nd_2O_3/Er_2O_3 doped and 0.1% RE_2O_3 doped TiO_2 powders are given in Figures 3.11 and 3.12. Lattice strain values are greater in doped powders than pure TiO_2 since pure TiO_2 is composed of 69% rutile. The presence of rutile phase (even trace amounts at 1% Er_2O_3 doping level) signicantly affects the strain in the nanostructure. Lattice strain in rutile particles may be less compared to anatase particles since rutile is more stable and has a more ordered structure. Presence of both rutile and anatase phase (with possible Er-Ti oxide phase) may be the main reason for the continuous lattice strain decrease with increasing Er_2O_3 doping level. The lattice strain of Nd_2O_3 doped TiO_2 powders increased beyond 0.5% doping level which may be due to the absence of rutile phase. The lattice strain did not show direct relation with RE ionic size as seen in Figure 3.12.

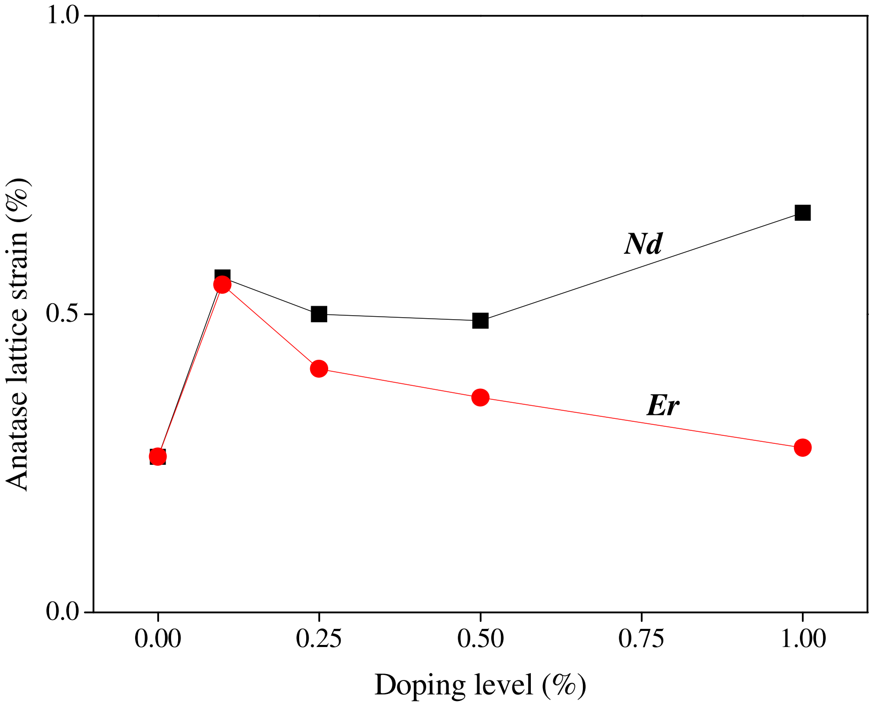

Figure 3.11. Anatase lattice strain in Nd_2O_3 and Er_2O_3 doped TiO_2 powders.

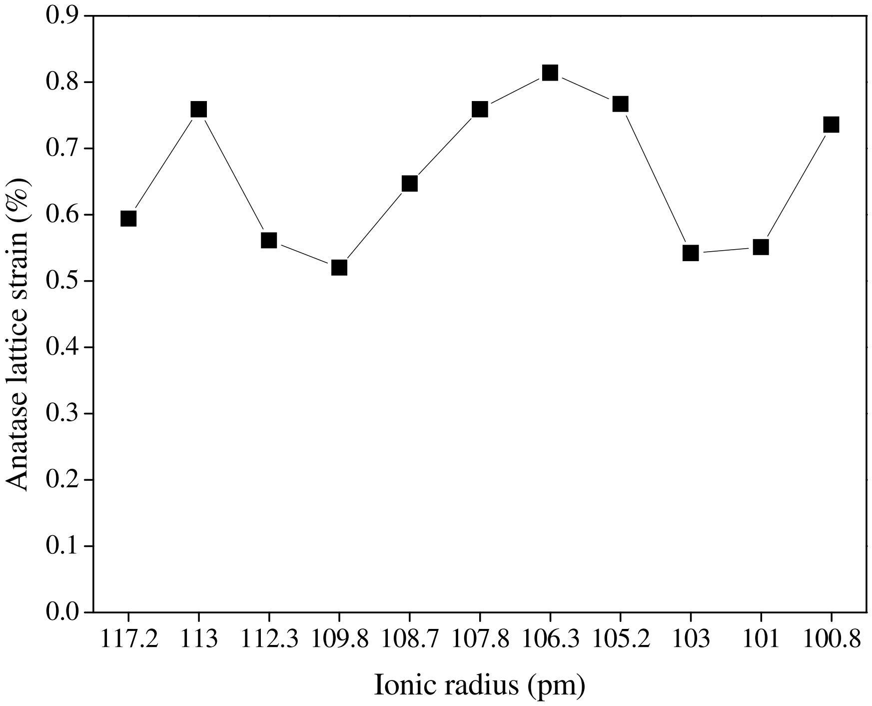

Figure 3.12. Anatase lattice strain in 0.1% RE_2O_3 doped TiO_2 powders.

The results of XPS analysis are given in Figures 4.13 and 4.14. Ti-O binding energy changes affected by the doping level and rare earth ionic size may be interpreted from Ti2p3/2 (~458.6 eV) and O1s (~529 eV) binding energies calculated from XPS spectra. Both binding energies of the doped powders are lower than pure TiO_2 which may be due to a decrease in the rutile weight fraction and formation of oxygen defective structure. The binding energies slightly decreased with increasing doping level and rare earth ionic size (excluding Ce and Zr since doping level is lower for them). These results support the XRD analysis (lattice constants, lattice strain, and crystallite size) that doping TiO_2 with RE ions significantly changes the local environment of Ti^{4+} and O^{2-} ions and the bonding energy of Ti-O is affected by the electropositivity of RE ions. Formation of RE-O-Ti or RE-O bonds in the interstitials or on the grain boundaries decreased the binding energies of Ti2p3/2 and O1s also which depend on the RE ionic size.

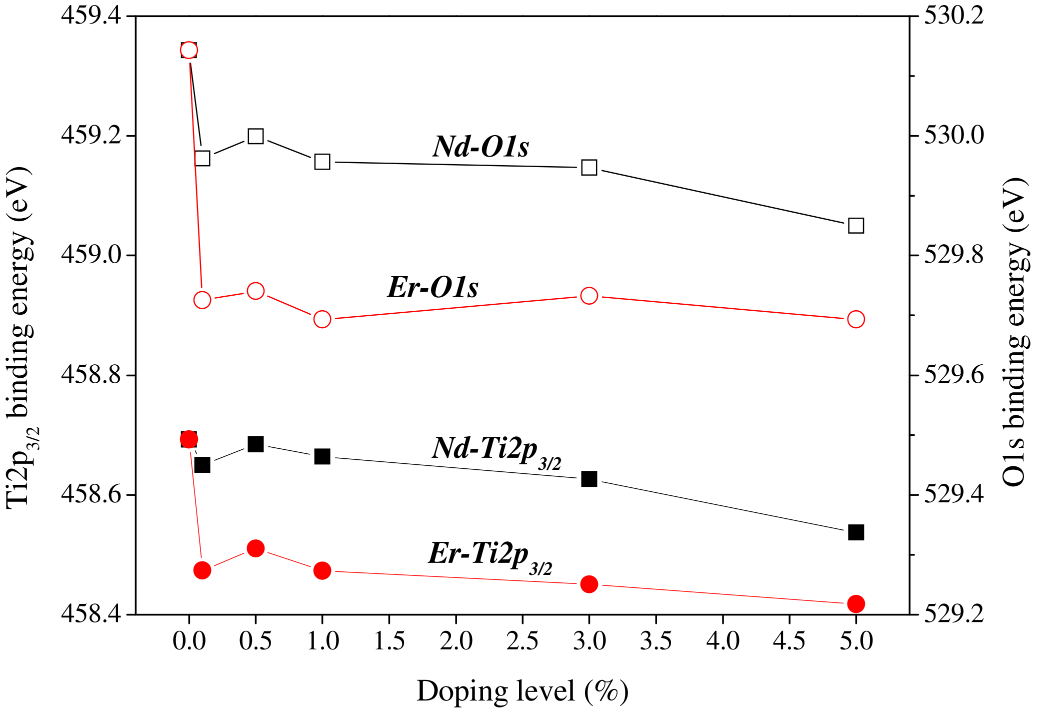

Figure 3.13. $Ti2p_{3/2}$ and O1s binding energies of Nd_2O_3 and Er_2O_3 doped TiO_2 powders.

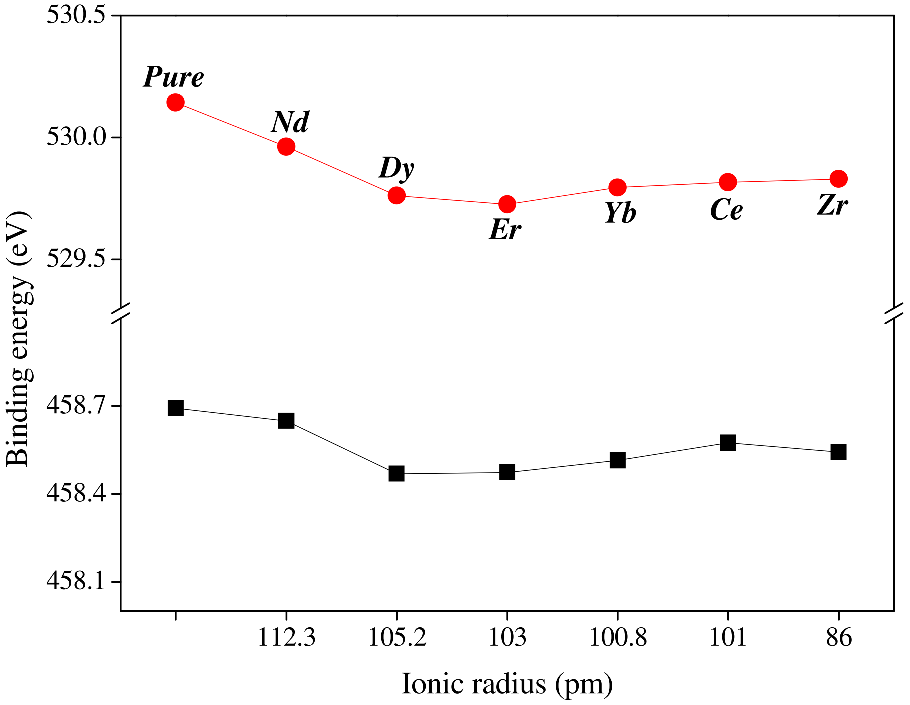

Figure 3.14. $Ti2p_{3/2}$ and O1s binding energies of 0.1% RE_2O_3 doped TiO_2 powders: (■) $Ti2p_{3/2}$, (●) O1s.

UV-Vis DR spectra of Nd_2O_3, Er_2O_3 and 0.1% RE_2O_3 doped TiO_2 powders heat treated at 700°C are shown in Figures 3.15, 3.16 and 3.17, respectively. REE doping significantly affects the UV-Vis light absorption properties of TiO_2, as shown in the figures. The spectra of RE_2O_3 doped TiO_2 showed blue shift (shift to lower wavelengths). XRD results indicated that pure TiO_2 is composed of anatase and rutile phases and REE doping may alter the phase composition by the inhibition of AR phase transformation. Pure TiO_2 at 700°C would have a bandgap energy between that of anatase (3.2 eV) and rutile (3.0 eV) since its nanostructure is composed of these phases according to the XRD patterns. The bandgap energy of TiO_2 may also be tuned between these values depending on the doping level since REE doping level significantly affects the phase composition. According to the obtained results, the calculated direct bandgap energy of pure TiO_2 at 700°C is 3.08 eV and varies between 3.13 and 3.24 eV with RE_2O_3 doping level. These results supported the XRD results which indicated that RE ions may accommodate in the interstitials or segregate on the grain boundaries without a substitutional accommodation. Substitutional doping would cause a red shift in the band edge position since additional energy levels would be introduced in the bandgap of TiO_2.

Blue-shift in the bandgap energy does not always signify a decrease in the visible light absorption, since there are several absorption bands in the visible region as shown in the figures. The large absorption bands at the wavelengths of 515, 529, 588, 684, 747 nm and relatively narrower bands at at 463, 476, 628 nm are the characteristics absorption bands of Nd^{3+} ion resulting from 4f-4f transitions. These bands are at the wavelengths of 452, 490, 522, 654 nm for Er_2O_3, 450, 474, 487, 587, 596 nm for Pr, 405 and 478 for Sm, 545 and 754 nm for Dy_2O_3 doping, however these absorption bands are more significant for Nd_2O_3 and Er_2O_3 doping.

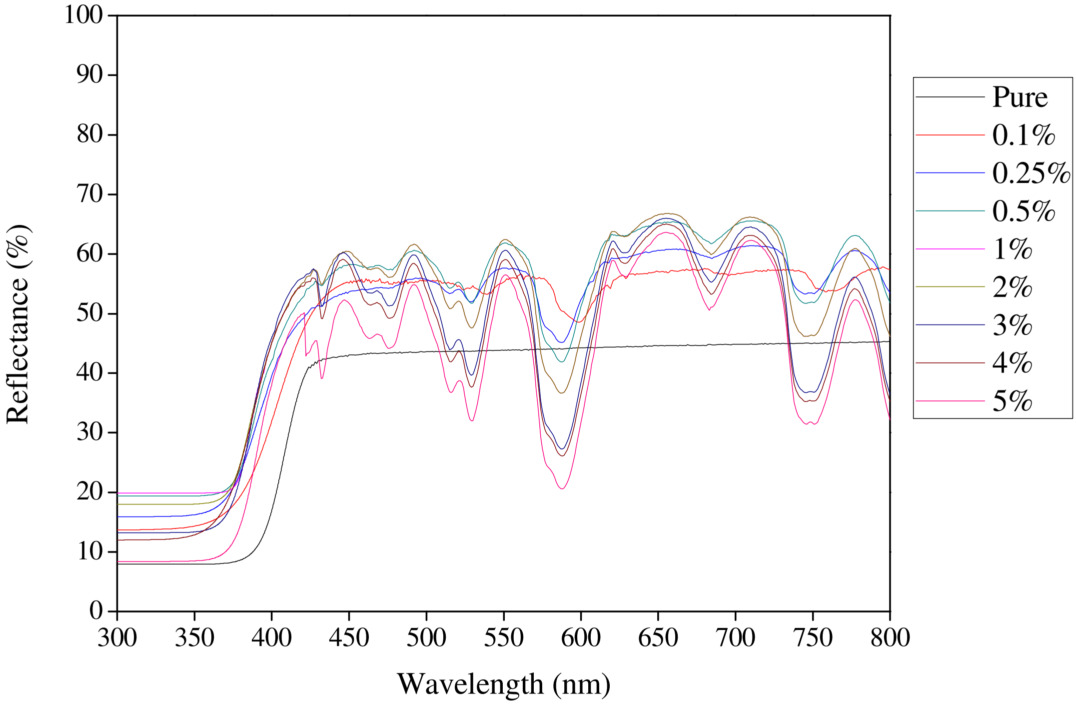

Figure 3.15. UV-Vis DR spectra of Nd_2O_3 doped TiO_2 powders.

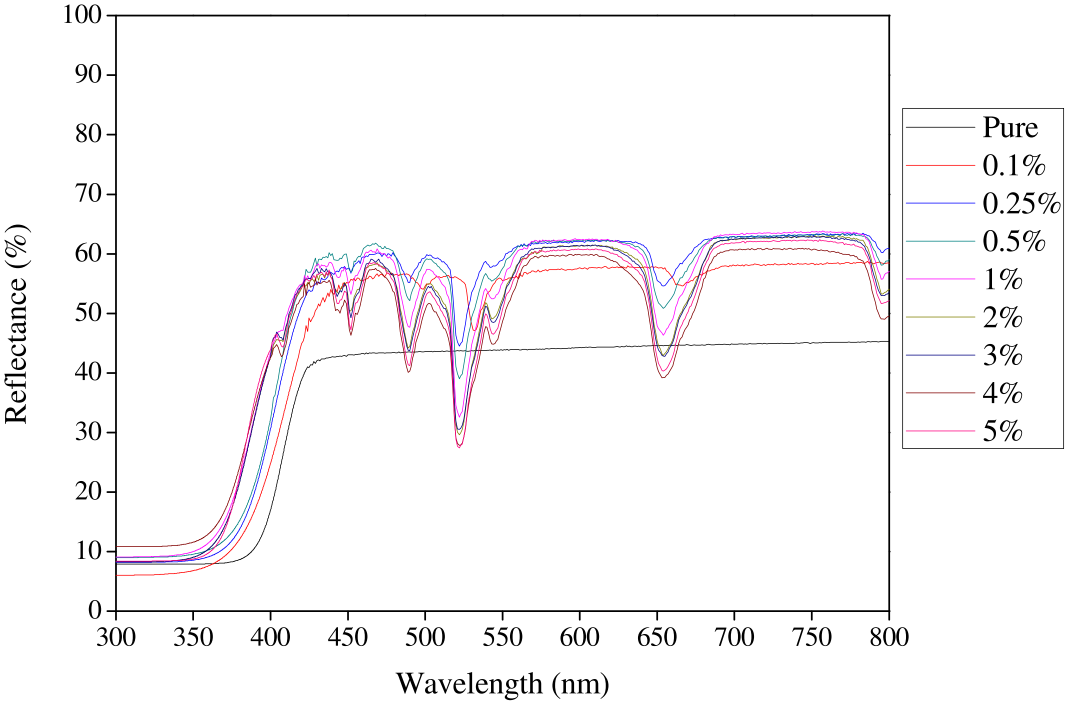

Figure 3.16. UV-Vis DR spectra of Er_2O_3 doped TiO_2 powders.

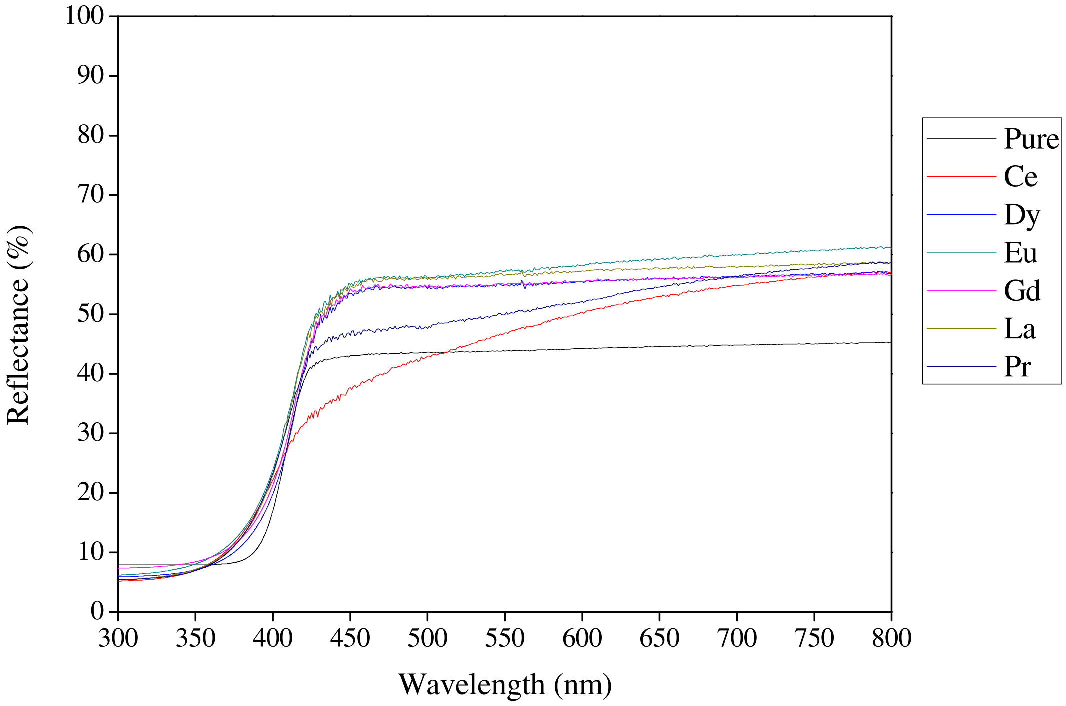

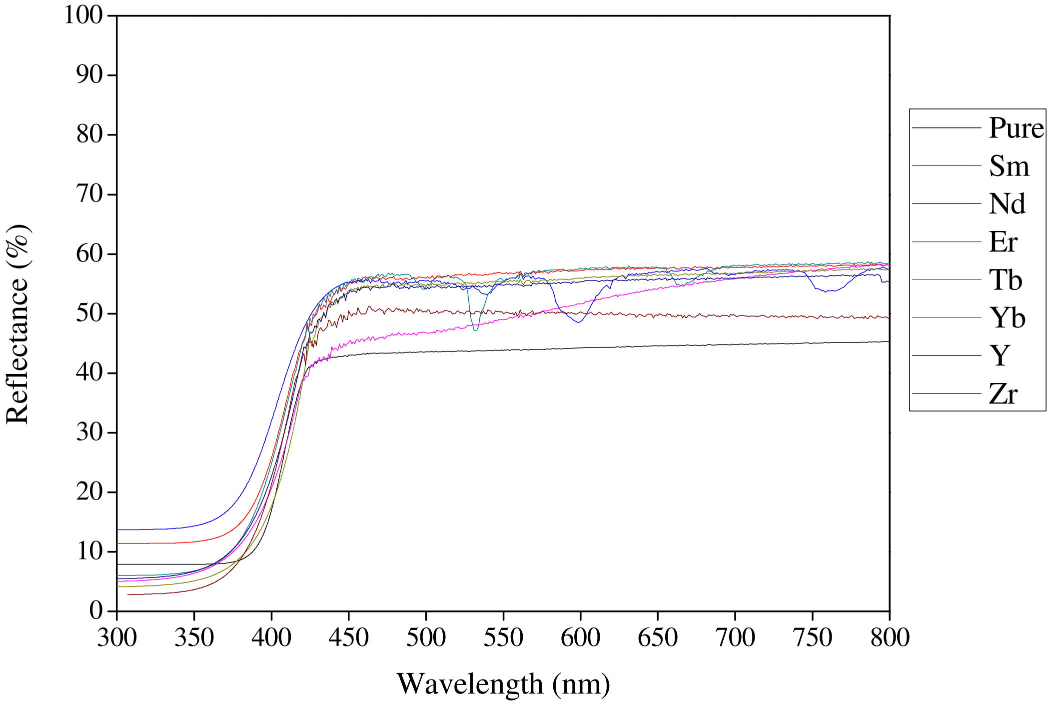

Figure 3.17. UV-Vis DR spectra of 0.1% RE_2O_3 doped TiO_2 powders.

3.3.2. Photocatalytic Activities of the Powders

Photocatalytic water splitting activities of in situ copper photodeposited 0.1% Nd_2O_3 doped sol-gel TiO_2 powders heat treated at 700°C with various copper contents (wt.%) are given in Figure 3.18. These experiments were conducted to investigate the effect of Cu loading on the photocatalytic water splitting activity of TiO_2 and set a Cu loading level for further investigation of the effect of doping level and RE ionic radius. The optimum copper loading was found to be 0.25 wt.%. There are two possible reasons for obtaining an optimum Cu loading level. The number of electron sinks/reaction sites or the size of the CuO_x particles (Montini et al. 2011) strictly depend on the number of Cu^{2+} molecules. At low Cu loading a decrease in the number of reaction sites or decrease in the particle size may affect the interaction of reacting molecules (H_2O and methanol) with TiO_2 or TiO_2-CuO_x junctions. Blocking light from reaching the TiO_2 surface at high Cu loading due to the larger size of the clusters may also be the reason for obtaining relatively lower activities at high Cu loading. As a result, 0.25 wt.% Cu loading was selected for the further experiments.

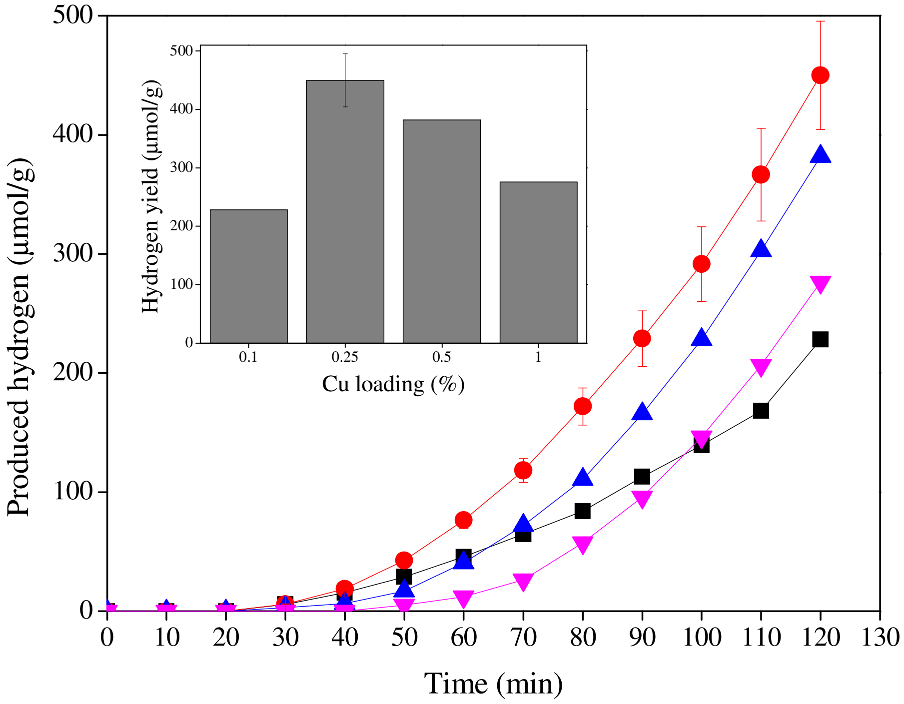

Figure 3.18. Time dependent hydrogen production with in situ copper photodeposited 0.1% Nd_2O_3 doped TiO_2 powder with various Cu loading amounts [(■) 0.1%, (●) 0.25%, (▲) 0.5%, (▼) 1% all in wt.% elemental Cu]. In the inset CO/H_2 ratios and hydrogen yields obtained in 2 hours are given.

Time dependent hydrogen production, CO/H_2 ratios and hydrogen yields obtained in 2 hours (inset) with in situ copper photodeposited Nd_2O_3 and Er_2O_3 doped TiO_2 powders are given in Figure 3.19 and 3.20, respectively. Hydrogen production with the photocatalysts were given per unit surface area basis to evaluate the effect of REE doping on the surface reactivity. The highest activities were obtained with 0.1% Nd_2O_3 and 0.1&0.25% Er_2O_3 doped TiO_2 powders with the lowest CO/H_2 ratios. CO is formed by the decomposition of formic acid derived from methanol which may poison the catalyst and decrease the photocatalytic activity, so minimum amount of CO production is desired to have high photocatalytic activities and to produce high purity hydrogen (Wu 2008). Especially low Nd_2O_3 and Er_2O_3 doping levels generated highly active surfaces when compared to higher doping levels despite the higher surface areas. Phase structure (composition) may be considered to be the main reason for obtaining higher activities at low doping levels. Phase structure analysis indicated that RE ions cannot enter TiO_2 lattice (substitutionally) and inhibit the AR phase transformation by interstitial or segregated RE ions. Tuned AR ratio by phase inhibition or the absorption of visible light photons by RE ions and transfer to anatase TiO_2 may enhance the light absorption properties of TiO_2. Another possible reason may be the increased electron-hole separation rates in the anatase-rutile junctions defined by the phase structure or TiO_2-RE_2O_3 junctions. Anatase-rutile ratio is crucial in photocatalysis since anatase is known to be more active and light absorption of rutile is better than anatase.

Light absorption in a wider range of UV-Vis spectrum is provided by the 4f-4f transitions of REEs, and the intensity of the absorption at certain wavelengths in the visible region increases with RE_2O_3 doping level; however it was found that there is an optimum doping level of REEs. Excess amount of RE oxide level in the interstitials or on the grain boundaries can block the anatase TiO_2 surface, hence decrease the photocatalytic activity. The results indicated that the photocatalytic activity of a photocatalyst is not only determined by its light absorption properties, but also the crystalline nanophase structure. Crystallite sizes at 0.1 and 0.25% doping level for Nd_2O_3 and Er_2O_3 were ~20-30 nm. Large crystallites would have more contact points with the reactant (H_2O) since the surface of the relatively smaller crystallites (at higher doping levels) may be blocked by the segregated RE oxides. There may be an optimum RE doping level for obtaining high photocatalytic water splitting activities determined by the nanophase composition, crystallite size and light absorption properties.

There two possible reactions occurring in the photocatalytic water splitting in the presence of a sacrificial reagent (electron donor/hole scavenger). The oxidation of methanol by the valence band holes of TiO_2 (which is highly oxidative) (Puskelova et al. 2014) producing hydrogen atom and methoxy group (Kandiel et al. 2014) and the reduction of hydrogen ions by the electrons injected by Cu species on the surface of TiO_2. RE ions can interact with methanol (Lewis base) as Lewis acid due to their partial unoccupied 4f atomic orbits (Reszczynska et al. 2015, Xie et al. 2005). REE incorporation may also have enhanced the adsorption of reactants which is a crucial step in catalysis.

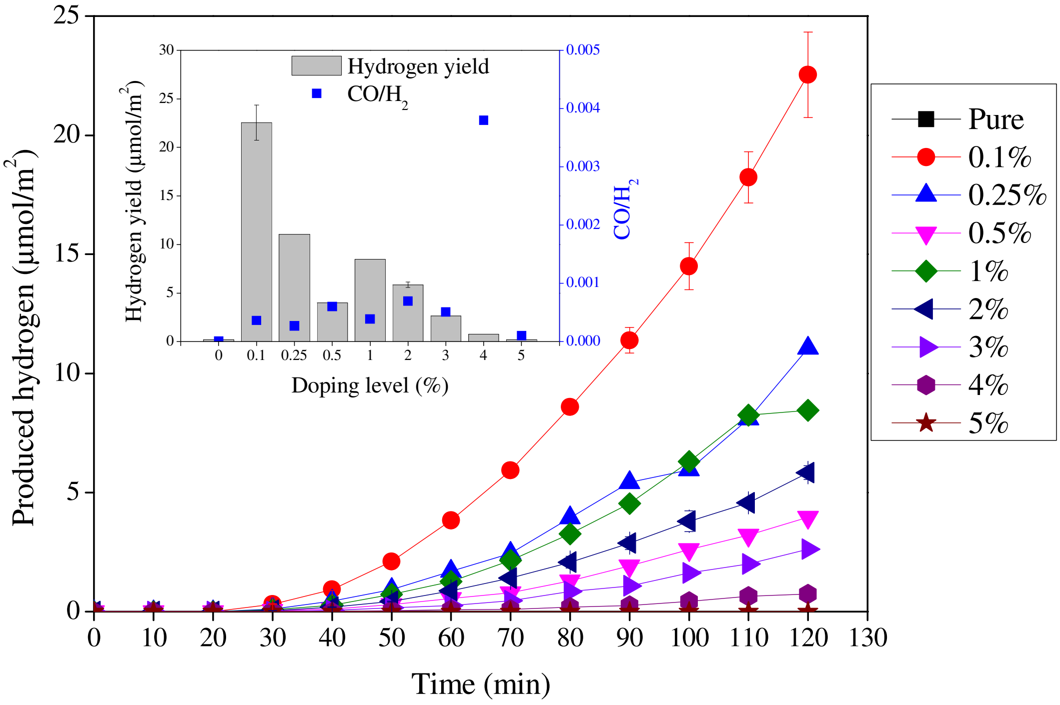

Figure 3.19. Time dependent hydrogen production with in situ copper photodeposited Nd_2O_3 doped TiO_2 powders. In the inset CO/H_2 ratios and hydrogen yields obtained in 2 hours are given.

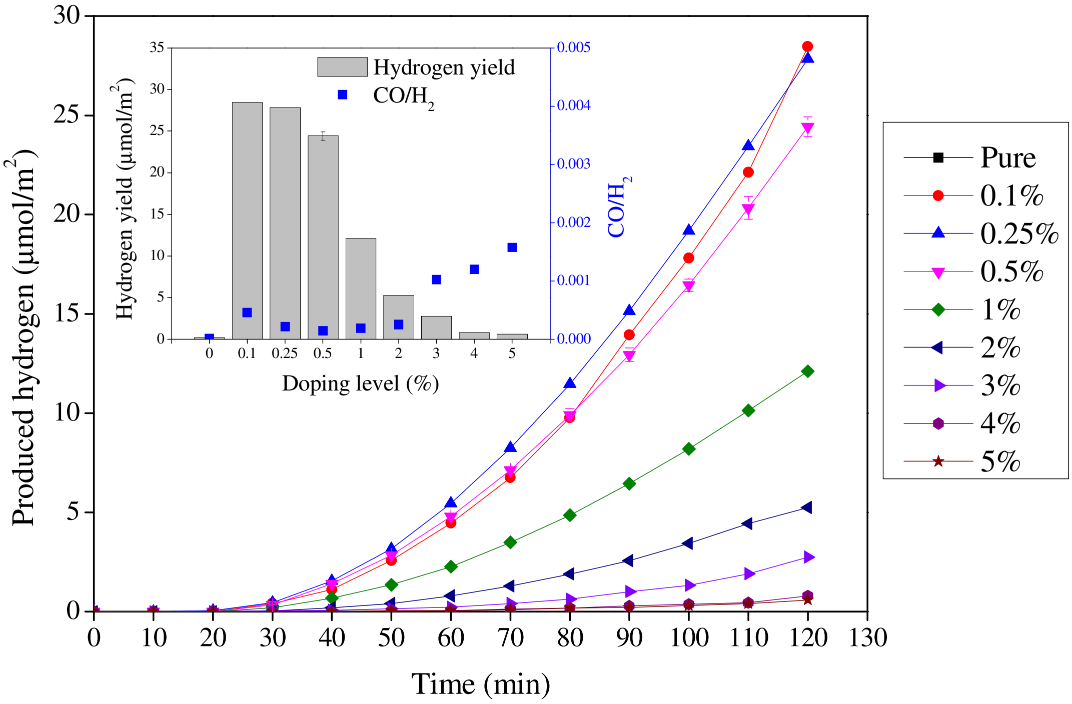

Figure 3.20. Time dependent hydrogen production with in situ copper photodeposited Er_2O_3 doped TiO_2 powders. In the inset CO/H_2 ratios and hydrogen yields obtained in 2 hours are given.

Photocatalytic water splitting activities of in situ copper photodeposited 0.1% RE_2O_3 doped TiO_2 powders are given in Figure 3.21. The activities for all doped powders were higher than that of pure TiO_2. The highest activities were obtained with CeO_2 and ZrO_2 doped powders. CeO_2 and ZrO_2 doped TiO_2 powders will be excluded while interpreting the effect of RE element on the activity since Ce and Zr were doped at a level half of the other REEs in elemental basis (0.1% CeO_2 and ZrO_2 and also their oxidation states are 4+). The highest photocatalytic water splitting activity was obtained with La and Sm doped TiO_2 powders and the activity changed in the following order: La>Sm>Eu>Pr>Gd>Er>Nd>Tb>Yb>Dy. Figure 3.22 was constructed for a better understanding of the effect of RE ionic radius on the photocatalytic water splitting activity of TiO_2.

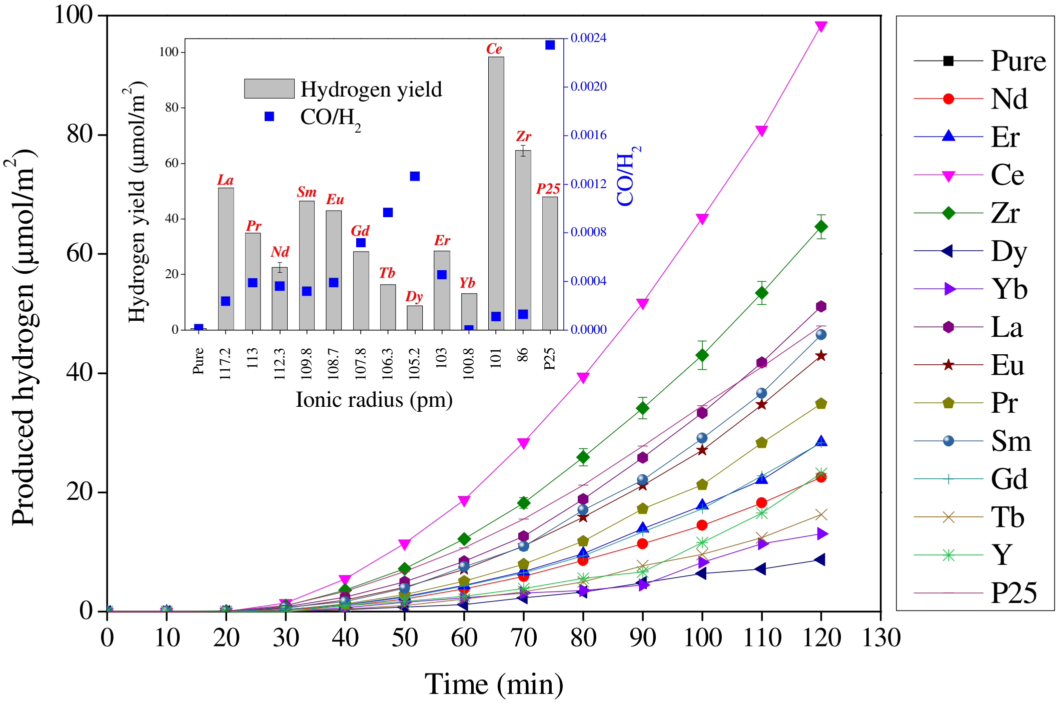

Figure 3.21. Time dependent hydrogen production with in situ copper photodeposited 0.1% RE_2O_3 doped TiO_2 powders. In the inset CO/H_2 ratios and hydrogen yields obtained in 2 hours are given.

The relationship between the phase structure and the photocatalytic water splitting activity of 0.1% RE_2O_3 doped TiO_2 powders is shown in Figure 3.22. The formation of surface phase junctions between anatase and rutile nanoparticles may enhance the charge separation by promoting the transfer of photogenerated electrons from rutile conduction band to Cu species on anatase (Zhang et al. 2008) for the reduction of hydrogen produced by the oxidation of methanol/water in the valence band of rutile or anatase. The cooperation between anatase and rutile phases in the photocatalytic water splitting can be seen from Figure 3.22. The highest activities were obtained when anatase and rutile crystallite sizes were comparably small (for larger RE ionic sizes) and anatase weight fractions were high. In general, activity was found to be directly proportional to the anatase weight fraction, however a relationship could not be constructed according to anatase-crystallite size since photocatalytic water splitting process is a multi variable process including light absorption, charge separation or adsorption of the reactants. It was found that light absorption properties of TiO_2 can be enhanced by tuning AR phase ratio by doping with RE ions with different light absorption characteristics. RE ions may also affect the adsorption of methanol by lewis acid-base interactions. REEs are known to be good lewis acids which can form complexes with lewis bases such as alcohols (Xie et al. 2005) and are known to be "chameleons" of coordination chemistry due to their adaptation to many coordination environments. The coordination number hence the hydration number of REEs increases with increasing ionic radius which can increase the adsorption of water and methanol. Larger RE ions have coordination number of 9 and smaller ions have 8 (Bunzli et al 2000). The obtained results clearly indicated that doping TiO_2 with relatively larger ionic radii REEs may significantly enhance the photocatalytic water splitting activity more than smaller ionic radii REEs due to the higher presence of anatase phase weight fractions and increased reactant adsorption capacities originating from REE coordination chemistry.

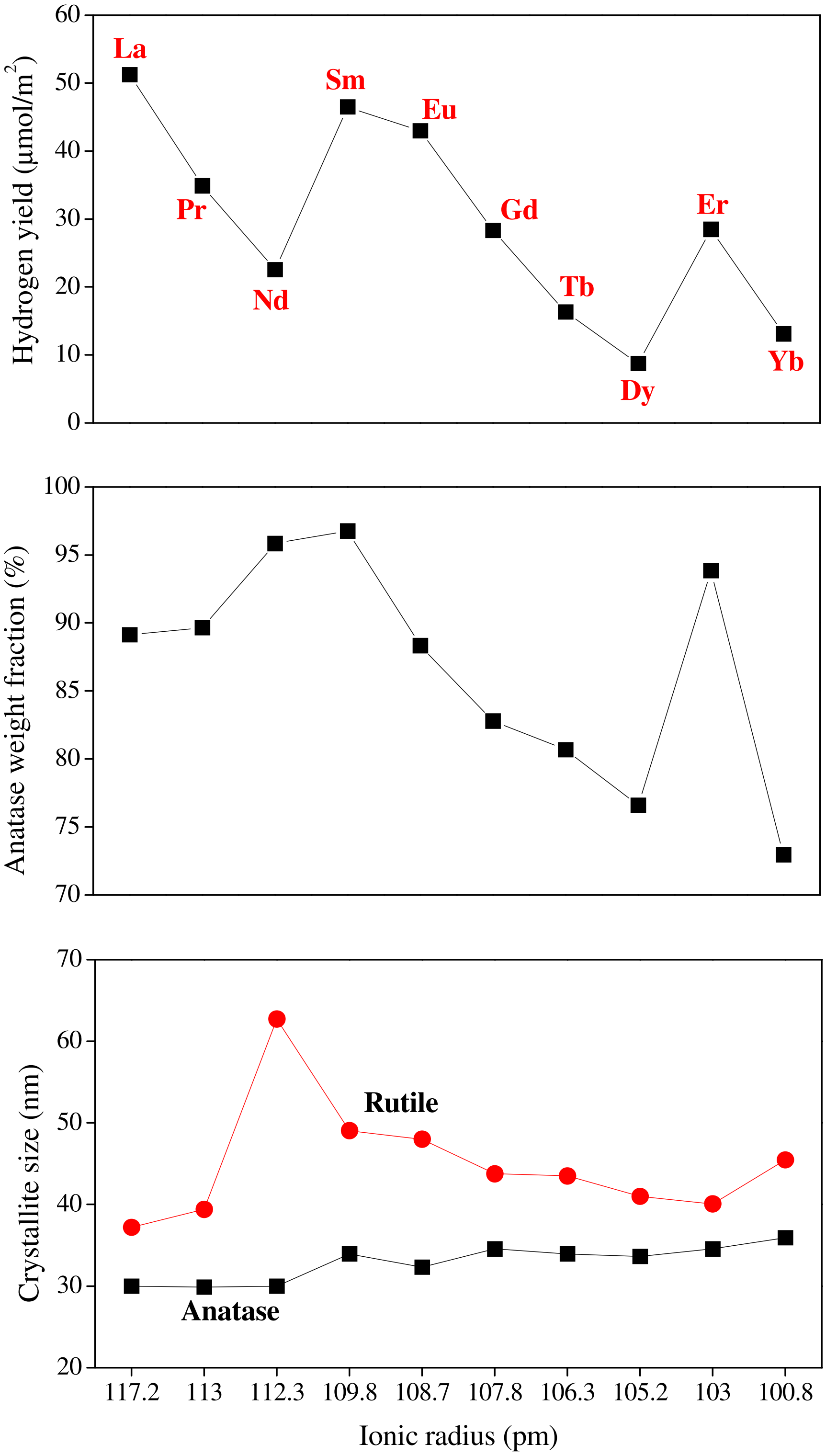

Figure 3.22. The relationship between the phase structure and the photocatalytic water splitting activities of 0.1% RE_2O_3 doped TiO_2 powders.

Photocatalytic reduction of CO_2 in the presence of water was conducted by using the same photocatalysts used in photocatalytic water splitting experiments without using Cu as co-catalyst. The gaseous products were tracked and CO was determined to be the main product of photocatalytic CO_2 reduction experiments. Lower CH_4 production compared to CO and trace amounts of H_2 evolution were also obtained with the prepared powders.

Time dependent CO production and CO yields in 6 hours (inset) with 0-5% Nd doped and 0.1% RE_2O_3 doped TiO_2 powders are given in Figures 3.23 and 3.24, respectively. CO production rates gradually decreased with time as shown in the figures. The possible reasons are the saturation of the adsorption sites by the intermediate products (Kwak et al. 2015) or the decrease of the reactant (dissolved CO_2 products: HCO^-, H_2CO_3, CO_2 (g)) concentration in the reaction medium.

CO production increased significantly with Nd doping. Lower amount of CO were produced with 0.25-5% Nd_2O_3 doped TiO_2 compared to 0.1% Nd_2O_3 doped TiO_2 powder. Highest CO production rates were obtained at low doping levels (0.1%) as obtained in the water splitting experiments. There are several reasons for obtaining higher activities at low doping levels as discussed above. The activity order is the same as water splitting activities according to the doping level and showed variation depending on the RE ionic radius. The reason for obtaining varying activities with RE ionic radius may be the different interaction of dissolved CO_2 in aqueous media. At pH 7 (0.1 M NaOH purged with CO_2) the dissolution products of CO_2 are ~80% HCO_3^- and ~20% CO_2 (Pedersen et al. 2013). According to a study conducted by Luo and Byrne (2004), the formation constants of $RE(HCO_3^-)$ and $RE(CO_3^{2-})$ are higher for REEs with smaller ionic radii. In other words, the interaction of HCO_3^- or CO_3^{2-} is stronger with smaller radii REs. The lower adsorption of these dissolved ions by TiO_2 powders doped with relatively large ionic radii REs may be compensated with the higher production rates of H_2 and e^- pairs in the water splitting reaction involved in the photocatalytic CO_2 reduction. According to the reactions given below CO_2 photoreduction is a multielectronic process which directly affects the product distribution. Formation of CO and trace amounts of H_2 indicated that independent reactions involving 2 electrons and 8 electrons forming CO (reaction 4) and CH_4 (reaction 5), respectively (Tahir and Amin 2013) are the main reactions involving C in the photocatalytic reduction of CO_2 unlike a Fisher-Tropsch mechanism (reaction 6) (Hoffman et al. 2011). The limited solubility of CO and H_2 molecules in water may restrain the further reduction to form molecules with higher carbon numbers, thus CO, CH_4 and H_2 leave the aqueous media and accumulate in the head space of the reactor.

$TiO_2 + h\nu \rightarrow \frac{1}{2} O_2 + H^+ + e^-$	(reaction 1)
$CO_2 + e^- \rightarrow CO_2^-$	(reaction 2)
$2H^+ + 2e^- \rightarrow H_2$	(reaction 3)
$CO_2 + 2H^+ + 2e^- \rightarrow CO + H_2O$	(reaction 4)
$CO_2 + 8H^+ + 8e^- \rightarrow CH_4 + 2H_2O$	(reaction 5)
$(2n + 1)H_2 + nCO \rightarrow C_nH_{(2n+2)} + nH_2O$	(reaction 6)

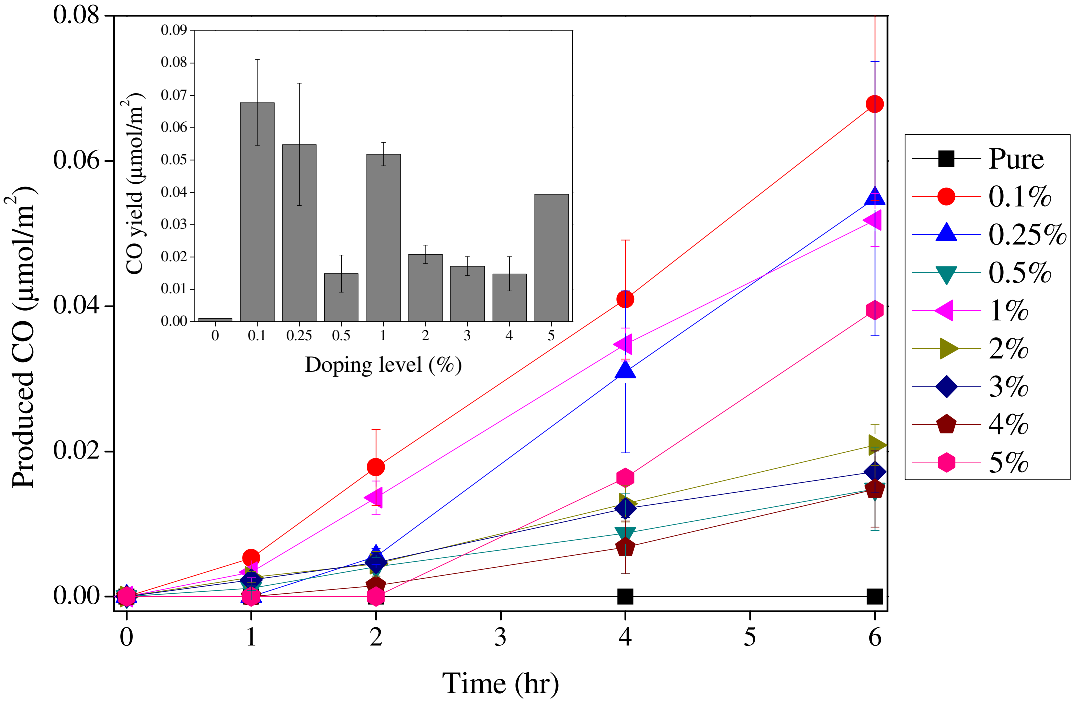

Figure 3.23. Time dependent CO production with Nd_2O_3 doped TiO_2 powders. In the inset CO yields obtained in 6 hours are given.

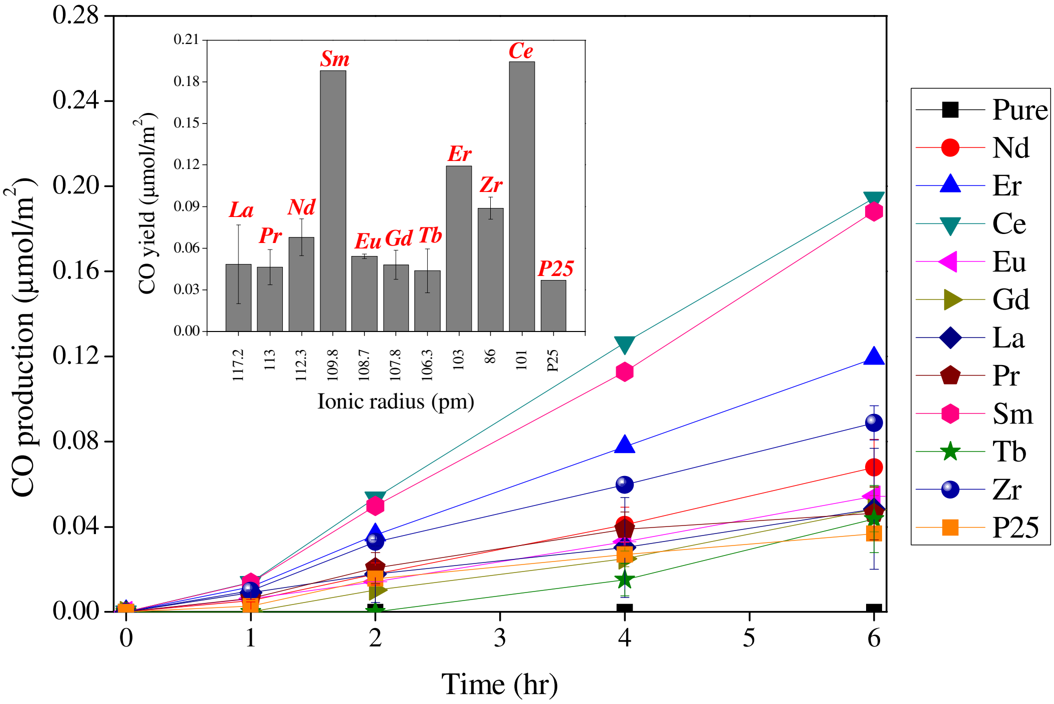

Figure 3.24. Time dependent CO production with 0.1% RE_2O_3 doped TiO_2 powders. In the inset CO yields obtained in 6 hours are given.

CH_4 and H_2 yields in 6 hours with the photocatalysts are given in Table 3.3. These gases were not observed with the photocatalytsts which were not given in the table. Methane (CH_4) and H_2 (mostly in trace amounts) formation was observed with all RE_2O_3 doped TiO_2 powders; however CH_4 was only quantifiable with the powders given in the table. The order of the magnitude of CH_4 production activities were almost the same as CO and H_2 (from the photocatalytic water splitting experiments) production activities. Highest yields of CH_4 were obtained with Sm_2O_3, CeO_2 and ZrO_2 doped TiO_2 powders with an exception of Gd_2O_3 doped TiO_2.

Table 3.3. CH_4 and H_2 yields of the powder suspensions.

Photocatalyst	**CH_4 (nanomol/m$^2_{cat}$.6h)**	**H_2 (µmol/m$^2_{cat}$.6h)**
01Nd	0.69	Trace
025Nd	0.51	Trace
05Nd	0.71	Trace
1Nd	0.14	Trace
01Er	1.9	Trace
01Gd	2.99	Trace
01Sm	4.02	Trace
01Ce	2.27	0.22
01Zr	1.09	Trace
P25	0.87	Trace

Possible reaction pathways for CO_2 photoreduction by RE_2O_3 doped TiO_2 powders are schematically given in Figure 3.25. According to the proposed mechanism simultaneous multi-electronic processes occur during the photocatalytic reduction of CO_2. Electron-hole pairs are generated when TiO_2 excited with the wavelengths no less than its bandgap energy. Generated holes react with water adsorbed on the surface of TiO_2 to produce $\cdot OH$, H^+ and O_2. H· radicals are formed by the interaction of H^+ ions with excited electrons. Union of two H^+ ions forms one H_2 molecule. Electrons interact with CO_2 molecules and HCO_3^- ions to form $\cdot CO_2^-$ radicals (Hussain et al. 2015, Sreekanth and Phani 2014). H· and $\cdot CO_2^-$ radicals react to form CO. CO may be reduced by one electron to $\cdot CO^-$. Reaction of H· radical with $\cdot CO^-$ yields ·C and OH^-. Consequtive addition of H· to ·C yields $\cdot CH_3$ radicals. Finally, CH_4 (methane) molecules are formed when $\cdot CH_3$ radicals react with H· radicals.

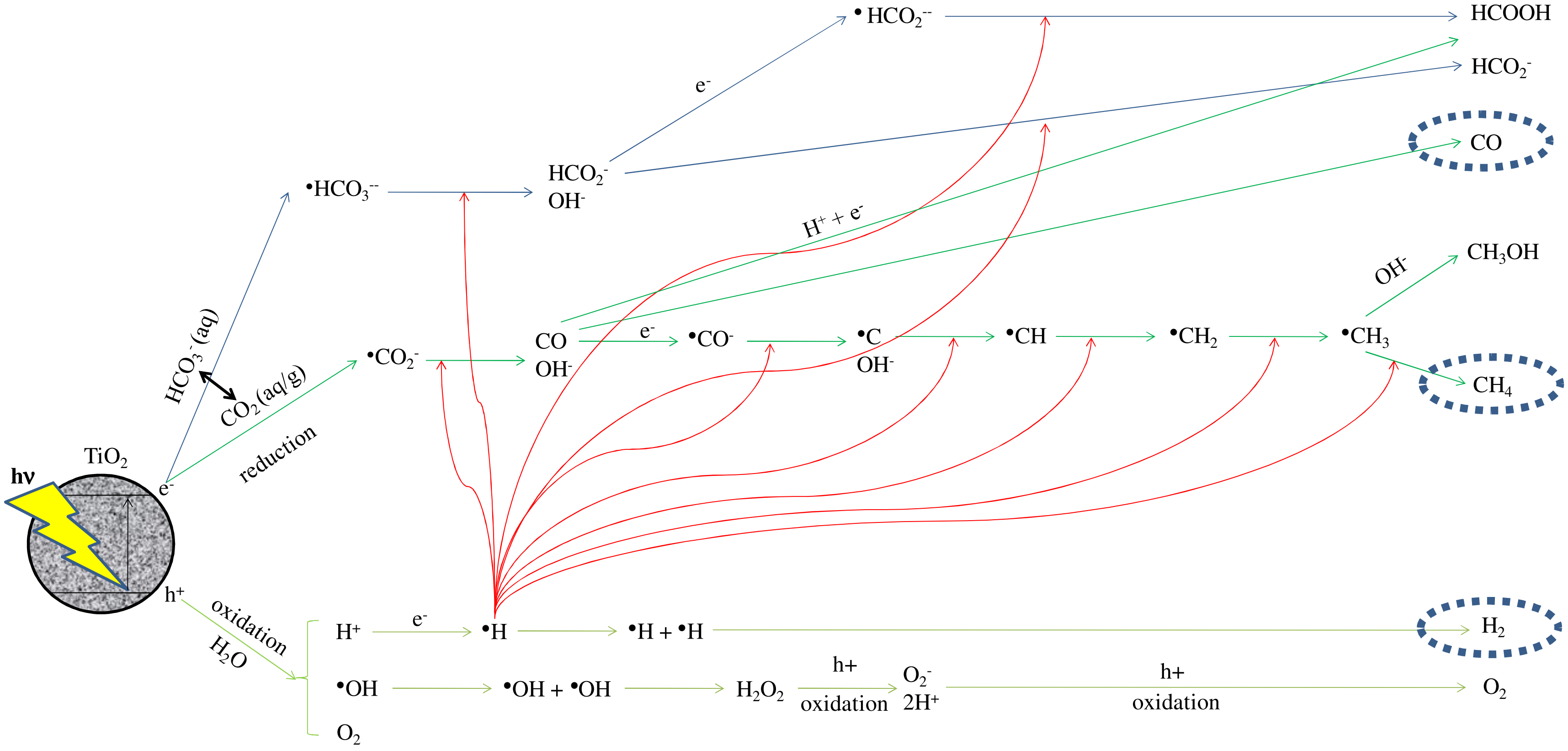

Figure 3.25. Probable reaction pathways for CO_2 photoreduction with RE_2O_3 doped TiO_2 powders.

3.4. Conclusions

In this study, RE_2O_3 doped TiO_2 powders were prepared by using sol-gel technique and their photocatalytic activities in water splitting and CO_2 reduction were investigated. XRD, XPS and UV-Vis DRS results indicated that RE ion incorporation in TiO_2 matrix significantly inhibit the AR phase transformation kinetics depending on the doping level and RE ionic size. RE_2O_3 doping was found to enhance the light absorption of TiO_2 by varying the AR ratio or absorbing photons in the visible light region due to REs' 4f-4f transition. The highest artificial photosynthesis (photocatalytic water splitting and CO_2 reduction) activities were obtained with large ionic radii REEs doped TiO_2 powders at 0.1% doping level. The obtained higher activities at low doping levels with larger ionic radii REs were attributed to the obtained optimum phase structure which has significant influence on the light absorption and charge carrier separation. RE oxides and oxygen defects formed by REE incorporation in the TiO_2 matrix was found to enhance the photocatalytic activity by forming locations where charge carrier separation was enhanced. The results of this study indicated that an optimum AR ratio which may be tuned by RE_2O_3 doping is crucial in photocatalytic water splitting and CO_2 reduction since it is known that anatase is more photoactive than rutile and rutile absorbs light more efficiently than anatase.

CHAPTER 4

THE EFFECT OF POWDER PREPARATION METHOD ON THE ARTIFICIAL PHOTOSYNTHESIS ACTIVITIES OF NEODYMIUM DOPED TITANIA POWDERS

4.1. Introduction

Research on the utilization of solar energy in order to satisfy the increasing energy demand and to decrease the “Greenhouse Effect” gained significant interest in the last couple of decades. Artificial photosynthesis is being considered as a promising technique for the synthesis of renewable, sustainable fuels like methane, methanol and hydrogen and the reduction of the global CO_2 content in the environment (Cogdell et al. 2010). Many photocatalytic materials were prepared for their use in artificial photosynthesis since the first pioneering studies conducted by Fujishima and Honda (Fujishima et al. 1972, Inoue et al. 1979).

TiO_2 based materials are mostly preferred materials for artificial photosynthesis applications towards solving environmental and energy problems by utilizing solar energy due to its chemical, optical and photocatalytic properties. Wide bandgap of TiO_2 (anatase 3.2 eV, rutile 3.0 eV) is a drawback limiting the light absorption to only UV region representing 5% of the solar radiation. There are several methods for the enhancement of photocatalytic activity of TiO_2 such as doping (Tahir and Amin 2013), combining with low bandgap materials (Ahmad Beigi et al. 2014), dye sensitization (Qin et al. 2013) or using different synthesis routes. Sol-gel, precipitation or hydrothermal methods are used to prepare highly active TiO_2 based photocatalysts (Tseng et al. 2004, Ong et al. 2013, Menendez-Flores et al. 2011).

Doped TiO_2 phases were synthesized with various methods in many studies for the use in photocatalytic water splitting in the last 15 years. A comprehensive review was conducted by Ni et al. (2007) including the mechanism of photocatalytic water splitting and TiO_2 modification methods to improve the hydrogen production activity.

Research conducted in the last 10 years showed that rare earths, such as La, Nd, Eu, Sm, Yb, Pr and Ce doped TiO_2 showed higher activities than pure TiO_2 due to their enhanced light absorption, higher surface areas and altered phase structure (Bellardita et al. 2007 and 2011, Chiou and Juang 2007, Hassan et al. 2012, Jian et al. 2010, Reszczynska et al. 2014, Romero et al. 2010, Tong et al. 2007, Wang et al. 2010, Xie and Yuan 2004, Xie et al. 2005, Xu et al. 2009, Yan et al. 2005). These studies are mostly on the environmental applications like photocatalytic degradation of dyes as probe molecules used for the simulation of polluted water.

Rare earth element incorporated titania phases were used in a few studies towards hydrogen production by water splitting (Asal et al. 2011, Puskelova 2014, Zalas and Laniecki 2005, Zhang et al. 2013) and CO_2 photoreduction related artificial photosynthesis (Liu et al. 2015, Matejova et al. 2014, Ogura et al. 1992, Wang et al. 2013, Zhao et al. 2012). Research on these materials has great importance to improve the current state of understanding.

In the present work neodymium (Nd) doped TiO_2 powders were prepared by using four different chemical routes. The effects of powder preparation method and Nd doping on the nanostructure and electronic properties of TiO_2 were investigated. The photocatalytic activities of these powders in artificial photosynthesis were determined. The observed photocatalytic activities were related to the powder properties altered by the employed preparation method and Nd doping.

4.2. Materials and Methods

4.2.1. Preparation of the Powders

TiO_2 powders were prepared by using sol-gel and chemical precipitation methods. Sol-gel TiO_2 powders were prepared by the dropwise addition of a solution (nitric acid (HNO_3, Merck 65%) and water in ethanol (Merck absolute)) to a titanium tetraisopropoxide (TTIP, Aldrich 97%)/ethanol solution under vigorous stirring at room temperature. The resulting transparent sols with the molar ratios of TTIP:H_2O:HNO_3:EtOH as 1:2:0.06:5.9 were stirred until complete gelation was observed. The obtained gels were dried at 50°C overnight prior to heat treatment at 600°C and 700°C for 3 hours. Sol-gel TiO_2 powders were coded as SG. Three different routes were used in the precipitation method. Hydrolyzed TTIP was dissolved in 2.1 M H_2SO_4 or 3.3 M HNO_3 solutions in order to prepare 0.67 M and 0.61 M Ti^{4+} solutions, respectively. These solutions were then added dropwise to an aqueous 1.2 M NH_4OH solution. The powders prepared by using H_2SO_4 or HNO_3 were coded as SP and NP, respectively. The final powder was prepared by the dropwise addition of 1.6 M TTIP/ethanol solution to a 0.65 M NH_4OH/ethanol solution and this powder was coded as AP. Powder precipitates were centrifuged, washed and dried at 70°C overnight prior to heat treatment at 600°C and 700°C for 3 hours.

Neodymium (Nd) doped TiO_2 powders were prepared with the same routes. Predetermined amount of neodymium nitrate (($Nd(NO_3)_3.5H_2O$ Aldrich 99.9% trace metal basis) was added to TTIP containing solutions in precipitation methods and to HNO_3/H_2O/Ethanol solution in sol-gel method. Powder preparation processes are schematically shown in Figure 4.1.

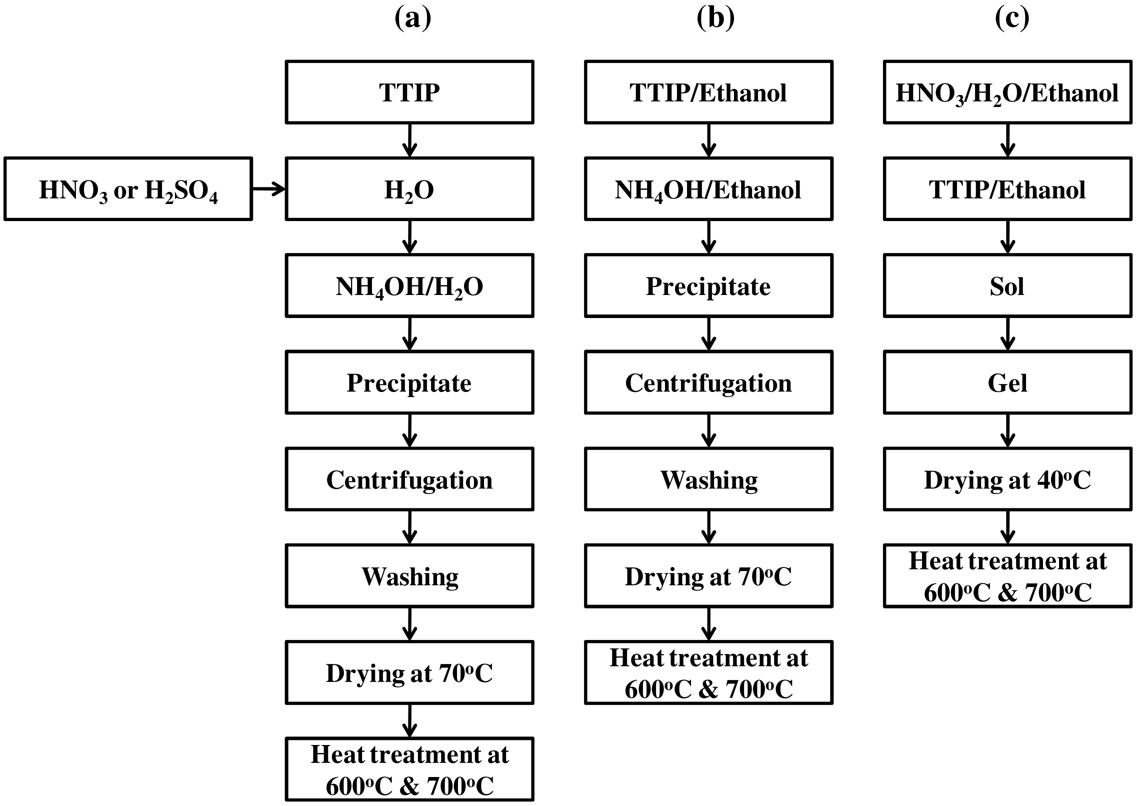

Figure 4.1. Powder preparation process flow diagrams: (a) NP and SP, (b) AP, (c) SG.

Deposition of copper on the prepared TiO_2 powders was performed by in-situ photodeposition. Copper stock solution was first prepared by dissolving copper (II) nitrate ($Cu(NO_3)_2.2.5H_2O$ Aldrich 99.9% trace metal basis) in deionized water at room temperature with a concentration of $1.5x10^{-4}$ g Cu/mL (2.4 mM Cu^{2+} ions). TiO_2 powders (0.15 g) were dispersed in water and the suspension was sonicated to break up loosely attached aggregates. Required amounts of Cu stock solution and methanol (Merck, absolute) were then added and made up to the final volume (100 mL, 25 % v/v methanol-water) and the irradiation was started. A schematic illustration of copper photodeposition process is given in Figure 4.2.

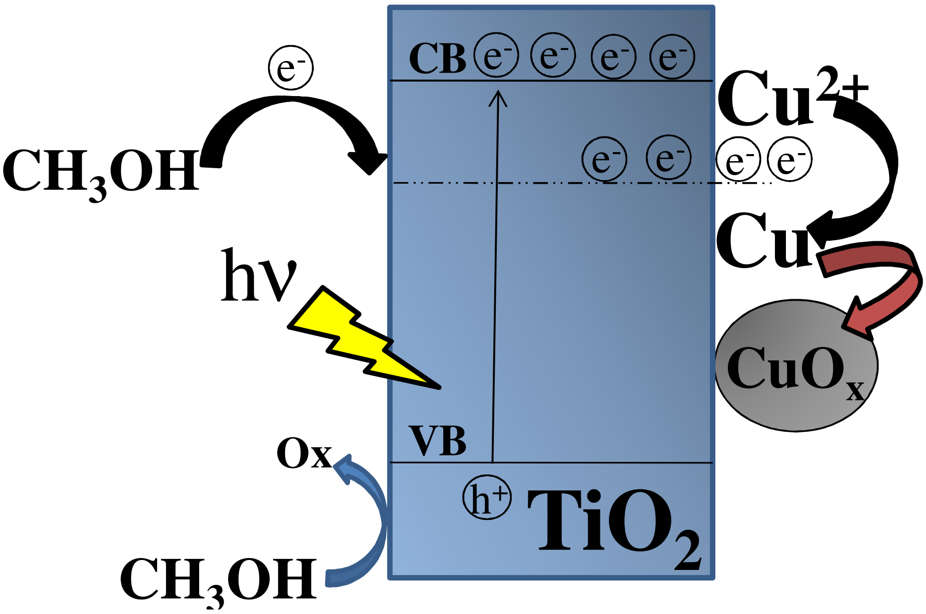

Figure 4.2. Schematic illustration of copper photodeposition on TiO_2.

4.2.2. Characterization of the Powders

Phase characterization of the prepared powders was performed on Philips X'pert Pro XRD equipment with monochromated high-intensity (λ=1.54Å) CuKα radiation. The scanning rate was set as 2.5 2Θ/min between 5^o and 80^o with 0.033^o step size. Characterization was conducted with 1-2 g powder pressed in an aluminum cassette which was also used as reference material to calculate the accurate peak positions.

The crystallite sizes were calculated from the broadening of the (101) reflection for anatase and (110) reflection for rutile using Scherrer's equation:

$$d = \frac{k.\lambda}{\beta.\cos\theta} \tag{4.1}$$

where d is the crystallite size (nm), k is the shape constant (0.9 for spherical particles), λ is the X-ray wavelength (nm), β is the full width at half maximum of the selected peak and θ is the Bragg's angle of diffraction (Sun et al. 2014).

The rutile and anatase weight fractions were determined by using the following relation:

$$x_A = \left(1 + 1.26\frac{I_R}{I_A}\right)^{-1} \tag{4.2}$$

where x_A is the anatase weight fraction, I_R and I_A are the intensities of the rutile (110) and anatase (101) peaks, respectively (Spurr and Mayers 1957).

The determination of the crystal lattice constants for tetragonal geometry (a and c) was conducted using the following expression:

$$\frac{1}{d_{hkl}^2} = \frac{h^2+k^2}{a^2} + \frac{l^2}{c^2} \tag{4.3}$$

where d_{hkl} is the interplane distance and hkl are the Miller (plane) indices. The lattice constants were determined by selecting two peaks ((101) and (200) peaks for anatase) (Tripathi et al. 2013).

Lattice strain in the TiO_2 crystal lattice was calculated by using Williamson-Hall (W-H) plot with at least 4 diffraction peaks to be used in the following relation:

$$\frac{\beta\cos\theta}{\lambda} = \frac{1}{\sigma} + \frac{\eta.\sin\theta}{\lambda} \tag{4.4}$$

where σ is the effective particle size and η is the effective strain (Tripathi et al. 2013).

X-ray photoelectron spectroscopy (XPSSPECS EA 300) was used to identify the existence and bonding states of the elements (electronic structure of the surface) in the prepared powders. Carbon C1s line at 284.8 eV was taken as a reference for the correction of the peak shifts (Kruse and Chenakin 2011). The fitting of C1s spectrum was performed by Gaussian line shape with constant background (Cappelletti et al. 2008) and fitting of O1s and Ti2p spectra were performed by pseudo-Voigt line shape with Shirley background. Peak fitting examples are given in Appendices and in the figures. Quantitative analyses for the calculation of O:Ti atomic ratios were performed by using the corresponding peak areas and the atomic sensitivity factors of S, O and Ti as 0.54, 0.66 and 1.8, respectively (Wagner et al. 1981).

Optical absorption characteristics of the prepared powders were investigated by using UV-Vis Spectrophotometer (Perkin Elmer Lamda25) equipped with DRS (Diffuse Reflectance Spectrometer) accessory. Pellets with 15mm diameter and 2-3mm thickness were prepared with uniaxial press for the optical characterization. Bandgaps of the prepared powders were determined by using Kubelka-Munk transformation for indirect bandgap (n=0.5):

$$\mathrm{F(R)} = \frac{(1-\mathrm{R})^{\mathrm{n}}}{2\mathrm{R}} \tag{4.5}$$

where R is the reflectance and F(R) is Kubelka-Munk function (Lopez et al. 2012).

Nitrogen adsorption and desorption isotherms and surface areas were obtained with a Micromeritics Gemini V.

Artificial photosynthesis products (H_2, CO, CH_4) were identified and quantified by Agilent 7820A (Gas Chromatograph-GC) equipped with a Molecular Sieve 5A column and thermal conductivity detector (TCD). He (High purity, 99.99%) carrier gas volumetric flow rate was 20 mL/min. Inlet, oven and detector temperature was 200°C, 105°C and 250°C, respectively.

4.2.3. Artificial Photosynthesis Experimental Setup

Photocatalytic water splitting and CO_2 reduction setup was constructed as shown in Figure 4.3. The setup consists of mainly 3 parts:

- High purity (99.99%) CO_2 and N_2 source.

- Pyrex glass photoreactor with N_2/CO_2 inlet and product gas outlet connecting to online GC in water splitting experiments or sealed with a rubber septum for the sampling of gaseous products evolved in CO_2 reduction experiments. Total volume of the reactor was 133 mL, liquid and gas volumes were 100 mL and 33 mL, respectively. Continuous agitation was supported by a magnetic bar and a stirrer during the photocataytic activity tests to avoid mass transfer limitations and to hold the photocatalyst particles suspended.
- GC system for tracing artificial photosynthesis products.

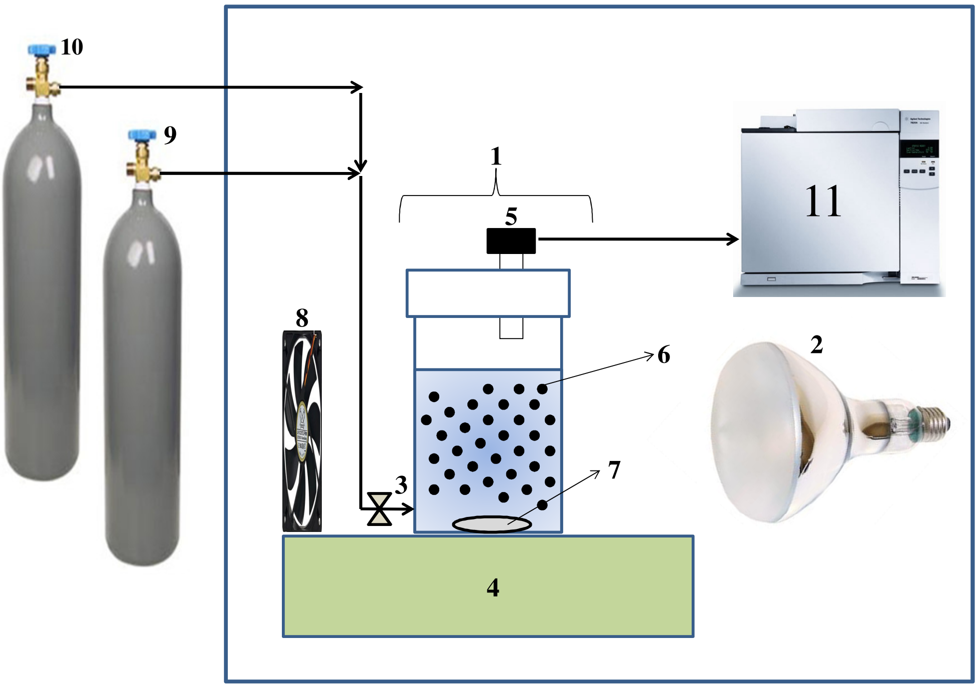

Figure 4.3. Photocatalytic water splitting/CO_2 reduction setup. 1: Photoreactor, 2: UV-Vis lamp, 3: N_2/CO_2 inlet, 4: Magnetic stirrer, 5: Gas outlet, 6: Photocatalyst particles, 7: Magnetic bar, 8: Cooling fan, 9: N_2 tube, 10: CO_2 tube, 11: Gas Chromatograph.

Photocatalytic water splitting experiments were performed in continuous (by online GC quantification) operating mode. Photocatalytic water splitting experiments were performed with in situ Cu photodeposited powders. Photocatalyst powders were dispersed in the reaction mixture which contaings 25 v.% methanol and predetermined amount of Cu^{2+} aqueous solution. N_2 was purged for 15 minutes prior to illumination in order to maintain anaerobe conditions in the reactor. Samples were taken by GC sampling valve (0.5 mL loop) every 10 minutes. Online calibration was conducted by a gaseous mixture containing H_2, CO and CH_4 (Refinery Gas Test Sample Agilent P/N 5080-8755). Online injections (four times) were performed by a sampling valve of the GC system. A sample chromatogram of the refinery gas test sample is given in Figure 4.4.

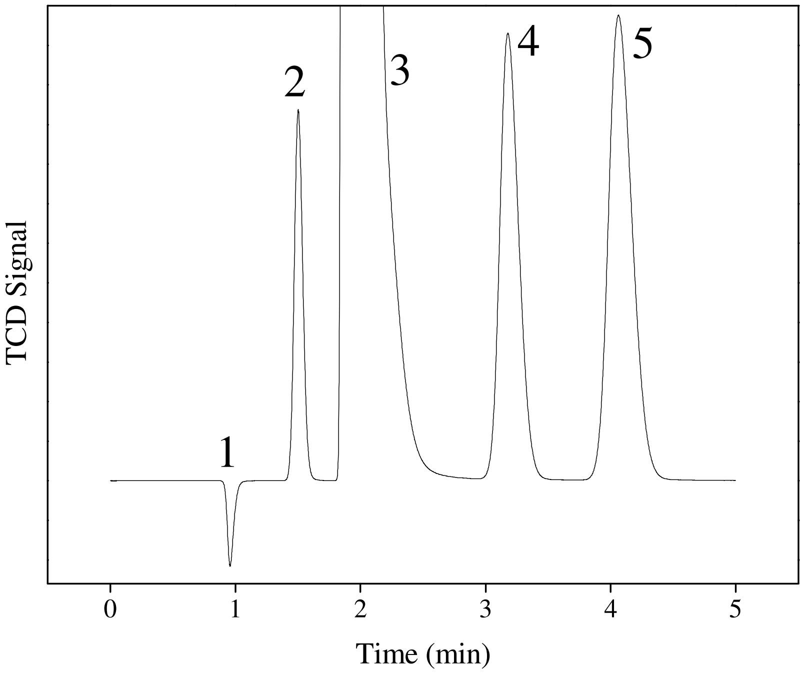

Figure 4.4. Sample chromatogram of the refinery gas test sample. Elution order: 1: H_2, 2: O_2, 3: N_2, 4: CH_4, 5: CO.

Photocatalytic CO_2 reduction experiments were performed in batch mode. Photocatalyst powders were dispersed in 0.1M NaOH to enhance CO_2 solubility in water and act as hole scavenger. CO_2 was purged for 30 minutes prior to illumination to saturate the 0.1M NaOH solution. The solution pH decreased from 12.6 to 6.9 at the end of CO_2 purge. Gas samples (Volume: 1 mL) were taken with predetermined time intervals and injected to GC system manually with a gas-tight syringe (Agilent, PN 5190-1535, 2.5 mL). The temperature inside the photoreactor was kept at ~45°C by using a cooling fan and the pressure in the headspace was 1-1.1 bar during the experiments.

Calibration curves as shown in Figures 4.5, 4.6 and 4.7 were constructed by using the refinery gas test sample to quantify the products evolved during photocatalytic CO_2 reduction. Samples with varying volumes were taken from H_2 tube, diluted with N_2

in the photoreactor (133 mL) and injected to GC for manual calibration of H_2. CO and CH_4 were calibrated by using the refinery gas test sample. CO was calibrated with two points (four repeats) and CH_4 was calibrated with one point (four repeats).

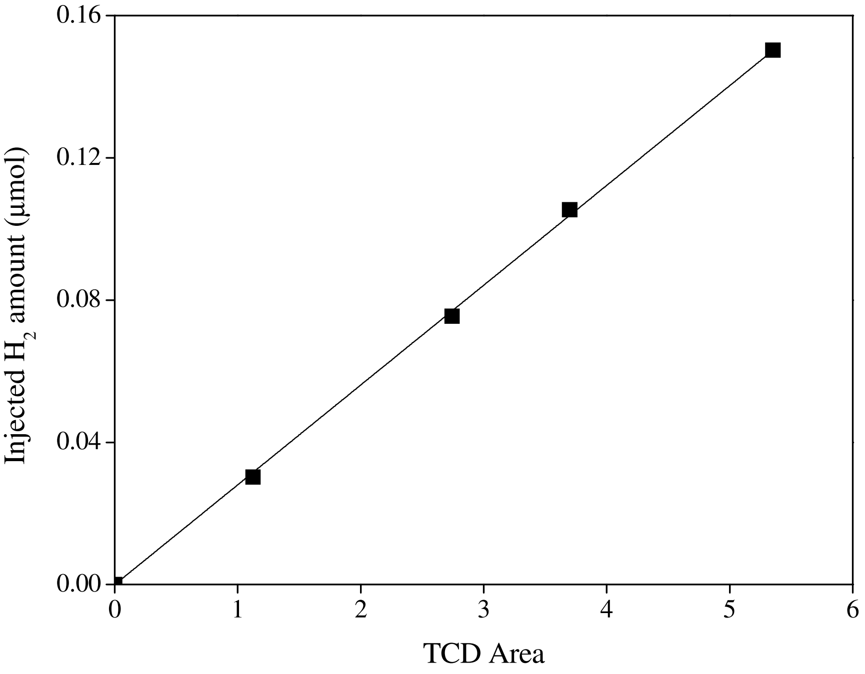

Figure 4.5. Calibration line for H_2 quantification.

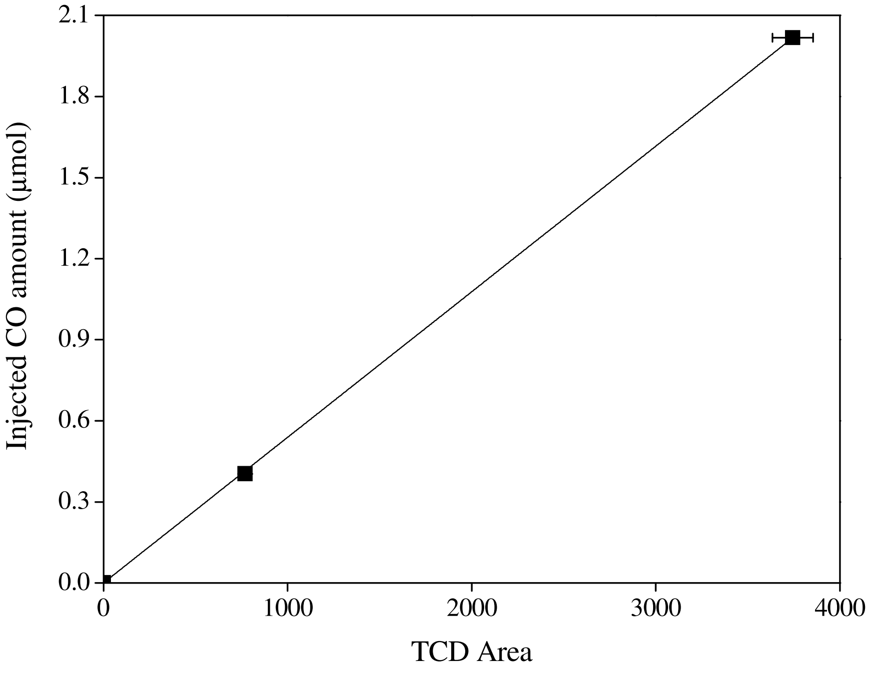

Figure 4.6. Calibration line for CO quantification.

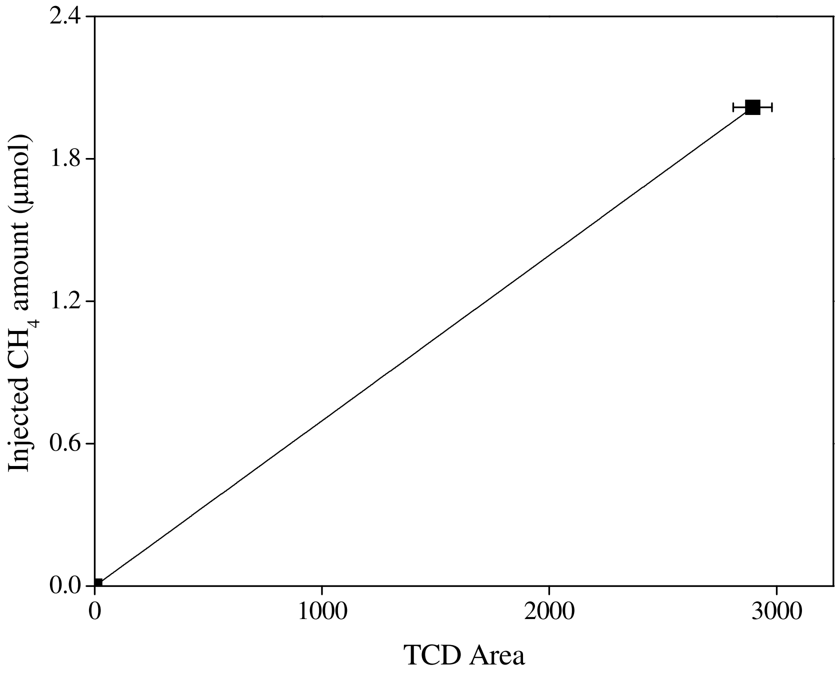

Figure 4.7. Calibration line for CH_4 quantification.

4.3. Results and Discussion

4.3.1. Characterization of the Powders

XRD patterns of pure/doped TiO_2 powders heat treated at 600°C and 700°C are given in Figures 4.8 and 4.9, respectively. The characteristic diffraction peaks of anatase (JCPDS Card #841286) were identified in the XRD patterns of all the prepared powders. Anatase phase was found to be the only phase for pure SP powder while it coexists with the rutile phase (JCPDS Card #870920) in the pure powders AP, NP and SG (in trace amounts) heat treated at 600°C. Anatase was the only phase for the doped powders heat treated at this temperature. The nanophase structure of the pure powders heat treated at 700°C was dominated by rutile with an exception of SP powder. The main phase in the doped powders heat treated at this temperature was anatase. The phase structure and physical properties such as crystallite size, rutile weight fraction, lattice constants, lattice strain and BET surface area (S_{BET}) of the powders are summarized in Table 4.1.

Anatase crystallite sizes vary between 34.1 and 17.8 nm for the pure powders heat treated at 600°C and decreased to 23.7-16.2 range with Nd doping. The crystallite sizes increased with the heat treatment temperature for both pure and doped powders. Rutile weight fraction was found to be highest for the pure NP powders at 600 and 700°C.

Anatase lattice constant c changed significantly with the preparation method and Nd doping. The lattice constant c values were calculated as the lowest for SP powders and the highest for SG powders except the doped powders heat treated at 700°C. Nd doping was determined to decrease the lattice constant c which may attributed to the formation of oxygen vacancies by the incorporation of Nd ions in the interstitials of TiO_2 lattice or segregation of these ions as separate oxide phases on the grain boundaries of TiO_2. It is difficult for Nd^{3+} ions to replace with Ti^{4+} ions in the lattice (Sibu et al. 2002) since the ionic radius of Nd^{3+} (112.3) is between that of Ti^{4+} (68 pm) and O^{2-} (132 pm).

The lower lattice constant c values obtained with NP and SP powders (except the doped powders at 700°C) were attributed to the formation of oxygen vacancies created by substitutional incorporation of N or S atoms for O and Ti atoms in the TiO_2 lattice, respectively or to significantly lower crystallite sizes compared to SG and AP powders. Substitutional incorporation may be possible since high concentrations of HNO_3 or H_2SO_4 were used during the synthesis of these powders. Nitrogen atoms most likely substituted with the lattice oxygen forming N-Ti-N bond and formed a mixed N2p state with O2p state above the valence band (Yang et al. 2010). Substitution of S with O is difficult since S^{2-} ion (0.17 nm) is relatively larger than O^{2-} ion (0.126 nm) compared to N^{3-} ion (0.132 nm). More energy is required for the formation of Ti-S bond instead of Ti-O bond; however XPS analysis revealed that Ti2p3/2 binding energy of SP powder was higher than the other powders which can be interpreted as Ti-S bonds were formed in the SP powder. The level of S substitution may be at a very low level since S^{2-} peak was not detected in XP spectrum of the SP powder. The substitution of Ti^{4+} (0.068 nm) with S^{4+} (0.037) or S^{6+} (0.029) is more favorable (Yu et al. 2005) which was also confirmed by our XPS results.

Lattice constant change also depends on the crystallite size. A decrease in crystallite size may lead to a contraction in the lattice as observed in SP. The lattice strains were determined to be highest for SP and lowest for NP (again except for the doped powders at 700°C). Lattice strain did not show a direct correlation with the crystallite size and showed variation depending on the phase composition. A negative slope in the W-H plot indicates the presence of compressive strain, while a positive slope indicates the presence of tensile strain (Maurya et al. 2011). All the prepared powders showed tensile strain; the variations are significant and can be related to the significant variation in crystallite sizes and phase compositions. Highest tensile strain was calculated for SP which has smaller crystallites and a nanophase structure dominated by anatase. However, NP, which has relatively smaller crystallite sizes, showed lower strain compared to SG and AP powders. It is well known that strain can be reduced by increasing the heat treatment temperature for ceramic materials. Excess number of disordered atoms and defects on the grain boundaries are present in the microstructure of the powders heat treated at low temperatures. These atoms and defects cause a stress field (surface strain). Increase in the heat treatment temperature causes some structural changes such as grain growth and phase change. The level of disorder and the number of defects decrease at higher temperatures. XRD patterns of NP powders showed that this powder can be stabilized at lower temperature compared to the other powders. Anatase to rutile phase transformation occurs at lower temperature and a less defective structure can be formed by NP compared to other powders.

Surface areas of the prepared powders were determined to be in the following order: SP>NP>AP>SG. Powders with higher surface areas can be prepared by precipitation method compared to sol-gel method. The reason for the higher surface area with SP powder compared to the other precipitation powders could be attributed to the presence of SO_4^{2-} ions in the nanostructure inhibiting the anatase to rutile phase transformation.

In general the change in the nanophase structure were similar for the pure and doped powders heat treated at 600°C, however at 700°C, SO_4^{2-} or NO_x ions are in tendency to leave the nanostructure due the increased heat treatment temperature. So the effect of these ions on the nanophase evolution was minimized by increasing the heat treatment temperature.

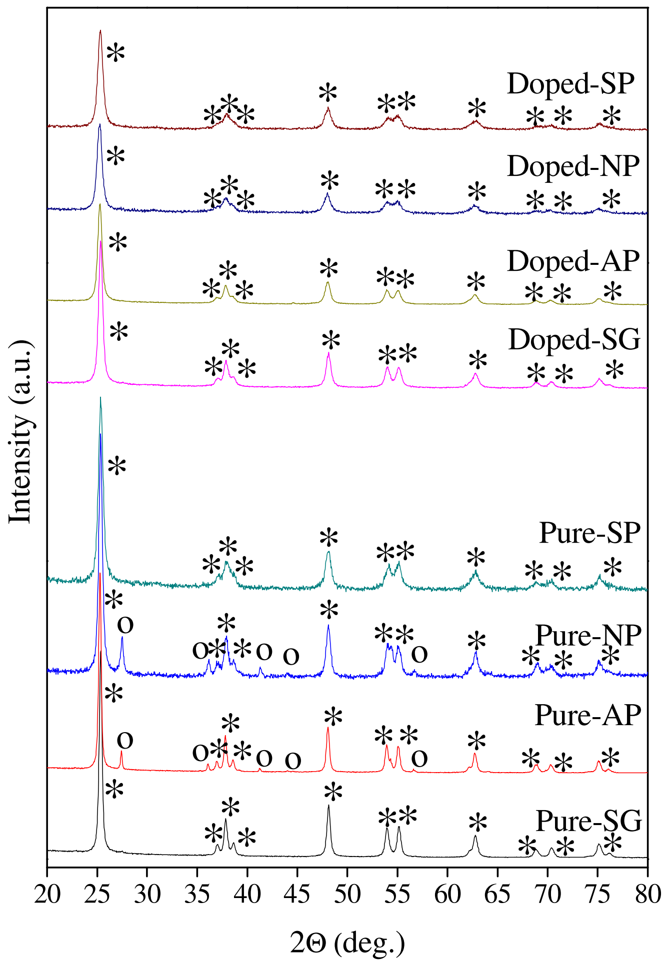

Figure 4.8. XRD patterns of pure/doped powders heat treated at 600°C (*: anatase, o: rutile).

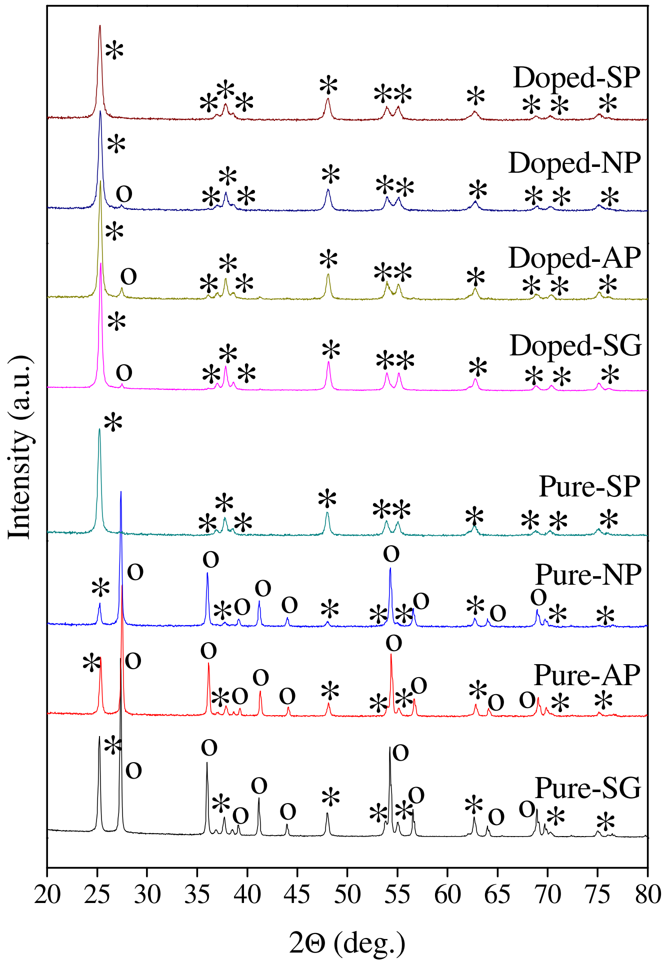

Figure 4.9. XRD patterns of pure/doped powders heat treated at 700°C (*: anatase, o: rutile).

Table 4.1. Properties of the powders.

Photocatalyst	**Anatase crystallite size (nm)**	**Rutile wt. frac. (%)**	**Anatase lattice parameters**		**Anatase lattice strain (%)**	**S_{BET} (m^2/g)**	**Zeta potential (mV)**
			a (Å)	**c (Å)**			
Pure-SG-600	29.2	0	3.78	9.58	0.57	2.5	-34.7 (±0.7)
Pure-AP-600	34.1	10.0	3.77	9.39	0.56	27.3	-31.0 (±4.1)
Pure-NP-600	22.6	15.9	3.77	9.35	0.48	54.5	-29.1 (±4.9)
Pure-SP-600	17.8	0	3.78	9.31	0.78	84.5	-35.0 (±1.2)
Doped-SG-600	23.7	0	3.78	9.45	0.53	24.6	-32.4 (±1.5)
Doped-AP-600	19.2	0	3.78	9.41	0.77	47.7	-37.3 (±9.0)
Doped-NP-600	16.3	0	3.78	9.33	0.68	88.4	-35.5 (±5.5)
Doped-SP-600	16.2	0	3.77	9.26	1.17	83.2	-26.5 (±3.9)

(cont. on next page)

Table 4.1. (cont.).

Photocatalyst	Anatase crystallite size (nm)	Rutile wt. frac. (%)	Anatase lattice parameters		Anatase lattice strain (%)	S_{BET} (m^2/g)	Zeta potential (mV)
			a (Å)	c (Å)			
Pure-SG-700	45.2	69.1	3.78	9.60	0.26	2.0	-33.7 (±3.6)
Pure-AP-700	40.8	74.7	3.77	9.42	-0.54	15.8	-35.5 (±2.1)
Pure-NP-700	37.2	89.0	3.77	9.47	N/A	14.2	-35.5 (±2.5)
Pure-SP-700	27.9	1.2	3.77	9.39	0.59	50.2	-28.6 (±2.6)
Doped-SG-700	29.2	4.2	3.77	9.38	0.56	18.9	-29.7 (±3.1)
Doped-AP-700	27.4	9.3	3.77	9.39	0.65	33.8	-31.8 (±5.0)
Doped-NP-700	23.1	3.8	3.77	9.37	0.34	55.5	-29.8 (±3.4)
Doped-SP-700	22.3	Trace	3.77	9.38	0.19	57.7	-35.0 (±2.8)

UV-Vis DR spectra of the prepared powders are given in Figures 4.10-4.13. Calculated bandgap energies were given in Table 4.2. DR spectra of NP and SP indicated absorption in the blue and green light region for pure and doped powders heat treated at 600°C. N or S doping of TiO_2 matrix may have created energy levels slightly above the valence band edge of TiO_2. This phenomenon increased the light absorption range of NP and SP powders. However visible light absorption can also be attributed to a typical absorption feature of N and S doped TiO_2 based materials arising from the electron transfer from surface states of NO_x (Di Valentin et al. 2007) or SO_4^{2-} species to the conduction band of TiO_2 (Nishikiori et al. 2013, Zhang et al. 2013). The calculated bandgaps given in Table 4.2 indicated that NP and SP powders can utilize the visible light photons. High concentrations of HNO_3 and H_2SO_4 used in the preparation media most likely caused the formation of NO_x or SO_4^{2-} species and substitutional exchange of O and Ti atoms in relatively low levels for NP and SP, respectively. The spectra of Nd doped powders showed blue shift (shift to lower wavelengths), however a blue-shift in the bandgap energy does not always signify a decrease in the visible light absorption, since there are several absorption bands in the visible region as shown in the figures. The large absorption bands at the wavelengths of 515, 529, 588, 684, 747 nm are the characteristics absorption bands of Nd^{3+} ion resulting from 4f-4f transitions

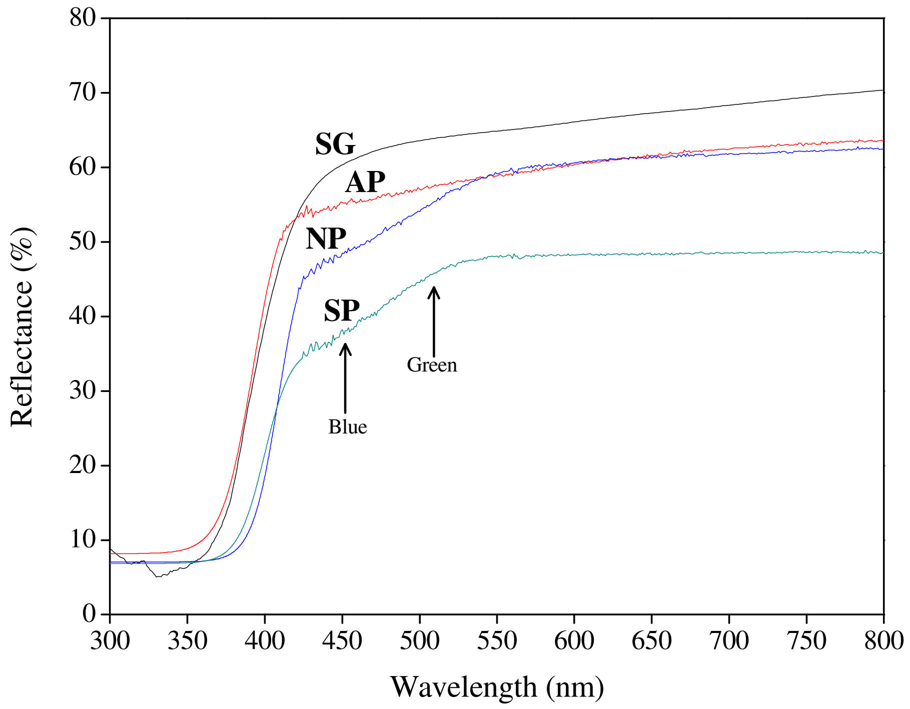

Figure 4.10. UV-Vis DR spectra of pure TiO_2 powders heat treated at 600^oC.

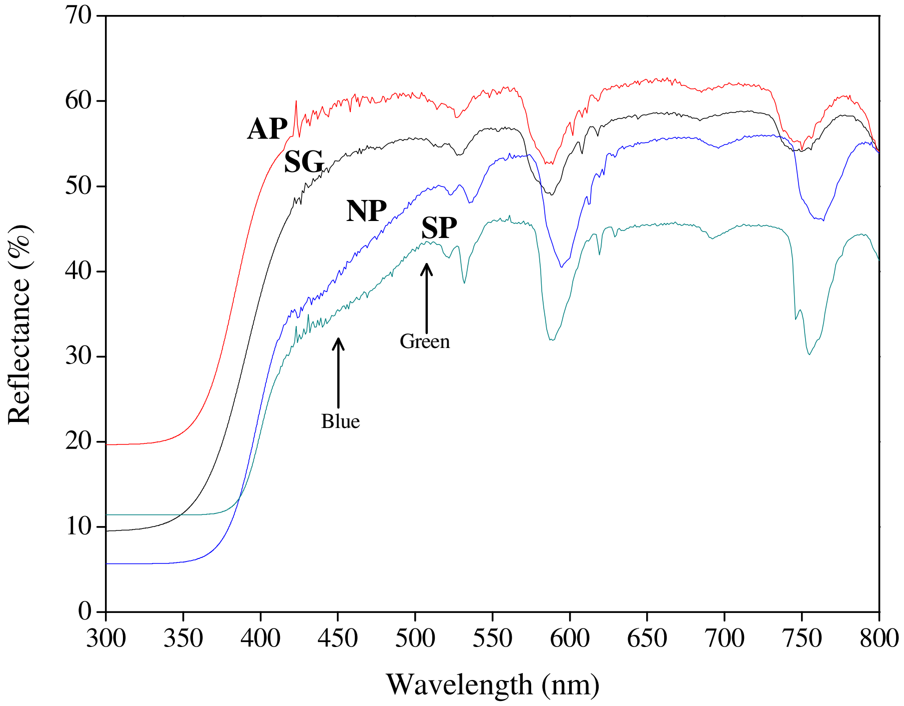

Figure 4.11. UV-Vis DR spectra of doped TiO_2 powders heat treated at 600^oC.

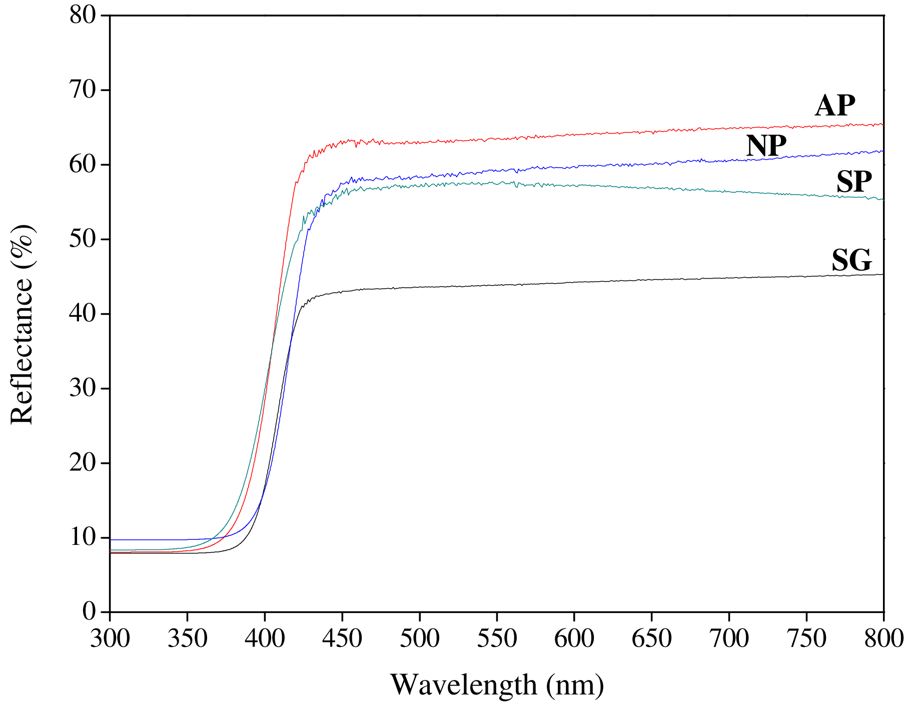

Figure 4.12. UV-Vis DR spectra of pure TiO_2 powders heat treated at 700°C.

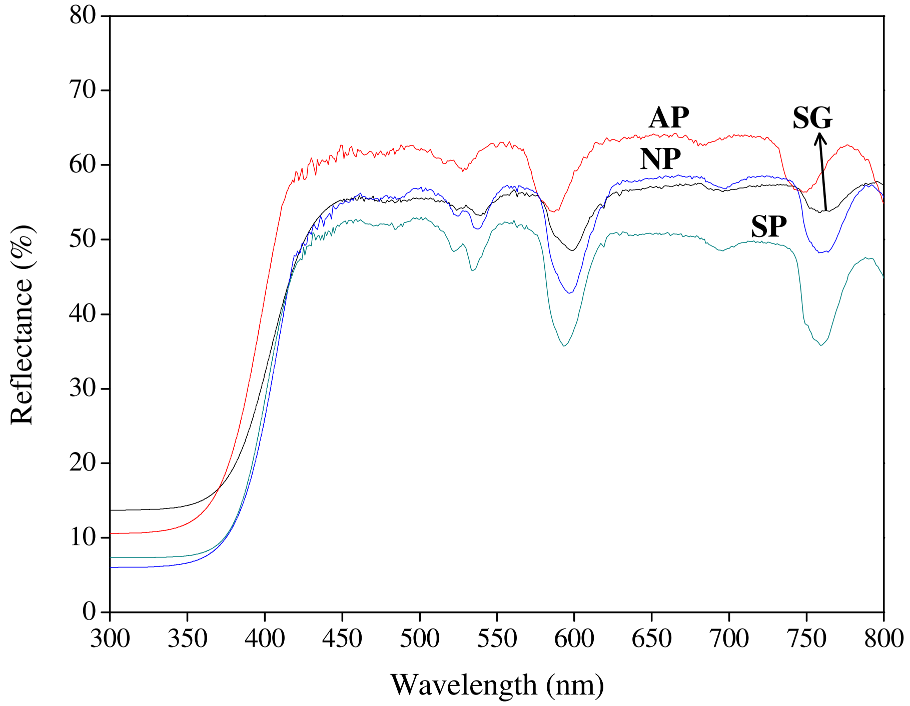

Figure 4.13. UV-Vis DR spectra of doped TiO_2 powders heat treated at 700°C.

O1s and Ti2p spectra of the powders are given in Figures 4.14-4.17 and S2p and N1s XPS speactra of SP and NP powders are given in Figure 4.18. Ti2p core level spectrum contains two main peaks of Ti2p$_{1/2}$ and Ti2p$_{3/2}$. The Ti2p$_{1/2}$ and Ti2p$_{3/2}$ spin-orbital splitting photoelectrons for all powders are located at binding energies of c.a. 465.2 and 459.3 eV, respectively. The difference between these two peaks is about 5.9 eV which showed that prepared pure and doped TiO_2 powders mostly consist of Ti^{4+} oxidation state with small contribution of Ti^{3+} which is formed due to oxygen deficiencies in TiO_2 lattice. O1s peak appearing at 529 eV is attributed to the signal of oxygen in TiO_2 lattice. Shoulder appearing at 531.5 eV is the signal of Ti-OH or C-OH. S2p peak position at 169 eV was attributed to S^{6+}. This peak can be assigned to the presence of SO_4^{2-} ions originating from H_2SO_4. The intensity of this peak increased with Nd doping and decreased with increasing heat treatment temperature which may indicate that Nd doping may increase the binding of Ti with S and sulfated TiO_2 may be easily prepared by using Nd as the dopant. The decrease in the intensity of this peak at 700^{o}C may be attributed to SO_4^{2-} ions' leaving the nanostructure.

The results indicated that substitution of sulfur and oxygen atoms might have occurred at low levels due to the absence of S^{2-} binding energy at 163 eV (Nishikiori et al. 2013, Yan et al. 2011). SO_4^{2-} ions mostly locate on the grain boundaries restraining the growth of anatase crystallites. N1s spectra of the NP powders indicated that molecularly chemisorbed and interstitial N atoms may be present in the nanostructure of these powders according to the presence of the peak at ~400 eV (Peng et al. 2008). The peak appearing around 396-397.5 eV attributed to Ti-N bond for the pure NP powder heat treated at 700^{o}C indicated a possible N substitution in the TiO_2 lattice which was absent in the other powders.

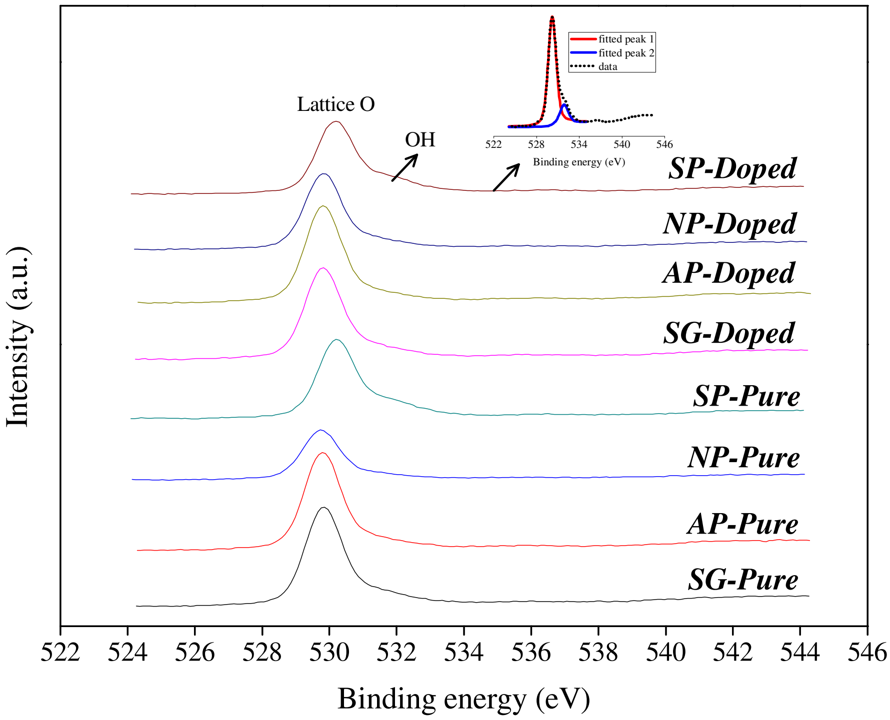

Figure 4.14. O1s XPS spectra of pure/doped TiO_2 powders heat treated at 600^oC.

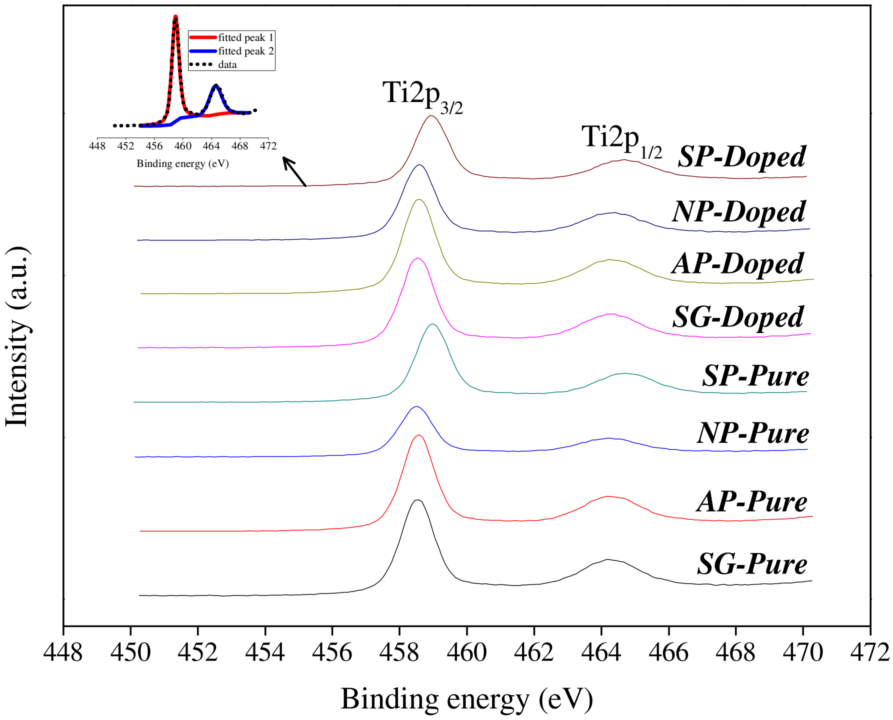

Figure 4.15. Ti2p XPS spectra of pure/doped TiO_2 powders heat treated at 600^oC.

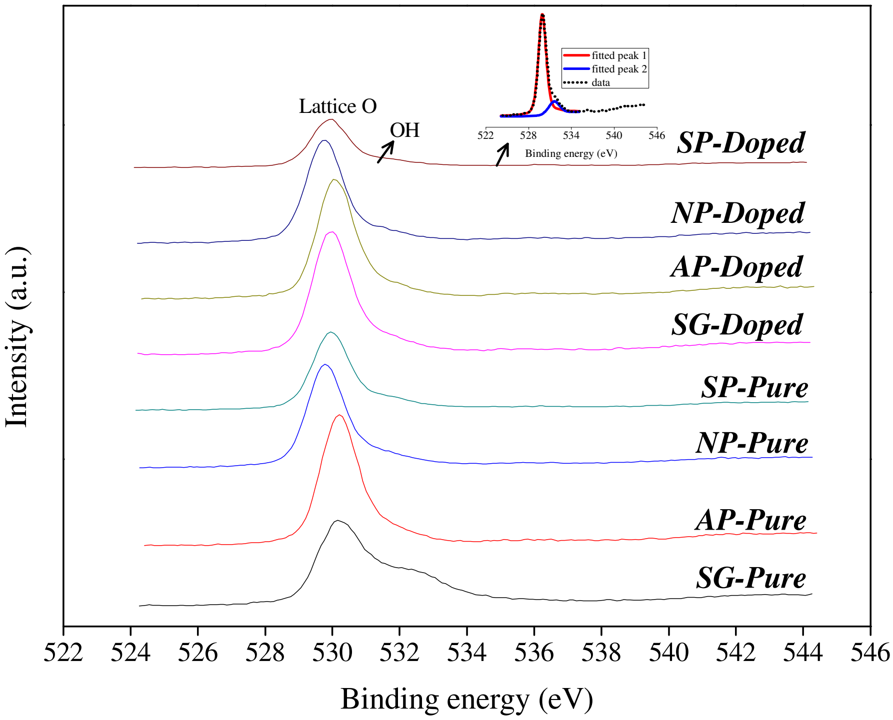

Figure 4.16. O1s XPS spectra of pure/doped TiO_2 powders heat treated at 700°C.

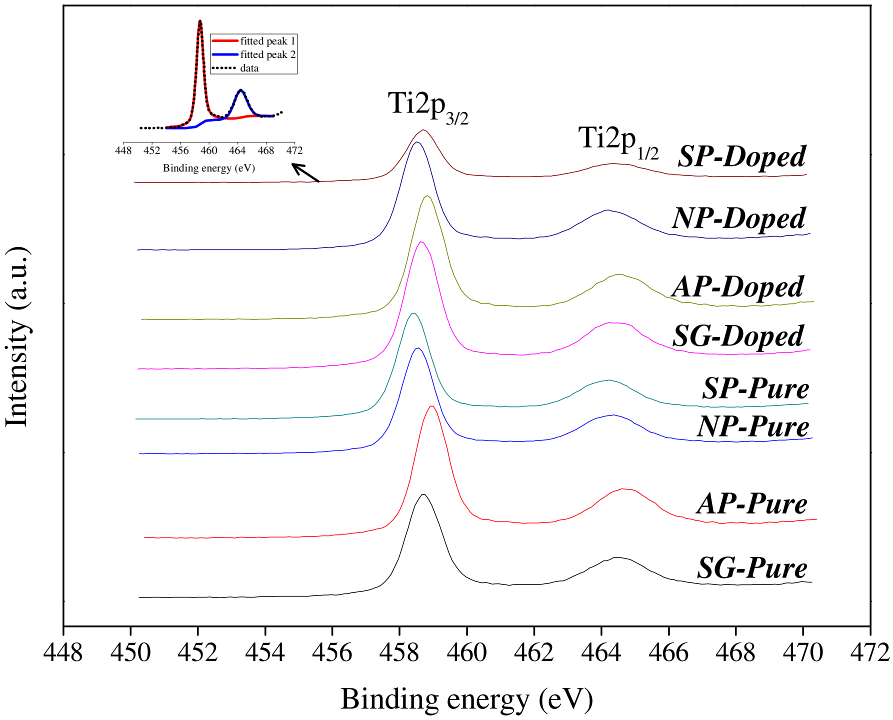

Figure 4.17. Ti2p XPS spectra of pure/doped TiO_2 powders heat treated at 700°C.

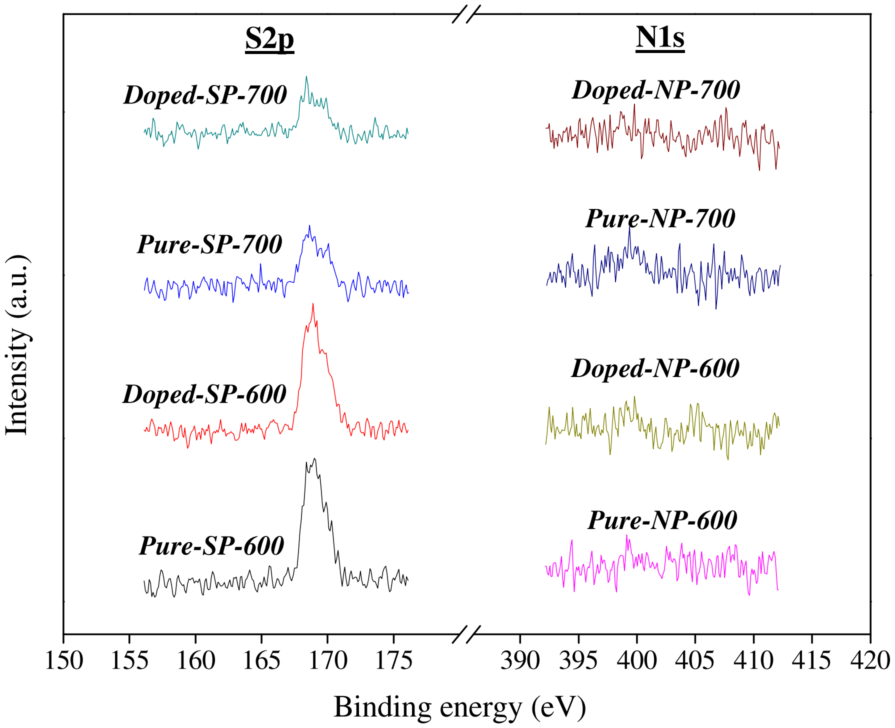

Figure 4.18. S2p/N1s XPS spectra of SP/NP powders.

Binding energies of Ti2$p_{3/2}$ of pure and doped TiO_2 powders heat treated at 600°C and 700°C are given in Figure 4.19. SP powders heat treated at 600°C possessed higher binding energies due to a possible Ti-S bonding. Substitution of S with O is difficult since S^{2-} ion (170 pm) is relatively larger than O^{2-} ion (126 pm) compared to N^{3-} ion (132 pm). More energy is required for the formation of Ti-S bond instead of Ti-O bond; however XPS analysis revealed that Ti2p3/2 binding energy of SP powders at 600°C were higher than the other powders which may be interpreted as Ti-S bonds were formed in the SP powder. The level of S substitution may be at a very low level since S^{2-} peak was not detected in the XP spectra of the SP powders. The substitution of Ti^{4+} (68 pm) with S^{4+} (37 pm) or S^{6+} (29 pm) is more favorable (Yu et al. 2005) which was also confirmed by our XPS results. The lower binding energies of NP and SP powders heat treated at 700°C indicated the presence of a more oxygen defective structure for NP and SP compared to AP which may be due to the presence of substitutional N or S atoms in the TiO_2 lattice. Nd doping caused a decrease in the Ti2$p_{3/2}$ binding energies which may be due to the presence of increased oxygen defects compared to the pure TiO_2 powders. Some electronic properties such as O:Ti and S:Ti ratios derived from XPS and bandgap energies estimated from UV-Vis DR spectra of the powders are given in Table 4.2. The results indicated that most of the powders are oxygen deficient according to O:Ti ratios and the level of deficiency was increased with Nd doping at 700°C. The calculated S:Ti ratios indicated that the level of S content increased with Nd doping for both heat treatment temperatures which may due to the affinity of rare earth ions to sulfate ion. The table also indicated that S content decreased with increasing heat treatment temperature.

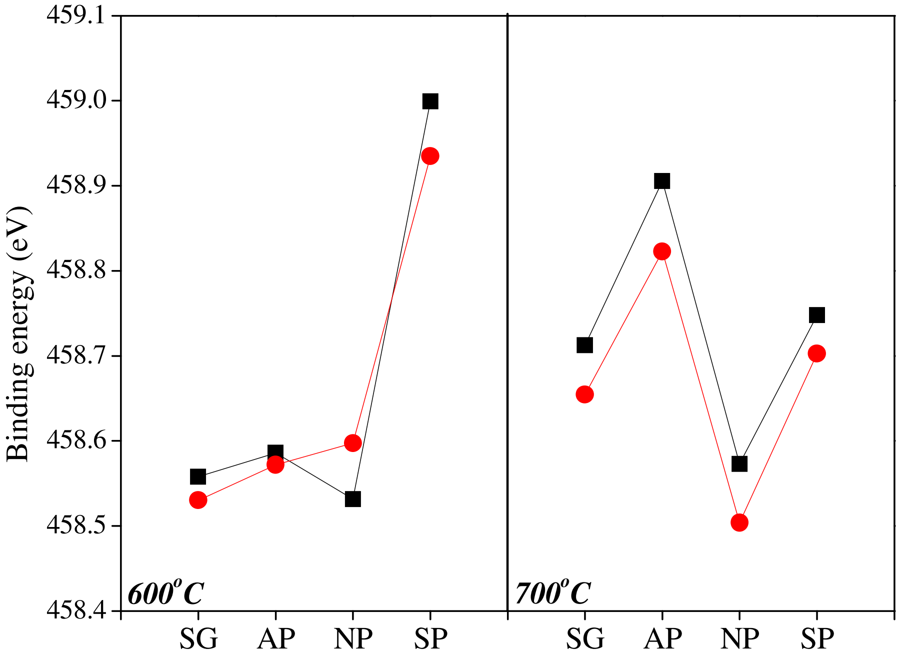

Figure 4.19. Binding energies of Ti2$p_{3/2}$ of pure/doped TiO_2 powders: (■) pure, (●) doped.

Table 4.2. Electronic properties of the powders.

Photocatalyst	**O:Ti ratio**	**S:Ti ratio**	**Direct / Indirect bandgap energy (eV)**
Pure-SG-600	1.82	-	3.28 / 3.07
Pure-AP-600	1.99	-	3.26 / 3.05
Pure-NP-600	1.90	-	3.10 / 2.93
Pure-SP-600	1.92	0.035	3.15 / 2.93
Doped-SG-600	1.98	-	3.28 / 2.90
Doped-AP-600	1.99	-	3.24 / 2.93
Doped-NP-600	2.04	-	3.19 / 2.94
Doped-SP-600	1.98	0.101	3.08 / 2.83
Pure-SG-700	1.79	-	3.08 / 2.89
Pure-AP-700	2.12	-	3.15 / 2.94
Pure-NP-700	2.07	-	3.04 / 2.86
Pure-SP-700	1.94	0.044	3.17 / 2.92
Doped-SG-700	2.28	-	3.13 / 2.81
Doped-AP-700	1.91	-	3.23 / 2.93
Doped-NP-700	2.05	-	3.19 / 2.90
Doped-SP-700	2.11	0.052	3.17 / 2.94
Degussa	2.04	-	3.14 / 2.94

4.3.2. Photocatalytic Activities of the Powders

Time dependent hydrogen production, CO/H_2 ratios and hydrogen yields obtained in 2 hours with in situ copper photodeposited pure and TiO_2 powders prepared by using different methods are given in Figures 4.20-4.23. Hydrogen productions and yields with the prepared photocatalysts were given per unit surface area basis to investigate the effect of Nd doping and preparation method on the surface reactivity. At the first stages of photocatalytic water splitting, hydrogen producion rates are low for all the powders since in situ Cu photodeposition takes place during this period. H_2 develops in the head space of the photoreactor after a while and continues to evolve linearly after a certain time.

According to the Figures 4.20 and 4.21 the highest activities were obtained with NP powders heat treated at 600°C. The activities increased with Nd doping for SG and AP powders. The lowest CO/H_2 ratios were obtained with the doped powders. A possible reason is the increased electron-hole separation rates by the anatase-rutile junctions defined by the phase structure or TiO_2-Nd junctions for the doped powders. Anatase-rutile ratio is crucial in photocatalysis since anatase is more active and light absorption of rutile is better than that of anatase.

The highest activity was obtained with pure AP powder heat treated at 700°C and activities increased with Nd doping for NP and SG powders according to the Figures 4.22 and 4.23. The lowest CO/H_2 ratios were obtained again with the doped powders.

Phase structure may be considered to be the main reason for obtaining higher activities with pure NP powder heat treated at 600°C and pure AP powder heat treated at 700°C. XRD analyses indicated that these powders possessed higher crystallite sizes and rutile weight fractions. A developed crystalline structure and nanophase composition may very important for the separation of charge carriers and light absorption. Pure AP powder heat treated at 700°C does not have blue and green light absorption bands, however the light absorption capacity may have increased due to the presence of rutile at a higher weight fraction compared to the other powders.

CO/H_2 ratio is also an important parameter in the photocatalytic production of H_2. CO is formed by the decomposition of formic acid derived from methanol which may poison the catalyst and decrease the photocatalytic activity, so minimum amount of CO production is desired to have high photocatalytic activities and to produce high purity hydrogen (Wu 2008). The highest CO/H_2 ratios were obtained with the powders possessing the highest H_2 production activities. The presence of lower anatase content in these powders may have decreased the oxidation rate of CO to CO_2 or the production of H_2 and CO_2 may be increased compared to the production of H_2 and CO.

The obtained high CO/H_2 ratios with the powders possessing the highest H_2 production activities may limit their use in the photocatalytic water splitting applications since producing high purity H_2 may be more important than producing H_2 in higher quantities. Separation costs may be crucial. Hence an optimum H_2 production rate with low CO/H_2 ratio may be chosen as a design criterion in the production of sustainable and clean energy. In this respect doped NP powders heat treated at 600° or 700°C are more considerable.

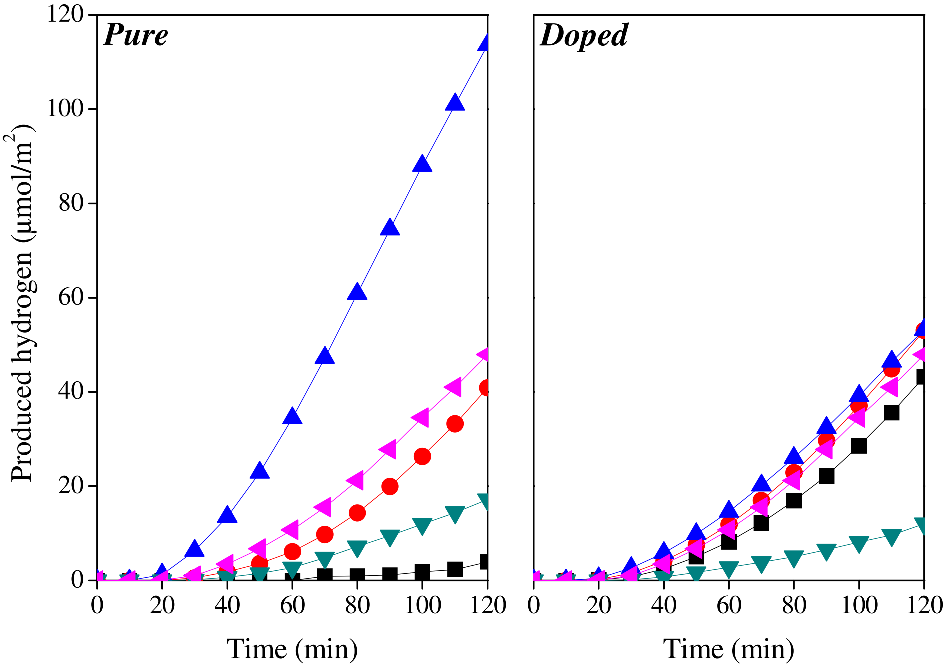

Figure 4.20. Time dependent hydrogen production with in situ Cu photodeposited pure/doped TiO_2 powders heat treated at 600°C: (■) SG, (●) AP, (▲) NP, (▼) SP, (◀) P25.

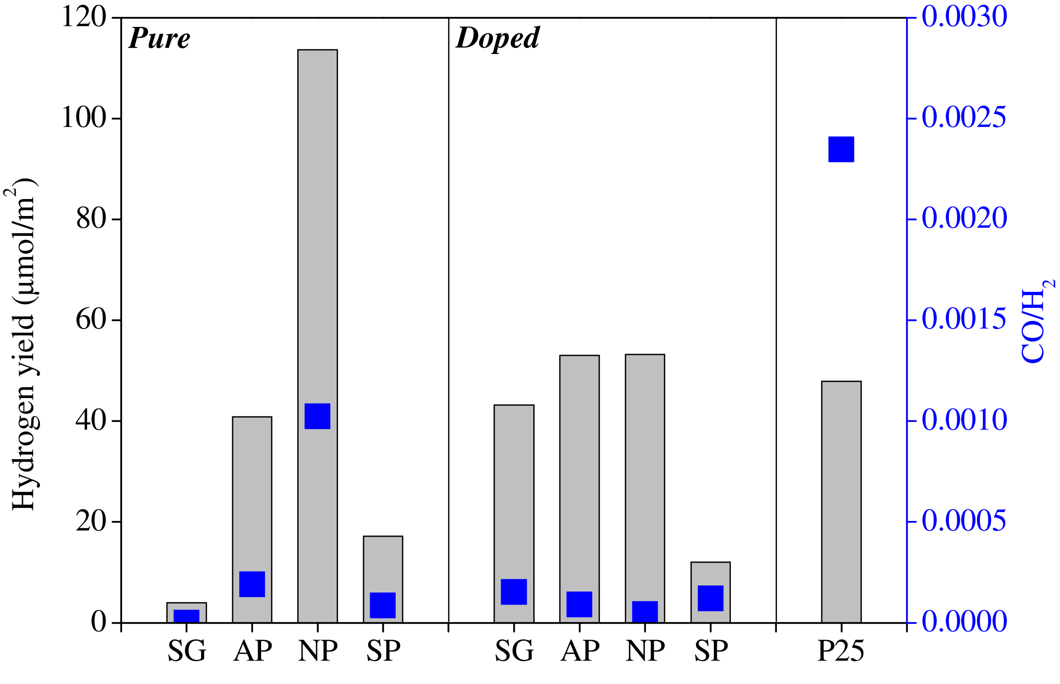

Figure 4.21. Hydrogen yields and CO/H_2 ratios obtained in 2 hours with in situ Cu photodeposited pure/doped TiO_2 powders heat treated at 600°C.

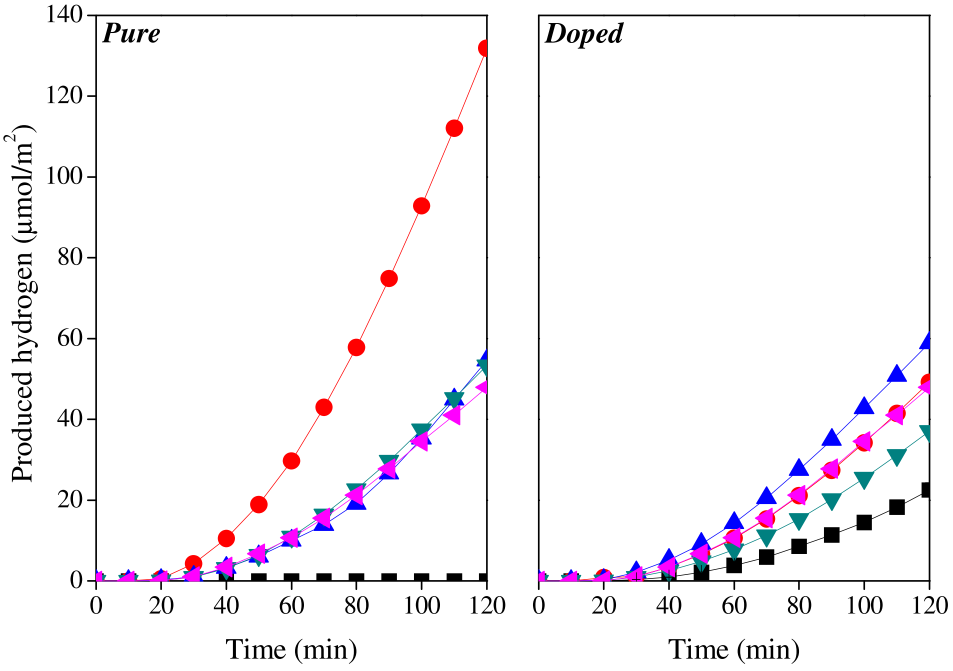

Figure 4.22. Time dependent hydrogen production with in situ Cu photodeposited pure/doped TiO_2 powders heat treated at 700°C: (■) SG, (●) AP, (▲) NP, (▼) SP, (◀) P25.

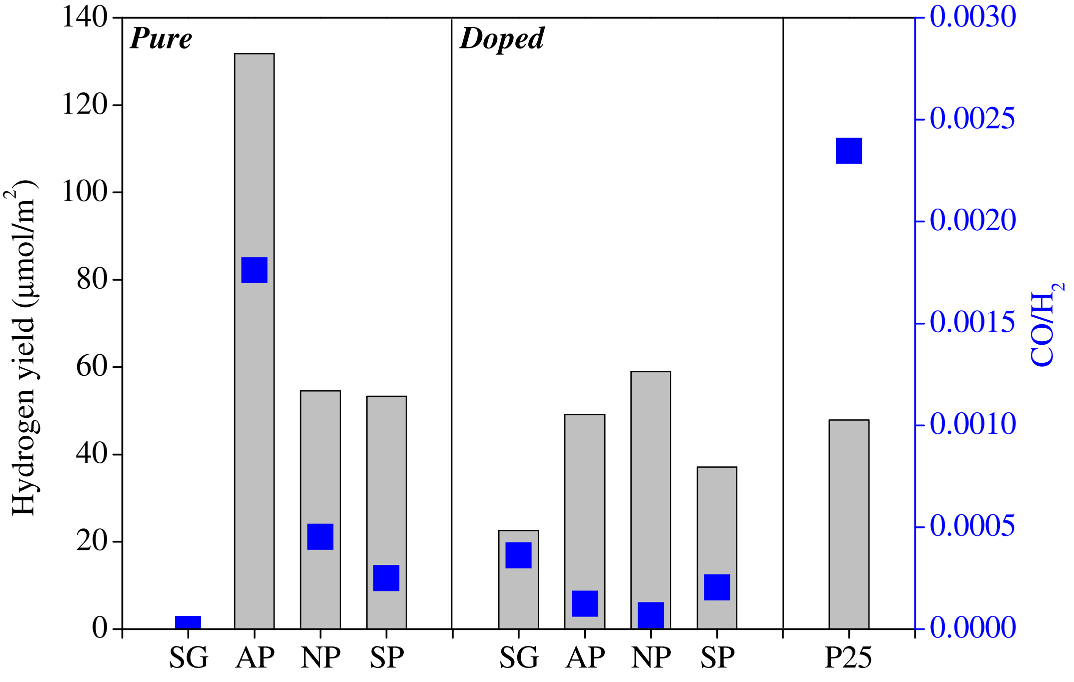

Figure 4.23. Hydrogen yields and CO/H_2 ratios obtained in 2 hours with in situ Cu photodeposited pure/doped TiO_2 powders heat treated at 700°C.

Photocatalytic reduction of CO_2 in the presence of water was conducted by using the same photocatalysts used in photocatalytic water splitting experiments without using Cu as co-catalyst. The gaseous products were tracked and CO was determined to be the main product of photocatalytic CO_2 reduction experiments. Lower CH_4 production amounts compared to CO and trace amounts of H_2 evolution were also obtained with the prepared powders. Photocatalytic CO_2 reduction activities of pure and doped TiO_2 powders heat treated at 600^oC and 700^oC are given in Figure 4.24 and Table 4.3.

CO yields were found to be the highest for pure SG and NP powders heat treated at 600^oC and 700^oC, respectively. It was found that the produced CO amounts generally decreased with Nd doping in per unit area basis and increased in per amount of the powder basis. The increase in the surface area with Nd doping may be the main reason for the increased CO production amounts. At pH 7 (0.1 M NaOH purged with CO_2) the dissolution products of CO_2 are ~80% HCO_3^- and ~20% CO_2 (Pedersen et al. 2013). The interaction of HCO_3^- or CO_3^{2-} with TiO_2 surface may have increased with Nd doping due to the surface area increase. CH_4 and H_2 production were also found to be the highest for the same powders. This may indicate that independent reactions involving 2 electrons and 8 electrons forming CO (reaction 4) and CH_4 (reaction 5), respectively (Tahir and Amin 2013) are the main reactions involving C in the photocatalytic reduction of CO_2 unlike a Fisher-Tropsch mechanism (reaction 6) (Hoffman et al. 2011). The limited solubility of CO and H_2 molecules in water may restrain the further reduction to form molecules with higher carbon numbers, thus CO, CH_4 and H_2 leave the aqueous media and accumulate in the head space of the reactor.

$TiO_2 + h\nu \rightarrow \frac{1}{2} O_2 + H^+ + e^-$ (reaction 1)
$CO_2 + e^- \rightarrow CO_2^-$ (reaction 2)
$2H^+ + 2e^- \rightarrow H_2$ (reaction 3)
$CO_2 + 2H^+ + 2e^- \rightarrow CO + H_2O$ (reaction 4)
$CO_2 + 8H^+ + 8e^- \rightarrow CH_4 + 2H_2O$ (reaction 5)
$(2n+1)H_2 + nCO \rightarrow C_nH_{(2n+2)} + nH_2O$ (reaction 6)

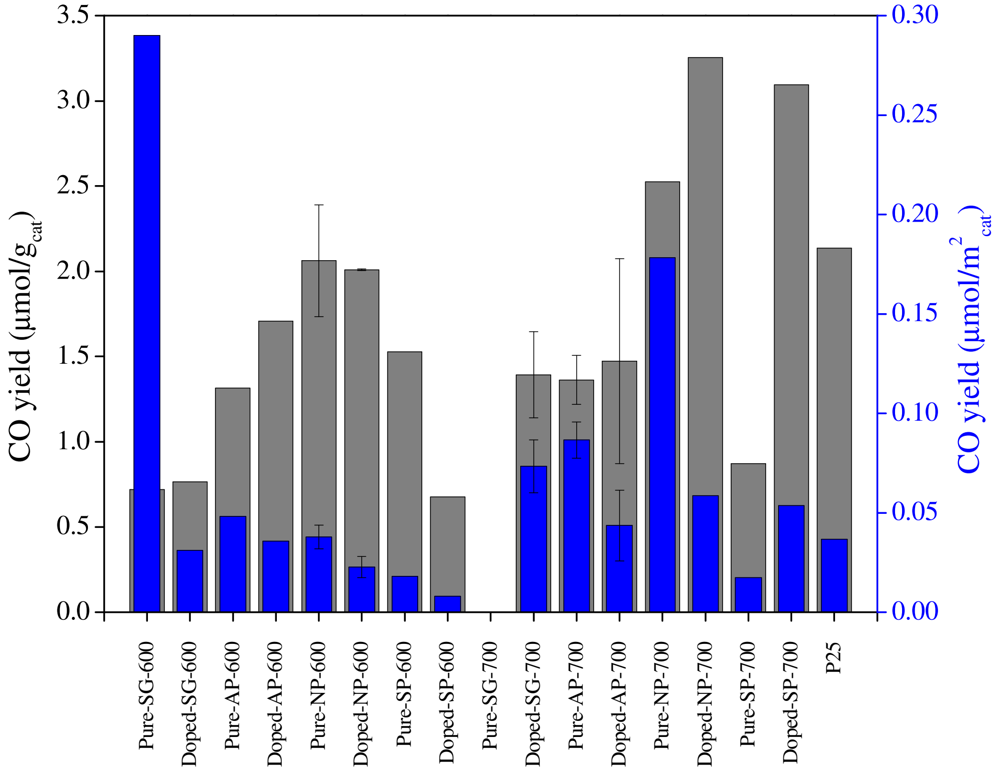

Figure 4.24. CO yields obtained in 6 hours with pure/doped TiO_2 powders heat treated at 600°C and 700°C.

Table 4.3. CH_4 and H_2 yields of the powder suspensions.

Photocatalyst	**CH_4 (nanomol/m^2_{cat}.6h)**	**H_2 (μmol/m^2_{cat}.6h)**
Pure-SG-600	11.09	0
Pure-AP-600	trace	trace
Pure-NP-600	0.15	0.05
Pure-SP-600	0	trace
Doped-SG-600	1.03	trace
Doped-AP-600	trace	0.07
Doped-NP-600	0.29	trace
Doped-SP-600	0	trace
Pure-SG-700	0	0
Pure-AP-700	1.02	trace
Pure-NP-700	21.91	trace
Pure-SP-700	1.12	0.04
Doped-SG-700	0.69	trace
Doped-AP-700	1.16	trace
Doped-NP-700	1.45	0.05
Doped-SP-700	0.69	0.11
Degussa	0.87	Trace

Probable reaction pathways for CO_2 photoreduction by pure/doped doped TiO_2 powders are schematically given in Figure 4.25. According to the proposed mechanism simultaneous multi-electronic processes occur during the photocatalytic reduction of CO_2. Electron-hole pairs are generated when TiO_2 excited with the wavelengths no less than its bandgap energy. Generated holes react with water adsorbed on the surface of TiO_2 to produce ·OH, H^+ and O_2. H· radicals are formed by the interaction of H^+ ions with excited electrons. Union of two H^+ ions forms one H_2 molecule. Electrons interact with CO_2 molecules and HCO_3^- ions to form $\cdot CO_2^-$ radicals (Hussain et al. 2015, Sreekanth and Phani 2014). H· and $\cdot CO_2^-$ radicals react to form CO. CO may be reduced by one electron to $\cdot CO^-$. Reaction of H· radical with $\cdot CO^-$ yields ·C and OH^-. Consequtive addition of H· to ·C yields $\cdot CH_3$ radicals. Finally, CH_4 (methane) or CH_3OH (methanol) molecules are formed when $\cdot CH_3$ radicals react with H· radicals.

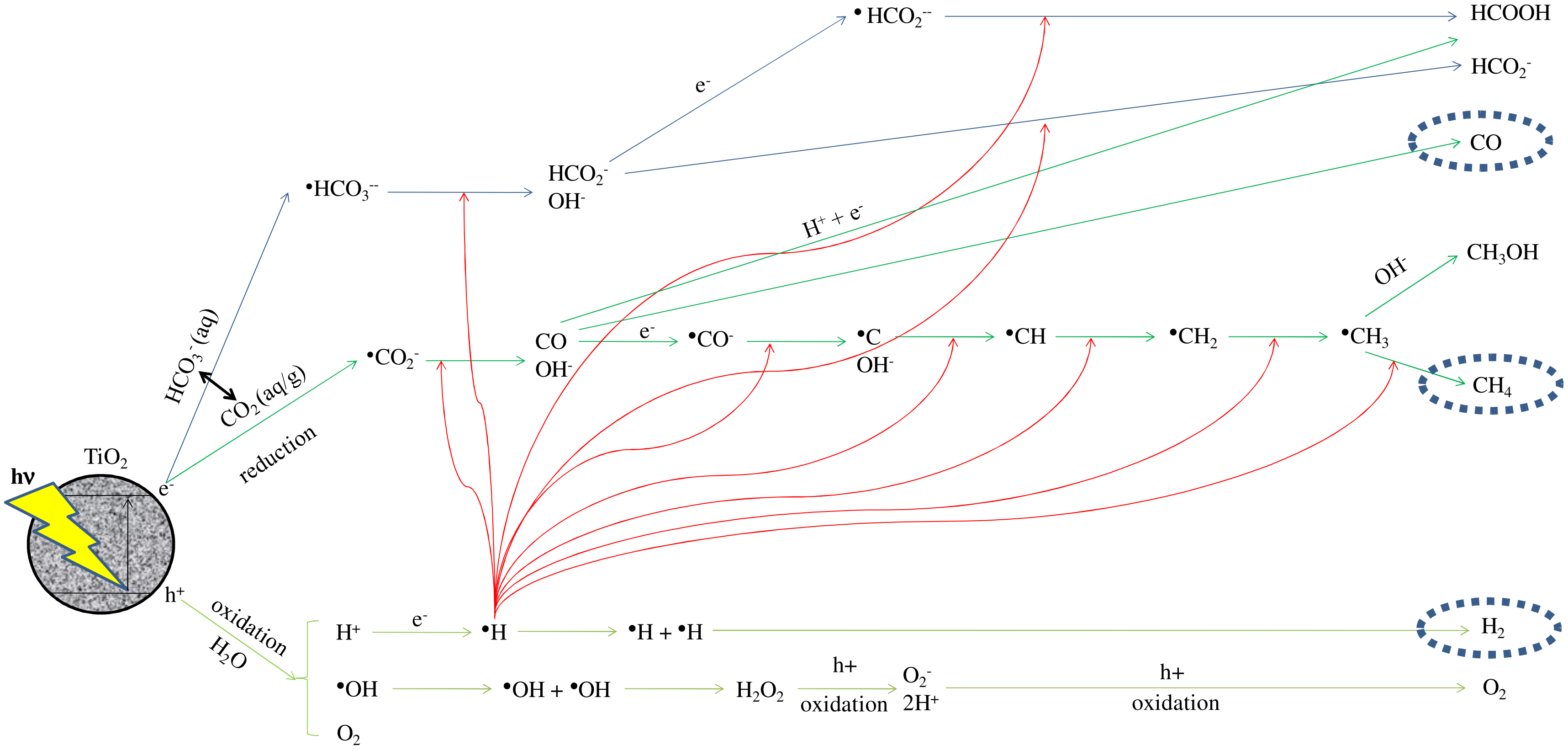

Figure 4.25. Probable reaction pathways for CO_2 photoreduction with pure/doped TiO_2 powders prepared with different chemical routes.

4.4. Conclusions

In this study photocatalytic water splitting and CO_2 reduction activities of pure and Nd doped TiO_2 powders prepared by different chemical routes were evaluated.

XRD, UV-Vis DRS and XPS analyses were conducted in order to develop a correlation between the photocatalytic activity and the powder properties altered by Nd doping and the preparation method employed. N and S doping in the TiO_2 lattice was induced by using excess amounts HNO_3 and H_2SO_4 in the powder preparation media. The use of H_2SO_4 for the dissolution of TiO_2 precipitate formed by hydrolyzing TTIP led to the presence residual SO_4^{2-} ions in the grain boundaries along with possible substitutional S accommodation in the Ti^{4+} sites. Lattice constant c was changed significantly by the preparation method and Nd doping. Nd doping was determined to decrease the lattice constant c which may attributed to the formation of oxygen vacancies by the incorporation of Nd ions in the interstitials of TiO_2 lattice or segregation of these ions as separate oxide phases on the grain boundaries of TiO_2.

In general the change in the nanophase structure were similar for the pure and doped powders heat treated at 600°C, however at 700°C, SO_4^{2-} or NO_x ions are in tendency to leave the nanostructure due the increased heat treatment temperature. So the effect of these ions on the nanophase evolution was minimized by increasing the heat treatment temperature.

The XPS results indicated that most of the powders are oxygen deficient and the level of deficiency was increased with Nd doping at 700°C.

UV-Vis DR spectra of NP and SP indicated an absorption in the blue and green light region for pure and doped powders heat treated at 600°C due to the new energy levels slightly above the valence band edge of TiO_2 created by N or S doping. The large absorption bands at the wavelengths of 515, 529, 588, 684, 747 nm detected for Nd doped powders were assigned to the characteristics absorption bands of Nd^{3+} ion resulting from 4f-4f transitions.

The highest photocatalytic water splitting activity was obtained with pure AP powder heat treated at 700°C and activities increased with Nd doping for NP and SG powders. XRD analyses indicated that these powders possessed higher crystallite sizes and rutile weight fractions. A developed crystalline structure and nanophase composition may be very important for the separation of charge carriers and light absorption.

The highest CO/H_2 ratios were obtained with the powders possessing the highest H_2 production activities. The presence of lower anatase content in these powders may have decreased the oxidation rate of CO to CO_2 or the production of H_2 and CO_2 may be increased compared to the production of H_2 and CO.

CO was determined to be the main product of photocatalytic CO_2 reduction experiments. Lower CH_4 production amounts compared to CO and trace amounts of H_2 evolution were also obtained with the prepared powders. Produced CO amounts were found to be the highest for pure SG and NP powders heat treated at 600^{o}C and 700^{o}C, respectively. It was found that the produced CO amounts generally decreased with Nd doping in per unit area basis and increased in per amount of the powder. The increased CO production amounts was attributed to the increase in the surface area with Nd doping.

Artificial photosynthesis experiments indicated that photocatalytic activity may significantly depend on the nanophase structure of the photocatalyst. These findings revealed that high photocatalytic activities can be achieved by an optimization in the nanophase structure and electronic properties which can be probably designed by the employed powder preparation method.

CHAPTER 5

PREPARATION AND CHARACTERIZATION OF La-Ti PYROCHLORES PREPARED BY SULFATE OR NITRATE ROUTE

5.1. Materials and Methods

5.1.1. Preparation of the Powders

Acidic 1 M Ti^{4+} stock solution was prepared in order to be used in different La/Ti compositions by dissolving titanium precipitate (prepared by hydrolyzing appropriate amount of TTIP) in H_2SO_4 and HNO_3 solution. Predetermined amount of La_2O_3 powder was then added to this solution. La^{3+} and Ti^{4+} ions were co-precipitated by dropwise addition of this solution to 2.47 M NH_4OH solution. pH of the final solution was controlled by addition of 2.47 M NH_4OH solution in order to maintain pH above 9.5. Precipitates were centrifuged and washed before drying at 70°C for 2 days prior to heat treatment between 400 and 1200°C for 3 hours. This process was repeated for every target composition. Thus TiO_2 powders containing 18-50 mol % La_2O_3 (47-80 weight %) were prepared. Every composition was prepared to have 25 g final oxide and then divided into 8 pieces with equal weights to be heat treated between 400 and 1200°C. Target compositions are: $La_2Ti_1O_5$, $La_2Ti_2O_7$, $La_2Ti_3O_9$, $La_4Ti_3O_{12}$, $La_4Ti_9O_{24}$, $La_2Ti_0O_3$, $La_0Ti_1O_2$. Selected compositions and heat treatment temperatures were applied in the preparation of pyrochlores by using HNO_3 according to information obtained in sulfate powder characterization. Sulfate and nitrate powders were coded as SP and NP, respectively. A schematic representation of chemical co-precipitation method is given in Figure 5.1.

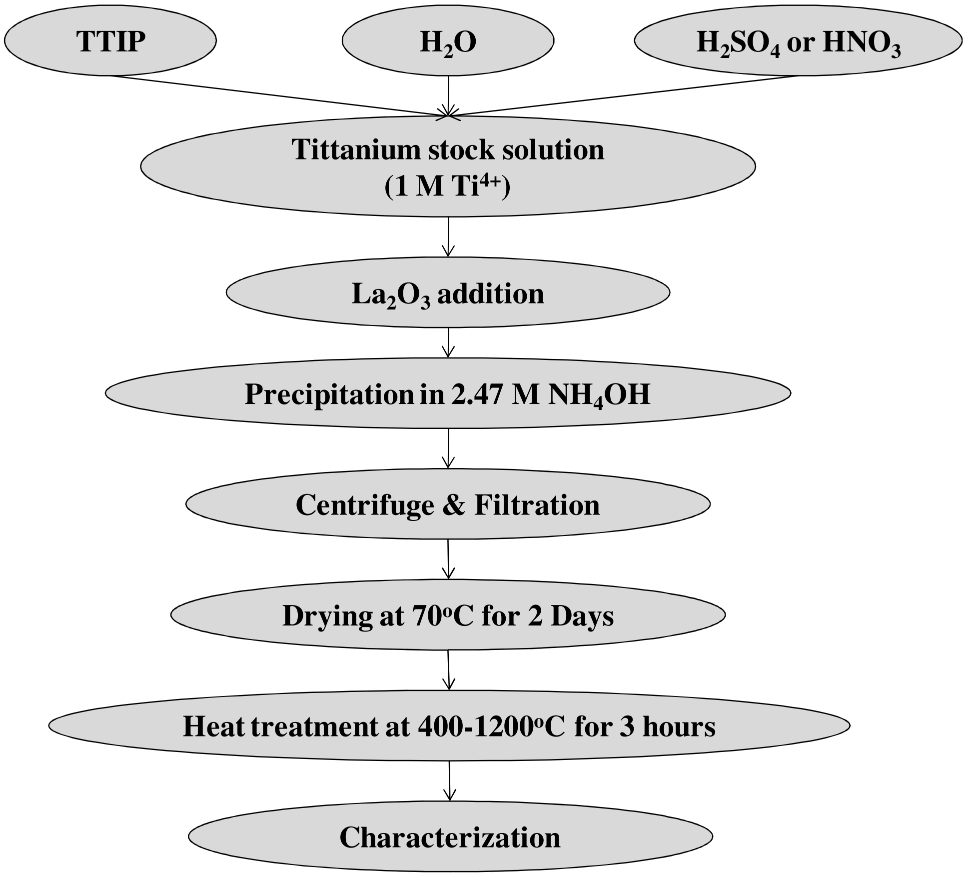

Figure 5.1. Schematic representation of chemical co-precipitation method.

5.1.2. Characterization of the Powders

Phase characterization of the prepared powders was performed on Philips X'pert Pro XRD equipment with monochromated high-intensity (λ=1.54Å) CuKα radiation. The scanning rate was set as 2.5 2Θ/min between 5° and 80° with 0.033° step size. Characterization was conducted with 1-2 g powder pressed in an aluminum cassette which was also used as reference material to calculate the accurate peak positions.

The crystallite sizes were calculated from the broadening of the (101) reflection for anatase and (110) reflection for rutile using Scherrer's equation:

$$d = \frac{k.\lambda}{\beta.\cos\theta} \tag{5.1}$$

where d is the crystallite size (nm), k is the shape constant (0.9 for spherical particles), λ is the X-ray wavelength (nm), β is the full width at half maximum (FWHM) of the selected peak and θ is the Bragg's angle of diffraction (Sun et al. 2014).

The rutile and anatase weight fractions were determined from the relation:

$$x_A = \left(1 + 1.26\frac{I_R}{I_A}\right)^{-1} \tag{5.2}$$

where x_A is the anatase weight fraction, I_R and I_A are the intensities of the rutile (110) and anatase (101) peaks, respectively (Spurr and Mayers 1957).

Elemental sulfur in the La-Ti pyrochlore powders was quantified by XRF Ametek Spectro IQ II.

5.2. Results and Discussion

XRD patterns, crystallite sizes and anatase-rutile weight fractions of SP pure TiO_2 powders are given in Figures 5.2, 5.3 and Figure 5.4, respectively. Anatase phase transformed into rutile phase at 800°C and above temperatures in pure SP powders. SP powders dried at 70°C were amorphous. Crystallite size of anatase phase was between 15 and 20 nm at 400-600°C and significant increase was observed above 600°C. Rutile phase began to appear at 800°C and crystallite sizes were calculated as 60-100 nm for 800-900°C. The higher anatase-rutile phase transformation temperature compared to literature values are thought to be due to sulfate ions inhibiting the phase transformation. The presence of sulfate ions was shown by XRF. Sulfur amounts (in elemental basis) were determined as 0.95, 0.08598, 0.00617, 0.00303, 0.00363 ve 0.00319 at 400, 700, 900, 1000, 1100 ve 1200°C, respectively. It was observed that sulfate ions left the structure by increasing heat treatment temperature. The effect of the presence of residual sulfate ions originating from chemical precipitation method on the anatase-rutile phase transformation was eliminated by using HNO_3 instead of H_2SO_4 in the preparation procedure.

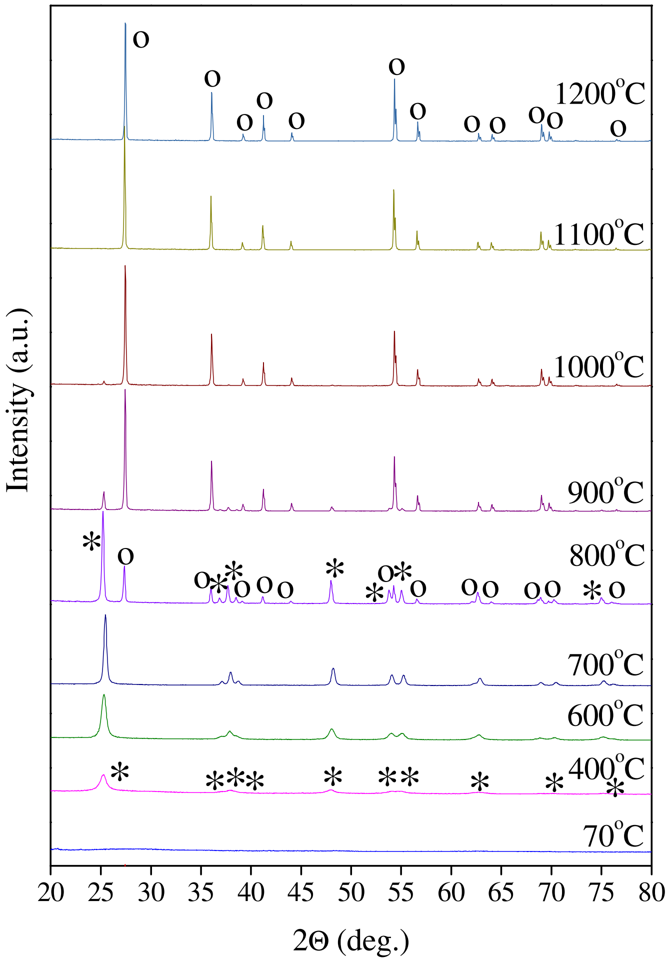

Figure 5.2. XRD patterns of pure SP powders (*: anatase, o: rutile).

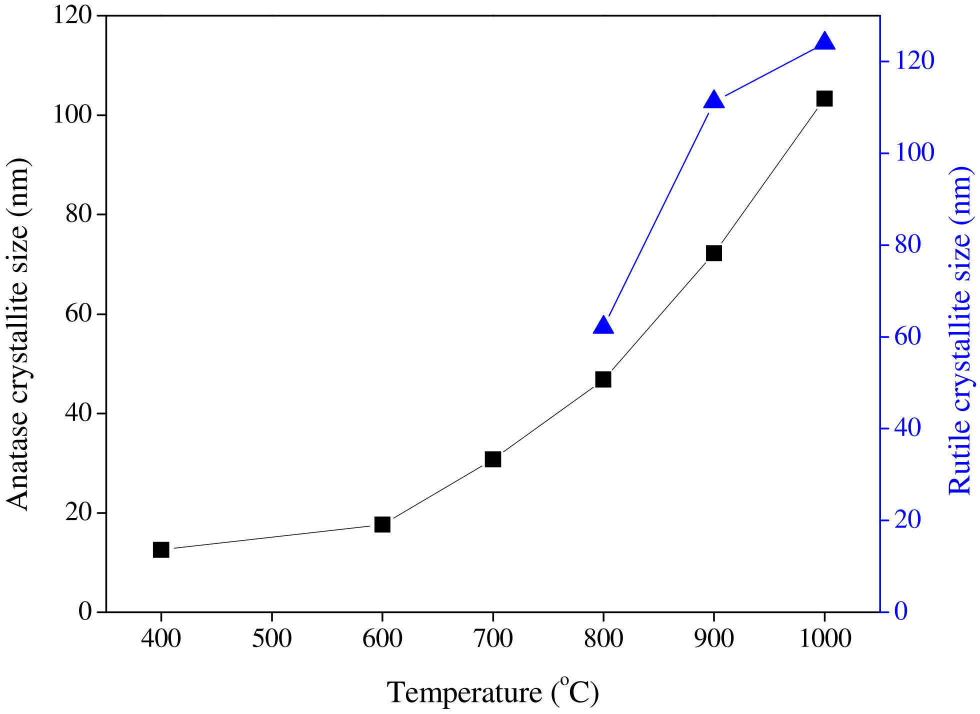

Figure 5.3. Crystallite sizes of pure SP powders: (■) anatase, (▲) rutile.

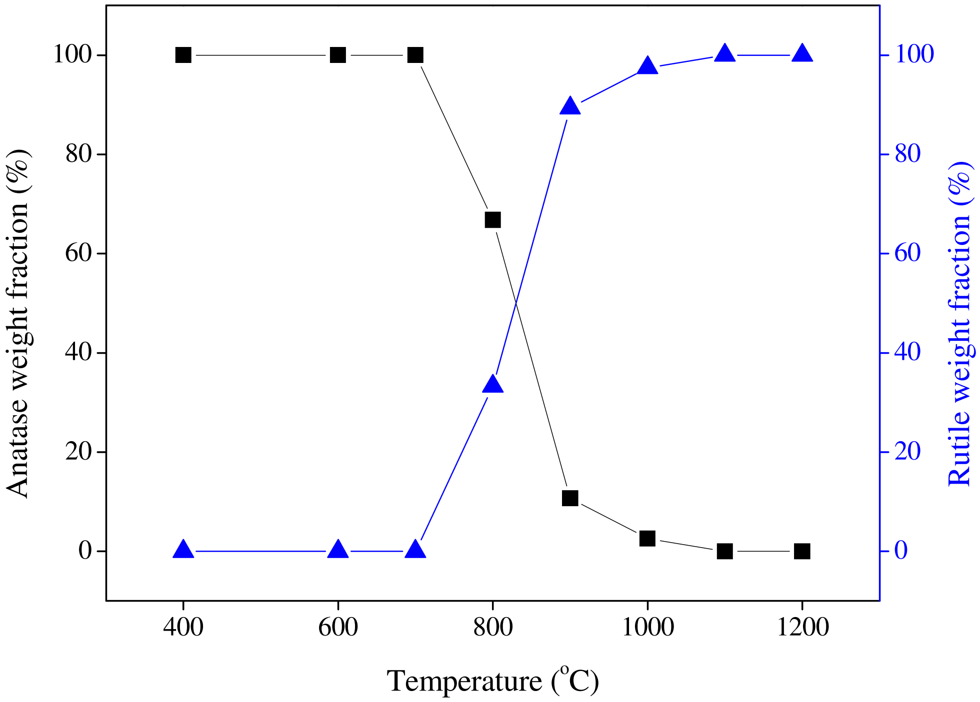

Figure 5.4. Anatase-rutile weight fractions of pure SP powders: (■) anatase, (▲) rutile.

XRD patterns of the prepared SP La-Ti pyrochlores are given in Figures 5.5 and 5.6. JCPDS Data Base (cards of $La_xTi_yO_z$ phases are given in APPENDICES) was used in order to explain the phase evolution of La-Ti pyrochlores with powder composition and heat treatment temperature. 215 powders were mainly composed of $La_2Ti_2O_7$ with trace amounts of La_2TiO_5, $La_4Ti_3O_{12}$ and some sulfate containing phases. Stable formation of $La_2Ti_2O_7$ phase at 800°C and above temperatures was observed for 227 target composition. However, $La_2Ti_2O_7$, $La_4Ti_9O_{24}$ and small amounts of lanthanum sulfate compounds were formed for 4924 target composition. $La_2Ti_3O_9$ compound was not observed in 239 target composition. $La_4Ti_9O_{24}$ compound was observed at low temperatures and $La_2Ti_2O_7$ compound was observed at high temperatures with the targeted composition. $La_2Ti_2O_7$ compound was detected as the major phase in all XRD patterns with small amounts of targeted compositions La_2TiO_5, $La_4Ti_3O_{12}$ and lanthanum sulfate compounds. Almost all the powders were amorphous under 800°C heat treatment temperature. The XRD reflections of La-Ti phyrochlore phases first appeared at 800°C for 227, 239, 4312 and 700°C for 4924 target compositions. All the powders were crystalline at all heat treatment temperatures for 215 target composition.

The amount of sulfate content increased with increasing La content of the powder according to the XRF results. Sulfate was not detected in the powders heat treated above 1000°C. Sulfate contents were detected as 0.00617, 0.4776, 0.2069, 0.456, 0.74061 and 1.044 % (elemental basis) for the target compositions of 4924, 239, 227, 4312, 215 (in the increasing order of La content), respectively prepared at 900°C heat treatment temperature. Sulfate content in the pure TiO_2 powders decreased with increasing heat treatment temperature. The pure TiO_2 powder heat treated at 400°C contains 0.95% sulfate, while it decreased to 0.08598%, 0.00617%, 0.00303%, 0.00363% and 0.00319% in the powders heat treated at 700°C, 900°C, 1000°C, 1100°C and 1200°C, respectively.

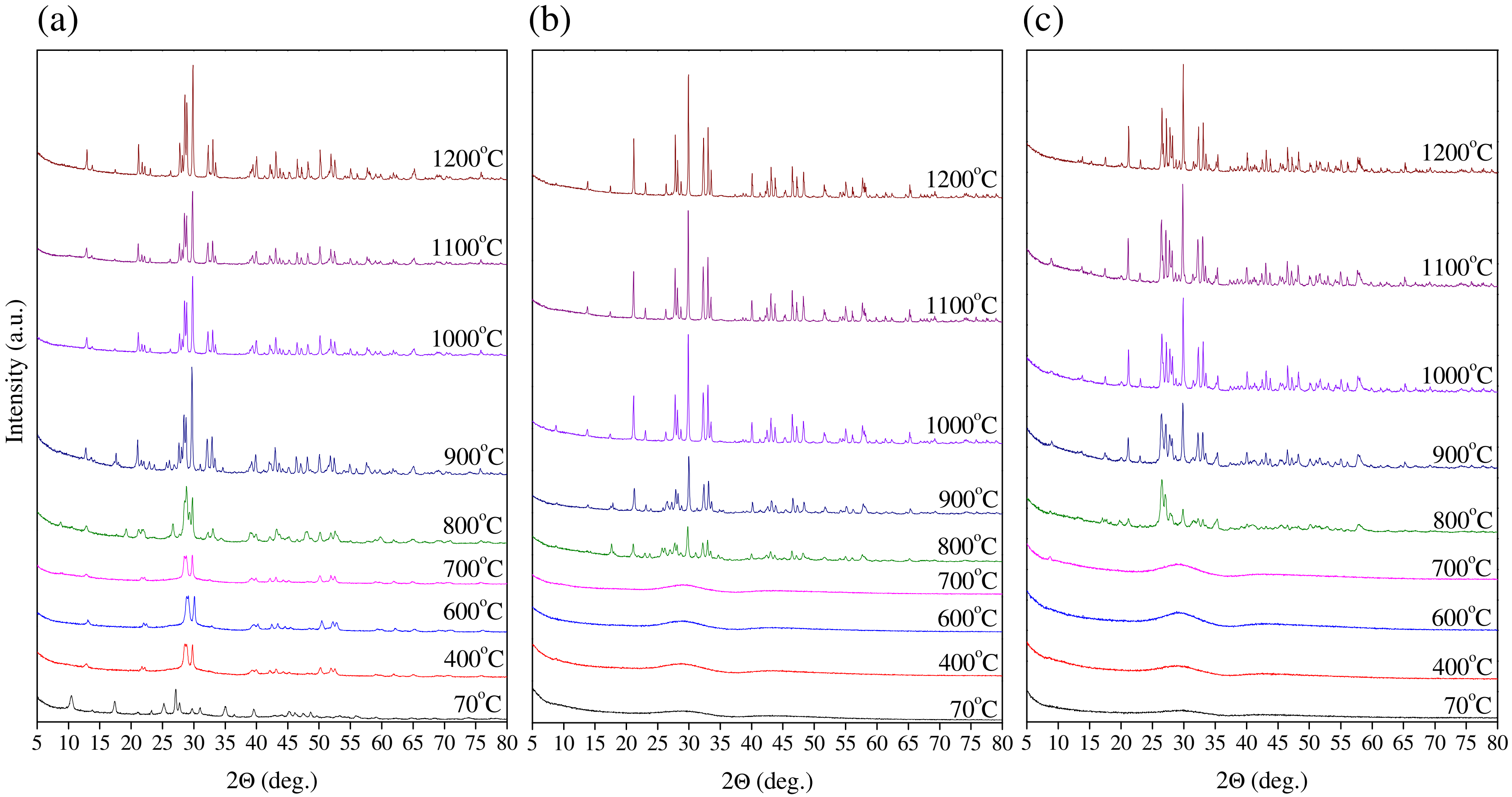

Figure 5.5. XRD patterns of SP powders with the target compositions: (a) 215, (b) 227, (c) 239.

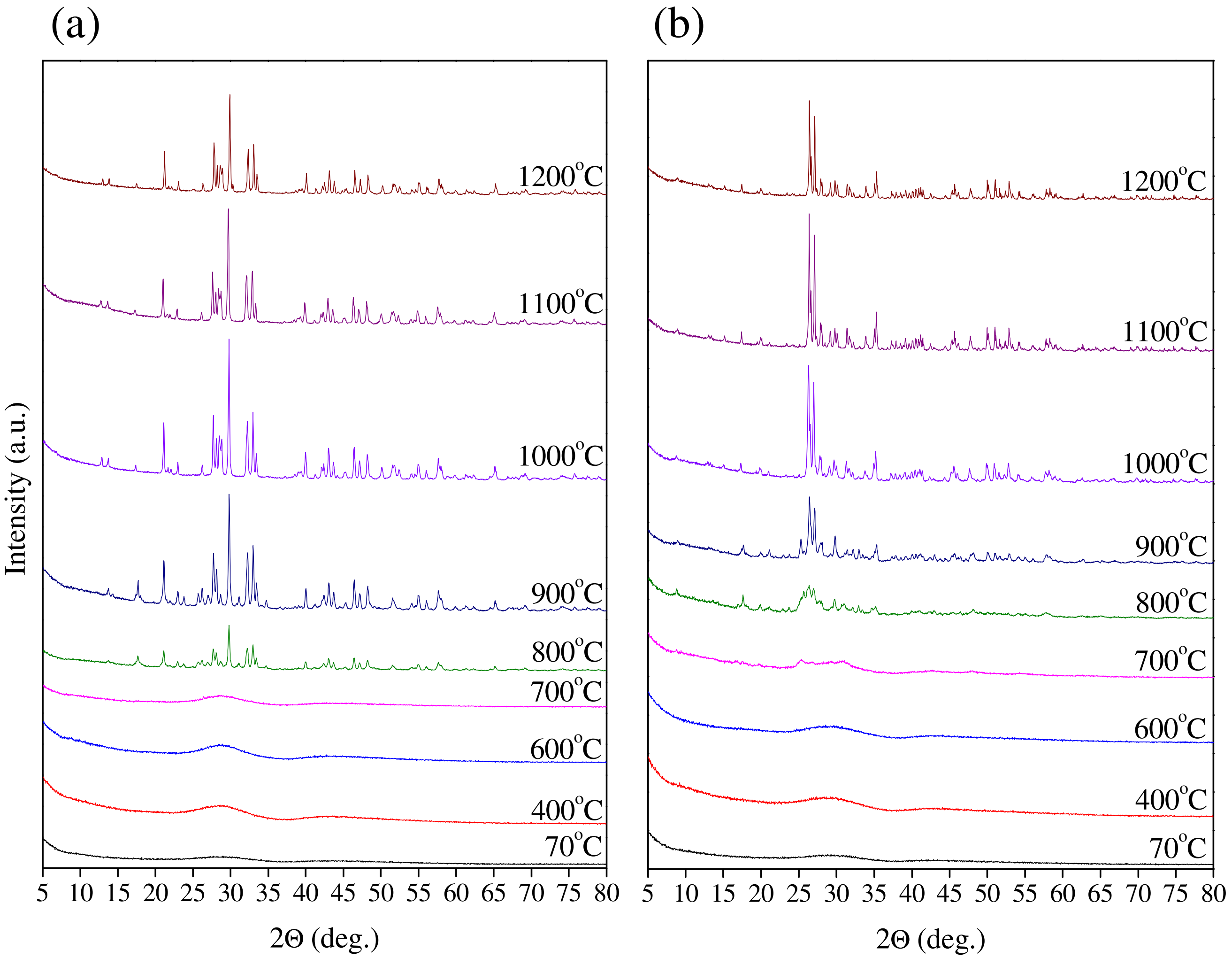

Figure 5.6. XRD patterns of SP powders with the target compositions: (a) 4312, (b) 4924.

XRD patterns, crystallite sizes and anatase-rutile weight fractions of pure NP TiO_2 powders are given in Figures 5.7, 5.8 and Figure 5.9, respectively. Pure TiO_2 has amorphous characteristics at 70°C while it was pure anatase, anatase-rutile mixture and pure rutile at 600°C, 700°C and 800°C, respectively. Pure SP TiO_2 powders had the same phase characteristics at 600°C and 1000°C, however in NP powder heat treated at 800°C mainly consisted of rutile phase, which is the opposite in the SP powder at the same temperature. This information shows that sulfate ions have certain impact on the phase structure evolution. The crystallite sizes calculated were higher than SP powders for the same temperatures and the anatase weight fraction was 30 and 20% in SP and NP powders at 700°C, respectively. The obtained information showed that the presence of sulfate ions has an inhibitory effect on the phase transformation kinetics of anatase to rutile.

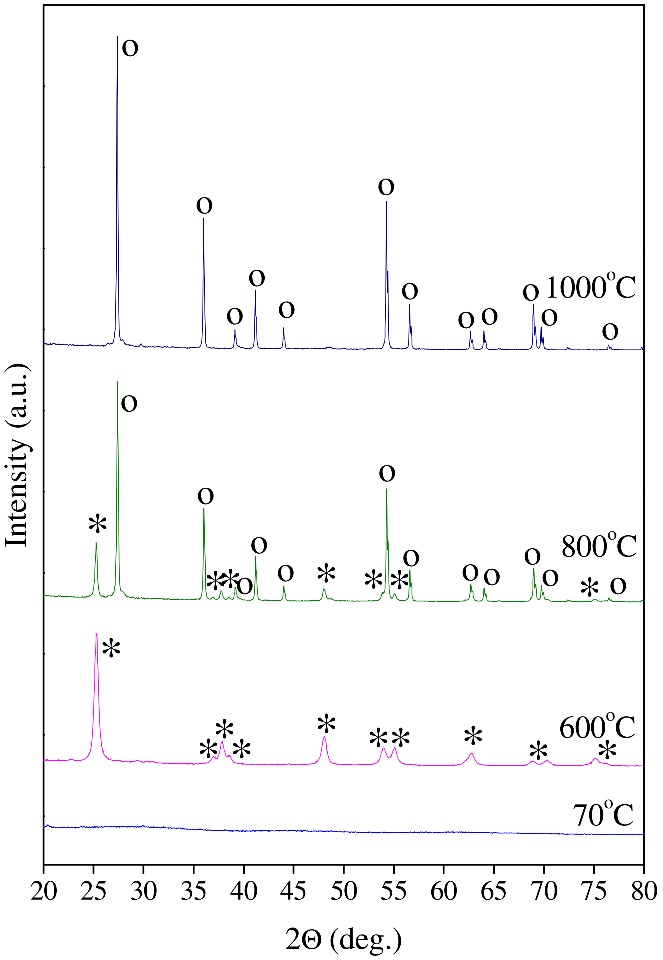

Figure 5.7. XRD patterns of pure NP powders (*: anatase, o: rutile).

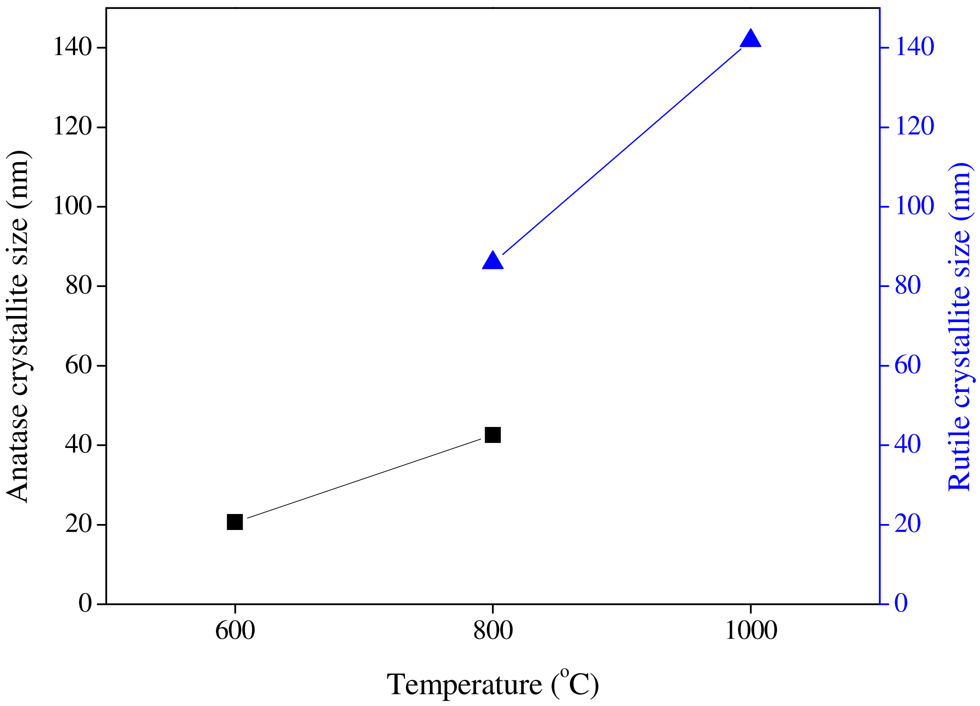

Figure 5.8. Crystallite sizes of pure NP powders: (■) anatase, (▲) rutile.

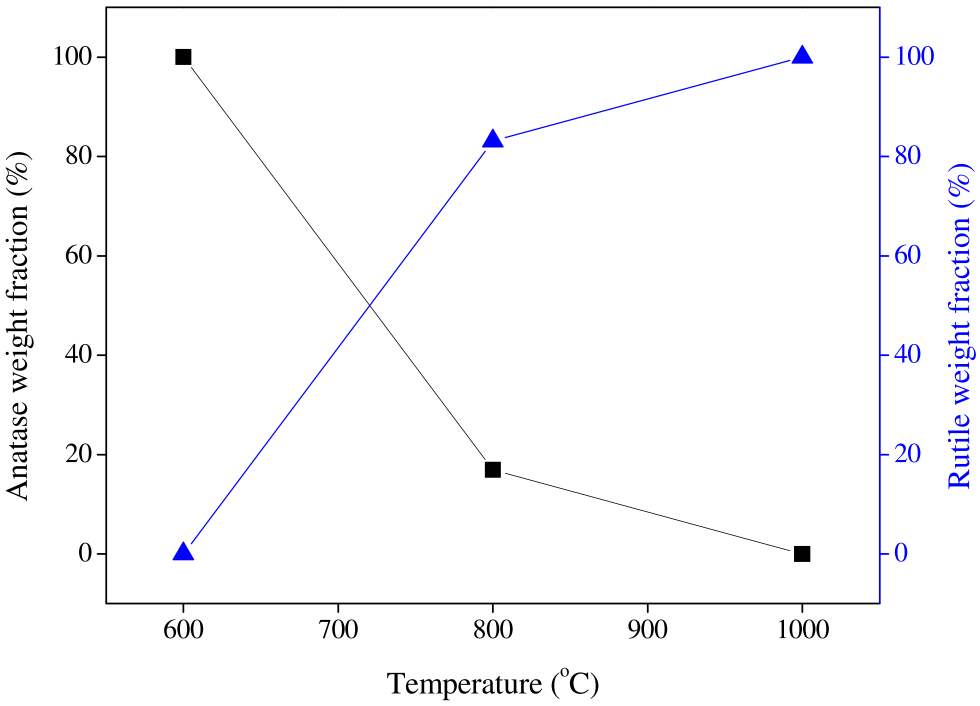

Figure 5.9. Anatase-rutile weight fractions of pure NP powders: (■) anatase, (▲) rutile.

XRD patterns of the prepared NP La-Ti pyrochlores are given in Figure 5.10. NP 215 powders have amorphous characteristics at 70°C and 600°C and La_2TiO_5 phase was detected at 800°C and this powder was well crystallised at 1000°C. La_2TiO_5 phase which was the target composition was the main phase with small amounts of $La_4Ti_3O_{12}$ phase in this powder. La_2TiO_5 phase was not observed in the powders prepared with sulfuric acid for this composition. Almost pure $La_2Ti_2O_7$ powders were also prepared with nitric acid as with sulfuric acid at 800°C and above temperatures. The powders prepared with $La_4Ti_3O_{12}$ composition were composed of mainly La_2TiO_5 phase with trace amounts of $La_2Ti_2O_7$ phase, $La_4Ti_3O_{12}$ phase was not observed.

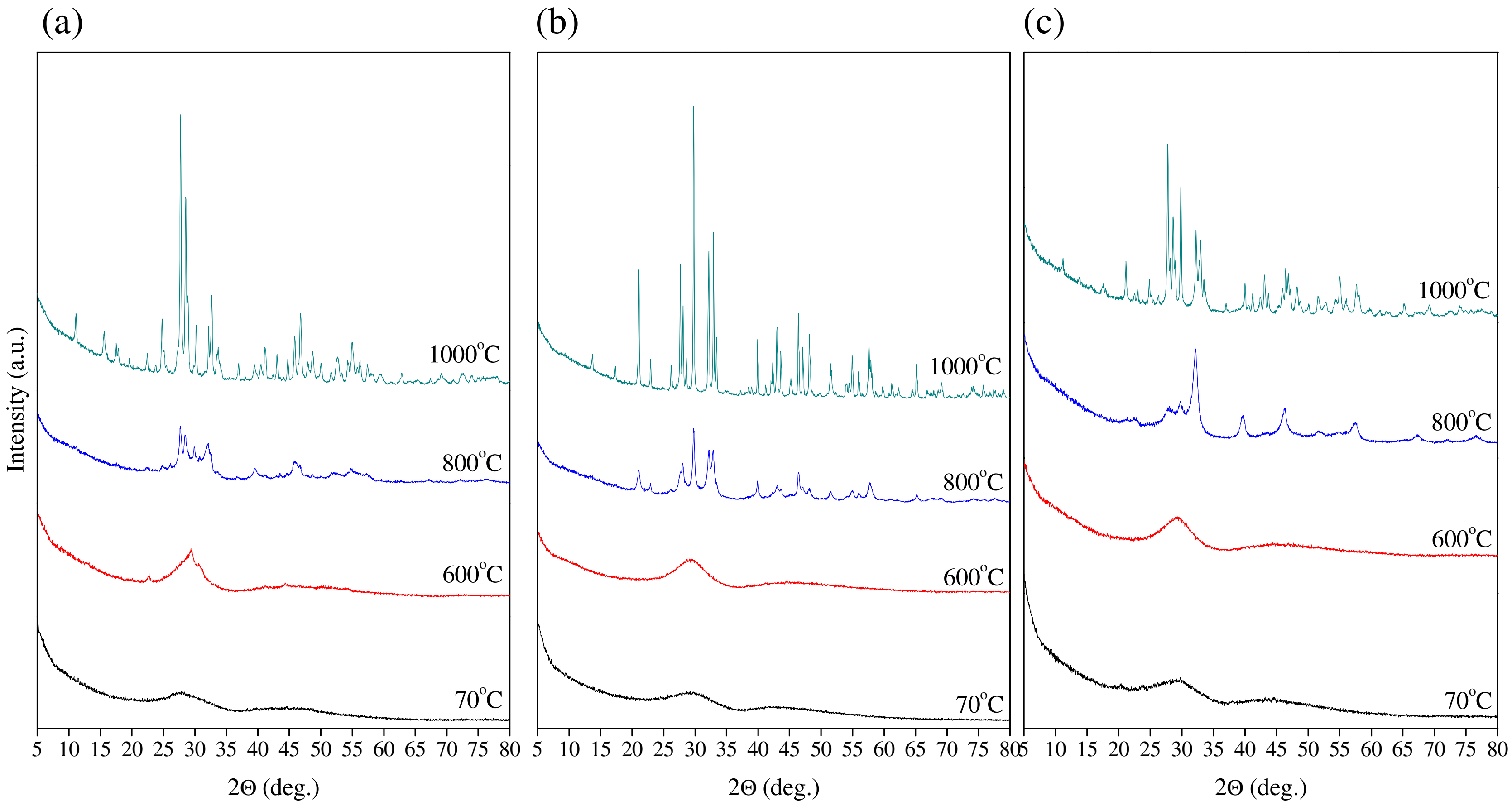

Figure 5.10. XRD patterns of NP powders with the target compositions: (a) 215, (b) 227, (c) 4312.

5.3. Conclusions

The nanophase structure analysis of the powders containing 47-80 wt.% La_2O_3 prepared by the chemical co-precipitation method in the sulfate or nitrate media and heat treated between 40-1200^oC indicated that $La_2Ti_2O_7$ phase was formed for all the target compositions. The stable formation of $La_2Ti_2O_7$ phase was detected in the SP powders heat treated at 800^oC and beyond. The anatase to rutile phase transformation was significantly inhibited by the residual sulfate ions originating from H_2SO_4 used in the preparation of these powders. Crystalline structures of the NP powders were detected to be more developed when compared to the SP powders which was more significant for the pure powders. The anatase wt.% of the pure NP and SP powders heat treated at 800^oC were calculated as 67 and 17, respectively. The obtained results indicated that phase evolution was significantly inhibited by the residual sulfate ions in pure TiO_2 and La-Ti pyrochlores.

CHAPTER 6

PHASE STRUCTURE AND OPTICAL PROPERTIES OF Nd_2O_3-CeO_2 CO-DOPED SOL-GEL TITANIA POWDERS

6.1. Materials and Methods

6.1.1. Preparation of the Powders

Nd_2O_3-CeO_2 co-doped TiO_2 powders were prepared by sol-gel using titanium tetraisopropoxide (TTIP, Aldrich 97%) as titanium precursor. Cerium(III) nitrate hexahydrate ($Ce(NO_3)_3.6H_2O$, Aldrich 99.99% trace metal basis), neodymium nitrate hexahydrate ($Nd(NO_3)_3.6H_2O$, Aldrich 99.99% trace metal basis) containing ethanol/HNO_3/water solution was added dropwise into TTIP/ethanol solution under vigorous stirring at room temperature. The sols were stirred until complete gelation was observed. The obtained gels were dried at 50^oC overnight prior to heat treatment at 400-1000^oC for 3 hours. Gelation time for undoped TiO_2 was 3 minutes and the time necessary for the complete gelation of the co-doped TiO_2 sols increased up to more than 3 weeks (20%) from 45 minutes (0.5%) with doping. Increasing in the gelation time with doping level may be due to increase of nitrate ions originating from the use of nitrate salts of rare earths as dopant precursors. A schematic representation of Nd_2O_3-CeO_2 co-doped TiO_2 powder preparation process is given in Figure 6.1.

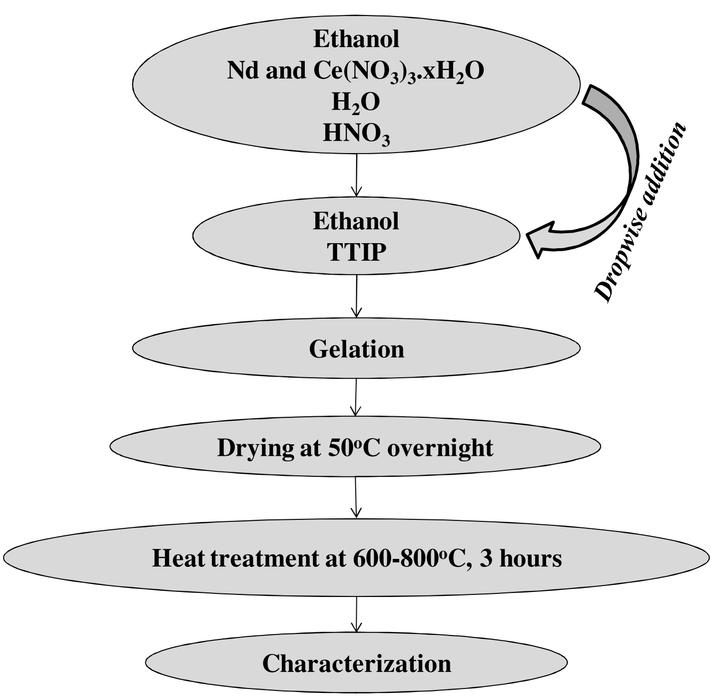

Figure 6.1. A schematic representation of Nd_2O_3-CeO_2 co-doped sol-gel TiO_2 powder preparation process.

6.1.2. Characterization of the Powders

Phase characterization of the prepared powders was performed on Philips X'pert Pro XRD equipment with monochromated high-intensity (λ=1.54Å) CuKα radiation. The scanning rate was set as 2.5 2Θ/min between 5^o and 80^o with 0.033^o step size. Characterization was conducted with 1-2 g powder pressed in an aluminum cassette which was also used as reference material to calculate the accurate peak positions.

The crystallite sizes were calculated from the broadening of the (101) reflection for anatase and (110) reflection for rutile using Scherrer's equation:

$$d = \frac{k.\lambda}{\beta.\cos\theta} \tag{6.1}$$

where d is the crystallite size (nm), k is the shape constant (0.9 for spherical particles), λ is the X-ray wavelength (nm), β is the full width at half maximum (FWHM) of the selected peak and θ is the Bragg's angle of diffraction (Sun et al. 2014).

Optical absorption characteristics of the prepared powders were investigated by using UV-Vis Spectrophotometer (Perkin Elmer Lamda25) equipped with DRS (Diffuse

Reflectance Spectrometer) accessory. Pellets with 15mm diameter and 2-3mm thickness were prepared with uniaxial press for the optical characterization.

6.2. Results and Discussion

XRD patterns of Nd_2O_3-CeO_2 co-doped (at high and low concentrations) TiO_2 powders heat treated at 600, 700, 800°C are shown in Figures 6.2, 6.3 and 6.4, respectively. Anatase was detected to be the main phase at all doping levels and heat treatment temperatures. At 600°C anatase was the only phase, at 700°C and 0.5% doping level rutile phase was detected and at 800°C rutile formed even at 1% doping level. At 20% doping level at 800°C, mixed NdCeTiO phases were detected. The phase transformation inhibition was also detected as in the mono doped TiO_2 powders.

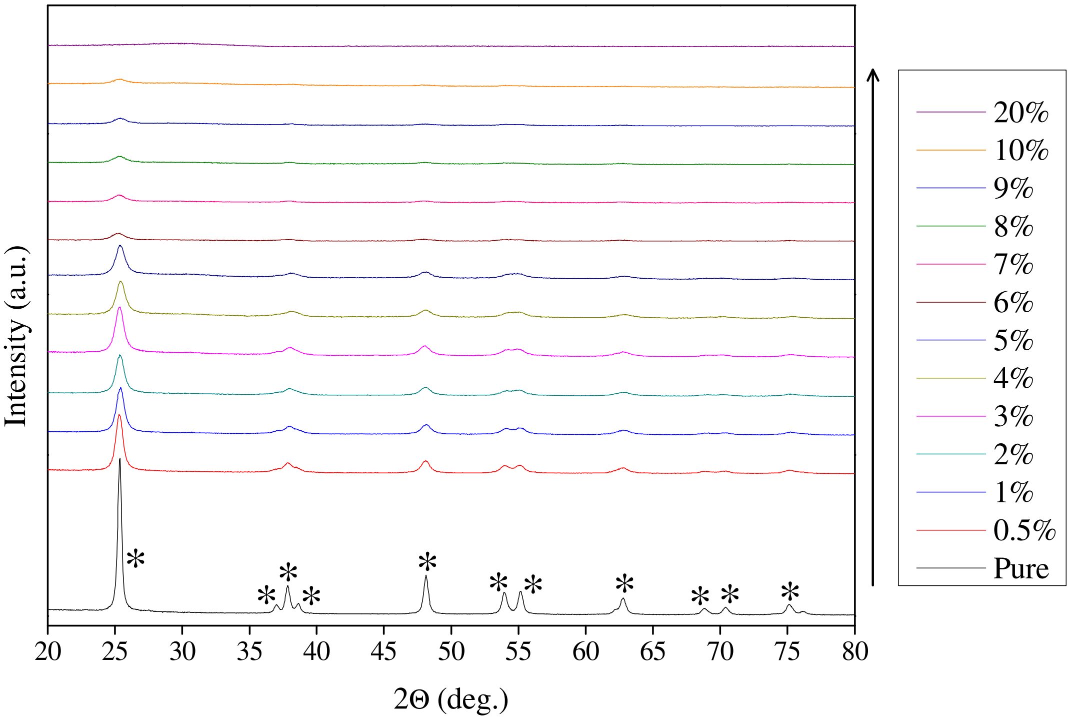

Figure 6.2. XRD patterns of Nd_2O_3-CeO_2 co-doped TiO_2 powders heat treated at 600°C.

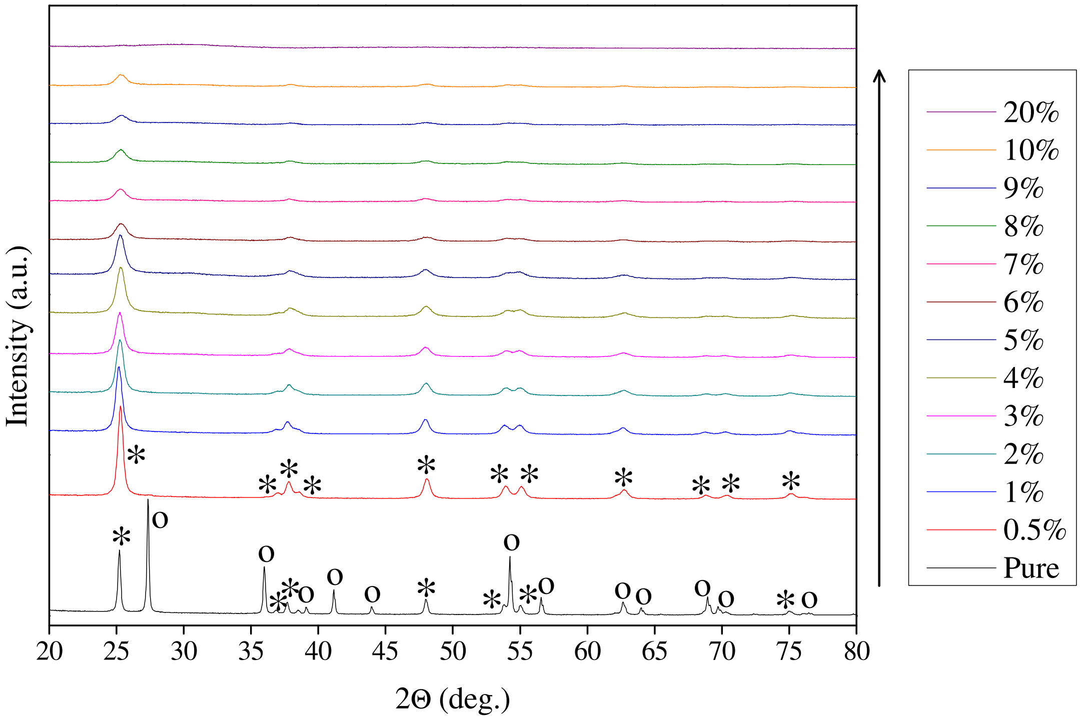

Figure 6.3. XRD patterns of Nd_2O_3-CeO_2 co-doped TiO_2 powders heat treated at 700°C.

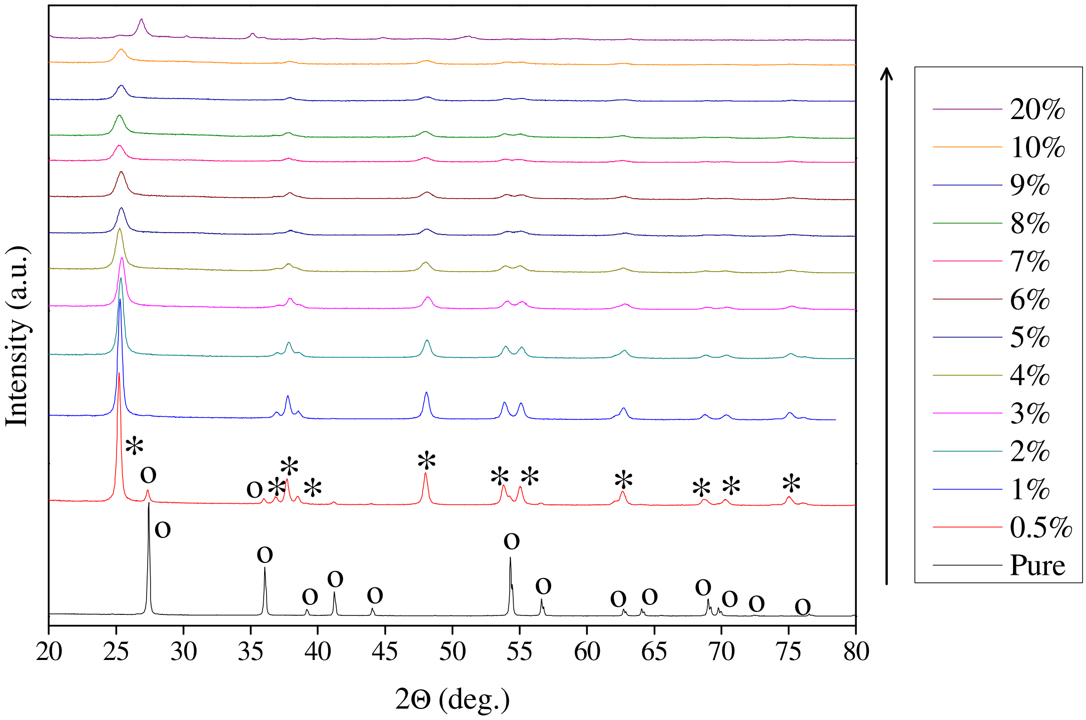

Figure 6.4. XRD patterns of Nd_2O_3-CeO_2 co-doped TiO_2 powders heat treated at 800°C.

Anatase crystallite sizes of Nd_2O_3-CeO_2 co-doped TiO_2 powders are shown in Figure 6.5. Crystallite size was detected to increase with increasing heat treatment temperature and decrease with increasing doping level as found for individual doping of Nd_2O_3 and CeO_2. Crystallite sizes were determined to be between the crystallite sizes of Nd_2O_3 and CeO_2 mono doped TiO_2 powders at the same doping level. As an example, for 5% doping level at 800°C, these values are 10.27, 20.05 and 13.97 for Nd_2O_3, CeO_2 doped and Nd_2O_3-CeO_2 co-doped TiO_2 powders.

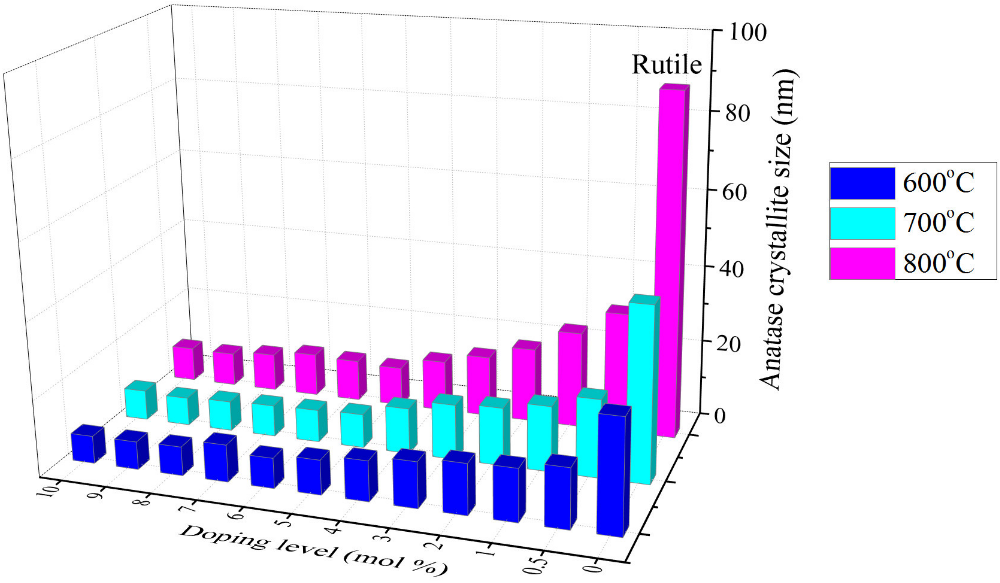

Figure 6.5. Anatase crystallite sizes of Nd_2O_3-CeO_2 co-doped TiO_2 powders heat treated in the 600-800°C temperature range

UV-Vis DR spectra of Nd_2O_3-CeO_2 co-doped TiO_2 powders are shown in Figure 6.6. The spectra indicated that Nd_2O_3-CeO_2 co-doping caused a composite effect on the optical characteristics of TiO_2. Absorption edge shifts as in the individual doping with CeO_2 and characteristic absorption peaks were detected in the visible region as in the individual Nd_2O_3 doping. The intensities of the absorption bands in the visible region increased with increasing heat treatment temperature.

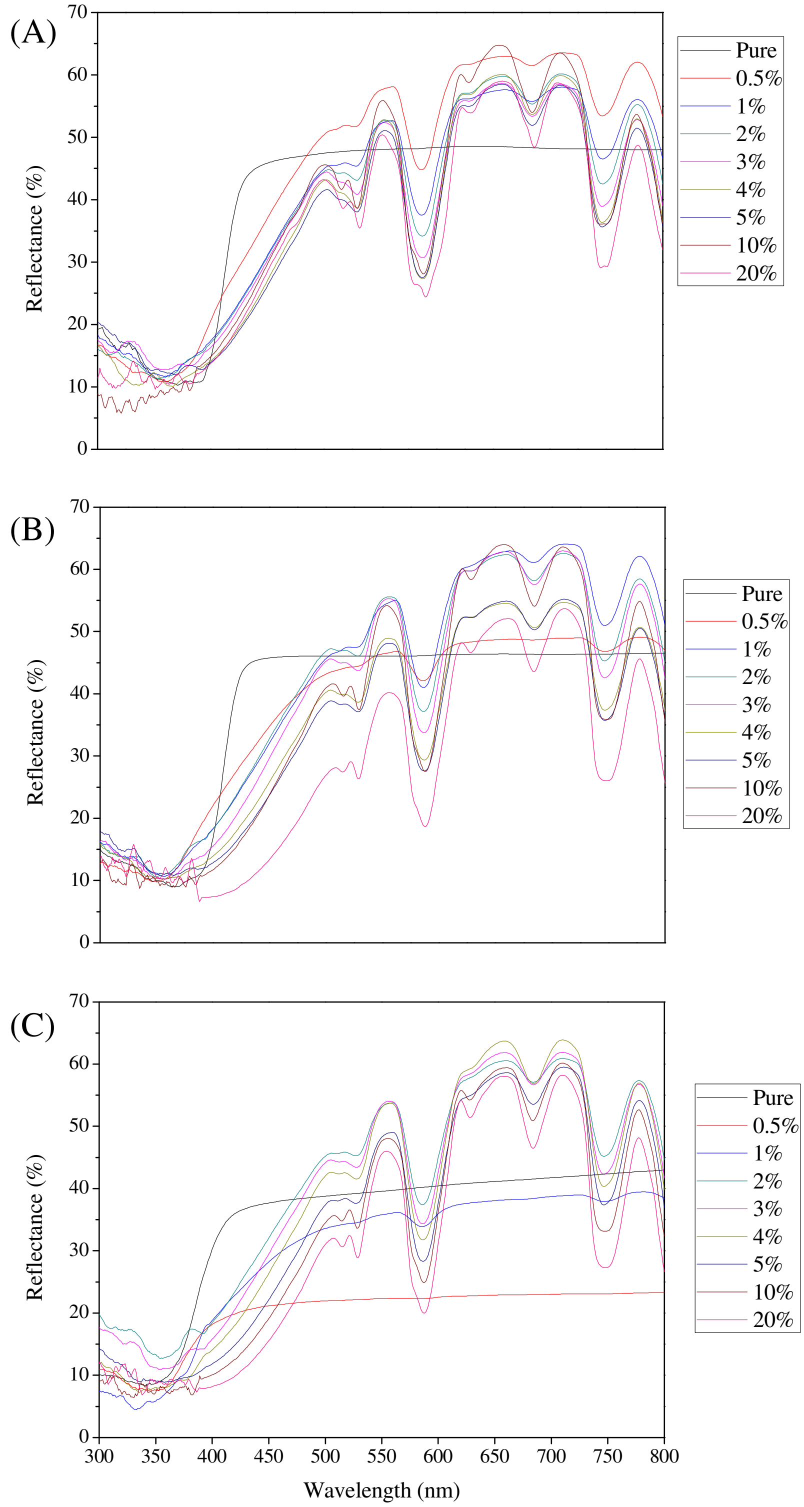

Figure 6.6. UV-Vis DR spectra of Nd_2O_3-CeO_2 co-doped TiO_2 powders heat treated in the 600-800°C temperature range.

6.3. Conclusions

In this study, Nd_2O_3-CeO_2 co-doped TiO_2 powders were prepared by using sol-gel technique. XRD and UV-Vis DRS analysis were performed for the investigation of co-doping effect on the nanophase structure and optical properties of TiO_2. XRD analysis indicated that the phase transformation of anatase to rutile was also inhibited by Nd_2O_3-CeO_2 co-doping as observed in mono doped TiO_2 powders. Crystallite sizes were determined to be between the crystallite sizes of Nd_2O_3 and CeO_2 mono doped TiO_2 powders at the same doping level and heat treatment temperature. The UV-Vis DR spectra of the powders indicated that Nd_2O_3-CeO_2 co-doping caused a composite effect on the optical characteristics of TiO_2. These characterization results are preliminary studies for the investigation of Nd_2O_3-CeO_2 co-doping effect on the nanophase structure and the electronic properties of TiO_2.

CHAPTER 7

CONCLUSIONS

In this thesis, REE doped/undoped TiO_2 photocatalysts were prepared by using sol-gel and chemical co-precipitation techniques. The location of dopant ion and the effect of REE doping on the phase and electronic structure, physicochemical and optical properties of TiO_2 were investigated by XRD, UV-Vis DRS, XPS, TEM, DLS, N_2 adsorption-desorption. Photocatalytic water splitting and CO_2 reduction activities of the prepared powders were determined and the photocatalytic activities of the prepared powders were evaluated in relation with their nanophase structure, crystallite size, surface area, light absorption and electronic properties.

In Chapter 2, the location of the dopant ion and the effect of REE doping on the nanophase structure, physical and electronic properties of TiO_2 were investigated. Volume average particle size and gelation time of RE_2O_3 doped TiO_2 sols increased with doping level. The gelation of pure TiO_2 sol completed in 3 minutes; whereas gelation time of 5% Nd_2O_3 doped TiO_2 sol completed in a week. Anatase was determined to be the main phase in all doped TiO_2 powders up to 900^{o}C. Rutile formation was observed beginning with 700^{o}C and rutile was the dominant phase with $RE_2Ti_2O_7$ phases at 1000^{o}C. $RE_2Ti_2O_7$ phases first appeared at 2% doping levels at 800^{o}C for RE ions with small ionic radii (between Eu and Yb). $Nd_4Ti_9O_{24}$ phase was formed at 10% doping level at 800^{o}C and even at low doping levels at 900 and 1000^{o}C. It was found that the phase evolution from anatase to rutile was significantly inhibited by RE_2O_3 doping. The results indicated that RE ions can accommodate in the TiO_2 lattice interstitial voids or segregate on the grain boundaries of TiO_2 crystallites rather than a substitutional accommodation. Resulting lattice oxygen and structural defects developed due to the presence of RE ions in the microstructure can significantly affect the nanophase, physical and electronic properties of TiO_2. Nitrogen adsorption-desorption analyses of the prepared powders showed that RE_2O_3 doping increased the surface area of TiO_2. Er_2O_3 doped TiO_2 powders possessed higher surface areas than Nd_2O_3 doped TiO_2 powder, loss of surface area at 5% doping level was determined to be at a lower level for Er_2O_3 compared to Nd_2O_3. Crystallite sizes of Nd_2O_3 doped TiO_2

powders calculated by using Scherrer Equation from XRD patterns were determined to be similar with the results of TEM analyses. Nd_2O_3 amount was calculated as 5.4% (molar basis) for 5Nd700 which showed that intended composition of 5% Nd_2O_3 was achieved.

In Chapter 3, the photocatalytic activities of RE_2O_3 doped sol-gel TiO_2 powders in water splitting and CO_2 reduction were investigated. RE doping was found to enhance the light absorption of TiO_2 by varying the AR ratio or absorbing photons in the visible light region due to REEs' 4f-4f transition. The highest artificial photosynthesis (photocatalytic water splitting and CO_2 reduction) activities were obtained with large ionic radii REs doped TiO_2 powders at 0.1% doping level. The obtained higher activities at low doping levels with larger ionic radii REs were attributed to the obtained optimum phase structure which has significant influence on the light absorption and charge carrier separation. RE oxides and oxygen defects formed by REE incorporation in the TiO_2 matrix was found to enhance the photocatalytic activity by forming locations where charge carrier separation was enhanced. The results of this study indicated that an optimum AR ratio which may be tuned by RE_2O_3 doping is crucial in photocatalytic water splitting and CO_2 reduction since it is known that anatase is more photoactive than rutile and rutile absorbs light more efficiently than anatase.

In Chapter 4, the photocatalytic water splitting and CO_2 reduction activities of pure and Nd_2O_3 doped TiO_2 powders prepared by different chemical routes were evaluated. N and S doping in the TiO_2 lattice was induced by using excess amounts HNO_3 and H_2SO_4 in the powder preparation media. The use of H_2SO_4 for the dissolution of TiO_2 precipitate formed by hydrolyzing TTIP led to the presence residual SO_4^{2-} ions in the grain boundaries along with possible substitutional S accommodation in the Ti^{4+} sites. In general the change in the nanophase structure were similar for the pure and doped powders heat treated at 600°C, however at 700°C, SO_4^{2-} or NO_x ions are in tendency to leave the nanostructure due the increased heat treatment temperature. So the effect of these ions on the nanophase evolution was minimized by increasing the heat treatment temperature. The XPS results indicated that most of the powders are oxygen deficient and the level of deficiency was increased with Nd_2O_3 doping at 700°C. UV-Vis DR spectra of NP and SP indicated an absorption in the blue and green light region for pure and doped powders heat treated at 600°C due to the new energy levels slightly above the valence band edge of TiO_2 created by N or S doping. The large absorption bands at the wavelengths of 515, 529, 588, 684, 747 nm detected for Nd_2O_3 doped powders were assigned to the characteristics absorption bands of Nd^{3+} ion resulting from 4f-4f transitions. The highest photocatalytic water splitting activity was obtained with pure AP powder heat treated at 700°C and activities increased with Nd doping for NP and SG powders. XRD analyses indicated that these powders possessed higher crystallite sizes and rutile weight fractions. A well developed crystalline structure and nanophase composition may be very important for the separation of charge carriers and light absorption. CO was determined to be the main product of photocatalytic CO_2 reduction experiments. Lower CH_4 production amounts compared to CO and trace amounts of H_2 evolution were also obtained with the prepared powders. Produced CO amounts were found to be the highest for pure SG and NP powders heat treated at 600°C and 700°C, respectively. It was found that the produced CO amounts generally decreased with Nd_2O_3 doping in per unit area basis and increased in per amount of the powder. The increase in the CO production amounts was attributed to the increase in the surface area with Nd_2O_3 doping. Artificial photosynthesis experiments indicated that photocatalytic activity may significantly depend on the nanophase structure of the photocatalyst. These findings revealed that high photocatalytic activities can be achieved by an optimization in the nanophase structure and electronic properties which can be probably designed by the employed powder preparation method.

The preliminary results of nanophase structure and optical characterization of La-Ti phyrochlores and Nd_2O_3-CeO_2 co-doped TiO_2 powders prepared for the use in artificial photosynthesis were given in Chapter 5 and 6, respectively. La-Ti pyrochlores were prepared by chemical co-precipitation by using H_2SO_4 and HNO_3 for dissolving titanium precipitate. $La_2Ti_1O_5$, $La_2Ti_2O_7$, $La_2Ti_3O_9$, $La_4Ti_3O_{12}$, $La_4Ti_9O_{24}$ compounds along with pure TiO_2 and La_2O_3 were the target compositions. $La_2Ti_2O_7$ and $La_4Ti_3O_{12}$ with trace amounts of lanthanum sulfates which may have formed due to incomplete removal of the sulfate ions from the hydroxide co-precipitates were found to be the dominant phases in these powders after heat treatment in the 400-1200°C temperature range. Synthesis of Nd_2O_3-CeO_2 co-doped TiO_2 powders were performed by using sol-gel technique. Anatase was the only phase at 600°C, rutile phase was detected at 700°C at 0.5% doping level and at 800°C at 1% doping level. NdCeTiO phases were detected at 20% doping level and 800°C. Crystallite sizes were between that of individually doped Nd_2O_3 and CeO_2 powders. Absorption edge shifted as in the individual doping with CeO_2 and characteristic absorption peaks occurred in the visible region as in the individual Nd_2O_3 doping. Increasing the heat treatment temperature resulted an increase in the intensity of the absorption peaks in the visible region.

Characterization results of the sol-gel powders prepared in the range of 0.1-5% doping level were presented in Chapter 2. Increasing the range beyond 5% doping level may create valuable information about the nanophase structure and optical properties about the possibly formed nanocomposites of RE_2O_3-TiO_2. Different preparation methods may also be applied in order to investigate the effects of the preparation method on the nanophase structure evolution of RE_2O_3 doped TiO_2 powders.

The powders prepared at lower doping levels (0.1% and 0.25%) showed higher photocatalytic activities water splitting and CO_2 reduction as presented in Chapter 3. Lower doping levels such as 0.05% and 0.01% may be applied for the determination of the lowest limit of RE_2O_3 doping level at which higher photocatalytic activities may still be obtained.

The powders prepared by precipitation methods showed enhanced photocatalytic activities in artificial photosynthesis as discussed in Chapter 4. Different doping levels may also be applied for these powders and their photocatalytic activities may be evaluated in order to investigate the effect of the doping level in chemically precipitated TiO_2 powders.

The results of the nanophase structure and optical characterization of the powders presented in Chapter 5 and 6 may be coupled with their artificial photosynthesis activities. A correlation between the nanophase structure of La-Ti phyrochlores or Nd_2O_3-CeO_2 co-doped TiO_2 powders and the artificial photosynthesis activities of these powders may be developed.

REFERENCES

Abe, R. 2010. "Recent progress on photocatalytic and photoelectrochemical water splitting under visible light irradiation" Journal of Photochemistry and Photobiology C: Photochemistry Reviews. 11: 179-209.

Abou Asi, M., He, C., Su, M., Xia, D., Lin, L., Deng, H., Xiong, Y., Qiu, R., Li, X.-z. 2011. "Photocatalytic reduction of CO_2 to hydrocarbons using $AgBr/TiO_2$ nanocomposites under visible light" Catalysis Today. 175: 256-263.

Adachi G., Imanaka N., Kang Z.C. “Binary Rare Earth Oxides” Springer Science Business Media, U.S.A., 2004.

Ahmad Beigi, A., Fatemi, S., Salehi, Z. 2014. "Synthesis of nanocomposite CdS/TiO_2 and investigation of its photocatalytic activity for CO_2 reduction to CO and CH_4 under visible light irradiation" Journal of CO_2 Utilization. 7: 23-29.

Akpan, U.G., Hameed, B.H. 2010. "The advancements in sol–gel method of doped-TiO_2 photocatalysts" Applied Catalysis A: General. 375: 1-11.

Anpo, M. 2013. "Photocatalytic reduction of CO_2 with H_2O on highly dispersed Ti-oxide catalysts as a model of artificial photosynthesis" Journal of CO_2 Utilization. 1: 8-17.

Anpo, M., Kamat, P.V. “Environmentally Benign Photocatalysts Applications of Titanium Oxide-based Materials” Springer, U.S.A, 2010.

Antić, Ž., Krsmanović, R.M., Nikolić, M.G., Marinović-Cincović, M., Mitrić, M., Polizzi, S., Dramićanin, M.D. 2012. "Multisite luminescence of rare earth doped TiO_2 anatase nanoparticles" Materials Chemistry and Physics. 135: 1064-1069.

Asal, S., Saif, M., Hafez, H., Mozia, S., Heciak, A., Moszyński, D., Abdel-Mottaleb, M.S.A. 2011. "Photocatalytic generation of useful hydrocarbons and hydrogen from acetic acid in the presence of lanthanide modified TiO_2" International Journal of Hydrogen Energy. 36: 6529-6537.

Bae, S.W., Borse, P.H., Hong, S.J., Jang, J.S., Lee, J.S., Jeong, E.D., Hong, T.E., Yoon, J.H., Jin, J.S., Kim, H.G. 2007. "Photophysical Properties of Nanosized Metal-Doped TiO_2 Photocatalyst Working under Visible Light" Journal of the Korean Physical Society. 51: 22-26.

Baeissa, E.S. 2014. "Green synthesis of methanol by photocatalytic reduction of CO_2 under visible light using a graphene and tourmaline co-doped titania nanocomposites" Ceramics International. 40: 12431-12438.

Baiju, K.V., Periyat, P., Wunderlich, W., Krishna Pillai, P., Mukundan, P., Warrier, K.G.K. 2007. "Enhanced photoactivity of neodymium doped mesoporous titania synthesized through aqueous sol–gel method" Journal of Sol-Gel Science and Technology. 43: 283-290.

Bellardita, M., Addamo, M., Di Paola, A., Palmisano, L. 2007. "Photocatalytic behaviour of metal-loaded TiO_2 aqueous dispersions and films" Chemical Physics. 339: 94-103.

Bellardita, M., Di Paola, A., Palmisano, L., Parrino, F., Buscarino, G., Amadelli, R. 2011. "Preparation and photoactivity of samarium loaded anatase, brookite and rutile catalysts" Applied Catalysis B: Environmental. 104: 291-299.

Beranek, R., Kisch, H. 2008. "Tuning the optical and photoelectrochemical properties of surface-modified TiO_2" Photochem Photobiol Sci. 7: 40-48.

Topuz, B., 2009. “Gas Permeation Through Sol-Gel Derived Alumina and Silica Based Membranes” PhD Thesis, Chemical Engineering Department - Izmir Institute of Technology, pp25-26.

Bokare, A., Pai, M., Athawale, A.A. 2013. "Surface modified Nd doped TiO_2 nanoparticles as photocatalysts in UV and solar light irradiation" Solar Energy. 91: 111-119.

Borlaf, M., Colomer, M.T., Moreno, R., Ortiz, A.L. 2013. "Effect of Er^{3+} doping on the thermal stability of TiO_2 nanoparticulate xerogels" Journal of Nanoparticle Research. 15: 1-10.

Borlaf, M., Colomer, M.T., Moreno, R., Ortiz, A.L. 2014. "Rare earth-doped TiO_2 nanocrystalline thin films: Preparation and thermal stability" Journal of the European Ceramic Society. 34: 4457-4462.

Bünzli, J.-C.G., André, N., Elhabiri, M., Muller, G., Piguet, C. 2000. "Trivalent lanthanide ions: versatile coordination centers with unique spectroscopic and magnetic properties" Journal of Alloys and Compounds. 303–304: 66-74.

Burns, A., Hayes, G., Li, W., Hirvonen, J., Demaree, J.D., Shah, S.I. 2004. "Neodymium ion dopant effects on the phase transformation in sol–gel derived titania nanostructures" Materials Science and Engineering: B. 111: 150-155.

Cappelletti, G., Bianchi, C.L., Ardizzone, S. 2008. "Nano-titania assisted photoreduction of Cr(VI)" Applied Catalysis B: Environmental. 78: 193-201.

Carp, O. 2004. "Photoinduced reactivity of titanium dioxide" Progress in Solid State Chemistry. 32: 33-177.

Castañeda-Contreras, J., Marañón-Ruiz, V.F., Chiu-Zárate, R., Pérez-Ladrón de Guevara, H., Rodriguez, R., Michel-Uribe, C. 2012. "Photocatalytic activity of erbium-doped TiO_2 nanoparticles immobilized in macro-porous silica films" Materials Research Bulletin. 47: 290-295.

Charanpahari, A., Umare, S.S., Sasikala, R. 2013. "Effect of Ce, N and S multi-doping on the photocatalytic activity of TiO_2" Applied Surface Science. 282: 408-414.

Chen, X., Shen, S., Guo, L., Mao, S.S. 2010. "Semiconductor-based Photocatalytic Hydrogen Generation" Chemical Reviews. 110: 6503-6570.

Chiou, C.H., Juang, R.S. 2007. "Photocatalytic degradation of phenol in aqueous solutions by Pr-doped TiO_2 nanoparticles" J Hazard Mater. 149: 1-7.

Choudhury, B., Borah, B., Choudhury, A. 2013. "Ce–Nd codoping effect on the structural and optical properties of TiO_2 nanoparticles" Materials Science and Engineering: B. 178: 239-247.

Choudhury, B., Choudhury, A. 2013. "Local structure modification and phase transformation of TiO_2 nanoparticles initiated by oxygen defects, grain size, and annealing temperature" International Nano Letters. 3: 55.

Cogdell, R.J., Brotosudarmo, T.H.P., Gardiner, A.T., Sanchez, P.M., Cronin, L. 2010. "Artificial photosynthesis – solar fuels: current status and future prospects" Biofuels. 1: 861-876.

Collings, A.F., Critchley, C. “Artificial Photosynthesis From Basic Biology to Industrial Application” Wiley-VCH, Germany, 2005.

Cong, Y., Zhang, J., Chen, F., Anpo, M. 2007. "Synthesis and Characterization of Nitrogen-Doped TiO_2 Nanophotocatalyst with High Visible Light Activity" The Journal of Physical Chemistry C. 111: 6976-6982.

Conti, J.J., Annual Energy Outlook 2014 with Projections to 2040, in: U.S.E.I. Administration (Ed.), 2014, pp. 1-269.

Das, S., Wan Daud, W.M.A. 2014. "Photocatalytic CO_2 transformation into fuel: A review on advances in photocatalyst and photoreactor" Renewable and Sustainable Energy Reviews. 39: 765-805.

de la Cruz Romero, D., Torres, G.T., Arévalo, J.C., Gomez, R., Aguilar-Elguezabal, A. 2010. "Synthesis and characterization of TiO_2 doping with rare earths by sol–gel method: photocatalytic activity for phenol degradation" Journal of Sol-Gel Science and Technology. 56: 219-226.

de_Richter, R.K., Ming, T., Caillol, S. 2013. "Fighting global warming by photocatalytic reduction of CO_2 using giant photocatalytic reactors" Renewable and Sustainable Energy Reviews. 19: 82-106.

Devi, L.G., Kumar, S.G. 2012. "Exploring the critical dependence of adsorption of various dyes on the degradation rate using Ln^{3+}-TiO_2 surface under UV/solar light" Applied Surface Science. 261: 137-146.

Dey, G.R. 2007. "Chemical Reduction of CO_2 to Different Products during Photo Catalytic Reaction on TiO_2 under Diverse Conditions: an Overview" Journal of Natural Gas Chemistry. 16: 217-226.

Di Valentin, C., Finazzi, E., Pacchioni, G., Selloni, A., Livraghi, S., Paganini, M.C., Giamello, E. 2007. "N-doped TiO_2: Theory and experiment" Chemical Physics. 339: 44-56.

Dong, F., Guo, S., Wang, H., Li, X., Wu, Z. 2011. "Enhancement of the Visible Light Photocatalytic Activity of C-Doped TiO_2 Nanomaterials Prepared by a Green Synthetic Approach" The Journal of Physical Chemistry C. 115: 13285-13292.

Dugandžić, I.M., Jovanović, D.J., Mančić, L.T., Zheng, N., Ahrenkiel, S.P., Milošević, O.B., Šaponjić, Z.V., Nedeljković, J.M. 2012. "Surface modification of submicronic TiO_2 particles prepared by ultrasonic spray pyrolysis for visible light absorption" Journal of Nanoparticle Research. 14: 1-11.

Fan, Y., Li, D., Deng, M., Luo, Y., Meng, Q. 2009. "An overview on water splitting photocatalysts" Frontiers of Chemistry in China. 4: 343-351.

Fujishima, A., Honda, K. 1972. "Electrochemical Photolysis of Water at a Semiconductor Electrode" Nature. 238: 37-38.

Fujishima, A., Rao, T.N., Tryk, D.A. 2000. "Titanium dioxide photocatalysis" Journal of Photochemistry and Photobiology C: Photochemistry Reviews. 1: 1-21.

Gao, H.T., Liu, W.C., Liu, G.J. 2012. "Facile Synthesis and Enhanced Photocatalysis of Sm Doped TiO_2" Advanced Materials Research. 490-495: 3272-3276.

Gázquez, M.J., Bolívar, J.P., Garcia-Tenorio, R., Vaca, F. 2014. "A Review of the Production Cycle of Titanium Dioxide Pigment" Materials Sciences and Applications. 05: 441-458.

Ghigna, P., Speghini, A., Bettinelli, M. 2007. "“Unusual Ln^{3+} substitutional defects”: The local chemical environment of Pr^{3+} and Nd^{3+} in nanocrystalline TiO_2 by Ln–K edge EXAFS" Journal of Solid State Chemistry. 180: 3296-3301.

Gong, W., Zhang, R. 2013. "Phase relationship in the TiO_2–Nd_2O_3 pseudo-binary system" Journal of Alloys and Compounds. 548: 216-221.

Gribb, A.A., Banfield, J.F. 1997. "Particle size effects on transformation kinetics and phase stability in nanocrystalline TiO_2" American Mineralogist. 82: 717-728.

Gui, M.M., Chai, S.-P., Xu, B.-Q., Mohamed, A.R. 2014. "Enhanced visible light responsive MWCNT/TiO2 core–shell nanocomposites as the potential photocatalyst for reduction of CO_2 into methane" Solar Energy Materials and Solar Cells. 122: 183-189.

Hammarstrom, L., Hammes-Schiffer, S. 2009. "Artificial Photosynthesis and Solar Fuels" Accounts of Chemical Research. 42: 1859-1860.

Hanaor, D.A.H., Sorrell, C.C. 2010. "Review of the anatase to rutile phase transformation" Journal of Materials Science. 46: 855-874.

Hassan, M.S., Amna, T., Yang, O.B., Kim, H.-C., Khil, M.-S. 2012. "TiO_2 nanofibers doped with rare earth elements and their photocatalytic activity" Ceramics International. 38: 5925-5930.

Heldt, H.-W. “The use of energy from sunlight by photosynthesis is the basis of life on earth” Plant Biochemistry, Elsevier Academic Press, U.S.A, 2005, pp. 45-66.

Hewer, T.L.R., Souza, E.C.C., Martins, T.S., Muccillo, E.N.S., Freire, R.S. 2011. "Influence of neodymium ions on photocatalytic activity of TiO_2 synthesized by sol–gel and precipitation methods" Journal of Molecular Catalysis A: Chemical. 336: 58-63.

Hishita, S., Mutoh, I., Koumoto, K., Yanagida, H. 1983. "Inhibition mechanism of the anatase-rutile phase transformation by rare earth oxides" Ceramics International. 9: 61-67.

Hoffmann, M.R., Martin, S.T., Choi, W., Bahnemann, D.W. 1995. "Environmental Applications of Semiconductor Photocatalysis" Chemical Reviews. 95: 69-96.

Hoffmann, M.R., Moss, J.A., Baum, M.M. 2011. "Artificial photosynthesis: semiconductor photocatalytic fixation of CO_2 to afford higher organic compounds" Dalton Trans. 40: 5151-5158.

Houghton, J. “Global Warming The Complete Briefing” Cambridge University Press, U.S.A, 2004.

http://solargis.info/doc/_pics/freemaps/1000px/ghi/SolarGIS-Solar-map-Turkey-en.png, Access date: 5.5.2015

http://www.globalwarmingart.com/wiki/File:Solar_Spectrum_png, Access date: 5.5.2015.

http://www.technologyreview.com/news/419976/fuel-from-the-sun/, Access date: 5.5.2015.

Hussain, M., Akhter, P., Russo, N., Saracco, G. 2013. "Novel Ti-KIT-6 material for the photocatalytic reduction of carbon dioxide to methane" Catalysis Communications. 36: 58-62.

Hussain, M., Akhter, P., Saracco, G., Russo, N. 2015. "Nanostructured TiO_2/KIT-6 catalysts for improved photocatalytic reduction of CO_2 to tunable energy products" Applied Catalysis B: Environmental. 170–171: 53-65.

Inoue, T., Fujishima, A., Konishi, S., Honda, K. 1979. "Photoelectrocatalytic reduction of carbon dioxide in aqueous suspensions of semiconductor powders" Nature. 277: 637-638.

Inoue, Y. 2009. "Photocatalytic water splitting by RuO_2-loaded metal oxides and nitrides with d0- and d10 -related electronic configurations" Energy & Environmental Science. 2: 364.

Izumi, Y. 2013. "Recent advances in the photocatalytic conversion of carbon dioxide to fuels with water and/or hydrogen using solar energy and beyond" Coordination Chemistry Reviews. 257: 171-186.

Jia, Y.Q. 1991. "Crystal radii and effective ionic radii of the rare earth ions" Journal of Solid State Chemistry. 95: 184-187.

Jian, Z., Pu, Y., Fang, J., Ye, Z. 2010. "Microemulsion synthesis of nanosized TiO_2 particles doping with rare-earth and their photocatalytic activity" Photochem Photobiol. 86: 1016-1021.

Jin, M., Nagaoka, Y., Nishi, K., Ogawa, K., Nagahata, S., Horikawa, T., Katoh, M., Tomida, T., Hayashi, J.i. 2008. "Adsorption properties and photocatalytic activity of TiO_2 and La-doped TiO_2" Adsorption. 14: 257-263.

Kalyanasundaram, K., Graetzel, M. 2010. "Artificial photosynthesis: biomimetic approaches to solar energy conversion and storage" Curr Opin Biotechnol. 21: 298-310.

Kandiel, T.A., Ivanova, I., Bahnemann, D.W. 2014. "Long-term investigation of the photocatalytic hydrogen production on platinized TiO_2: an isotopic study" Energy & Environmental Science. 7: 1420.

Kaneco, S., Kurimoto, H., Ohta, K., Mizuno, T., Saji, A. 1997. "Photocatalytic reduction of CO_2 using TiO_2 powders in liquid CO_2 medium" Journal of Photochemistry and Photobiology A: Chemistry. 109: 59-63.

Kaneko, M., Okura, I. “Photocatalysis Science and Technology” Springer, Germany, 2002.

Kibombo, H.S., Weber, A.S., Wu, C.-M., Raghupathi, K.R., Koodali, R.T. 2013. "Effectively dispersed europium oxide dopants in TiO_2 aerogel supports for enhanced photocatalytic pollutant degradation" Journal of Photochemistry and Photobiology A: Chemistry. 269: 49-58.

Kim, H.R., Lee, T.G., Shul, Y.-G. 2007. "Photoluminescence of La/Ti mixed oxides prepared using sol–gel process and their pCBA photodecomposition" Journal of Photochemistry and Photobiology A: Chemistry. 185: 156-160.

Kočí, K., Matějová, L., Reli, M., Čapek, L., Matějka, V., Lacný, Z., Kustrowski, P., Obalová, L. 2014. "Sol–gel derived Pd supported TiO_2-ZrO_2 and TiO_2 photocatalysts; their examination in photocatalytic reduction of carbon dioxide" Catalysis Today. 230: 20-26.

Kočí, K., Matějů, K., Obalová, L., Krejčíková, S., Lacný, Z., Plachá, D., Čapek, L., Hospodková, A., Šolcová, O. 2010. "Effect of silver doping on the TiO_2 for photocatalytic reduction of CO_2" Applied Catalysis B: Environmental. 96: 239-244.

Kočí, K., Obalová, L., Matějová, L., Plachá, D., Lacný, Z., Jirkovský, J., Šolcová, O. 2009. "Effect of TiO_2 particle size on the photocatalytic reduction of CO_2" Applied Catalysis B: Environmental. 89: 494-502.

KočÍ, K., ZatloukalovÁ, K., ObalovÁ, L., KrejČÍKovÁ, S., LacnÝ, Z., ČApek, L., HospodkovÁ, A., ŠOlcovÁ, O. 2011. "Wavelength Effect on Photocatalytic Reduction of CO_2 by Ag/TiO_2 Catalyst" Chinese Journal of Catalysis. 32: 812-815.

Kong, D., Tan, J.Z.Y., Yang, F., Zeng, J., Zhang, X. 2013. "Electrodeposited Ag nanoparticles on TiO_2 nanorods for enhanced UV visible light photoreduction CO_2 to CH_4" Applied Surface Science. 277: 105-110.

Kruse, N., Chenakin, S. 2011. "XPS characterization of Au/TiO_2 catalysts: Binding energy assessment and irradiation effects" Applied Catalysis A: General. 391: 367-376.

Kudo, A., Miseki, Y. 2009. "Heterogeneous photocatalyst materials for water splitting" Chem Soc Rev. 38: 253-278.

Kwak, B.S., Vignesh, K., Park, N.-K., Ryu, H.-J., Baek, J.-I., Kang, M. 2015. "Methane formation from photoreduction of CO_2 with water using TiO_2 including Ni ingredient" Fuel. 143: 570-576.

Labouriau, A., Earl, W.L. 1997. "Titanium solid-state NMR in anatase, brookite and rutile" Chemical Physics Letters. 270: 278-284.

Lee, C.-W., Antoniou Kourounioti, R., Wu, J.C.S., Murchie, E., Maroto-Valer, M., Jensen, O.E., Huang, C.-W., Ruban, A. 2014. "Photocatalytic conversion of CO_2 to hydrocarbons by light-harvesting complex assisted Rh-doped TiO_2 photocatalyst" Journal of CO_2 Utilization. 5: 33-40.

Li, F.B., Li, X.Z., Ao, C.H., Lee, S.C., Hou, M.F. 2005. "Enhanced photocatalytic degradation of VOCs using Ln^{3+}-TiO_2 catalysts for indoor air purification" Chemosphere. 59: 787-800.

Li, F.B., Li, X.Z., Hou, M.F. 2004. "Photocatalytic degradation of 2-mercaptobenzothiazole in aqueous La^{3+}–TiO_2 suspension for odor control" Applied Catalysis B: Environmental. 48: 185-194.

Li, F.B., Li, X.Z., Hou, M.F., Cheah, K.W., Choy, W.C.H. 2005. "Enhanced photocatalytic activity of Ce^{3+}–TiO_2 for 2-mercaptobenzothiazole degradation in aqueous suspension for odour control" Applied Catalysis A: General. 285: 181-189.

Li, Q., Zong, L., Li, C., Yang, J. 2014. "Photocatalytic reduction of CO_2 on MgO/TiO_2 nanotube films" Applied Surface Science. 314: 458-463.

Li, W., Frenkel, A.I., Woicik, J.C., Ni, C., Shah, S.I. 2005. "Dopant location identification in Nd^{3+}-dopedTiO_2 nanoparticles" Physical Review B. 72: 1-6.

Li, X., Liu, H., Luo, D., Li, J., Huang, Y., Li, H., Fang, Y., Xu, Y., Zhu, L. 2012. "Adsorption of CO_2 on heterostructure $CdS(Bi_2S_3)/TiO_2$ nanotube photocatalysts and their photocatalytic activities in the reduction of CO_2 to methanol under visible light irradiation" Chemical Engineering Journal. 180: 151-158.

Li, X., Xiong, R., Wei, G. 2008. "S–N Co-Doped TiO_2 Photocatalysts with Visible-Light Activity Prepared by Sol–Gel Method" Catalysis Letters. 125: 104-109.

Li, X., Zhuang, Z., Li, W., Pan, H. 2012. "Photocatalytic reduction of CO_2 over noble metal-loaded and nitrogen-doped mesoporous TiO_2" Applied Catalysis A: General. 429-430: 31-38.

Li, Y., Wang, W.-N., Zhan, Z., Woo, M.-H., Wu, C.-Y., Biswas, P. 2010. "Photocatalytic reduction of CO_2 with H_2O on mesoporous silica supported Cu/TiO_2 catalysts" Applied Catalysis B: Environmental. 100: 386-392.

Liang, C.H., Hou, M.F., Zhou, S.G., Li, F.B., Liu, C.S., Liu, T.X., Gao, Y.X., Wang, X.G., Lu, J.L. 2006. "The effect of erbium on the adsorption and photodegradation of orange I in aqueous Er^{3+}-TiO_2 suspension" J Hazard Mater. 138: 471-478.

Linsebigler, A.L., Lu, G., Yates, J.T. 1995. "Photocatalysis on TiO_2 Surfaces: Principles, Mechanisms, and Selected Results" Chemical Reviews. 95: 735-758.

Liu, G., Hoivik, N., Wang, K., Jakobsen, H. 2012. "Engineering TiO_2 nanomaterials for CO_2 conversion/solar fuels" Solar Energy Materials and Solar Cells. 105: 53-68.

Liu, S., Zhao, Z., Wang, Z. 2007. "Photocatalytic reduction of carbon dioxide using sol-gel derived titania-supported CoPc catalysts" Photochem Photobiol Sci. 6: 695-700.

Liu, Y., Zhou, S., Li, J., Wang, Y., Jiang, G., Zhao, Z., Liu, B., Gong, X., Duan, A., Liu, J., Wei, Y., Zhang, L. 2015. "Photocatalytic reduction of CO_2 with water vapor on surface La-modified TiO_2 nanoparticles with enhanced CH_4 selectivity" Applied Catalysis B: Environmental. 168-169: 125-131.

López R., Gómez R. 2012. “Band-gap energy estimation from diffuse reflectance measurements on sol–gel and commercial TiO_2: a comparative study” Journal of Sol-Gel Science and Technology. 61: 1-7.

Luo, W., Li, R., Liu, G., Antonio, M.R., Chen, X. 2008. "Evidence of Trivalent Europium Incorporated in Anatase TiO_2 Nanocrystals with Multiple Sites" The Journal of Physical Chemistry C. 112: 10370-10377.

Luo, Y.,Byrne, R. H. 2004. “Carbonate Complexation of Yttrium and the Rare Earth Elements in Natural Waters” Geochimica et Cosmochimica Acta. 68: 691-699.

Maeda, K. 2011. "Photocatalytic water splitting using semiconductor particles: History and recent developments" Journal of Photochemistry and Photobiology C: Photochemistry Reviews. 12: 237-268.

Magesh, G., Viswanathan, B., Viswanath, R.P., Varadarajan, T.K. 2009. "Photocatalytic behavior of CeO_2-TiO_2 system for the degradation of methylene blue" Indian Journal of Chemistry. 48A: 480-488.

Mahmodi, G., Sharifnia, S., Madani, M., Vatanpour, V. 2013. "Photoreduction of carbon dioxide in the presence of H_2, H_2O and CH_4 over TiO_2 and ZnO photocatalysts" Solar Energy. 97: 186-194.

Mao, J., Ye, L., Li, K., Zhang, X., Liu, J., Peng, T., Zan, L. 2014. "Pt-loading reverses the photocatalytic activity order of anatase TiO_2 {001} and {010} facets for photoreduction of CO_2 to CH_4" Applied Catalysis B: Environmental. 144: 855-862.

Marcì, G., García-López, E.I., Palmisano, L. 2014. "Photocatalytic CO_2 reduction in gas–solid regime in the presence of H_2O by using GaP/TiO_2 composite as photocatalyst under simulated solar light" Catalysis Communications. 53: 38-41.

Matějová, L., Kočí, K., Reli, M., Čapek, L., Hospodková, A., Peikertová, P., Matěj, Z., Obalová, L., Wach, A., Kuśtrowski, P., Kotarba, A. 2014. "Preparation, characterization and photocatalytic properties of cerium doped TiO_2: On the effect of Ce loading on the photocatalytic reduction of carbon dioxide" Applied Catalysis B: Environmental. 152-153: 172-183.

Matějová, L., Kočí, K., Reli, M., Čapek, L., Matějka, V., Šolcová, O., Obalová, L. 2013. "On sol–gel derived Au-enriched TiO_2 and TiO_2-ZrO_2 photocatalysts and their investigation in photocatalytic reduction of carbon dioxide" Applied Surface Science. 285: 688-696.

Maurya, A., Chauhan, P., Mishra, S.K., Srivastava, R.K. 2011. "Structural, optical and charge transport study of rutile TiO_2 nanocrystals at two calcination temperatures" Journal of Alloys and Compounds. 509: 8433-8440.

Menéndez-Flores, V.M., Nakamura, M., Kida, T., Jin, Z., Murakami, N., Ohno, T. 2011. "Controlled structure of anatase TiO_2 nanoparticles by using organic additives in a microwave process" Applied Catalysis A: General. 406: 119-123.

Merajin, M.T., Sharifnia, S., Hosseini, S.N., Yazdanpour, N. 2013. "Photocatalytic conversion of greenhouse gases (CO_2 and CH_4) to high value products using TiO_2 nanoparticles supported on stainless steel webnet" Journal of the Taiwan Institute of Chemical Engineers. 44: 239-246.

Moeller, T., Kremers, H.E. 1944. "Observations on the Rare Earths. LI. An Electrometric Study of the Precipitation of Trivalent Hydrous Rare Earth Oxides or Hydroxides" The Journal of Physical Chemistry. 48: 395-406.

Molinari, R., Marino, T., Argurio, P. 2014. "Photocatalytic membrane reactors for hydrogen production from water" International Journal of Hydrogen Energy. 39: 7247-7261.

Montini, T., Gombac, V., Sordelli, L., Delgado, J.J., Chen, X., Adami, G., Fornasiero, P. 2011. "Nanostructured Cu/TiO_2 Photocatalysts for H2 Production from Ethanol and Glycerol Aqueous Solutions" ChemCatChem. 3: 574-577.

Moore, R., Clark, W. D., Kingsley, R. S., Vodopich, D. "Botany" William C Brown Pub, U.S.A, 1995.

Nassoko, D., Li, Y.-F., Li, J.-L., Li, X., Yu, Y. 2012. "Neodymium-Doped TiO_2 with Anatase and Brookite Two Phases: Mechanism for Photocatalytic Activity Enhancement under Visible Light and the Role of Electron" International Journal of Photoenergy. 2012: 1-10.

Neatu, S., Macia-Agullo, J.A., Garcia, H. 2014. "Solar light photocatalytic CO_2 reduction: general considerations and selected bench-mark photocatalysts" Int J Mol Sci. 15: 5246-5262.

Nguyen-Phan, T.-D., Song, M.B., Kim, E.J., Shin, E.W. 2009. "The role of rare earth metals in lanthanide-incorporated mesoporous titania" Microporous and Mesoporous Materials. 119: 290-298.

Nguyen, T.-V., Wu, J.C.S. 2008. "Photoreduction of CO_2 in an optical-fiber photoreactor: Effects of metals addition and catalyst carrier" Applied Catalysis A: General. 335: 112-120.

Ni, M., Leung, M.K.H., Leung, D.Y.C., Sumathy, K. 2007. "A review and recent developments in photocatalytic water-splitting using TiO_2 for hydrogen production" Renewable and Sustainable Energy Reviews. 11: 401-425.

Nie, X., Zhuo, S., Maeng, G., Sohlberg, K. 2009. "Doping of TiO_2 Polymorphs for Altered Optical and Photocatalytic Properties" International Journal of Photoenergy. 2009: 1-22.

Ningthoujam, R.S., Sudarsan, V., Vatsa, R.K., Kadam, R.M., Jagannath, Gupta, A. 2009. "Photoluminescence studies on Eu doped TiO_2 nanoparticles" Journal of Alloys and Compounds. 486: 864-870.

Nishikiori, H., Hayashibe, M., Fujii, T. 2013. "Visible Light-Photocatalytic Activity of Sulfate-Doped Titanium Dioxide Prepared by the Sol–Gel Method" Catalysts. 3: 363-377.

Obregón, S., Kubacka, A., Fernández-García, M., Colón, G. 2013. "High-performance Er^{3+}–TiO_2 system: Dual up-conversion and electronic role of the lanthanide" Journal of Catalysis. 299: 298-306.

Ogura, K., Kawano, M., Yano, J., Sakata, Y. 1992. "Visible-light-assisted decomposition of H_2O and photomethanation of CO_2 over CeO_2-TiO_2 catalyst" Journal of Photochemistry and Photobiology A: Chemistry. 66: 91-97.

Ohno, T., Higo, T., Murakami, N., Saito, H., Zhang, Q., Yang, Y., Tsubota, T. 2014. "Photocatalytic reduction of CO_2 over exposed-crystal-face-controlled TiO_2 nanorod having a brookite phase with co-catalyst loading" Applied Catalysis B: Environmental. 152-153: 309-316.

Ola, O., Maroto-Valer, M., Liu, D., Mackintosh, S., Lee, C.-W., Wu, J.C.S. 2012. "Performance comparison of CO_2 conversion in slurry and monolith photoreactors using Pd and Rh-TiO_2 catalyst under ultraviolet irradiation" Applied Catalysis B: Environmental. 126: 172-179.

Ong, W.-J., Gui, M.M., Chai, S.-P., Mohamed, A.R. 2013. "Direct growth of carbon nanotubes on Ni/TiO_2 as next generation catalysts for photoreduction of CO_2 to methane by water under visible light irradiation" RSC Advances. 3: 4505.

Ozcan, O., Yukruk, F., Akkaya, E., Uner, D. 2007. "Dye sensitized artificial photosynthesis in the gas phase over thin and thick TiO_2 films under UV and visible light irradiation" Applied Catalysis B: Environmental. 71: 291-297.

Park, J.H., Kim, S., Bard, A.J. 2006. "Novel Carbon-Doped TiO_2 Nanotube Arrays with High Aspect Ratios for Efficient Solar Water Splitting" Nano Letters. 6: 24-28.

Pavasupree, S., Suzuki, Y., Pivsa-Art, S., Yoshikawa, S. 2005. "Preparation and characterization of mesoporous TiO_2–CeO_2 nanopowders respond to visible wavelength" Journal of Solid State Chemistry. 178: 128-134.

Pedersen, O., Colmer, T.D., Sand-Jensen, K. 2013. "Underwater photosynthesis of submerged plants - recent advances and methods" Front Plant Sci. 4: 140.

Peng, F., Cai, L., Yu, H., Wang, H., Yang, J. 2008. "Synthesis and characterization of substitutional and interstitial nitrogen-doped titanium dioxides with visible light photocatalytic activity" Journal of Solid State Chemistry. 181: 130-136.

Puskelova, J., Michal, R., Caplovicova, M., Antoniadou, M., Caplovic, L., Plesch, G., Lianos, P. 2014. "Hydrogen production by photocatalytic ethanol reforming using Eu- and S-doped anatase" Applied Surface Science. 305: 665-669.

Qian, W., Wei, W. Jianfeng, C., Guangwen, C., Kai, M., Haikui Z. 2012. "Novel synthesis of ZnPc/TiO_2 composite particles and carbon dioxide photo-catalytic reduction efficiency study under simulated solar radiation conditions" Colloids and Surfaces A: Physicochemical and Engineering Aspects. 409: 118-125.

Qin, G., Zhang, Y., Ke, X., Tong, X., Sun, Z., Liang, M., Xue, S. 2013. "Photocatalytic reduction of carbon dioxide to formic acid, formaldehyde, and methanol using dye-sensitized TiO_2 film" Applied Catalysis B: Environmental. 129: 599-605.

Raja, K.S., Smith, Y.R., Kondamudi, N., Manivannan, A., Misra, M., Subramanian, V. 2011. "CO_2 Photoreduction in the Liquid Phase over Pd-Supported on TiO_2 Nanotube and Bismuth Titanate Photocatalysts" Electrochemical and Solid-State Letters. 14: F5.

Rajalakshmi, K., Jeyalakshmi, V., Krishnamurthy, K.R., Viswanathan, B. 2012. "Photocatalytic reduction of carbon dioxide by water on titania: Role of photophysical and structural properties" Indian Journal of Chemistry. 51A: 411-419.

Ranade, M.R., Navrotsky, A., Zhang, H.Z., Banfield, J.F., Elder, S.H., Zaban, A., Borse, P.H., Kulkarni, S.K., Doran, G.S., Whitfield, H.J. 2002. "Energetics of nanocrystalline TiO_2" Proc Natl Acad Sci U S A. 99 Suppl 2: 6476-6481.

Rani, S., Bao, N., Roy, S.C. 2014. "Solar Spectrum Photocatalytic Conversion of CO_2 and Water Vapor Into Hydrocarbons Using TiO_2 Nanoparticle Membranes" Applied Surface Science. 289: 203-208.

Ranjit, K.T., Willner, I., Bossmann, S.H., Braun, A.M. 2001. "Lanthanide Oxide Doped Titanium Dioxide Photocatalysts: Effective Photocatalysts for the Enhanced Degradation of Salicylic Acid and t-Cinnamic Acid" Journal of Catalysis. 204: 305-313.

Rapsomanikis, A., Apostolopoulou, A., Stathatos, E., Lianos, P. 2014. "Cerium-modified TiO_2 nanocrystalline films for visible light photocatalytic activity" Journal of Photochemistry and Photobiology A: Chemistry. 280: 46-53.

Reszczyńska, J., Grzyb, T., Sobczak, J.W., Lisowski, W., Gazda, M., Ohtani, B., Zaleska, A. 2014. "Lanthanide co-doped TiO_2: The effect of metal type and amount on surface properties and photocatalytic activity" Applied Surface Science. 307: 333-345.

Reszczyńska, J., Grzyb, T., Sobczak, J.W., Lisowski, W., Gazda, M., Ohtani, B., Zaleska, A. 2015. "Visible light activity of rare earth metal doped (Er^{3+}, Yb^{3+} or Er^{3+}/Yb^{3+}) titania photocatalysts" Applied Catalysis B: Environmental. 163: 40-49.

Rockafellow, E.M., Stewart, L.K., Jenks, W.S. 2009. "Is sulfur-doped TiO_2 an effective visible light photocatalyst for remediation?" Applied Catalysis B: Environmental. 91: 554-562.

Ruzmanova, Y., Ustundas, M., Stoller, M., Chianese, A. 2013. "Photocatalytic Treatment of Olive Mill Wastewater by N-doped Titanium Dioxide Nanoparticles under Visible Light" Chemical Engineering Transections. 32: 2233-2238.

Saif, M., Abdel-Mottaleb, M.S.A. 2007. "Titanium dioxide nanomaterial doped with trivalent lanthanide ions of Tb, Eu and Sm: Preparation, characterization and potential applications" Inorganica Chimica Acta. 360: 2863-2874.

Sasirekha, N., Basha, S., Shanthi, K. 2006. "Photocatalytic performance of Ru doped anatase mounted on silica for reduction of carbon dioxide" Applied Catalysis B: Environmental. 62: 169-180.

Sato, S., Takahashi, R., Sodesawa, T., Igarashi, A., Inoue, H. 2007. "Catalytic reaction of 1,3-butanediol over rare earth oxides" Applied Catalysis A: General. 328: 109-116.

Setiawati, E., Kawano, K., Tsuboi, T., Seo, H.J. 2008. "Studies on Thermal Migration of Eu Ion Doped into TiO_2 Nanoparticles" Japanese Journal of Applied Physics. 47: 4651-4657.

Shah, S.I., Li, W., Huang, C.P., Jung, O., Ni, C. 2002. "Study of Nd^{3+}, Pd^{2+}, Pt^{4+}, and Fe^{3+} dopant effect on photoreactivity of TiO_2 nanoparticles" Proc Natl Acad Sci U S A. 99 Suppl 2: 6482-6486.

Shahmoradi, B., Ibrahim, I.A., Sakamoto, N., Ananda, S., Somashekar, R., Row, T.N., Byrappa, K. 2010. "Photocatalytic treatment of municipal wastewater using modified neodymium doped TiO_2 hybrid nanoparticles" J Environ Sci Health A Tox Hazard Subst Environ Eng. 45: 1248-1255.

Shen, H., Mi, L., Xu, P., Shen, W., Wang, P.-N. 2007. "Visible-light photocatalysis of nitrogen-doped TiO_2 nanoparticulate films prepared by low-energy ion implantation" Applied Surface Science. 253: 7024-7028.

Sibu, C.P., Kumar, S.R., Mukundan, P., Warrier, K.G.K. 2002. "Structural Modifications and Associated Properties of Lanthanum Oxide Doped Sol–Gel Nanosized Titanium Oxide" Chemistry of Materials. 14: 2876-2881.

Silija, P., Yaakob, Z., Suraja, V., Binitha, N.N., Akmal, Z.S. 2012. "An Enthusiastic Glance in to the Visible Responsive Photocatalysts for Energy Production and Pollutant Removal, with Special Emphasis on Titania" International Journal of Photoenergy. 2012: 1-19.

Silva, A.M.T., Silva, C.G., Dražić, G., Faria, J.L. 2009. "Ce-doped TiO_2 for photocatalytic degradation of chlorophenol" Catalysis Today. 144: 13-18.

Škapin, S.D., Kolar, D., Suvorov, D. 2000. "Phase stability and equilibria in the La_2O_3–TiO_2 system" Journal of the European Ceramic Society. 20: 1179-1185.

Slamet, Nasution, H., Purnama, E., Kosela, S., Gunlazuardi, J. 2005. "Photocatalytic reduction of CO_2 on copper-doped Titania catalysts prepared by improved-impregnation method" Catalysis Communications. 6: 313-319.

Spurr, R.A., Myers, H. 1957. "Quantitative Analysis of Anatase-Rutile Mixtures with an X-Ray Diffractometer" Analytical Chemistry. 29: 760-762.

Sreekanth, N., Phani, K.L. 2014. "Selective reduction of CO_2 to formate through bicarbonate reduction on metal electrodes: new insights gained from SG/TC mode of SECM" Chemical Communications. 50: 11143-11146.

Sun, Z., Hu, Z., Yan, Y., Zheng, S. 2014. "Effect of preparation conditions on the characteristics and photocatalytic activity of TiO_2/purified diatomite composite photocatalysts" Applied Surface Science. 314: 251-259.

Swamy, V., Menzies, D., Muddle, B.C., Kuznetsov, A., Dubrovinsky, L.S., Dai, Q., Dmitriev, V. 2006. "Nonlinear size dependence of anatase TiO_2 lattice parameters" Applied Physics Letters. 88: 243103.

Tahir, M., Amin, N.S. 2013. "Advances in visible light responsive titanium oxide-based photocatalysts for CO_2 conversion to hydrocarbon fuels" Energy Conversion and Management. 76: 194-214.

Tahir, M., Amin, N.S. 2015. "Indium-doped TiO_2 nanoparticles for photocatalytic CO_2 reduction with H_2O vapors to CH_4" Applied Catalysis B: Environmental. 162: 98-109.

Tahir, M., Amin, N.S. 2013. "Photocatalytic CO_2 reduction and kinetic study over In/TiO_2 nanoparticles supported microchannel monolith photoreactor" Applied Catalysis A: General. 467: 483-496.

Tahir, M., Amin, N.S. 2013. "Photocatalytic CO_2 reduction with H_2O vapors using montmorillonite/TiO_2 supported microchannel monolith photoreactor" Chemical Engineering Journal. 230: 314-327.

Tahir, M., Amin, N.S. 2013. "Photocatalytic reduction of carbon dioxide with water vapors over montmorillonite modified TiO_2 nanocomposites" Applied Catalysis B: Environmental. 142-143: 512-522.

Tahir, M., Amin, N.S. 2013. "Recycling of carbon dioxide to renewable fuels by photocatalysis: Prospects and challenges" Renewable and Sustainable Energy Reviews. 25: 560-579.

Tan, J.Z.Y., Fernández, Y., Liu, D., Maroto-Valer, M., Bian, J., Zhang, X. 2012. "Photoreduction of CO_2 using copper-decorated TiO_2 nanorod films with localized surface plasmon behavior" Chemical Physics Letters. 531: 149-154.

Tan, S.S., Zou, L., Hu, E. 2006. "Photocatalytic reduction of carbon dioxide into gaseous hydrocarbon using TiO_2 pellets" Catalysis Today. 115: 269-273.

Tang, C., Hou, W., Liu, E., Hu, X., Fan, J. 2014. "CeF_3/TiO_2 composite as a novel visible-light-driven photocatalyst based on upconversion emission and its application for photocatalytic reduction of CO_2" Journal of Luminescence. 154: 305-309.

Thompson, T.L., Yates, J.T. 2006. "Surface Science Studies of the Photoactivation of TiO_2 New Photochemical Processes" Chemical Reviews. 106: 4428-4453.

Tian, M., Wang, H., Sun, D., Peng, W., Tao, W. 2014. "Visible light driven nanocrystal anatase TiO_2 doped by Ce from sol–gel method and its photoelectrochemical water splitting properties" International Journal of Hydrogen Energy. 39: 13448-13453.

Tong, T., Zhang, J., Tian, B., Chen, F., He, D., Anpo, M. 2007. "Preparation of Ce-TiO_2 catalysts by controlled hydrolysis of titanium alkoxide based on esterification reaction and study on its photocatalytic activity" Journal of Colloid Interface Science. 315: 382-388.

Tripathi, A.K., Singh, M.K., Mathpal, M.C., Mishra, S.K., Agarwal, A. 2013. "Study of structural transformation in TiO_2 nanoparticles and its optical properties" Journal of Alloys and Compounds. 549: 114-120.

Truong, Q.D., Le, T.H., Liu, J.-Y., Chung, C.-C., Ling, Y.-C. 2012. "Synthesis of TiO_2 nanoparticles using novel titanium oxalate complex towards visible light-driven photocatalytic reduction of CO_2 to CH_3OH" Applied Catalysis A: General. 437-438: 28-35.

Tseng, I.H., Chang, W.-C., Wu, J.C.S. 2002. "Photoreduction of CO_2 using sol–gel derived titania and titania-supported copper catalysts" Applied Catalysis B: Environmental. 37: 37-48.

Tseng, I.H., Wu, J.C.S., Chou, H.-Y. 2004. "Effects of sol–gel procedures on the photocatalysis of Cu/TiO_2 in CO_2 photoreduction" Journal of Catalysis. 221: 432-440.

Tseng, T.K., Lin, Y.S., Chen, Y.J., Chu, H. 2010. "A review of photocatalysts prepared by sol-gel method for VOCs removal" Int J Mol Sci. 11: 2336-2361.

Uner, D., Oymak, M.M., İpek, B. 2011. "CO_2 utilisation by photocatalytic conversion to methane and methanol" International Journal of Global Warming. 3: 142-162.

Varghese, O.K., Paulose, M., LaTempa, T.J., Grimes, C.A. 2009. "High-Rate Solar Photocatalytic Conversion of CO_2 and Water Vapor to Hydrocarbon Fuels" Nano Letters. 9: 731-737.

Wagner, C.D., Davis, L. E., Zeller, M. V., Taylor, J. A., Raymond, R. H., Gale, L. H. 1981. “Empirical Atomic Sensitivity Factors for Quantitative Analysis by Electron Spectroscopy for Chemical Analysis” Surface and Interface Analysis. 3; 211-225.

Wang, C., Ao, Y., Wang, P., Hou, J., Qian, J. 2010. "Preparation, characterization and photocatalytic activity of the neodymium-doped TiO_2 hollow spheres" Applied Surface Science. 257: 227-231.

Wang, J., Ji, G., Liu, Y., Gondal, M.A., Chang, X. 2014. "Cu_2O/TiO_2 heterostructure nanotube arrays prepared by an electrodeposition method exhibiting enhanced photocatalytic activity for CO_2 reduction to methanol" Catalysis Communications. 46: 17-21.

Wang, P.-Q., Bai, Y., Liu, J.-Y., Fan, Z., Hu, Y.-Q. 2012. "One-pot synthesis of rutile TiO_2 nanoparticle modified anatase TiO_2 nanorods toward enhanced photocatalytic reduction of CO_2 into hydrocarbon fuels" Catalysis Communications. 29: 185-188.

Wang, Y., Li, B., Zhang, C., Cui, L., Kang, S., Li, X., Zhou, L. 2013. "Ordered mesoporous CeO_2-TiO_2 composites: Highly efficient photocatalysts for the reduction of CO_2 with H_2O under simulated solar irradiation" Applied Catalysis B: Environmental. 130-131: 277-284.

Windle, C.D., Perutz, R.N. 2012. "Advances in molecular photocatalytic and electrocatalytic CO_2 reduction" Coordination Chemistry Reviews. 256: 2562-2570.

Wojtowicz, J.A. 2001. "The Carbonate System in Swimming Pool Water" Journal of the Swimming Pool and Spa Industry. 4: 54-59.

Wu, G. 2008. "H_2 production with ultra-low CO selectivity via photocatalytic reforming of methanol on Au/TiO_2 catalyst" International Journal of Hydrogen Energy. 33: 1243-1251.

Wu, J.C.S., Lin, H.-M., Lai, C.-L. 2005. "Photo reduction of CO_2 to methanol using optical-fiber photoreactor" Applied Catalysis A: General. 296: 194-200.

Xiao, Q., Si, Z., Zhang, J., Xiao, C., Tan, X. 2008. "Photoinduced hydroxyl radical and photocatalytic activity of samarium-doped TiO_2 nanocrystalline" J Hazard Mater. 150: 62-67.

Xiao, Q., Si, Z., Zhang, J., Xiao, C., Yu, Z., Qiu, G. 2007. "Effects of samarium dopant on photocatalytic activity of TiO_2 nanocrystallite for methylene blue degradation" Journal of Materials Science. 42: 9194-9199.

Xie, J., Jiang, D., Chen, M., Li, D., Zhu, J., Lü, X., Yan, C. 2010. "Preparation and characterization of monodisperse Ce-doped TiO_2 microspheres with visible light photocatalytic activity" Colloids and Surfaces A: Physicochemical and Engineering Aspects. 372: 107-114.

Xie, Y., Yuan, C. 2004. "Characterization and photocatalysis of Eu^{3+}–TiO_2 sol in the hydrosol reaction system" Materials Research Bulletin. 39: 533-543.

Xie, Y., Yuan, C. 2004. "Photocatalysis of neodymium ion modified TiO_2 sol under visible light irradiation" Applied Surface Science. 221: 17-24.

Xie, Y., Yuan, C., Li, X. 2005. "Photosensitized and photocatalyzed degradation of azo dye using Ln^{n+}-TiO_2 sol in aqueous solution under visible light irradiation" Materials Science and Engineering: B. 117: 325-333.

Xin, Y., Liu, H. 2011. "Study on mechanism of photocatalytic performance of La-doped TiO_2/Ti photoelectrodes by theoretical and experimental methods" Journal of Solid State Chemistry. 184: 3240-3246.

Xu, J., Ao, Y., Fu, D., Yuan, C. 2009. "Synthesis of Gd-doped TiO_2 nanoparticles under mild condition and their photocatalytic activity" Colloids and Surfaces A: Physicochemical and Engineering Aspects. 334: 107-111.

Xu, Y.-H., Chen, C., Yang, X.-L., Li, X., Wang, B.-F. 2009. "Preparation, characterization and photocatalytic activity of the neodymium-doped TiO_2 nanotubes" Applied Surface Science. 255: 8624-8628.

Xue, L.M., Zhang, F.H., Fan, H.J., Bai, X.F. 2011. "Preparation of C Doped TiO_2 Photocatalysts and their Photocatalytic Reduction of Carbon Dioxide" Advanced Materials Research. 183-185: 1842-1846.

Yan, G., Zhang, M., Hou, J., Yang, J. 2011. "Photoelectrochemical and photocatalytic properties of N+S co-doped TiO_2 nanotube array films under visible light irradiation" Materials Chemistry and Physics. 129: 553-557.

Yan, X., He, J., G. Evans, D., Duan, X., Zhu, Y. 2005. "Preparation, characterization and photocatalytic activity of Si-doped and rare earth-doped TiO_2 from mesoporous precursors" Applied Catalysis B: Environmental. 55: 243-252.

Yang, G., Jiang, Z., Shi, H., Xiao, T., Yan, Z. 2010. "Preparation of highly visible-light active N-doped TiO_2 photocatalyst" Journal of Materials Chemistry. 20: 5301.

Yazdanpour, N., Sharifnia, S. 2013. "Photocatalytic conversion of greenhouse gases (CO_2 and CH_4) using copper phthalocyanine modified TiO_2" Solar Energy Materials and Solar Cells. 118: 1-8.

Yoneyama, H. 1997. "Photoreduction of carbon dioxide on quantized semiconductor nanoparticles in solution" Catalysis Today. 39: 169-175.

Yu, J.C., Ho, W., Yu, J., Yip, H., Wong, P.K., Zhao, J. 2005. "Efficient Visible-Light-Induced Photocatalytic Disinfection on Sulfur-Doped Nanocrystalline Titania" Environmental Science & Technology. 39: 1175-1179.

Zalas, M., Laniecki, M. 2005. "Photocatalytic hydrogen generation over lanthanides-doped titania" Solar Energy Materials and Solar Cells. 89: 287-296.

Zaleska, A. 2008. "Doped-TiO_2: A Review" Recent Patents on Engineering. 2: 157-164.

Zang, L. “Energy Efficiency and Renewable Energy Through Nanotechnology” Springer, U.S.A, 2011.

Zhang, H., Banfield, J.F. 2000. "Understanding Polymorphic Phase Transformation Behavior during Growth of Nanocrystalline Aggregates: Insights from TiO_2" The Journal of Physical Chemistry B. 104: 3481-3487.

Zhang, J., Xu, Q., Feng, Z., Li, M., Li, C. 2008. "Importance of the relationship between surface phases and photocatalytic activity of TiO_2" Angew Chem Int Ed Engl. 47: 1766-1769.

Zhang, J., Yan, S., Zhao, S., Xu, Q., Li, C. 2013. "Photocatalytic activity for H_2 evolution of TiO2 with tuned surface crystalline phase" Applied Surface Science. 280: 304-311.

Zhang, M., Wu, J., Lu, D., Yang, J. 2013. "Enhanced Visible Light Photocatalytic Activity for TiO_2 Nanotube Array Films by Codoping with Tungsten and Nitrogen" International Journal of Photoenergy. 2013: 1-8.

Zhang, Q.-H., Han, W.-D., Hong, Y.-J., Yu, J.-G. 2009. "Photocatalytic reduction of CO_2 with H_2O on Pt-loaded TiO_2 catalyst" Catalysis Today. 148: 335-340.

Zhang, Q., Li, Y., Ackerman, E.A., Gajdardziska-Josifovska, M., Li, H. 2011. "Visible light responsive iodine-doped TiO_2 for photocatalytic reduction of CO_2 to fuels" Applied Catalysis A: General. 400: 195-202.

Zhang, Q., Lin, C.-F., Chen, B.-Y., Ouyang, T., Chang, C.-T. 2015. "Deciphering Visible Light Photoreductive Conversion of CO_2 to Formic Acid and Methanol Using Waste Prepared Material" Environmental Science & Technology. 49: 2405-2417.

Zhang, Y., Zhang, H., Xu, Y., Wang, Y. 2004. "Significant effect of lanthanide doping on the texture and properties of nanocrystalline mesoporous TiO_2" Journal of Solid State Chemistry. 177: 3490-3498.

Zhao, C., Krall, A., Zhao, H., Zhang, Q., Li, Y. 2012. "Ultrasonic spray pyrolysis synthesis of Ag/TiO_2 nanocomposite photocatalysts for simultaneous H_2 production and CO_2 reduction" International Journal of Hydrogen Energy. 37: 9967-9976.

Zhao, C., Liu, L., Zhang, Q., Wang, J., Li, Y. 2012. "Photocatalytic conversion of CO_2 and H_2O to fuels by nanostructured Ce–TiO_2/SBA-15 composites" Catalysis Science & Technology. 2: 2558.

Zhao, L., Jiang, Q., Lian, J. 2008. "Visible-light photocatalytic activity of nitrogen-doped TiO_2 thin film prepared by pulsed laser deposition" Applied Surface Science. 254: 4620-4625.

Zhao, Z.-H., Fan, J.-M., Wang, Z.-Z. 2007. "Photo-catalytic CO_2 reduction using sol–gel derived titania-supported zinc-phthalocyanine" Journal of Cleaner Production. 15: 1894-1897.

Zhao, Z., Fan, J., Wang, J., Li, R. 2012. "Effect of heating temperature on photocatalytic reduction of CO_2 by N–TiO_2 nanotube catalyst" Catalysis Communications. 21: 32-37.

Zhou, S., Liu, Y., Li, J., Wang, Y., Jiang, G., Zhao, Z., Wang, D., Duan, A., Liu, J., Wei, Y. 2014. "Facile in situ synthesis of graphitic carbon nitride (g-C_3N_4)-N-TiO_2 heterojunction as an efficient photocatalyst for the selective photoreduction of CO_2 to CO" Applied Catalysis B: Environmental. 158-159: 20-29.

Zhu, J., Zäch, M. 2009. "Nanostructured materials for photocatalytic hydrogen production" Current Opinion in Colloid & Interface Science. 14: 260-269.

APPENDIX A

SAMPLE CALCULATIONS

XRD pattern of pure sol-gel TiO_2 powder heat treated at 700°C was selected for the sample calculations. Sample calculations for anatase crystal structure were shown.

The crystallite sizes were calculated from the broadening of the (101) reflection by using Scherrer's equation:

$$d = \frac{k.\lambda}{\beta.\cos\theta} \tag{A.1}$$

d: crystallite size (nm),
k: shape constant (0.9 for spherical particles),
λ: X-ray wavelength (0.154 nm),
β: full width at half maximum of the selected peak
θ is the Bragg's angle of diffraction (radian)

β values were determined by the software program X'Pert Plus. Peak broadening due to instrumentation was determined to be 0.112 for Philips X'pert Pro XRD equipment.

β (101) = 0.210^{o} = 0.0037 radian
β (instrument) = 0.112^{o} = 0.002 radian
β (true) = $(0.0037^{2}-0.002^{2})^{0.5}$ = 0.0031
$2\theta = 25.2^{o} \rightarrow \theta = 0.22$ radian
$d = \frac{0.9*0.154}{0.0031*cos0.22} = 45$ nm

The rutile and anatase weight fractions were determined by using the following relation:

$$x_A = \left(1 + 1.26\frac{I_R}{I_A}\right)^{-1} \tag{A.2}$$

x_A: anatase weight fraction,

x_B: rutile weight fraction

I_R: the intensity of the rutile (110) peak

I_A: the intensity of the anatase (101) peak

I_R and I_A were determined by the software program X'Pert Plus.

$I_R = 17845$

$I_A = 10057$

$$x_A = \left(1 + 1.26\frac{17845}{10057}\right)^{-1} = 0.31$$

$$x_B = 1 - x_A = 1 - 0.31 = 0.69$$

The determination of the lattice constants for tetragonal geometry (a and c) was conducted using the following expression by selecting two peaks ((101) and (200) peaks for anatase):

$$\frac{1}{d_{hkl}^2} = \frac{h^2+k^2}{a^2} + \frac{l^2}{c^2} \tag{A.3}$$

d_{hkl}: the interplane distance $d = (n^* \lambda)/(2^*\sin\theta)$ (Bragg's Law)

$n = 1$

$\lambda = 1.54$ Å

hkl: the Miller (plane) indices

Internal standard (aluminum cassette) was used for the correction of the peak positions of the planes (101) and (200).

Aluminum cassette peak position: 42.703° (Original aluminum peak position at 44.723° 2θ → (101) and (200) plane peaks are shifted by $+2.02^\circ$)

For the lattice plane (200)

$2\theta = 47.921^\circ$

Corrected $2\theta = 47.921+2.02 = 49.941^\circ$ → $\theta = 0.436$ radian d = (1.54/2/sin0.436) = 1.89

$$\frac{1}{1.89^2} = \frac{2^2+0^2}{a^2} + \frac{0^2}{c^2} \rightarrow \text{a} = 3.78\ \text{Å}$$

d (101) → 3.517

since a is known

$$\frac{1}{3.517^2} = \frac{2^2+1^2}{3.78^2} + \frac{1^2}{c^2} \rightarrow \text{c} = 9.597\ \text{Å}$$

Lattice strain in the TiO_2 crystal lattice was calculated by using Williamson-Hall (W-H) plot with at least 4 diffraction peaks to be used in the following relation:

$$\frac{\beta\cos\theta}{\lambda} = \frac{1}{\sigma} + \frac{\eta.\sin\theta}{\lambda} \tag{A.4}$$

σ: effective particle size

η: effective strain

β, $\cos\theta$ and $\sin\theta$ were calculated for 6 different planes of anatase and then $\beta\cos\theta/\lambda$ vs. $\sin\theta/\lambda$ is plotted as shown in Figure A1. The slope is the effective strain (η).

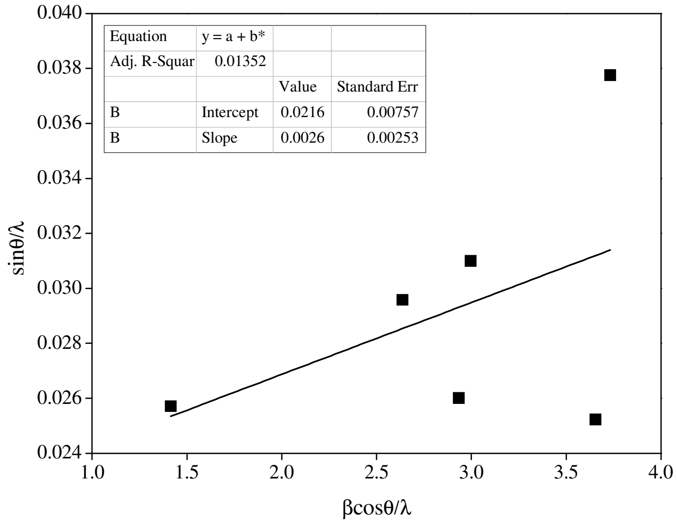

Figure A.1. Sample W-H plot.

Bandgap of a powder was determined by using Kubelka-Munk transformation and UV-Vis DR spectrum:

$$F(R) = \frac{(1-R)^n}{2R} \tag{A.5}$$

R: reflectance
F(R): Kubelka-Munk function
n = 1/2 for indirect bandgap and 2 for direct bandgap

$[F(R)*h*\nu]^n$ vs. photon energy ($h*\nu$) was plotted and a line was drawn tangent to the inflection point on the curve as seen in Figure A2 and the $h*\nu$ value at the intersection of extrapolation of the straight portion of the curve to zero absorption with photon energy axis i.e. $[F(R)*h*\nu]^n \rightarrow 0$ gave the bandgap energy. The plot in Figure A2 was constructed by using the UV-Vis DR spectrum of pure sol-gel TiO_2 powder heat treated at 600°C.

h: Planck’s constant = $4.14*10^{-15}$ eV/s
ν: speed of light = $3*10^{7}$ nm/s

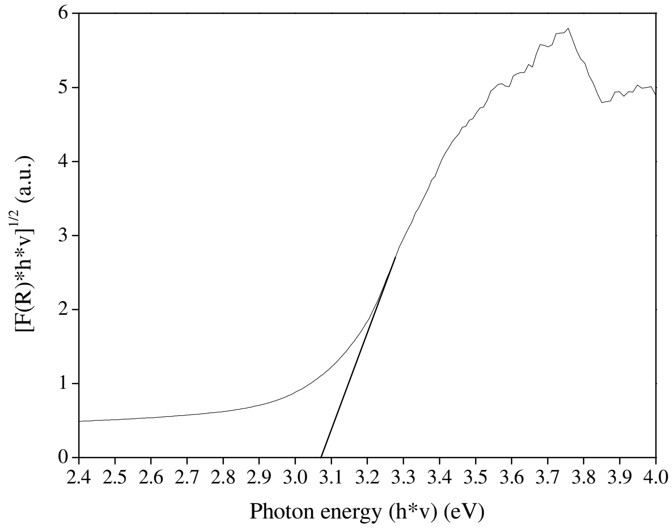

Figure A.2. Sample $[F(R)*h*v]^{1/2}$ vs. photon energy plot.

APPENDIX B

XRD PATTERNS OF THE SOL-GEL POWDERS

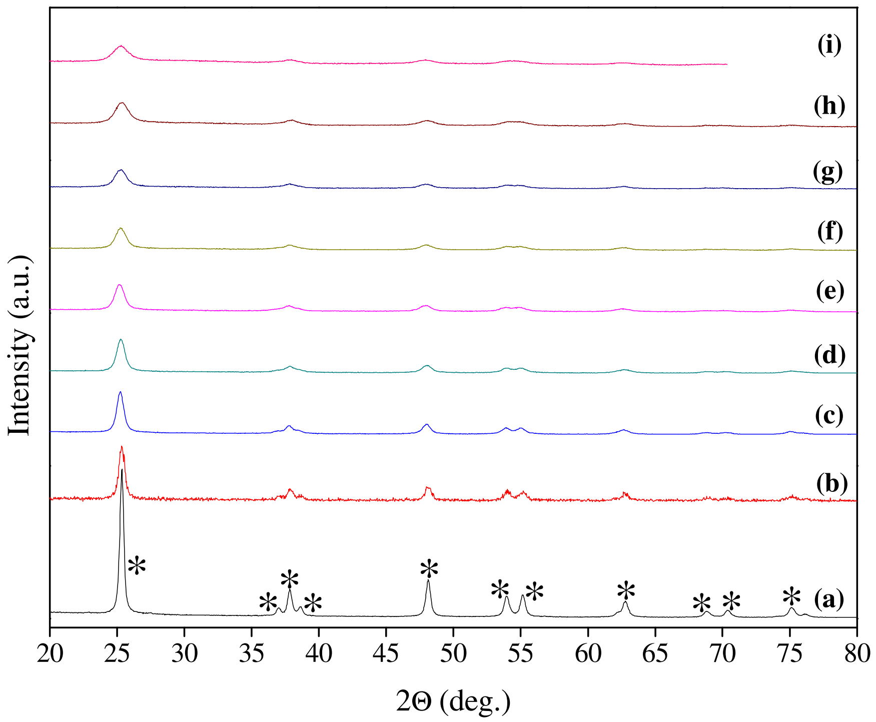

Figure A.3. XRD patterns of Er_2O_3 doped TiO_2 powders heat treated at 600°C: (a) pure, (b) 0.1% (c) 0.25%, (d) 0.5%, (e) 1%, (f) 2%, (g) 3%, (h) 4%, (i) 5% doped TiO_2 powder (*: anatase).

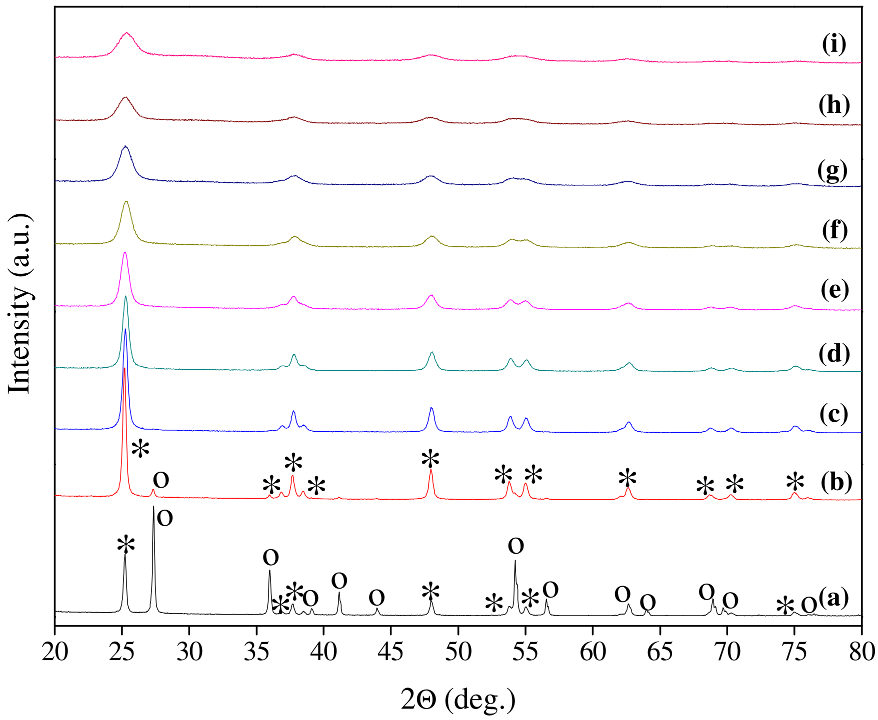

Figure A.4. XRD patterns of Er_2O_3 doped TiO_2 powders heat treated at 700°C: (a) pure, (b) 0.1% (c) 0.25%, (d) 0.5%, (e) 1%, (f) 2%, (g) 3%, (h) 4%, (i) 5% doped TiO_2 powder (*: anatase, o: rutile).

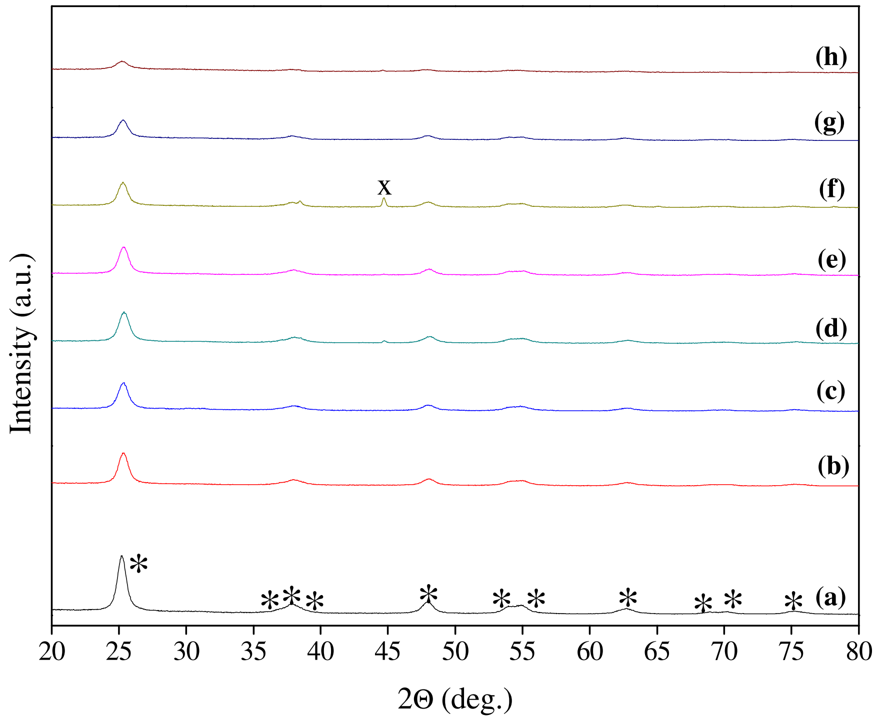

Figure A.5. XRD patterns of CeO_2 doped TiO_2 powders heat treated at 400°C: (a) pure, (b) 0.25%, (c) 0.5%, (d) 1%, (e) 2%, (f) 3%, (g) 4%, (h) 5% doped TiO_2 powder (*: anatase, x: aluminum sample holder).

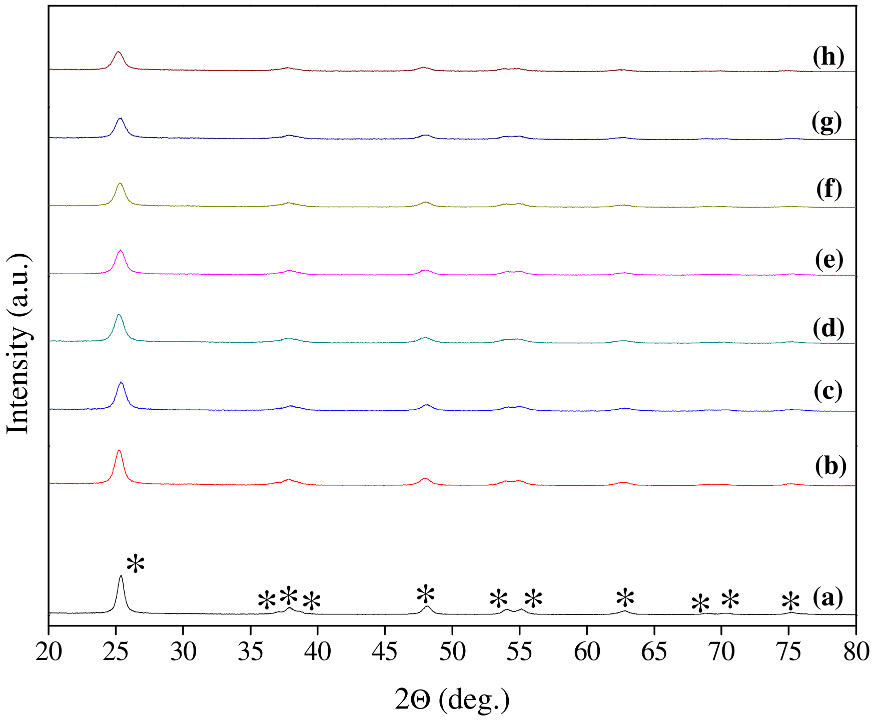

Figure A.6. XRD patterns of CeO_2 doped TiO_2 powders heat treated at 500°C: (a) pure, (b) 0.25%, (c) 0.5%, (d) 1%, (e) 2%, (f) 3%, (g) 4%, (h) 5% doped TiO_2 powder (*: anatase).

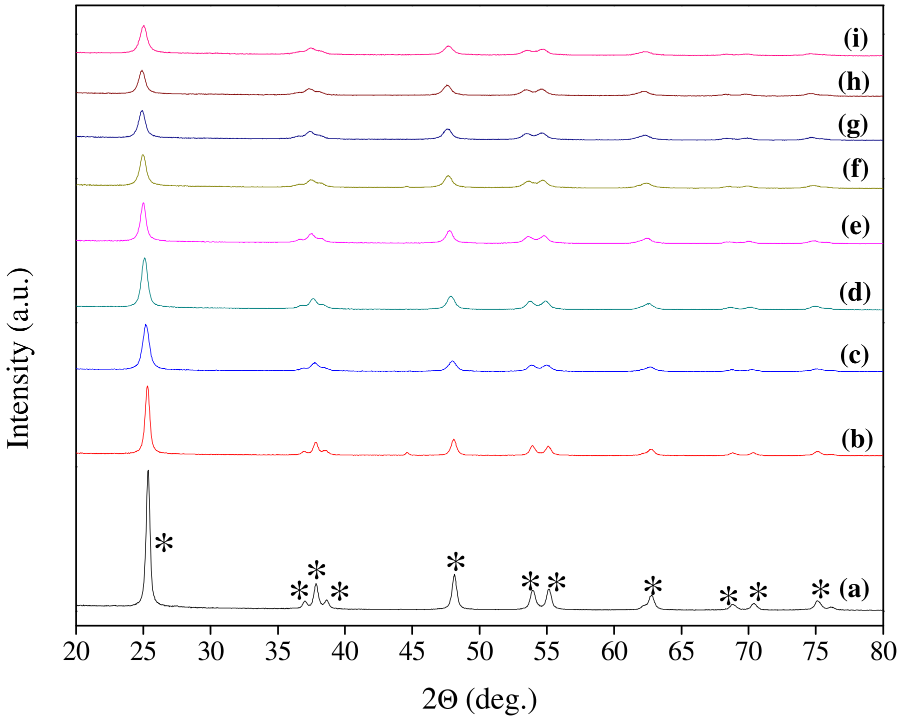

Figure A.7. XRD patterns of CeO_2 doped TiO_2 powders heat treated at 600°C: (a) pure, (b) 0.1% (c) 0.25%, (d) 0.5%, (e) 1%, (f) 2%, (g) 3%, (h) 4%, (i) 5% doped TiO_2 powder (*: anatase).

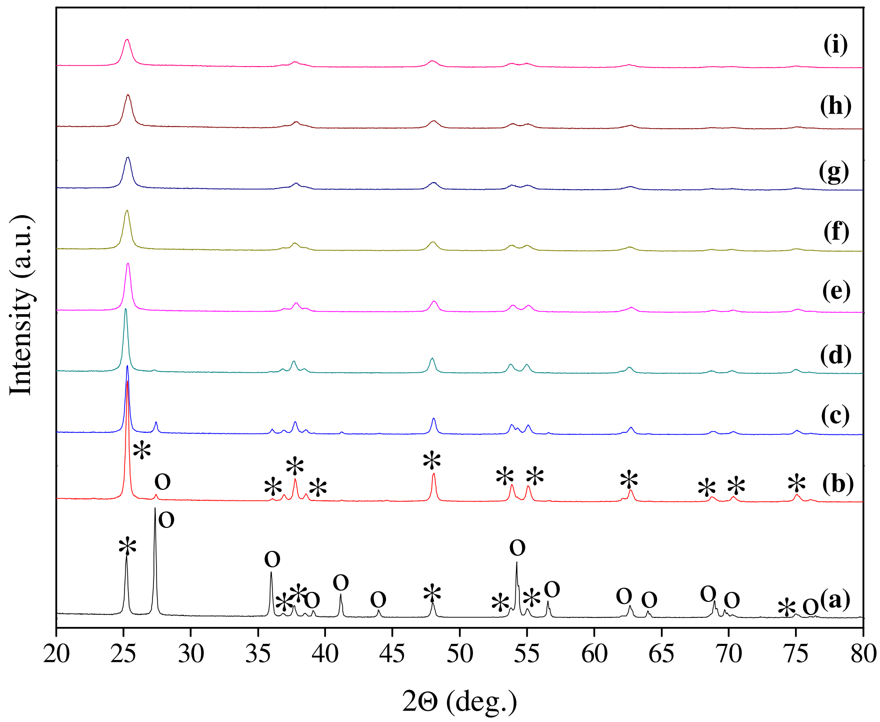

Figure A.8. XRD patterns of CeO_2 doped TiO_2 powders heat treated at 700°C: (a) pure, (b) 0.1% (c) 0.25%, (d) 0.5%, (e) 1%, (f) 2%, (g) 3%, (h) 4%, (i) 5% doped TiO_2 powder (*: anatase, o: rutile).

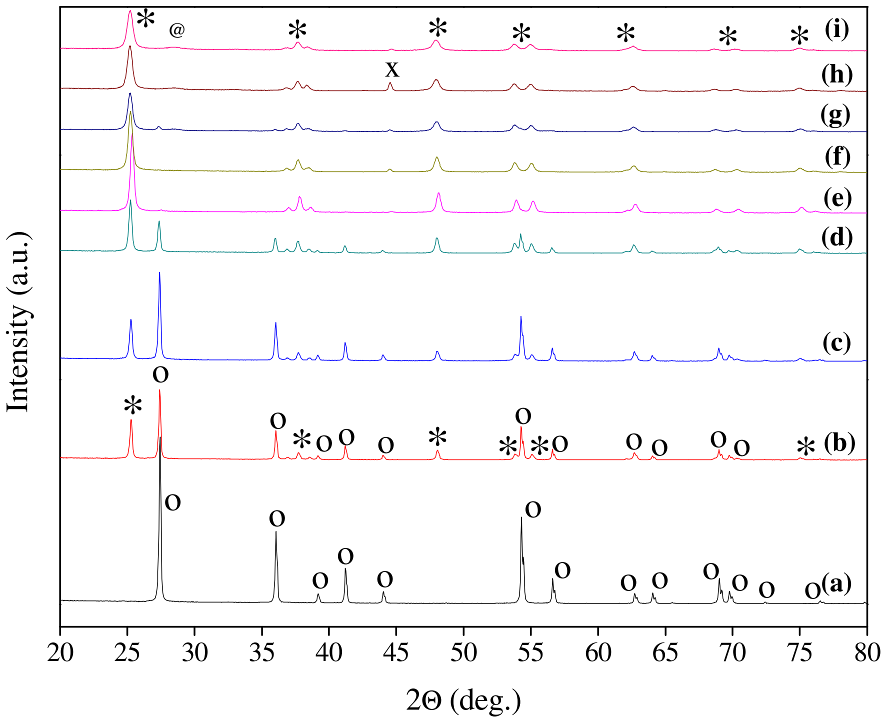

Figure A.9. XRD patterns of CeO_2 doped TiO_2 powders heat treated at 800°C: (a) pure, (b) 0.1% (c) 0.25%, (d) 0.5%, (e) 1%, (f) 2%, (g) 3%, (h) 4%, (i) 5% doped TiO_2 powder (*: anatase, o: rutile, @: CeO_2).

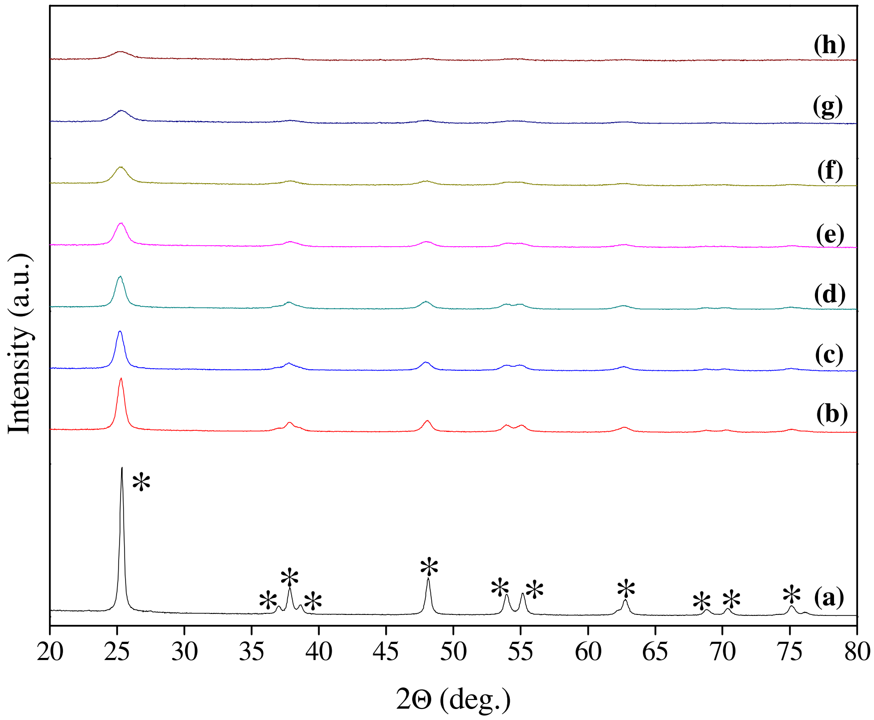

Figure A.10. XRD patterns of Dy_2O_3 doped TiO_2 powders heat treated at 600°C: (a) pure, (b) 0.25%, (c) 0.5%, (d) 1%, (e) 2%, (f) 3%, (g) 4%, (h) 5% doped TiO_2 powder (*: anatase).

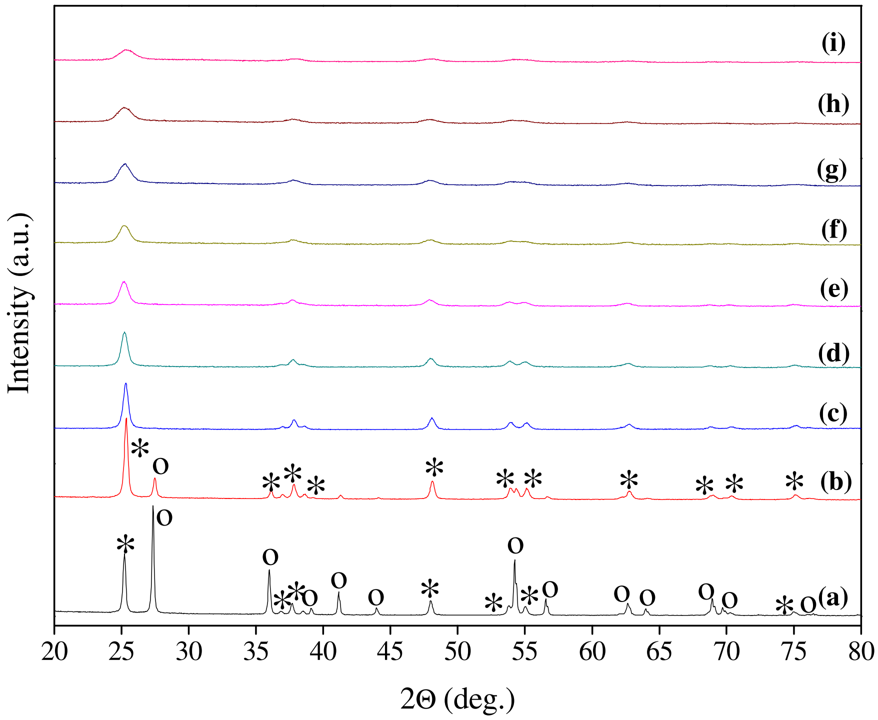

Figure A.11. XRD patterns of Dy_2O_3 doped TiO_2 powders heat treated at 700°C: (a) pure, (b) 0.1% (c) 0.25%, (d) 0.5%, (e) 1%, (f) 2%, (g) 3%, (h) 4%, (i) 5% doped TiO_2 powder (*: anatase, o: rutile).

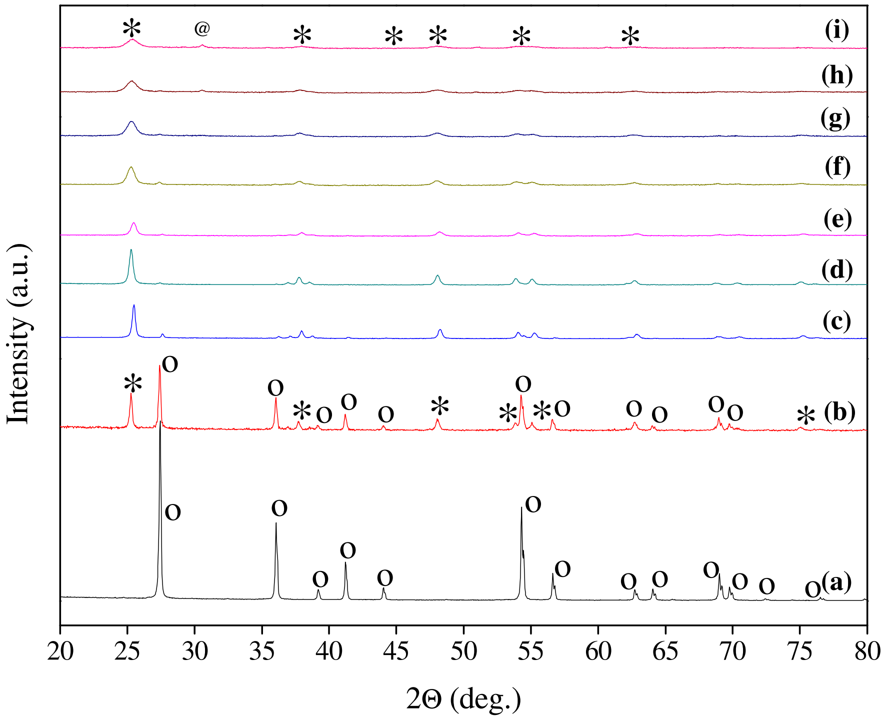

Figure A.12. XRD patterns of Dy_2O_3 doped TiO_2 powders heat treated at 800°C: (a) pure, (b) 0.1% (c) 0.25%, (d) 0.5%, (e) 1%, (f) 2%, (g) 3%, (h) 4%, (i) 5% doped TiO_2 powder (*: anatase, o: rutile, @: $Dy_2Ti_2O_7$).

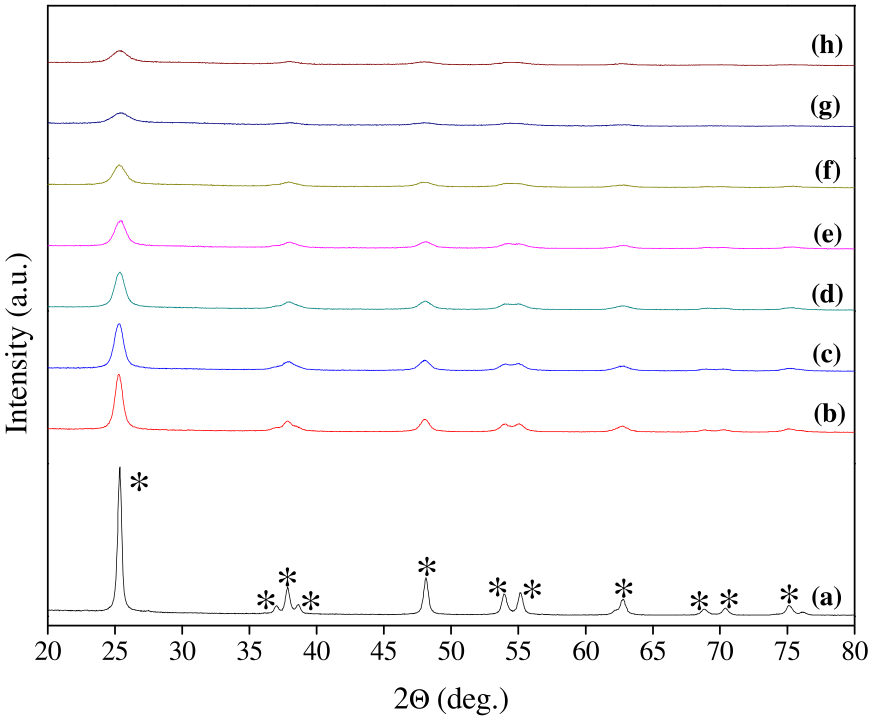

Figure A.13. XRD patterns of Pr_2O_3 doped TiO_2 powders heat treated at 600°C: (a) pure, (b) 0.25%, (c) 0.5%, (d) 1%, (e) 2%, (f) 3%, (g) 4%, (h) 5% doped TiO_2 powder (*: anatase).

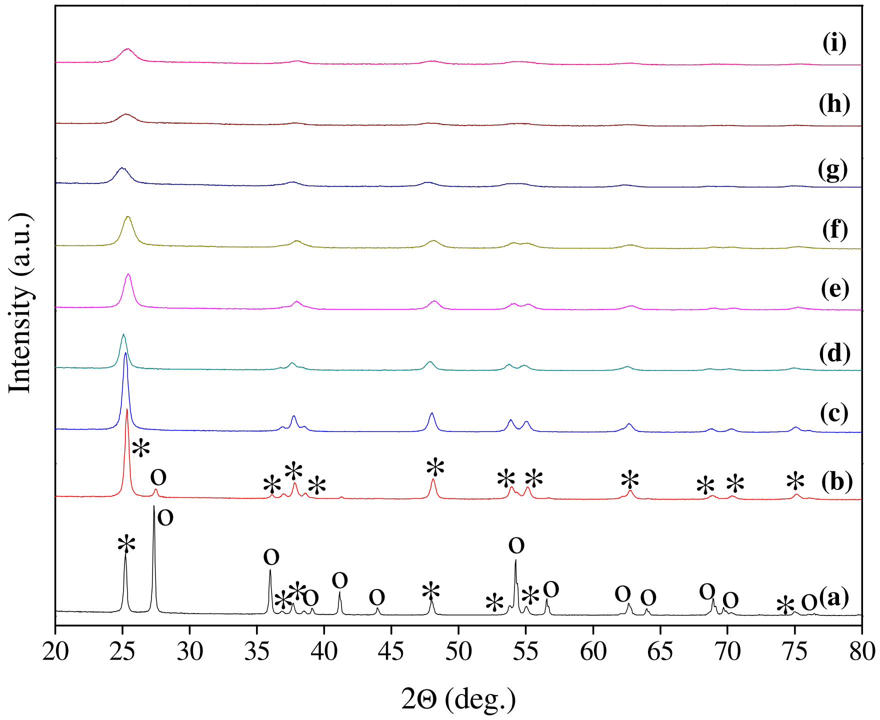

Figure A.14. XRD patterns of Pr_2O_3 doped TiO_2 powders heat treated at 700°C: (a) pure, (b) 0.1% (c) 0.25%, (d) 0.5%, (e) 1%, (f) 2%, (g) 3%, (h) 4%, (i) 5% doped TiO_2 powder (*: anatase, o: rutile).

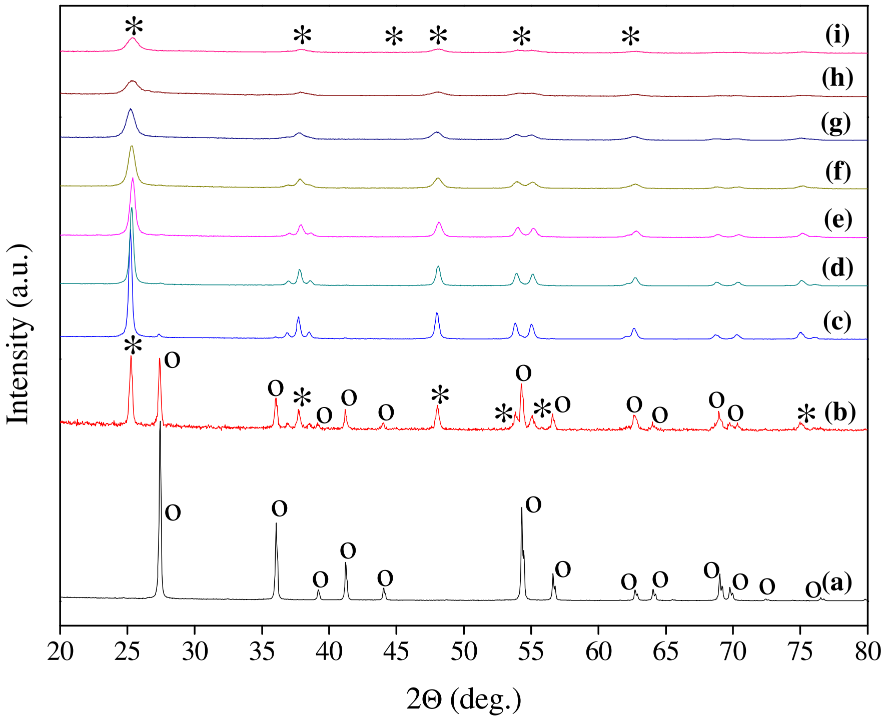

Figure A.15. XRD patterns of Pr_2O_3 doped TiO_2 powders heat treated at 800°C: (a) pure, (b) 0.1% (c) 0.25%, (d) 0.5%, (e) 1%, (f) 2%, (g) 3%, (h) 4%, (i) 5% doped TiO_2 powder (*: anatase, o: rutile).

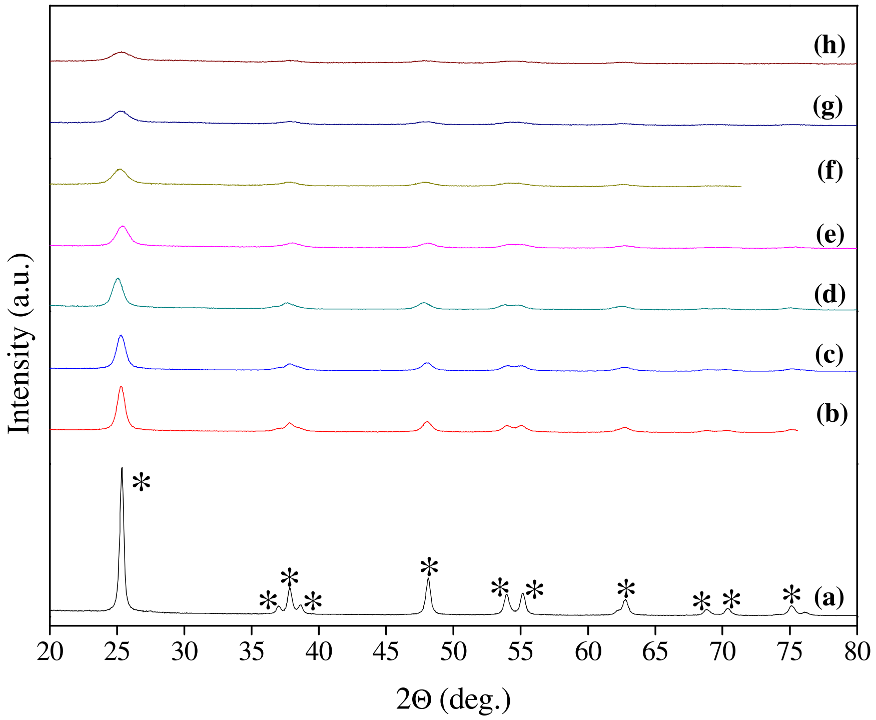

Figure A.16. XRD patterns of Sm_2O_3 doped TiO_2 powders heat treated at 600°C: (a) pure, (b) 0.25%, (c) 0.5%, (d) 1%, (e) 2%, (f) 3%, (g) 4%, (h) 5% doped TiO_2 powder (*: anatase).

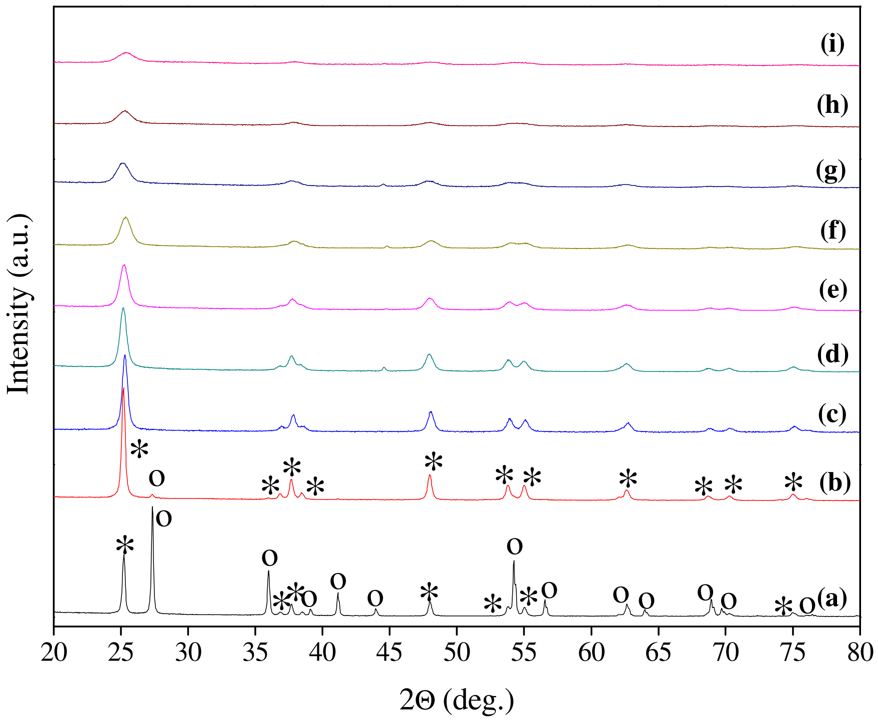

Figure A.17. XRD patterns of Sm_2O_3 doped TiO_2 powders heat treated at 700°C: (a) pure, (b) 0.1% (c) 0.25%, (d) 0.5%, (e) 1%, (f) 2%, (g) 3%, (h) 4%, (i) 5% doped TiO_2 powder (*: anatase, o: rutile).

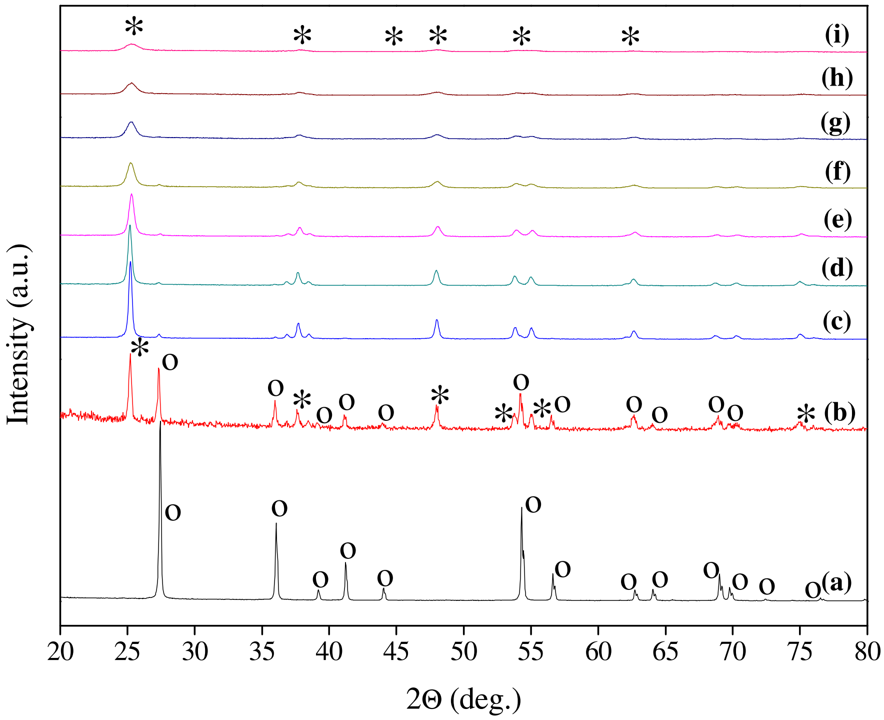

Figure A.18. XRD patterns of Sm_2O_3 doped TiO_2 powders heat treated at 800°C: (a) pure, (b) 0.1% (c) 0.25%, (d) 0.5%, (e) 1%, (f) 2%, (g) 3%, (h) 4%, (i) 5% doped TiO_2 powder (*: anatase, o: rutile).

APPENDIX C

SAMPLE XPS PEAK FITTINGS

The peak fitting of C1s spectrum was performed by Gaussian line shape and a constant base line, peak fittings of O1s and Ti2p were performed by pseudo-Voigt line shape and Shirley background which is more accurate for wider ranges. The same procedures were applied for the XPS spectra of the other powders prepared for this PhD study.

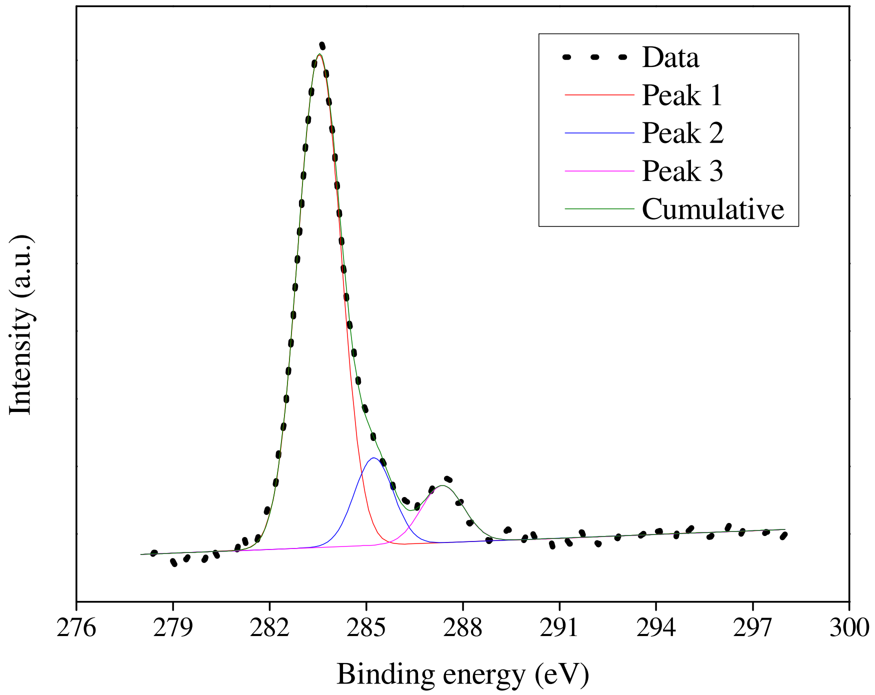

Figure A.19. C1s XPS spectrum of pure sol-gel TiO_2 powder heat treated at 600^oC.

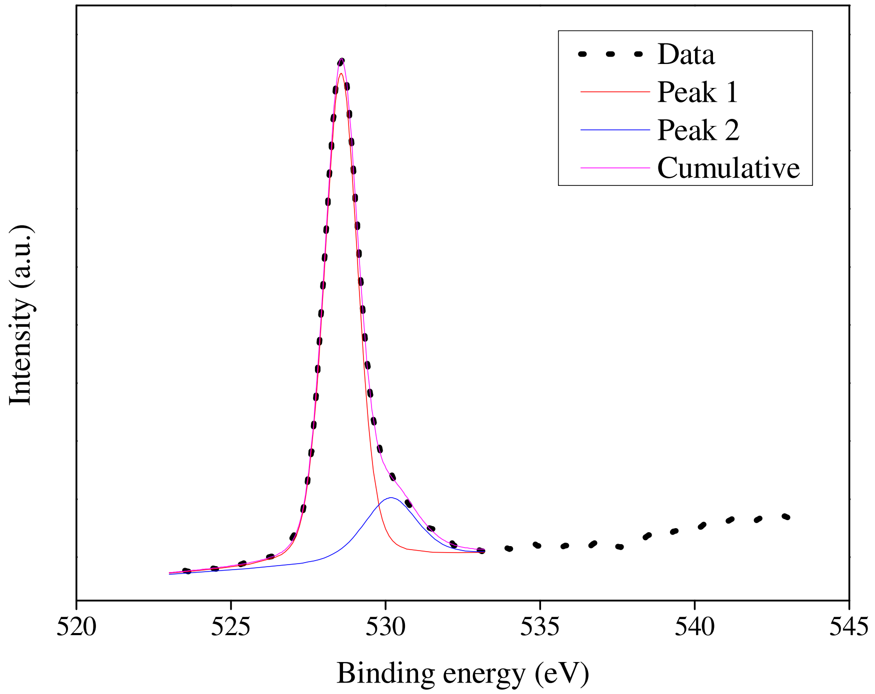

Figure A.20. O1s XPS spectrum of pure sol-gel TiO_2 powder heat treated at 600^oC.

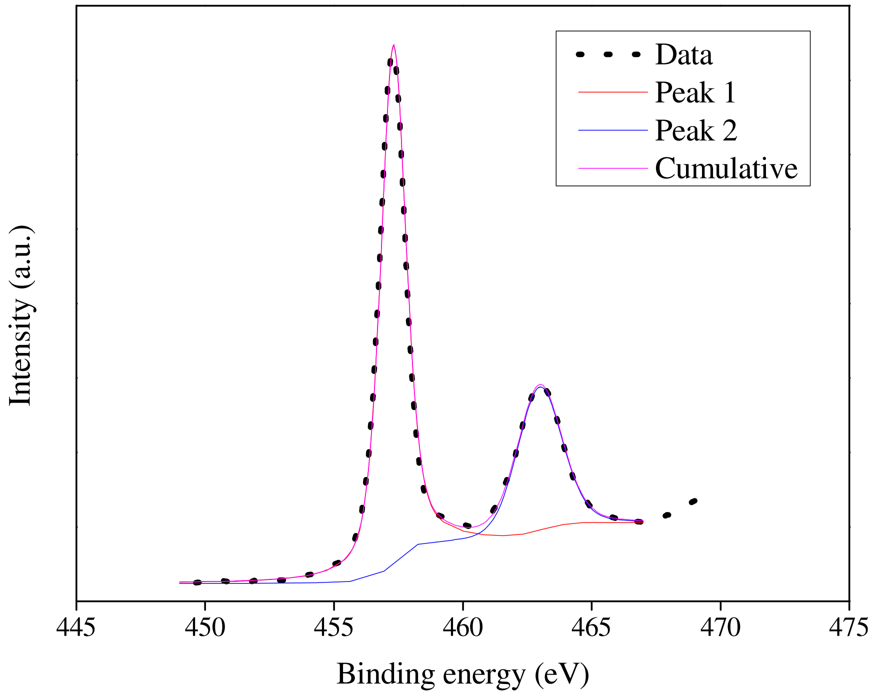

Figure A.21. Ti2p XPS spectrum of pure sol-gel TiO_2 powder heat treated at 600^oC.

APPENDIX D

JCPDS CARDS OF THE DETECTED PHASES

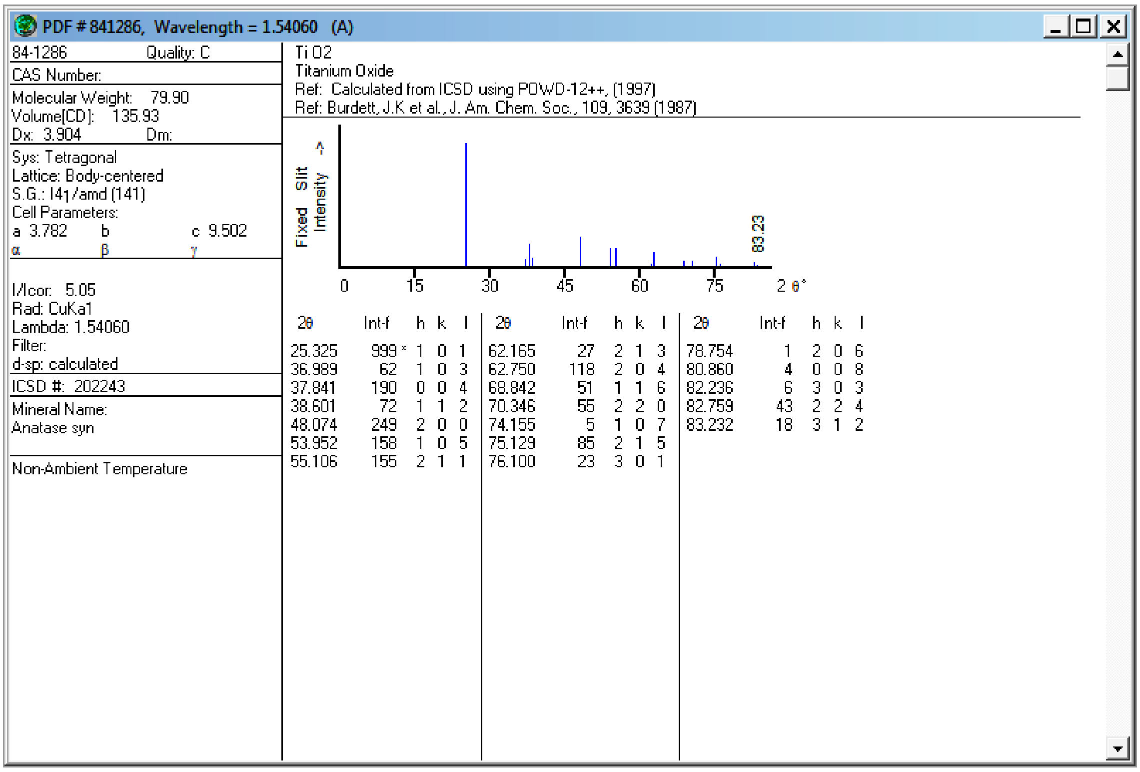

PDF # 841286, Wavelength = 1.54060 (A)

84-1286 Quality: C
CAS Number:
Molecular Weight: 79.90
Volume[CD]: 135.93
Dx: 3.904 Dm:
Sys: Tetragonal
Lattice: Body-centered
S.G.: I4$_1$/amd (141)
Cell Parameters:
a 3.782 b c 9.502
α β γ
I/Icor: 5.05
Rad: CuKa1
Lambda: 1.54060
Filter:
d-sp: calculated
ICSD #: 202243
Mineral Name:
Anatase syn
Non-Ambient Temperature

Ti O2
Titanium Oxide
Ref: Calculated from ICSD using POWD-12++, (1997)
Ref: Burdett, J.K et al., J. Am. Chem. Soc., 109, 3639 (1987)

2θ	Int-f	h	k	l	2θ	Int-f	h	k	l	2θ	Int-f	h	k	l
25.325	999 *	1	0	1	62.165	27	2	1	3	78.754	1	2	0	6
36.989	62	1	0	3	62.750	118	2	0	4	80.860	4	0	0	8
37.841	190	0	0	4	68.842	51	1	1	6	82.236	6	3	0	3
38.601	72	1	1	2	70.346	55	2	2	0	82.759	43	2	2	4
48.074	249	2	0	0	74.155	5	1	0	7	83.232	18	3	1	2
53.952	158	1	0	5	75.129	85	2	1	5					
55.106	155	2	1	1	76.100	23	3	0	1					

Figure A.22. JCPDS card of anatase TiO_2.

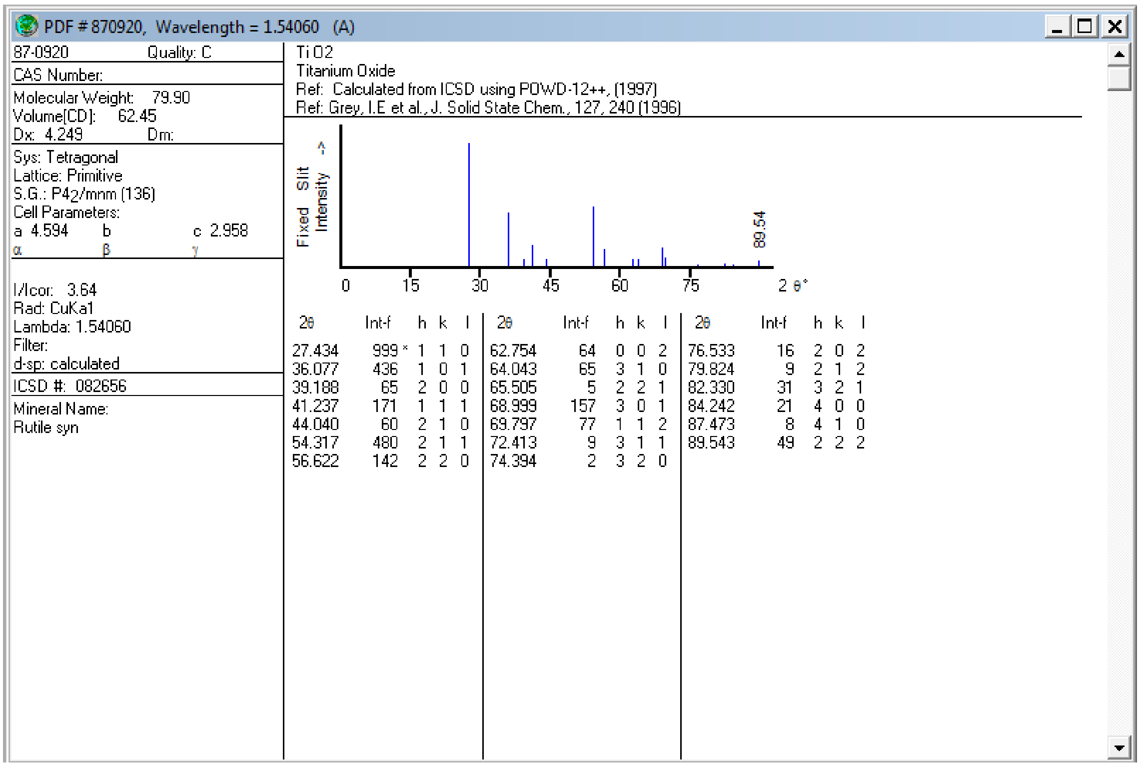

PDF # 870920, Wavelength = 1.54060 (A)

87-0920 Quality: C
CAS Number:
Molecular Weight: 79.90
Volume[CD]: 62.45
Dx: 4.249 Dm:
Sys: Tetragonal
Lattice: Primitive
S.G.: P42/mnm (136)
Cell Parameters:
a 4.594 b c 2.958
α β γ

I/Icor: 3.64
Rad: CuKa1
Lambda: 1.54060
Filter:
d-sp: calculated
ICSD #: 082656
Mineral Name:
Rutile syn

Ti O2
Titanium Oxide
Ref: Calculated from ICSD using POWD-12++, (1997)
Ref: Grey, I.E et al., J. Solid State Chem., 127, 240 (1996)

2θ	Int-f	h	k	l	2θ	Int-f	h	k	l	2θ	Int-f	h	k	l
27.434	999 *	1	1	0	62.754	64	0	0	2	76.533	16	2	0	2
36.077	436	1	0	1	64.043	65	3	1	0	79.824	9	2	1	2
39.188	65	2	0	0	65.505	5	2	2	1	82.330	31	3	2	1
41.237	171	1	1	1	68.999	157	3	0	1	84.242	21	4	0	0
44.040	60	2	1	0	69.797	77	1	1	2	87.473	8	4	1	0
54.317	480	2	1	1	72.413	9	3	1	1	89.543	49	2	2	2
56.622	142	2	2	0	74.394	2	3	2	0					

Figure A.23. JCPDS card of rutile TiO_2.

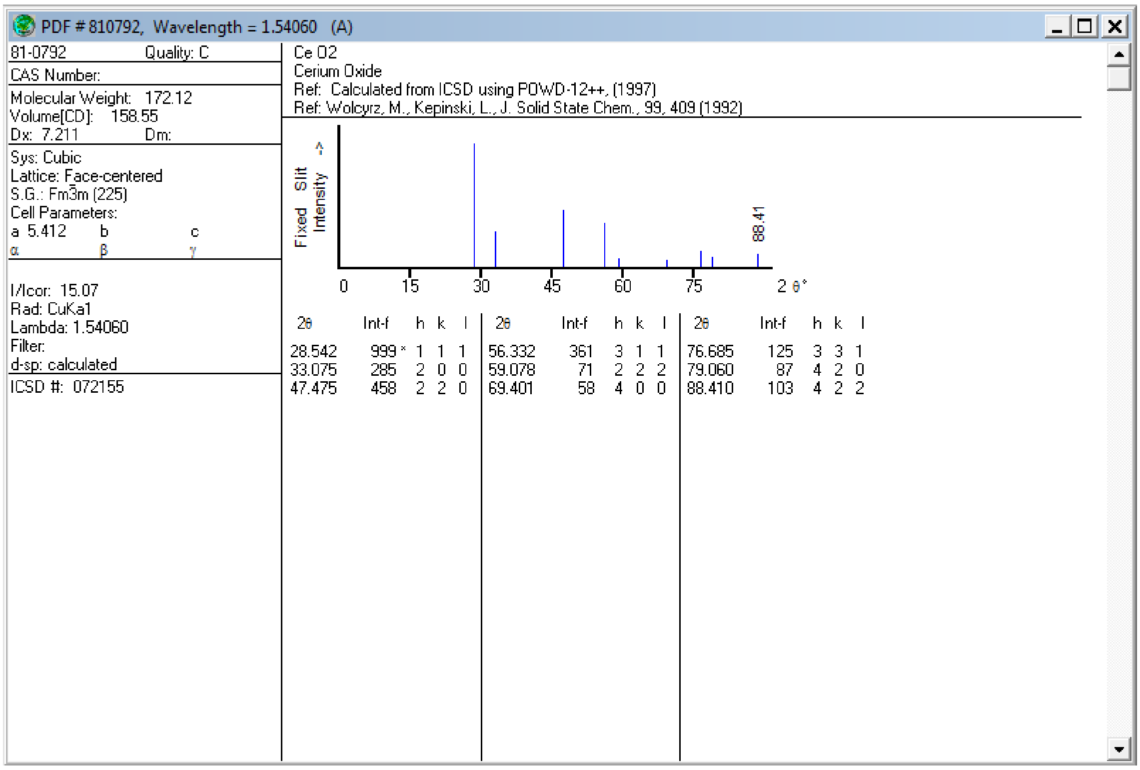

PDF # 810792, Wavelength = 1.54060 (A)

81-0792 Quality: C
CAS Number:
Molecular Weight: 172.12
Volume[CD]: 158.55
Dx: 7.211 Dm:
Sys: Cubic
Lattice: Face-centered
S.G.: Fm3̄m (225)
Cell Parameters:
a 5.412 b c
α β γ

I/Icor: 15.07
Rad: CuKa1
Lambda: 1.54060
Filter:
d-sp: calculated
ICSD #: 072155

Ce O2
Cerium Oxide
Ref: Calculated from ICSD using POWD-12++, (1997)
Ref: Wolcyrz, M., Kepinski, L., J. Solid State Chem., 99, 409 (1992)

2θ	Int-f	h	k	l	2θ	Int-f	h	k	l	2θ	Int-f	h	k	l
28.542	999 *	1	1	1	56.332	361	3	1	1	76.685	125	3	3	1
33.075	285	2	0	0	59.078	71	2	2	2	79.060	87	4	2	0
47.475	458	2	2	0	69.401	58	4	0	0	88.410	103	4	2	2

Figure A.24. JCPDS card of CeO_2.

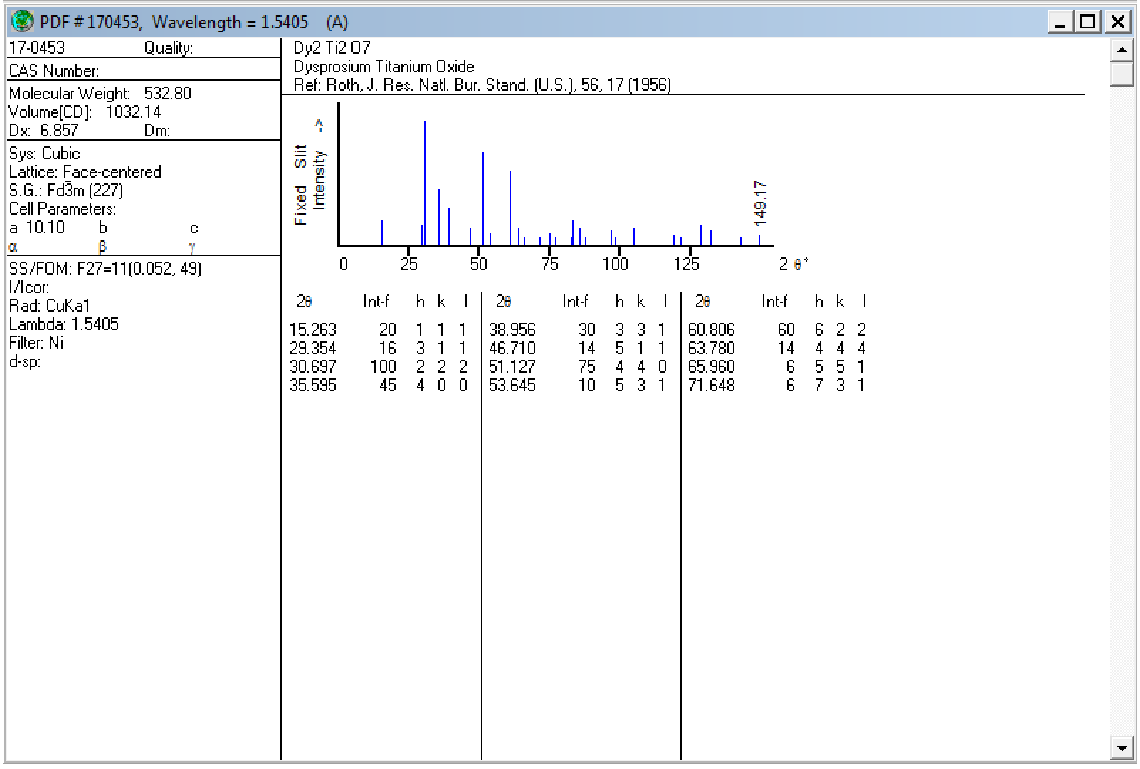

PDF # 170453, Wavelength = 1.5405 (A)

17-0453 Quality:

CAS Number:

Molecular Weight: 532.80
Volume[CD]: 1032.14
Dx: 6.857 Dm:

Sys: Cubic
Lattice: Face-centered
S.G.: Fd$\bar{3}$m (227)
Cell Parameters:
a 10.10 b c
α β γ

SS/FOM: F27=11(0.052, 49)
I/Icor:
Rad: CuKa1
Lambda: 1.5405
Filter: Ni
d-sp:

Dy2 Ti2 O7
Dysprosium Titanium Oxide
Ref: Roth, J. Res. Natl. Bur. Stand. (U.S.), 56, 17 (1956)

2θ	Int-f	h	k	l	2θ	Int-f	h	k	l	2θ	Int-f	h	k	l
15.263	20	1	1	1	38.956	30	3	3	1	60.806	60	6	2	2
29.354	16	3	1	1	46.710	14	5	1	1	63.780	14	4	4	4
30.697	100	2	2	2	51.127	75	4	4	0	65.960	6	5	5	1
35.595	45	4	0	0	53.645	10	5	3	1	71.648	6	7	3	1

Figure A.25. JCPDS card of $Dy_2Ti_2O_7$.

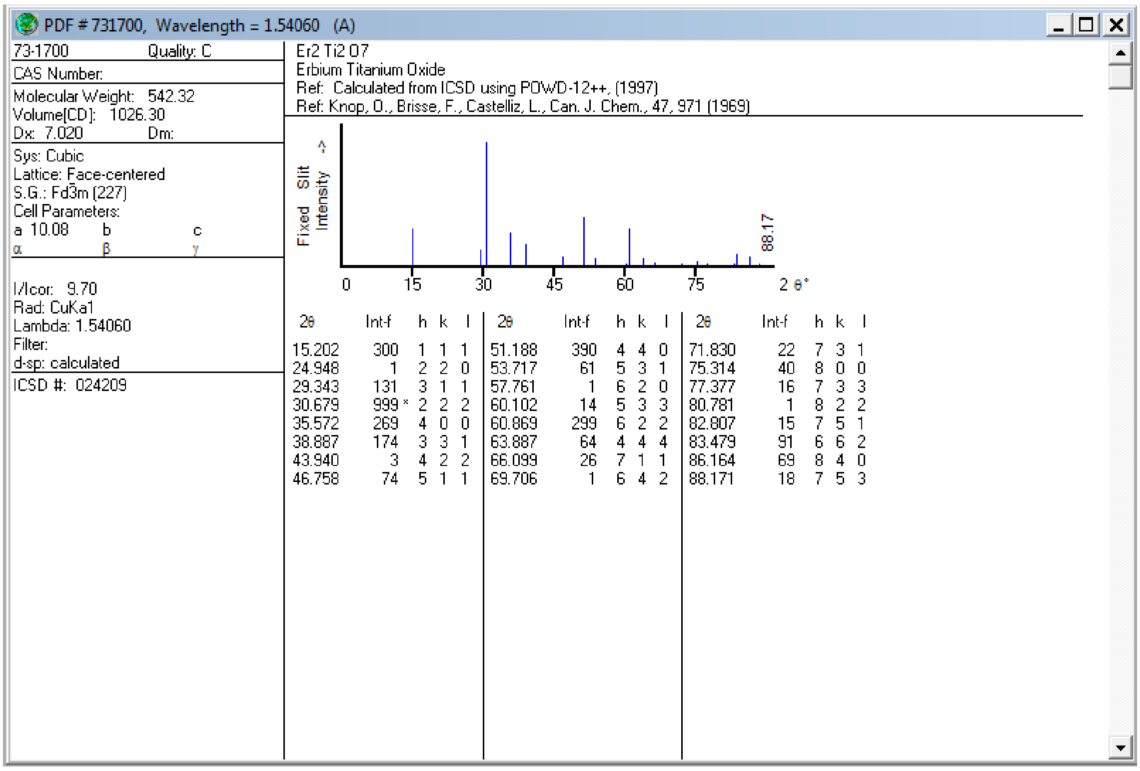

PDF # 731700, Wavelength = 1.54060 (A)

73-1700 Quality: C

CAS Number:

Molecular Weight: 542.32
Volume[CD]: 1026.30
Dx: 7.020 Dm:

Sys: Cubic
Lattice: Face-centered
S.G.: Fd$\bar{3}$m (227)
Cell Parameters:
a 10.08 b c
α β γ

I/Icor: 9.70
Rad: CuKa1
Lambda: 1.54060
Filter:
d-sp: calculated

ICSD #: 024209

Er2 Ti2 O7
Erbium Titanium Oxide
Ref: Calculated from ICSD using POWD-12++, (1997)
Ref: Knop, O., Brisse, F., Castelliz, L., Can. J. Chem., 47, 971 (1969)

2θ	Int-f	h	k	l	2θ	Int-f	h	k	l	2θ	Int-f	h	k	l
15.202	300	1	1	1	51.188	390	4	4	0	71.830	22	7	3	1
24.948	1	2	2	0	53.717	61	5	3	1	75.314	40	8	0	0
29.343	131	3	1	1	57.761	1	6	2	0	77.377	16	7	3	3
30.679	999 *	2	2	2	60.102	14	5	3	3	80.781	1	8	2	2
35.572	269	4	0	0	60.869	299	6	2	2	82.807	15	7	5	1
38.887	174	3	3	1	63.887	64	4	4	4	83.479	91	6	6	2
43.940	3	4	2	2	66.099	26	7	1	1	86.164	69	8	4	0
46.758	74	5	1	1	69.706	1	6	4	2	88.171	18	7	5	3

Figure A.26. JCPDS card of $Er_2Ti_2O_7$.

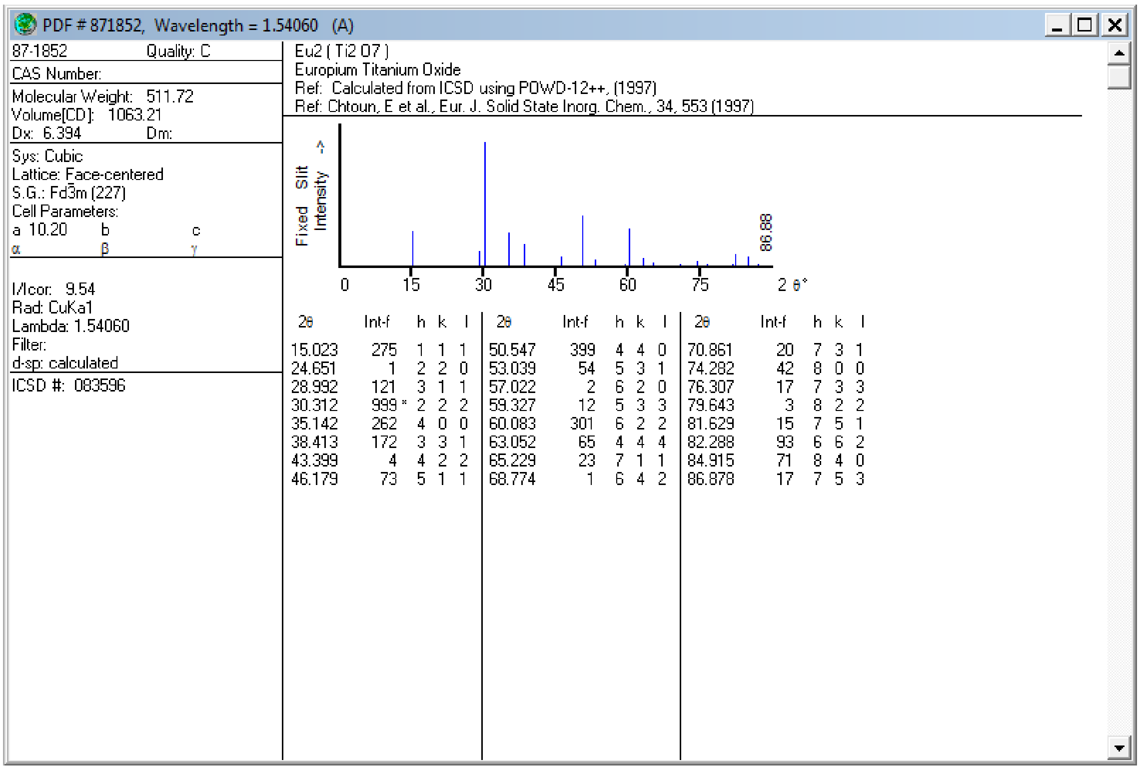

PDF # 871852, Wavelength = 1.54060 (A)

87-1852 Quality: C

CAS Number:

Molecular Weight: 511.72
Volume[CD]: 1063.21
Dx: 6.394 Dm:

Sys: Cubic
Lattice: Face-centered
S.G.: Fd$\bar{3}$m (227)
Cell Parameters:
a 10.20 b c
α β γ

I/Icor: 9.54
Rad: CuKa1
Lambda: 1.54060
Filter:
d-sp: calculated

ICSD #: 083596

Eu2 (Ti2 O7)
Europium Titanium Oxide
Ref: Calculated from ICSD using POWD-12++, (1997)
Ref: Chtoun, E et al., Eur. J. Solid State Inorg. Chem., 34, 553 (1997)

2θ	Int-f	h	k	l	2θ	Int-f	h	k	l	2θ	Int-f	h	k	l
15.023	275	1	1	1	50.547	399	4	4	0	70.861	20	7	3	1
24.651	1	2	2	0	53.039	54	5	3	1	74.282	42	8	0	0
28.992	121	3	1	1	57.022	2	6	2	0	76.307	17	7	3	3
30.312	999 *	2	2	2	59.327	12	5	3	3	79.643	3	8	2	2
35.142	262	4	0	0	60.083	301	6	2	2	81.629	15	7	5	1
38.413	172	3	3	1	63.052	65	4	4	4	82.288	93	6	6	2
43.399	4	4	2	2	65.229	23	7	1	1	84.915	71	8	4	0
46.179	73	5	1	1	68.774	1	6	4	2	86.878	17	7	5	3

Figure A.27. JCPDS card of $Eu_2Ti_2O_7$.

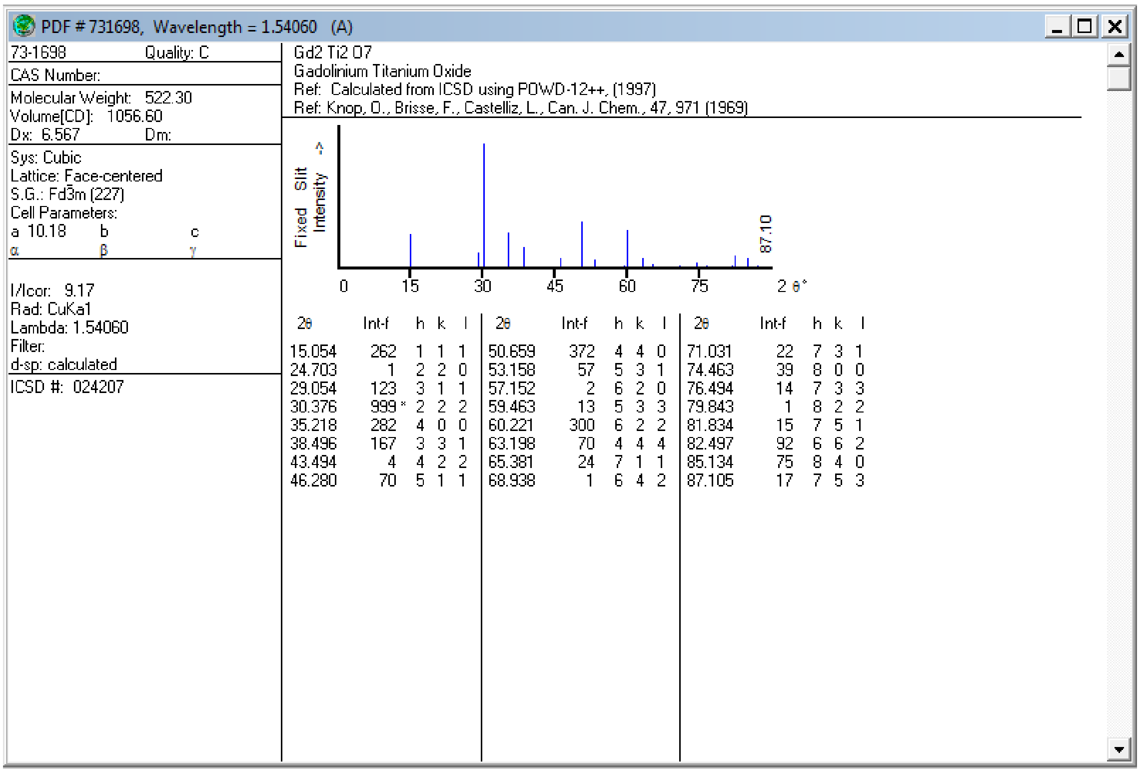

PDF # 731698, Wavelength = 1.54060 (A)

73-1698 Quality: C

CAS Number:

Molecular Weight: 522.30
Volume[CD]: 1056.60
Dx: 6.567 Dm:

Sys: Cubic
Lattice: Face-centered
S.G.: Fd$\bar{3}$m (227)
Cell Parameters:
a 10.18 b c
α β γ

I/Icor: 9.17
Rad: CuKa1
Lambda: 1.54060
Filter:
d-sp: calculated

ICSD #: 024207

Gd2 Ti2 O7
Gadolinium Titanium Oxide
Ref: Calculated from ICSD using POWD-12++, (1997)
Ref: Knop, O., Brisse, F., Castelliz, L., Can. J. Chem., 47, 971 (1969)

2θ	Int-f	h	k	l	2θ	Int-f	h	k	l	2θ	Int-f	h	k	l
15.054	262	1	1	1	50.659	372	4	4	0	71.031	22	7	3	1
24.703	1	2	2	0	53.158	57	5	3	1	74.463	39	8	0	0
29.054	123	3	1	1	57.152	2	6	2	0	76.494	14	7	3	3
30.376	999 *	2	2	2	59.463	13	5	3	3	79.843	1	8	2	2
35.218	282	4	0	0	60.221	300	6	2	2	81.834	15	7	5	1
38.496	167	3	3	1	63.198	70	4	4	4	82.497	92	6	6	2
43.494	4	4	2	2	65.381	24	7	1	1	85.134	75	8	4	0
46.280	70	5	1	1	68.938	1	6	4	2	87.105	17	7	5	3

Figure A.28. JCPDS card of $Gd_2Ti_2O_7$.

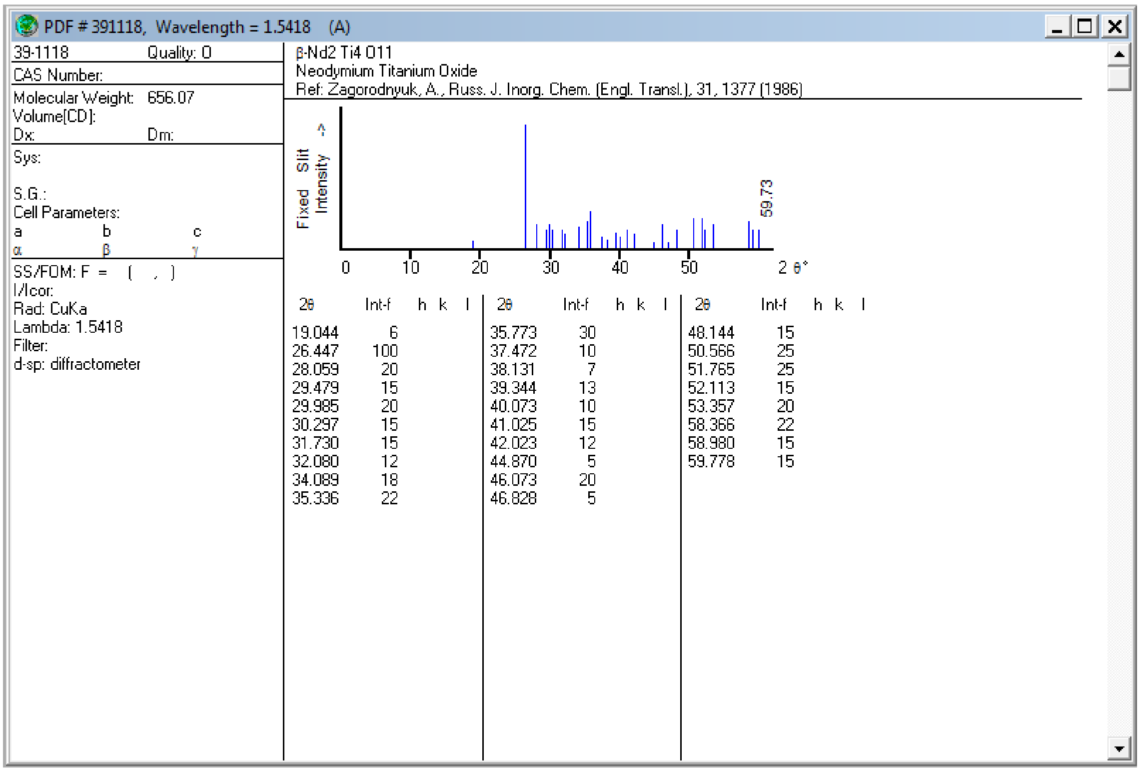

PDF # 391118, Wavelength = 1.5418 (A)

39-1118 Quality: O
CAS Number:
Molecular Weight: 656.07
Volume[CD]:
Dx: Dm:
Sys:
S.G.:
Cell Parameters:
a b c
α β γ
SS/FOM: F = (,)
I/Icor:
Rad: CuKa
Lambda: 1.5418
Filter:
d-sp: diffractometer

β-Nd2 Ti4 O11
Neodymium Titanium Oxide
Ref: Zagorodnyuk, A., Russ. J. Inorg. Chem. (Engl. Transl.), 31, 1377 (1986)

2θ	Int-f	h	k	l
19.044	6			
26.447	100			
28.059	20			
29.479	15			
29.985	20			
30.297	15			
31.730	15			
32.080	12			
34.089	18			
35.336	22			
35.773	30			
37.472	10			
38.131	7			
39.344	13			
40.073	10			
41.025	15			
42.023	12			
44.870	5			
46.073	20			
46.828	5			
48.144	15			
50.566	25			
51.765	25			
52.113	15			
53.357	20			
58.366	22			
58.980	15			
59.778	15			

Figure A.29. JCPDS card of $Nd_2Ti_4O_{11}$.

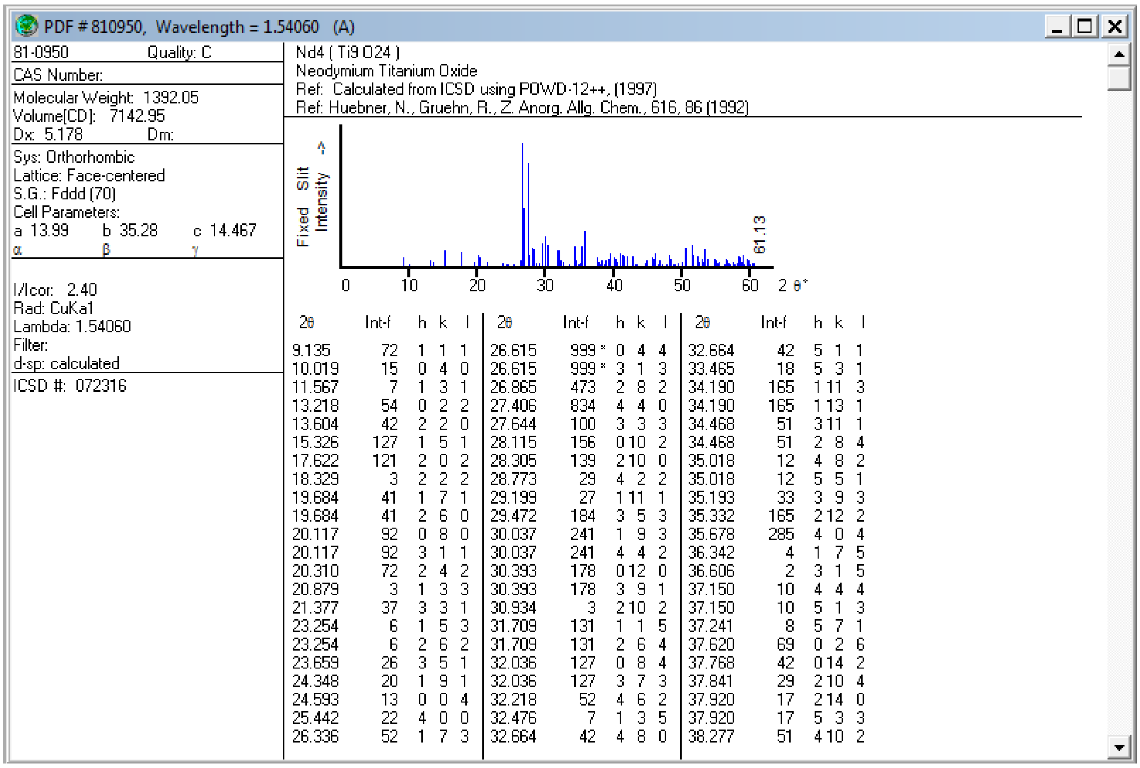

PDF # 810950, Wavelength = 1.54060 (A)

81-0950 Quality: C
CAS Number:
Molecular Weight: 1392.05
Volume[CD]: 7142.95
Dx: 5.178 Dm:
Sys: Orthorhombic
Lattice: Face-centered
S.G.: Fddd (70)
Cell Parameters:
a 13.99 b 35.28 c 14.467
α β γ
I/Icor: 2.40
Rad: CuKa1
Lambda: 1.54060
Filter:
d-sp: calculated
ICSD #: 072316

Nd4 (Ti9 O24)
Neodymium Titanium Oxide
Ref: Calculated from ICSD using POWD-12++, (1997)
Ref: Huebner, N., Gruehn, R., Z. Anorg. Allg. Chem., 616, 86 (1992)

2θ	Int-f	h	k	l
9.135	72	1	1	1
10.019	15	0	4	0
11.567	7	1	3	1
13.218	54	0	2	2
13.604	42	2	2	0
15.326	127	1	5	1
17.622	121	2	0	2
18.329	3	2	2	2
19.684	41	1	7	1
19.684	41	2	6	0
20.117	92	0	8	0
20.117	92	3	1	1
20.310	72	2	4	2
20.879	3	1	3	3
21.377	37	3	3	1
23.254	6	1	5	3
23.254	6	2	6	2
23.659	26	3	5	1
24.348	20	1	9	1
24.593	13	0	0	4
25.442	22	4	0	0
26.336	52	1	7	3
26.615	999 *	0	4	4
26.615	999 *	3	1	3
26.865	473	2	8	2
27.406	834	4	4	0
27.644	100	3	3	3
28.115	156	0	10	2
28.305	139	2	10	0
28.773	29	4	2	2
29.199	27	1	11	1
29.472	184	3	5	3
30.037	241	1	9	3
30.037	241	4	4	2
30.393	178	0	12	0
30.393	178	3	9	1
30.934	3	2	10	2
31.709	131	1	1	5
31.709	131	2	6	4
32.036	127	0	8	4
32.036	127	3	7	3
32.218	52	4	6	2
32.476	7	1	3	5
32.664	42	4	8	0
32.664	42	5	1	1
33.465	18	5	3	1
34.190	165	1	11	3
34.190	165	1	13	1
34.468	51	3	11	1
34.468	51	2	8	4
35.018	12	4	8	2
35.018	12	5	5	1
35.193	33	3	9	3
35.332	165	2	12	2
35.678	285	4	0	4
36.342	4	1	7	5
36.606	2	3	1	5
37.150	10	4	4	4
37.150	10	5	1	3
37.241	8	5	7	1
37.620	69	0	2	6
37.768	42	0	14	2
37.841	29	2	10	4
37.920	17	2	14	0
37.920	17	5	3	3
38.277	51	4	10	2

Figure A.30. JCPDS card of $Nd_4Ti_9O_{24}$.

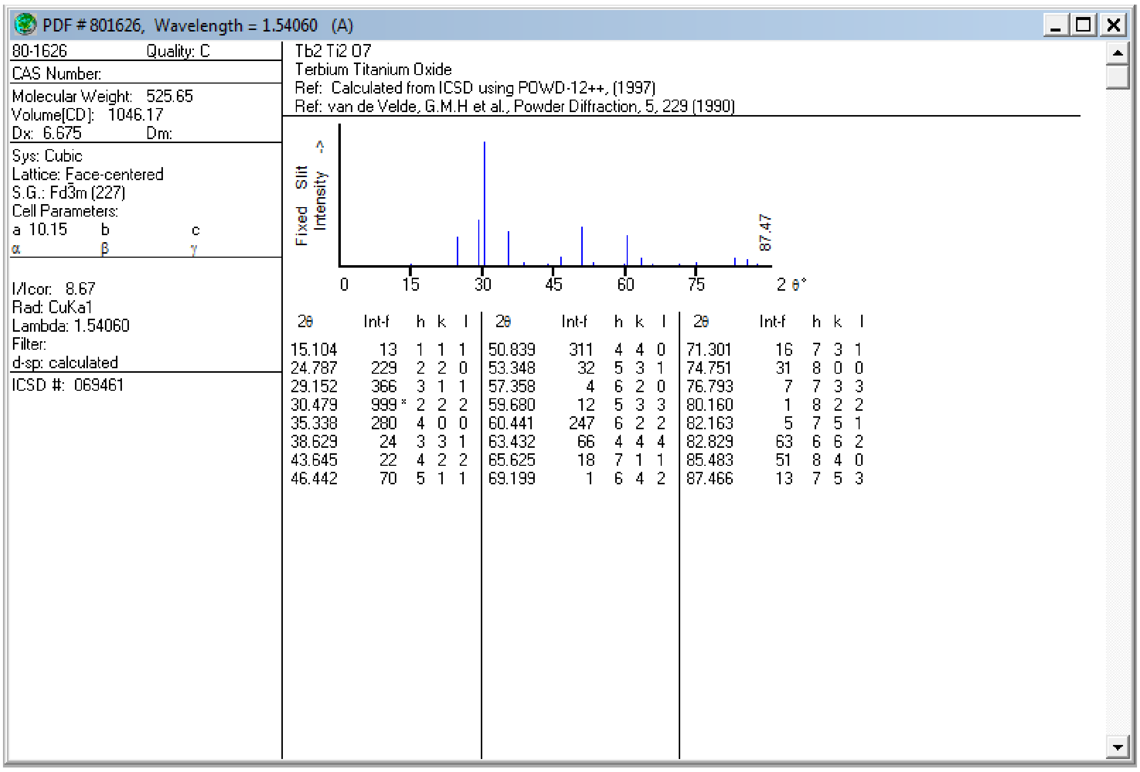

PDF # 801626, Wavelength = 1.54060 (A)

80-1626 Quality: C

CAS Number:

Molecular Weight: 525.65
Volume[CD]: 1046.17
Dx: 6.675 Dm:

Sys: Cubic
Lattice: Face-centered
S.G.: Fd$\bar{3}$m (227)
Cell Parameters:
a 10.15 b c
α β γ

I/Icor: 8.67
Rad: CuKa1
Lambda: 1.54060
Filter:
d-sp: calculated

ICSD #: 069461

Tb2 Ti2 O7
Terbium Titanium Oxide
Ref: Calculated from ICSD using POWD-12++, (1997)
Ref: van de Velde, G.M.H et al., Powder Diffraction, 5, 229 (1990)

2θ	Int-f	h	k	l	2θ	Int-f	h	k	l	2θ	Int-f	h	k	l
15.104	13	1	1	1	50.839	311	4	4	0	71.301	16	7	3	1
24.787	229	2	2	0	53.348	32	5	3	1	74.751	31	8	0	0
29.152	366	3	1	1	57.358	4	6	2	0	76.793	7	7	3	3
30.479	999 *	2	2	2	59.680	12	5	3	3	80.160	1	8	2	2
35.338	280	4	0	0	60.441	247	6	2	2	82.163	5	7	5	1
38.629	24	3	3	1	63.432	66	4	4	4	82.829	63	6	6	2
43.645	22	4	2	2	65.625	18	7	1	1	85.483	51	8	4	0
46.442	70	5	1	1	69.199	1	6	4	2	87.466	13	7	5	3

Figure A.31. JCPDS card of $Tb_2Ti_2O_7$.

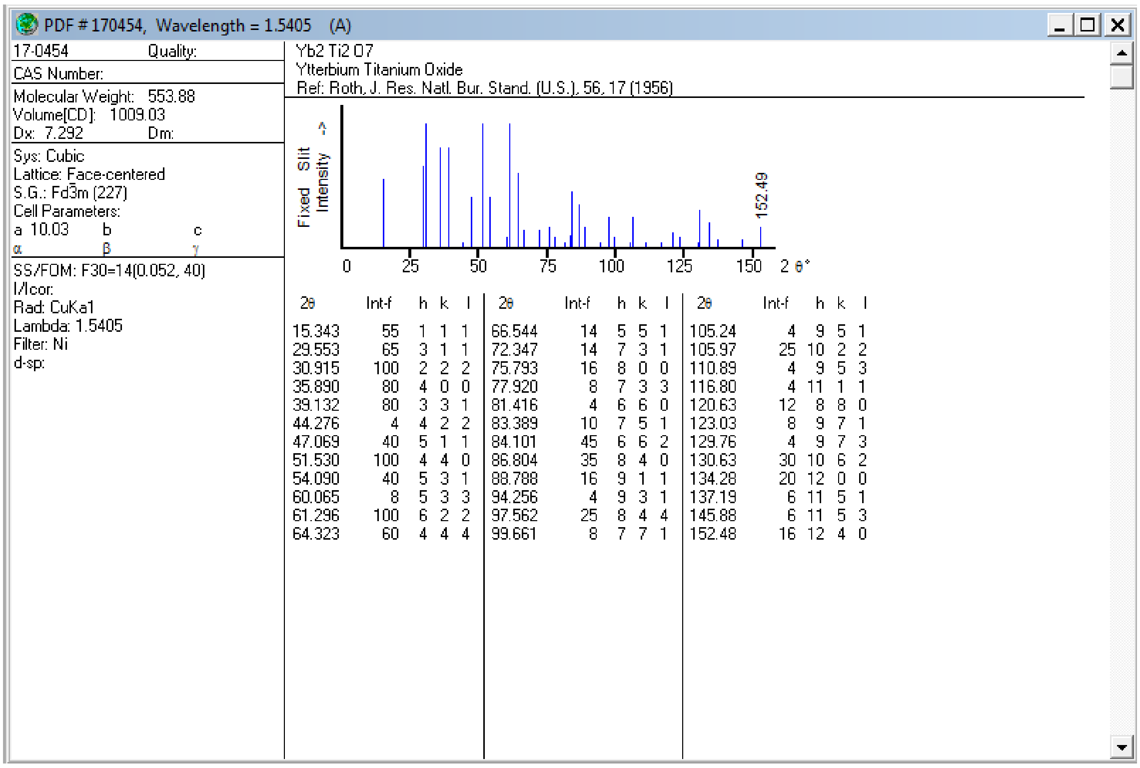

PDF # 170454, Wavelength = 1.5405 (A)

17-0454 Quality:

CAS Number:

Molecular Weight: 553.88
Volume[CD]: 1009.03
Dx: 7.292 Dm:

Sys: Cubic
Lattice: Face-centered
S.G.: Fd$\bar{3}$m (227)
Cell Parameters:
a 10.03 b c
α β γ

SS/FOM: F30=14(0.052, 40)
I/Icor:
Rad: CuKa1
Lambda: 1.5405
Filter: Ni
d-sp:

Yb2 Ti2 O7
Ytterbium Titanium Oxide
Ref: Roth, J. Res. Natl. Bur. Stand. (U.S.), 56, 17 (1956)

2θ	Int-f	h	k	l	2θ	Int-f	h	k	l	2θ	Int-f	h	k	l
15.343	55	1	1	1	66.544	14	5	5	1	105.24	4	9	5	1
29.553	65	3	1	1	72.347	14	7	3	1	105.97	25	10	2	2
30.915	100	2	2	2	75.793	16	8	0	0	110.89	4	9	5	3
35.890	80	4	0	0	77.920	8	7	3	3	116.80	4	11	1	1
39.132	80	3	3	1	81.416	4	6	6	0	120.63	12	8	8	0
44.276	4	4	2	2	83.389	10	7	5	1	123.03	8	9	7	1
47.069	40	5	1	1	84.101	45	6	6	2	129.76	4	9	7	3
51.530	100	4	4	0	86.804	35	8	4	0	130.63	30	10	6	2
54.090	40	5	3	1	88.788	16	9	1	1	134.28	20	12	0	0
60.065	8	5	3	3	94.256	4	9	3	1	137.19	6	11	5	1
61.296	100	6	2	2	97.562	25	8	4	4	145.88	6	11	5	3
64.323	60	4	4	4	99.661	8	7	7	1	152.48	16	12	4	0

Figure A.32. JCPDS card of $Yb_2Ti_2O_7$.

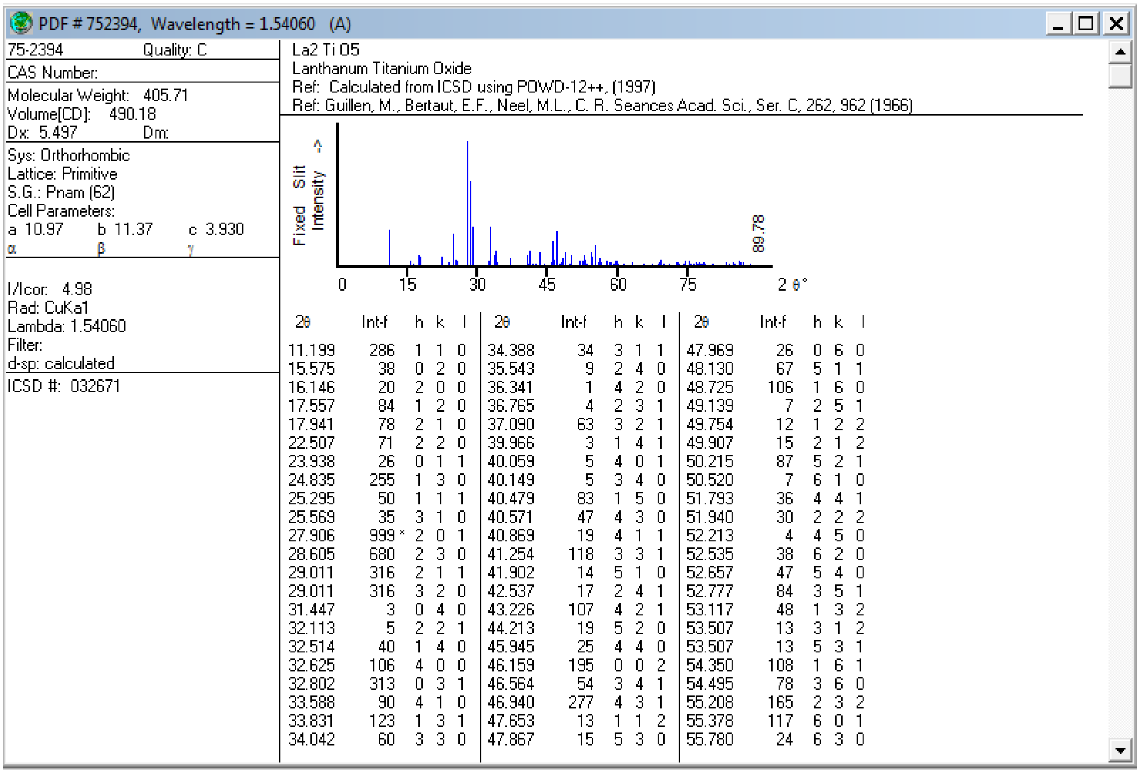

PDF # 752394, Wavelength = 1.54060 (A)

75-2394 Quality: C
CAS Number:
Molecular Weight: 405.71
Volume[CD]: 490.18
Dx: 5.497 Dm:
Sys: Orthorhombic
Lattice: Primitive
S.G.: Pnam (62)
Cell Parameters:
a 10.97 b 11.37 c 3.930
α β γ
I/Icor: 4.98
Rad: CuKa1
Lambda: 1.54060
Filter:
d-sp: calculated
ICSD #: 032671

La2 Ti O5
Lanthanum Titanium Oxide
Ref: Calculated from ICSD using POWD-12++, (1997)
Ref: Guillen, M., Bertaut, E.F., Neel, M.L., C. R. Seances Acad. Sci., Ser. C, 262, 962 (1966)

2θ	Int-f	h	k	l	2θ	Int-f	h	k	l	2θ	Int-f	h	k	l
11.199	286	1	1	0	34.388	34	3	1	1	47.969	26	0	6	0
15.575	38	0	2	0	35.543	9	2	4	0	48.130	67	5	1	1
16.146	20	2	0	0	36.341	1	4	2	0	48.725	106	1	6	0
17.557	84	1	2	0	36.765	4	2	3	1	49.139	7	2	5	1
17.941	78	2	1	0	37.090	63	3	2	1	49.754	12	1	2	2
22.507	71	2	2	0	39.966	3	1	4	1	49.907	15	2	1	2
23.938	26	0	1	1	40.059	5	4	0	1	50.215	87	5	2	1
24.835	255	1	3	0	40.149	5	3	4	0	50.520	7	6	1	0
25.295	50	1	1	1	40.479	83	1	5	0	51.793	36	4	4	1
25.569	35	3	1	0	40.571	47	4	3	0	51.940	30	2	2	2
27.906	999 *	2	0	1	40.869	19	4	1	1	52.213	4	4	5	0
28.605	680	2	3	0	41.254	118	3	3	1	52.535	38	6	2	0
29.011	316	2	1	1	41.902	14	5	1	0	52.657	47	5	4	0
29.011	316	3	2	0	42.537	17	2	4	1	52.777	84	3	5	1
31.447	3	0	4	0	43.226	107	4	2	1	53.117	48	1	3	2
32.113	5	2	2	1	44.213	19	5	2	0	53.507	13	3	1	2
32.514	40	1	4	0	45.945	25	4	4	0	53.507	13	5	3	1
32.625	106	4	0	0	46.159	195	0	0	2	54.350	108	1	6	1
32.802	313	0	3	1	46.564	54	3	4	1	54.495	78	3	6	0
33.588	90	4	1	0	46.940	277	4	3	1	55.208	165	2	3	2
33.831	123	1	3	1	47.653	13	1	1	2	55.378	117	6	0	1
34.042	60	3	3	0	47.867	15	5	3	0	55.780	24	6	3	0

Figure A.33. JCPDS card of $La_2Ti_1O_5$.

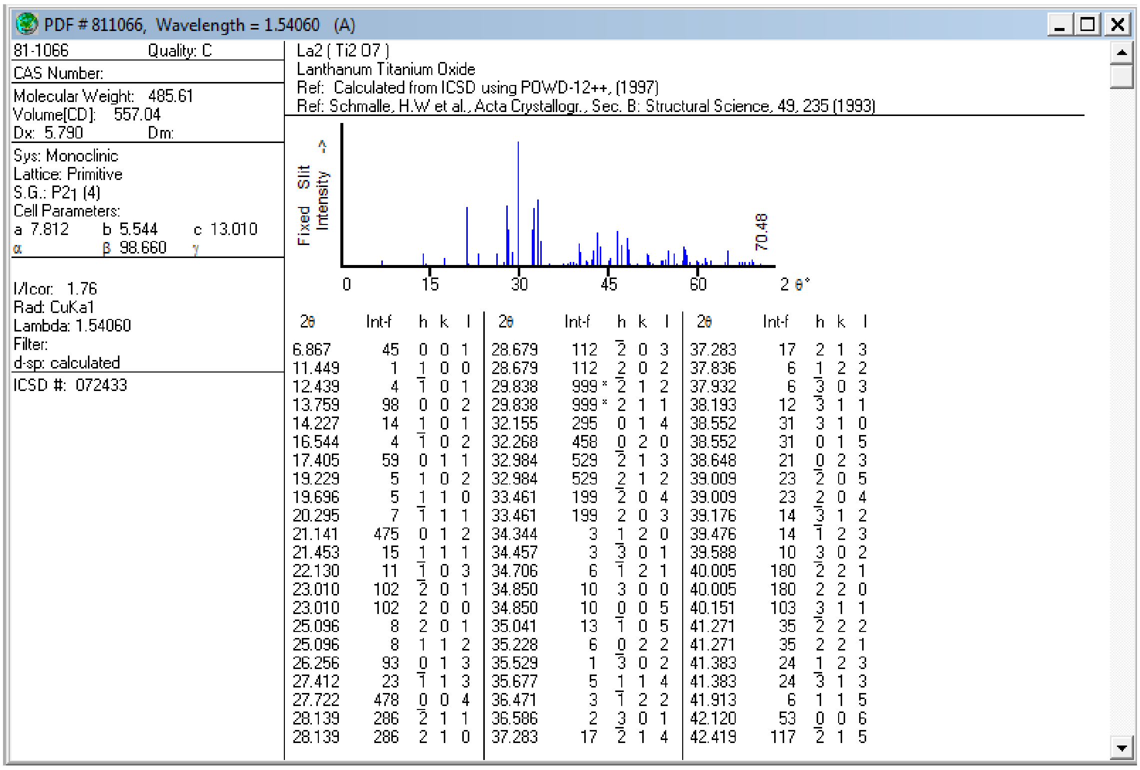

PDF # 811066, Wavelength = 1.54060 (A)

81-1066 Quality: C
CAS Number:
Molecular Weight: 485.61
Volume[CD]: 557.04
Dx: 5.790 Dm:
Sys: Monoclinic
Lattice: Primitive
S.G.: $P2_1$ (4)
Cell Parameters:
a 7.812 b 5.544 c 13.010
α β 98.660 γ
I/Icor: 1.76
Rad: CuKa1
Lambda: 1.54060
Filter:
d-sp: calculated
ICSD #: 072433

La2 (Ti2 O7)
Lanthanum Titanium Oxide
Ref: Calculated from ICSD using POWD-12++, (1997)
Ref: Schmalle, H.W et al., Acta Crystallogr., Sec. B: Structural Science, 49, 235 (1993)

2θ	Int-f	h	k	l	2θ	Int-f	h	k	l	2θ	Int-f	h	k	l
6.867	45	0	0	1	28.679	112	$\bar{2}$	0	3	37.283	17	2	1	3
11.449	1	1	0	0	28.679	112	2	0	2	37.836	6	1	2	2
12.439	4	$\bar{1}$	0	1	29.838	999 *	$\bar{2}$	1	2	37.932	6	$\bar{3}$	0	3
13.759	98	0	0	2	29.838	999 *	2	1	1	38.193	12	$\bar{3}$	1	1
14.227	14	1	0	1	32.155	295	0	1	4	38.552	31	3	1	0
16.544	4	$\bar{1}$	0	2	32.268	458	0	2	0	38.552	31	0	1	5
17.405	59	0	1	1	32.984	529	$\bar{2}$	1	3	38.648	21	0	2	3
19.229	5	1	0	2	32.984	529	2	1	2	39.009	23	$\bar{2}$	0	5
19.696	5	1	1	0	33.461	199	$\bar{2}$	0	4	39.009	23	2	0	4
20.295	7	$\bar{1}$	1	1	33.461	199	2	0	3	39.176	14	$\bar{3}$	1	2
21.141	475	0	1	2	34.344	3	1	2	0	39.476	14	$\bar{1}$	2	3
21.453	15	1	1	1	34.457	3	$\bar{3}$	0	1	39.588	10	3	0	2
22.130	11	$\bar{1}$	0	3	34.706	6	$\bar{1}$	2	1	40.005	180	$\bar{2}$	2	1
23.010	102	$\bar{2}$	0	1	34.850	10	3	0	0	40.005	180	2	2	0
23.010	102	2	0	0	34.850	10	0	0	5	40.151	103	3	1	1
25.096	8	2	0	1	35.041	13	$\bar{1}$	0	5	41.271	35	$\bar{2}$	2	2
25.096	8	1	1	2	35.228	6	0	2	2	41.271	35	2	2	1
26.256	93	0	1	3	35.529	1	$\bar{3}$	0	2	41.383	24	1	2	3
27.412	23	$\bar{1}$	1	3	35.677	5	1	1	4	41.383	24	$\bar{3}$	1	3
27.722	478	0	0	4	36.471	3	$\bar{1}$	2	2	41.913	6	1	1	5
28.139	286	$\bar{2}$	1	1	36.586	2	3	0	1	42.120	53	0	0	6
28.139	286	2	1	0	37.283	17	$\bar{2}$	1	4	42.419	117	$\bar{2}$	1	5

Figure A.34. JCPDS card of $La_2Ti_2O_7$.

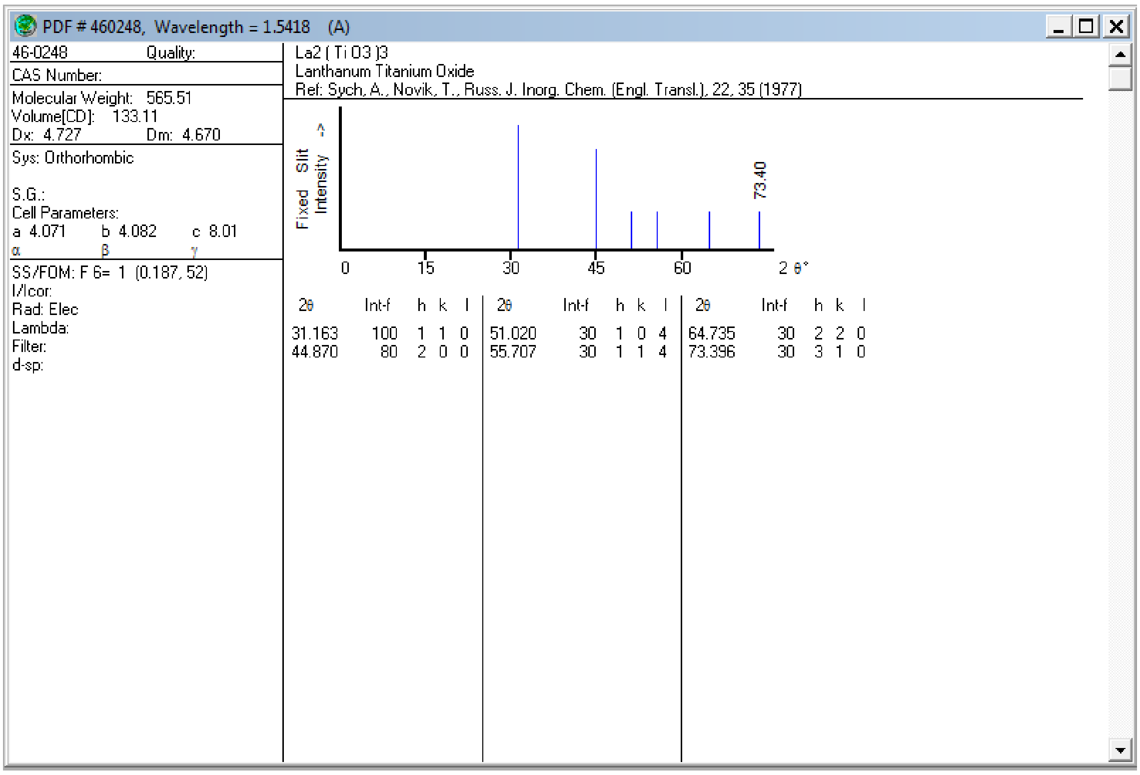

46-0248 Quality:

CAS Number:

Molecular Weight: 565.51
Volume[CD]: 133.11
Dx: 4.727 Dm: 4.670

Sys: Orthorhombic

S.G.:
Cell Parameters:
a 4.071 b 4.082 c 8.01
α β γ

SS/FOM: F 6= 1 (0.187, 52)
I/Icor:
Rad: Elec
Lambda:
Filter:
d-sp:

La2 (Ti O3)3
Lanthanum Titanium Oxide
Ref: Sych, A., Novik, T., Russ. J. Inorg. Chem. (Engl. Transl.), 22, 35 (1977)

2θ	Int-f	h	k	l	2θ	Int-f	h	k	l	2θ	Int-f	h	k	l
31.163	100	1	1	0	51.020	30	1	0	4	64.735	30	2	2	0
44.870	80	2	0	0	55.707	30	1	1	4	73.396	30	3	1	0

Figure A.35. JCPDS card of $La_2Ti_3O_9$.

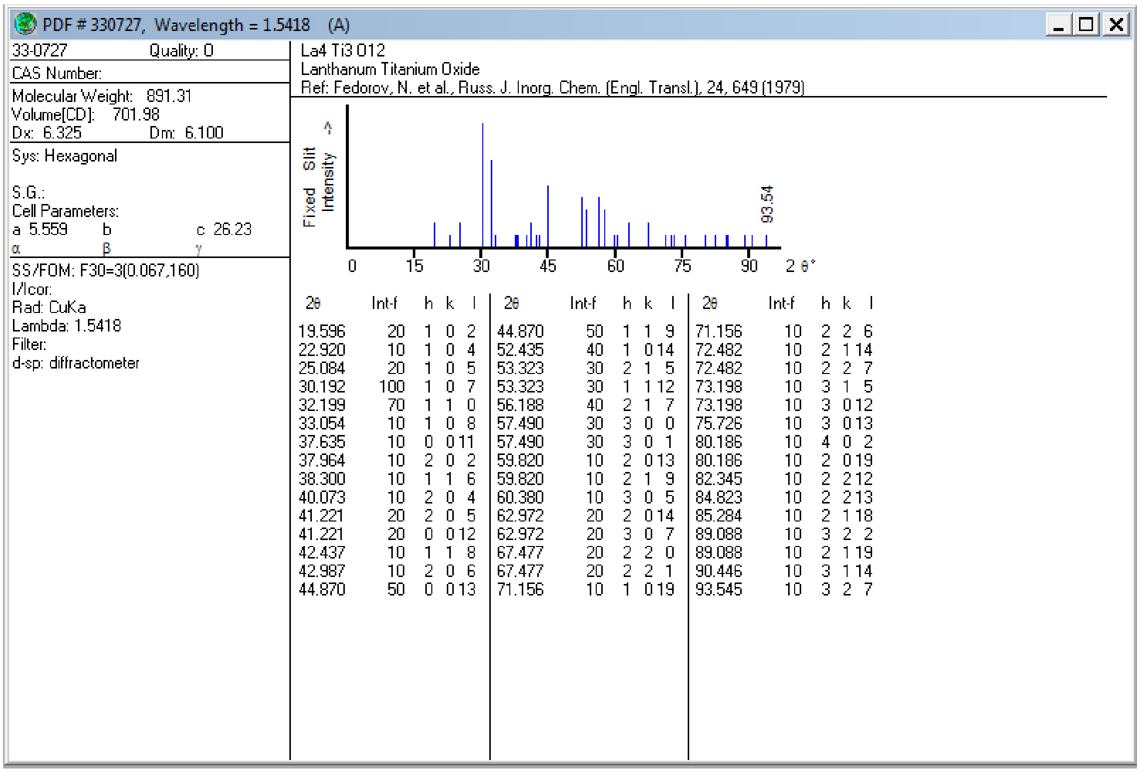

33-0727 Quality: 0

CAS Number:

Molecular Weight: 891.31
Volume[CD]: 701.98
Dx: 6.325 Dm: 6.100

Sys: Hexagonal

S.G.:
Cell Parameters:
a 5.559 b c 26.23
α β γ

SS/FOM: F30=3(0.067,160)
I/Icor:
Rad: CuKa
Lambda: 1.5418
Filter:
d-sp: diffractometer

La4 Ti3 O12
Lanthanum Titanium Oxide
Ref: Fedorov, N. et al., Russ. J. Inorg. Chem. (Engl. Transl.), 24, 649 (1979)

2θ	Int-f	h	k	l	2θ	Int-f	h	k	l	2θ	Int-f	h	k	l
19.596	20	1	0	2	44.870	50	1	1	9	71.156	10	2	2	6
22.920	10	1	0	4	52.435	40	1	0	14	72.482	10	2	1	14
25.084	20	1	0	5	53.323	30	2	1	5	72.482	10	2	2	7
30.192	100	1	0	7	53.323	30	1	1	12	73.198	10	3	1	5
32.199	70	1	1	0	56.188	40	2	1	7	73.198	10	3	0	12
33.054	10	1	0	8	57.490	30	3	0	0	75.726	10	3	0	13
37.635	10	0	0	11	57.490	30	3	0	1	80.186	10	4	0	2
37.964	10	2	0	2	59.820	10	2	0	13	80.186	10	2	0	19
38.300	10	1	1	6	59.820	10	2	1	9	82.345	10	2	2	12
40.073	10	2	0	4	60.380	10	3	0	5	84.823	10	2	2	13
41.221	20	2	0	5	62.972	20	2	0	14	85.284	10	2	1	18
41.221	20	0	0	12	62.972	20	3	0	7	89.088	10	3	2	2
42.437	10	1	1	8	67.477	20	2	2	0	89.088	10	2	1	19
42.987	10	2	0	6	67.477	20	2	2	1	90.446	10	3	1	14
44.870	50	0	0	13	71.156	10	1	0	19	93.545	10	3	2	7

Figure A.36. JCPDS card of $La_4Ti_3O_{12}$.

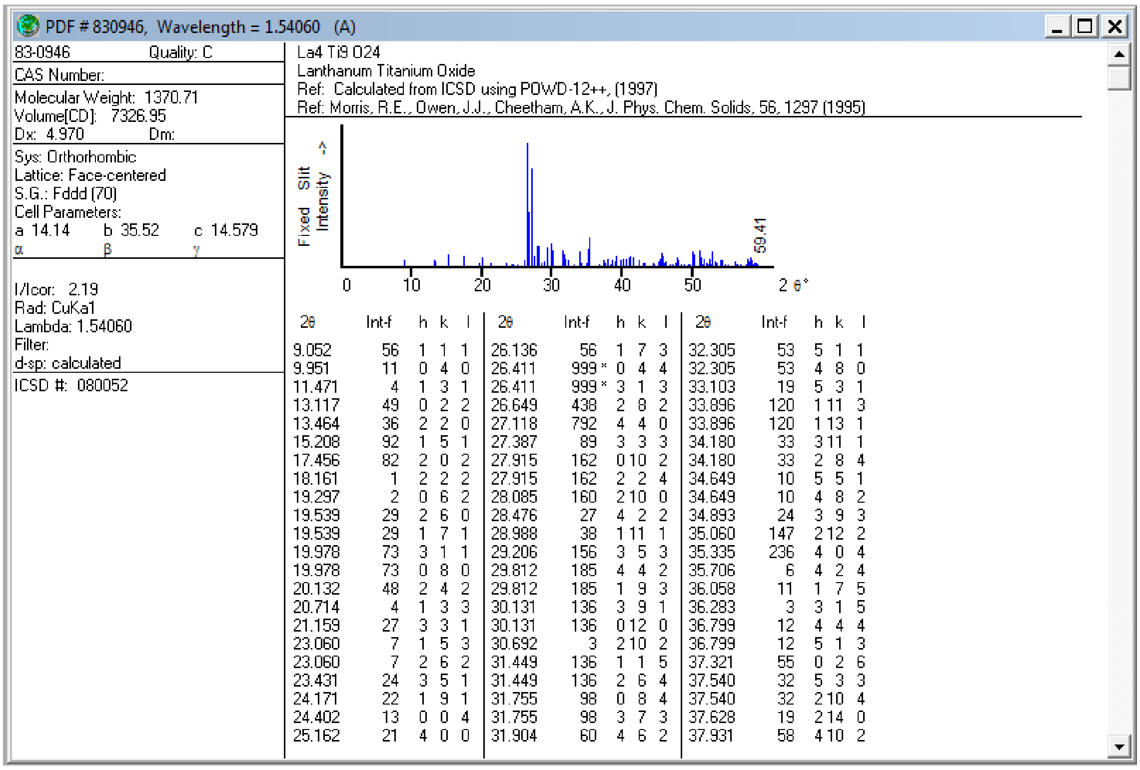

PDF # 830946, Wavelength = 1.54060 (A)

83-0946 Quality: C

CAS Number:

Molecular Weight: 1370.71
Volume[CD]: 7326.95
Dx: 4.970 Dm:

Sys: Orthorhombic
Lattice: Face-centered
S.G.: Fddd (70)
Cell Parameters:
a 14.14 b 35.52 c 14.579
α β γ

I/Icor: 2.19
Rad: CuKa1
Lambda: 1.54060
Filter:
d-sp: calculated

ICSD #: 080052

La4 Ti9 O24
Lanthanum Titanium Oxide
Ref: Calculated from ICSD using POWD-12++, (1997)
Ref: Morris, R.E., Owen, J.J., Cheetham, A.K., J. Phys. Chem. Solids, 56, 1297 (1995)

2θ	Int-f	h	k	l
9.052	56	1	1	1
9.951	11	0	4	0
11.471	4	1	3	1
13.117	49	0	2	2
13.464	36	2	2	0
15.208	92	1	5	1
17.456	82	2	0	2
18.161	1	2	2	2
19.297	2	0	6	2
19.539	29	2	6	0
19.539	29	1	7	1
19.978	73	3	1	1
19.978	73	0	8	0
20.132	48	2	4	2
20.714	4	1	3	3
21.159	27	3	3	1
23.060	7	1	5	3
23.060	7	2	6	2
23.431	24	3	5	1
24.171	22	1	9	1
24.402	13	0	0	4
25.162	21	4	0	0
26.136	56	1	7	3
26.411	999 *	0	4	4
26.411	999 *	3	1	3
26.649	438	2	8	2
27.118	792	4	4	0
27.387	89	3	3	3
27.915	162	0	10	2
27.915	162	2	2	4
28.085	160	2	10	0
28.476	27	4	2	2
28.988	38	1	11	1
29.206	156	3	5	3
29.812	185	4	4	2
29.812	185	1	9	3
30.131	136	3	9	1
30.131	136	0	12	0
30.692	3	2	10	2
31.449	136	1	1	5
31.449	136	2	6	4
31.755	98	0	8	4
31.755	98	3	7	3
31.904	60	4	6	2
32.305	53	5	1	1
32.305	53	4	8	0
33.103	19	5	3	1
33.896	120	1	11	3
33.896	120	1	13	1
34.180	33	3	11	1
34.180	33	2	8	4
34.649	10	5	5	1
34.649	10	4	8	2
34.893	24	3	9	3
35.060	147	2	12	2
35.335	236	4	0	4
35.706	6	4	2	4
36.058	11	1	7	5
36.283	3	3	1	5
36.799	12	4	4	4
36.799	12	5	1	3
37.321	55	0	2	6
37.540	32	5	3	3
37.540	32	2	10	4
37.628	19	2	14	0
37.931	58	4	10	2

Figure A.37. JCPDS card of $La_4Ti_9O_{24}$.

CURRICULUM VITAE

Education

Ph.D.	Chemical Engineering Department of Chemical Engineering Izmir Institute of Technology, Izmir, Turkey	July 2015
M.Sc.	Chemical Engineering Department of Chemical Engineering Hacettepe University, Ankara, Turkey	September 2008
B.S.	Chemical Engineering Department of Chemical Engineering Hacettepe University, Ankara, Turkey	June 2006

Projects

Nanodesign of rare-earth and transition metal incorporated titania nanocomposites and the investigation of their use in artificial photosynthesis, Türkiye Bilimsel ve Teknolojik Araştırma Kurumu Projesi, Proje no: 110M796, Proje Yürütücüsü: Dr. Muhsin Çiftçioğlu, Proje araştırma görevlisi: Hüsnü Arda Yurtsever, İZMİR, TURKEY, 2011-2014.

Kapiler elektrokromatografi için monolitik kolon üretim teknolojisinin geliştirilmesi, Türkiye Bilimsel ve Teknolojik Araştırma Kurumu Projesi, Proje no: 105M096, Proje Yürütücüsü: Dr. Ali Tuncel, Proje araştırma görevlisi: Hüsnü Arda Yurtsever, ANKARA, TURKEY, 2006-2008.

Peer Reviewed Publications

Photocatalytic Hydrogen Production with Erbium Doped Titania Powders, Hüsnü Arda Yurtsever, Muhsin Çiftçioğlu, Journal of Engineering and Fundamentals, 2(1), 26-37, 2015.

Capillary electrochromatography with new monolithic stationary phase based on a fluorinated monomer, trifluoroethyl methacrylate, Arda Yurtsever, Berna Saraçoğlu, Ali Tuncel, Electrophoresis, 30, 589–598, 2009.

Conference Proceedings and Presentations

Investigation of The Photocatalytic Water Splitting Activities of Er^{3+}/Nd^{3+} Doped TiO_2 Powders, Hüsnü Arda Yurtsever, Muhsin Çiftçioğlu, ECOSS30, 2014, TÜRKİYE, (Poster).

Phase Structure and Optical Properties of Rare Earth Doped TiO_2 Powders, Hüsnü Arda Yurtsever, Ahmet Sadık Yorulmaz, Muhsin Çiftçioğlu, ADVANCED MATERIALS, 2013, TÜRKİYE, (Oral)